frontiers | Research Topics

Planning and operation strategies for enhancing power system flexibility in low-carbon energy transition

Edited by
Mingfei Ban, Weijia Liu, Ying Xu and Yiyun Yao

Published in
Frontiers in Energy Research

ISSN 1664-8714
ISBN 978-2-8325-4501-0
DOI 10.3389/978-2-8325-4501-0

About Frontiers

Frontiers is more than just an open access publisher of scholarly articles: it is a pioneering approach to the world of academia, radically improving the way scholarly research is managed. The grand vision of Frontiers is a world where all people have an equal opportunity to seek, share and generate knowledge. Frontiers provides immediate and permanent online open access to all its publications, but this alone is not enough to realize our grand goals.

Frontiers journal series

The Frontiers journal series is a multi-tier and interdisciplinary set of open-access, online journals, promising a paradigm shift from the current review, selection and dissemination processes in academic publishing. All Frontiers journals are driven by researchers for researchers; therefore, they constitute a service to the scholarly community. At the same time, the *Frontiers journal series* operates on a revolutionary invention, the tiered publishing system, initially addressing specific communities of scholars, and gradually climbing up to broader public understanding, thus serving the interests of the lay society, too.

Dedication to quality

Each Frontiers article is a landmark of the highest quality, thanks to genuinely collaborative interactions between authors and review editors, who include some of the world's best academicians. Research must be certified by peers before entering a stream of knowledge that may eventually reach the public - and shape society; therefore, Frontiers only applies the most rigorous and unbiased reviews. Frontiers revolutionizes research publishing by freely delivering the most outstanding research, evaluated with no bias from both the academic and social point of view. By applying the most advanced information technologies, Frontiers is catapulting scholarly publishing into a new generation.

What are Frontiers Research Topics?

Frontiers Research Topics are very popular trademarks of the *Frontiers journals series*: they are collections of at least ten articles, all centered on a particular subject. With their unique mix of varied contributions from Original Research to Review Articles, Frontiers Research Topics unify the most influential researchers, the latest key findings and historical advances in a hot research area.

Find out more on how to host your own Frontiers Research Topic or contribute to one as an author by contacting the Frontiers editorial office: frontiersin.org/about/contact

Planning and operation strategies for enhancing power system flexibility in low-carbon energy transition

Topic editors

Mingfei Ban — Northeast Forestry University, China

Weijia Liu — National Renewable Energy Laboratory (DOE), United States

Ying Xu — Harbin Institute of Technology, China

Yiyun Yao — National Renewable Energy Laboratory (DOE), United States

Citation

Ban, M., Liu, W., Xu, Y., Yao, Y., eds. (2024). *Planning and operation strategies for enhancing power system flexibility in low-carbon energy transition*. Lausanne: Frontiers Media SA. doi: 10.3389/978-2-8325-4501-0

Table of contents

frontiers | Frontiers in Energy Research

TYPE Original Research
PUBLISHED 10 May 2023
DOI 10.3389/fenrg.2023.1182737

OPEN ACCESS

EDITED BY
Weijia Liu,
National Renewable Energy Laboratory (DOE), United States

REVIEWED BY
Hongxun Hui,
University of Macau, China
Mao Yang,
Northeast Electric Power University, China

*CORRESPONDENCE
Yibo Wang,
wangyibofangyuan@126.com

RECEIVED 09 March 2023
ACCEPTED 12 April 2023
PUBLISHED 10 May 2023

CITATION
Yuan Z, Wang Y, Xu Y, Liu C, Ge W, Cai G, Zhou J, Sun A, Liu X and Li B (2023), Day-ahead and intra-day two-stage low-carbon economic scheduling method considering multi-form energy-intensive load.
Front. Energy Res. 11:1182737.
doi: 10.3389/fenrg.2023.1182737

Day-ahead and intra-day two-stage low-carbon economic scheduling method considering multi-form energy-intensive load

Zhijun Yuan[1], Yibo Wang[1]*, Yueyang Xu[1], Chuang Liu[1], Weichun Ge[2], Guowei Cai[1], Jianing Zhou[1], Ao Sun[3], Xin Liu[3] and Baihe Li[4]

[1]Key Laboratory of Modern Power System Simulation and Control and Renewable Energy Technology, Northeast Electric Power University, Jilin, China, [2]State Grid Liaoning Electric Power Supply Co, Ltd, Shenyang, China, [3]Changchun Power Supply Company, State Grid Jilin Electric Power Co, Ltd, Changchun, China, [4]Jilin Thermal Power Plant of Guoneng Jilin Longhua Thermal Power Co, Ltd, Jilin, China

To solve the problem of the large gap in the regulation resources of the power system due to the large number of wind power connected to the grid and to help achieve the strategic energy goal of "carbon neutrality and carbon peaking," the demand-side adjustable energy-intensive load is taken as the research object in this paper, and a two-stage low-carbon economic scheduling method of the wind power system with multi-form energy-intensive load (MEL) is proposed. First, the operating characteristics of the system with MEL are analyzed. At the same time, a refined mathematical model that conforms to the actual operation characteristics is established. Then, the complementary low-carbon characteristics of the source-charge side and the difference in the response characteristics of the demand-side MEL are considered. Meanwhile, combining with the energy storage system, a day-ahead and intra-day two-stage low-carbon economic scheduling model of the wind power system with MEL is constructed. Finally, an example of the improved IEEE-39 bus system is analyzed to verify the effectiveness of the proposed scheduling method in the low-carbon economic scheduling of wind power systems and to provide a reference for power grid scheduling.

KEYWORDS

multi-form energy-intensive load, day-ahead and intra-day two-stage, wind power consumption, operating costs, low-carbon economic scheduling

1 Introduction

On 22 September 2020, China announced at the 75th United Nations General Assembly that "China strives to peak its carbon dioxide emissions by 2030 and works to achieve its carbon neutrality goal by 2060." The decarbonization of the power system is one of the most important means of achieving this goal. On the one hand, to achieve the goal of "carbon peaking and carbon neutrality," it is necessary to explore the low-carbon characteristics of the source side of the power system, to transform conventional thermal power units into carbon capture units on the power side, and to use CO_2 produced by them for storage, so that

carbon capture units can be used as an ideal complementary power source for wind power (Guo et al., 2022; Jiaming et al., 2015). On the other hand, the goal of "carbon neutrality and carbon peaking" will inevitably lead to the rapid development of wind power, which has a low marginal cost of system generation and no carbon emissions. According to the "List of Basic Electricity Statistics for 2020" published by the China Electricity Council, the installed capacity of wind power in 2020 will be as high as 281.65 million kilowatts, a year-on-year increase of 34.66%. While wind power output has day-to-day variability, uncertainty, and anti-regulation characteristics (Luo et al., 2014; Bao et al., 2016; Ge et al., 2019), its large-scale grid connection will lead to a large gap in power system regulation resources.

The demand side of important components in the power system as a regulating resource is an effective way to solve the aforementioned problem and has achieved rapid development in recent years (Jia et al., 2022; Afzalan and Jazizadeh, 2020; Tindemans et al., 2015; Teng et al., 2015). The representative energy-intensive load in the controllable load has attracted much attention from regulatory resources because of its characteristics of large monomer volume, fast response speed, and high level of production automation (Yang et al., 2020; Liao et al., 2018; Li et al., 2019). In 2022, the total electricity consumption of China's four major energy-intensive industries was 2,301.9 billion kWh. Among them, the electricity consumption of the chemical industry was 546.1 billion kWh, the electricity consumption of the building materials industry was 401.7 billion kWh, the electricity consumption of the ferrous metal smelting industry was 609 billion kWh, and the electricity consumption of the non-ferrous metal smelting industry was 745.2 billion kWh. China has built energy-intensive enterprises near large-scale new energy bases in the northwest, northeast, and Inner Mongolia Autonomous Region, which has practical engineering significance for local wind power consumption. Therefore, the participation of energy-intensive industries in power grid regulation has huge economic and environmental benefits.

The participation of high energy load in power grid regulation has existed at home and abroad, and good results have been achieved. Peng et al. (2017) comprehensively considered the high energy load and the operating characteristics of wind power and established a source–load coordinated multi-objective optimization model with the goal of maximum wind power consumption and minimum system operating cost, which provides a reference for dispatchers. Liu et al. (2015) considered the cross-sectional power constraint and load matching upward adjustment capacity and the degree of load participation and proposed a quantitative pre-assessment method for wind/photovoltaic capacity of power grid with energy-intensive load participation, which has important engineering practical significance for improving the wind power consumption level of the system. Based on the actual situation of new energy in Gansu Province, Li et al. (2016) analyzed its local consumption potential, relying on the "double alternative" strategy and considering the operation characteristics of high energy load of smart parks, and maximized the local consumption level of new energy. From the aforementioned research, it can be seen that the participation of energy-intensive load in system regulation is of far-reaching significance. The researchers have made in-depth discussions on source–load coordinated scheduling, market assistance, evaluation methods, energy policies, *etc.*, which have slowed down the regulation pressure of conventional units, reduced the operating cost of the power system, and improved the wind power consumption level of the power system. However, the aforementioned literature mainly focuses on the research of single-form energy-intensive load, and relatively few studies consider the actual operating characteristics of energy-intensive enterprises. The analysis of MEL is relatively rare, and the impact of response differences and actual operation characteristics of MEL on power grid regulation and control is not considered. Therefore, to more accurately tap the adjustment potential and flexibility of system demand-side resources, this paper considers those MELs that meet the actual operation characteristics and use them to regulate for low-carbon economic optimization and dispatch of the wind power system.

At the same time, with the constant maturity of energy storage technology, new energy storage technologies have many advantages, such as high security, high flexibility, and high economy; combined with the successive introduction of national energy-storage-related policies and the increasingly perfect business model of energy storage, the market prospect of energy storage participation in grid regulation and control has become increasingly broad, which is of far-reaching significance for the safe and flexible operation of the power grid economy (Neubauer and Simpson, 2013; Shi et al., 2022). At the same time, carbon capture technology is constantly improving, and operating costs are decreasing (Ji et al., 2013; Akbari-Dibavar et al., 2021). At present, ordinary carbon capture technologies mainly include carbon capture and storage (CCS) and carbon capture, utilization, and storage (CCUS). Two technologies are suitable for different scenarios. Research has shown that in the context of low carbon prices, promoting CCS technology that focuses on storage is constrained and limited by high costs. Compared to CCS, CCUS technology, which considers carbon dioxide as a resource and focuses on recycling, has a greater likelihood of being promoted and applied in the future. At the same time, the country should vigorously support CCUS technological innovation, carry out CCUS pilot demonstrations in key industries in an orderly manner, and provide preferential financial and tax policies for carbon capture projects. Its large-scale application is possible, which will bring substantial breakthroughs to the low-carbon operation of the power system at the source.

In summary, to solve the problem of the large gap in power system regulation resources caused by a high proportion of new energy connected to the grid and to accelerate the realization of the strategic goal of "dual carbon," this paper takes the load of the load-side multi-form adjustable energy-intensive industry as the regulatory object. At the same time, by transforming conventional units into carbon capture units and load-side energy storage to further tap the low carbon and flexibility of the system, a low-carbon economic dispatching method of wind power systems considering MEL is proposed. It improves the level of wind power consumption of the system, alleviates the pressure of regulating resources, and concurrently takes into account the economy, low carbon, and flexibility of the system to provide a reference for power grid dispatching.

The remainder of the paper is organized as follows: in **Section 2**, the operating characteristics of polymorphic MEL are analyzed and a mathematical model that conforms to the actual operating characteristics is established, comprehensively considering the

flexibility of low-carbon complementarity of source–load storage. In Section 3, a day-ahead and intra-day low-carbon economic dispatch model for wind power systems with MEL is established. The improved IEEE-39 node is used to conduct a case analysis to verify the effectiveness of the proposed method in Section 4. Conclusion is drawn in Section 5

2 Analysis and modeling of MEL

2.1 Analysis of characteristics

Energy-intensive load is the load whose energy value accounts for more than 30%. According to the differences in operation and regulation characteristics, the energy-intensive load can be divided into discrete, continuous, and time-shifted forms, as shown in **Figure 1**. Its main distribution is in several industries, such as ferrous metals, non-ferrous metals, machining, petrochemicals, and construction materials.

Discrete adjustable energy-intensive loads have many characteristics, such as large regulation capacity, small load fluctuations, stable regulation characteristics, and relatively slow response times, and cannot be continuously regulated. In contrast, minimum regulation intervals should be met. The regulation characteristics of the continuous adjustable energy-intensive load are as follows: small adjusting capacity, short adjusting interval time, and can make rapid adjustment repeatedly according to the demand. The adjustment characteristics of the time-shift type with the adjustable energy-intensive load are as follows: the adjustment speed is relatively slow; in the scheduling period, the load power waveform is unchanged before and after adjustment; and at the same time, the minimum transfer duration constraint should be satisfied. A comparison of the regulation characteristics of the three forms of energy-intensive load is shown in **Table 1**.

2.2 Modeling of MEL

Since energy-intensive load has complex operating characteristics and the enterprise has the pursuit of profit maximization behavior, the modeling should take into account not only the operating characteristics of the energy-intensive load but also the operating costs of the enterprise. The cost of regulation comprises the cost incurred by the time-of-use electricity price before and after load regulation and the subsidy paid by the electricity supplier to customers participating in incentivized demand response. An advanced modeling of each form of energy-intensive load according to its operational and regulatory characteristics is given as follows:

1) Discrete adjustable energy-intensive load. Considering the operational characteristics and cost constraints of the discrete adjustable energy-intensive load, the model is established as follows:

Power constraint:

$$P_{\mathrm{lsh}}(t) = P_{\mathrm{1s-base}}(t) + P_{\mathrm{ls-up}}(t) - P_{\mathrm{ls-down}}(t). \tag{1}$$

Adjust the upper and lower limit constraints:

$$\begin{cases} S_1(t) P_{\mathrm{ls-up-min}} \le P_{\mathrm{ls-up}}(t) \le S_1(t) P_{\mathrm{ls-up-max}} \\ S_2(t) P_{\mathrm{ls-down-min}} \le P_{\mathrm{ls-down}}(t) \le S_2(t) P_{\mathrm{ls-down-max}}. \end{cases} \tag{2}$$

State constraint:

$$S_1(t) + S_2(t) \le 1. \tag{3}$$

Number of adjustment constraints:

$$0 \le \sum_{t=2}^{T} \left(|S_1(t) - S_1(t-1)| + |S_2(t) - S_2(t-1)| \right)/2 \le M. \tag{4}$$

Adjusting the duration constraints:

$$\begin{cases} |S_1(t-1) - S_1(t)|\,|S_1(t-1)| \left\{ T_1 - \sum_{t-1-T_1}^{t-1} |S_1(t)| \right\} \ge 0, \\ |S_2(t-1) - S_2(t)|\,|S_2(t-1)| \left\{ T_2 - \sum_{t-1-T_2}^{t-1} |S_2(t)| \right\} \ge 0. \end{cases} \tag{5}$$

Planned production constraint:

$$\sum_{t=1}^{T} \lambda_1 \left(P_{\mathrm{ls-base}}(t) + P_{\mathrm{1s-up}}(t) - P_{\mathrm{ls-down}}(t) \right) \ge E_{\mathrm{ls-plan}}. \tag{6}$$

Adjusting cost:

$$C_{\mathrm{ls}} = \sum_{t=1}^{T} \left(P_{\mathrm{ls-up}}(t) - P_{\mathrm{ls-down}}(t) \right) C(t) + \sum_{t=1}^{T} K_{\mathrm{ls}}(t), \tag{7}$$

where $P_{\mathrm{lsh}}(t)$ is the power of the discrete adjustable energy-intensive load after regulation at time t, $P_{\mathrm{1s\text{-}bass}}(t)$ is the base load at time t, $P_{\mathrm{ls\text{-}up}}(t)$ is the amount of upward adjustment at moment t, and $P_{\mathrm{ls\text{-}down}}(t)$ is the amount of downward adjustment at moment t; $S_1(t)$ is the discrete adjustable energy-intensive load up-regulation state decision variable, $S_2(t)$ is the load down state decision variable, $P_{\mathrm{ls\text{-}up\text{-}min}}$ is the minimum value of upregulation, $P_{\mathrm{ls\text{-}up\text{-}max}}$ is the maximum value of upregulation, $P_{\mathrm{ls\text{-}down\text{-}min}}$ is the minimum value of downregulation, $P_{\mathrm{ls\text{-}down\text{-}max}}$ is the maximum value of downregulation, and M is the maximum number of regulation; T_1 is the maximum upregulation duration and T_2 is the maximum downregulation duration; λ_1 is the regulated efficiency and $E_{\mathrm{ls\text{-}plan}}$ is the daily planned output; and C_{ls} is the total cost of load regulation, $C(t)$ is the load time-of-use price at time t, and $K_{\mathrm{ls}}(t))$ is the response subsidy cost at time t.

2) Continuous adjustable energy-intensive load. Considering the operational characteristics and cost constraints of the continuous adjustable energy-intensive load, the model is established as follows:

Power constraint:

$$P_{\mathrm{lxh}}(t) = P_{\mathrm{lx-base}}(t) + P_{\mathrm{lx-up}}(t) - P_{\mathrm{lx-down}}(t). \tag{8}$$

Output upper and lower bound constraints:

$$P_{\mathrm{lx-min}} \le P_{\mathrm{lxh}}(t) \le P_{\mathrm{lx-max}}. \tag{9}$$

Regulation rate constraint:

$$P_{\mathrm{lx-down}}(t) \le P_{\mathrm{lxh}}(t) - P_{\mathrm{lxh}}(t-l) \le P_{\mathrm{lx-up}}(t). \tag{10}$$

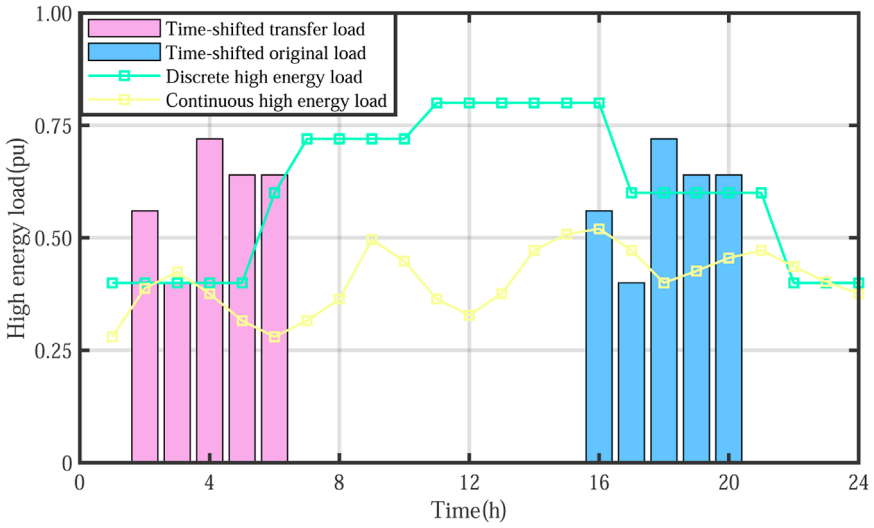

FIGURE 1
Operational characteristics of MEL.

TABLE 1 MEL regulation characteristics.

Energy-intensive load type	Regulation type	Range of adjustment	Example
Discrete	Discrete regulation	Wide range	Electrolytic aluminum
Continuous	Continuous regulation	Small range	Iron alloy
Time-shifted	Time-shifted regulation	—	Peripheral equipment

Upper and lower regulation limit constraints:

$$\begin{cases} S_3(t)P_{\text{lx-up-min}} \le P_{\text{lx-up}}(t) \le S_3(t)P_{\text{lx-up-max}}, \\ S_4(t)P_{\text{lx-down-min}} \le P_{\text{lx-down}}(t) \le S_4(t)P_{\text{lx-down-max}}. \end{cases} \tag{11}$$

State constraint:

$$S_3(t) + S_4(t) \le 1. \tag{12}$$

Production constraint:

$$\sum_{t=1}^{T} \lambda_k P_{\text{lxh}}(t) \ge E_{\text{lx-plan}}. \tag{13}$$

Adjusting cost:

$$C_{\text{lx}} = \sum_{t=1}^{T} \left(P_{\text{lx-up}}(t) - P_{\text{lx-down}}(t)\right) C(t) + \sum_{t=1}^{T} K_{\text{lx}}(t), \tag{14}$$

where $P_{\text{lxh}}(t)$ is the power at time t after the regulation of the continuous regulated energy-intensive load, $P_{\text{lx-up}}(t)$ is the upregulation at time t, and $P_{\text{lx-down}}(t)$ is the downregulation at time t; $P_{\text{lx-min}}$ is the minimum output value and $P_{\text{lx-max}}$is the maximum power output; $P_{\text{lx-down}}(t)$ is the regulated downhill rate and $P_{\text{lx-up}}(t)$is the regulated uphill rate; $S_3(t)$ is the load up decision variable and $S_4(t)$ is the load down decision variable; and λ_k is the regulated efficiency and $E_{\text{lx-plan}}$is the continuous energy-intensive load daily production plan; C_{lx} is the total cost of regulating the load, $C(t)$ is the load time-of-use electricity price at time t, and $K_{\text{lx}}(t)$ is the response subsidy cost at time t.

3) Time-shifted adjustable energy-intensive load

Considering the operational characteristic and cost constraints of time-shifted adjustable energy-intensive load, the model is established as follows:

Power constraint:

$$P_{\text{syh}}(t) = S_5(t)P_{\text{syq}}(t). \tag{15}$$

Time-shift time constraint:

$$\left\{|S_5(t-1)|\,|S_5(t-1) - S_5(t)|\left\{\sum_{t-1-T_{\min}}^{t-1} |S_5(t)| - T_{\min}\right\} \ge 0 \right. \tag{16}$$

Planned production constraint:

$$\sum_{t=1}^{T} \lambda_j P_{\text{syh}}(t) \ge E_{sy-\text{plan}}. \tag{17}$$

Adjusting cost:

$$C_{\text{sy}} = \sum_{t=1}^{T} \left(P_{\text{syh}}(t) - P_{\text{syq}}(t)\right) C(t) + \sum_{t=1}^{T} K_{\text{sy}}(t), \tag{18}$$

where $P_{\text{syq}}(t)$ is the load capacity at moment t before regulation and $P_{\text{syh}}(t)$ is the load capacity at moment t after regulation; λ_j is the regulated work efficiency and $S_5(t)$ is the time-shifted decision variable at moment t; $T_{\min}$ is the minimum shift duration constraint; $E_{sy\text{-plan}}$is the time-shifted energy-intensive load daily production plan; and C_{sy} is the total cost of regulating the load and $K_{\text{sy}}(t)$ is the response subsidy cost at moment t.

3 Day-ahead and intra-day two-stage low-carbon economic scheduling model

This paper comprehensively considers the energy time-shifting and low-carbon characteristics of carbon capture units under the comprehensive operation mode of the source side and the zero-carbon and low-cost characteristics of wind power, and MEL on the load side and the configured energy storage system are jointly incorporated into the low-carbon economic dispatch to realize the mining of low-carbon characteristics on both sides of the source and load. At the same time, to reduce the adverse impact caused by the error between the planned output of wind power and the intra-day forecast value through the difference in the response characteristics of MEL, it is reasonably arranged to participate in the scheduling plan of two different periods of day-ahead and intra-day. Then, a two-stage low-carbon economic dispatching method of the wind power system with MEL is proposed. In the day-ahead low-carbon economy dispatch stage, conventional and carbon capture units are taken as the control objects on the source side; on the load side, the discrete adjustable energy-intensive load, and time-shifted adjustable energy-intensive load with slow response speed and non-continuous adjustment suitable for regulation in a long time scale are taken as the control objects, and the wind power forecast and output in the previous stage are dynamically responded and a day-long low-carbon economic dispatching plan considering the source–load coordinated scheduling characteristics is formulated to deeply explore the low-carbon and economic nature of the system. In the intra-day stage, based on the day-ahead scheduling, the energy storage system with fast response speed and continuous regulation suitable for optimal regulation and control under a short time scale is taken as the adjustment object, and the dynamic response to the wind power forecast and output in the intra-day stage is formulated, taking into account the economy and flexibility of system operation to provide a reference for power grid dispatching. A two-stage low-carbon economic scheduling method for the wind power system with MEL is proposed. The process is shown in Figure 2.

3.1 Day-ahead scheduling model

During the day-ahead scheduling phase, the time-shifted adjustable energy-intensive load and the discrete adjustable energy-intensive load, which have a relatively slow response, are used as the regulation objects. The total operating cost of the system is minimized and used as the objective function, and the scheduling plan is made 24 h in advance, with a scheduling time scale of 1 h. In this case, the continuous adjustable energy-intensive load is considered part of the conventional load and does not participate in the system regulation.

Objective function:

$$F_1 = \min\left(C_{cg} + C_{cb} + C_{aw} + C_{ls} + C_{sy} + C_{nh} + C_{fc} + C_{zj} + C_{cd} + C_{cgc}\right), \tag{19}$$

TABLE 2 Thermal power unit parameters.

Unit number	Max/min output/MW	Cost parameter/(a/b/c)	Carbon emission intensity/(t/MW•h)
G1	450/150	0.00013/0.232/16.0073	0.90
G2	130/20	0.0012/0.28/4.0736	0.98
G3	300/60	0.0001/0.25/10.45	0.95
G4	120/47	0.0011/0.28/4.0536	0.99

$$\begin{cases} C_{cg} = \sum_{i=1}^{N_{cg}} \sum_{t=1}^{24} U_i(t)\left(a_i P_{cg,i}^2(t) + b_i P_{cg,i}(t) + c_i\right), \\ C_{cb} = \sum_{j=1}^{N_{cb}} \sum_{t=1}^{24} U_j(t)\left(a_j P_{cb,j}^2(t) + b_j P_{cb,j}(t) + c_j\right), \\ C_{aw} = K_{aw} \sum_{t=1}^{T} \left(P_{wfore}(t) - P_w(t)\right), \\ C_{nh} = \sum_{j=1}^{N_{cb}} \sum_{t=1}^{24} \left(P_{Dj}(t) + P_{Bj}(t)\right) C(t), \\ C_{fc} = K_{fc} \sum_{j=1}^{N_{cb}} \sum_{t=1}^{24} E_{j,total-cog}(t) \\ C_{zj} = \dfrac{C_{tb}(1+\alpha)^{N_{zj}}\alpha}{365\left((1+\alpha)^{N_{zj}} - 1\right)} + \dfrac{C_{ry} V_{ry} (1+\alpha)^{N_{ry}}\alpha}{365\left((1+\alpha)^{N_{ry}} - 1\right)}, \\ C_{cd} = K_c \sum_{j=1}^{N_{cb}} \sum_{t=1}^{24} \left(E_{cb,j}(t) - \beta E_{j,total-co,}(t)\right), \\ C_{cgc} = K_c \sum_{i=1}^{N_{cg}} \sum_{t=1}^{24} P_{cg,i}(t), \end{cases} \tag{20}$$

where F_1 is the total operating cost of the economic scheduling day-ahead of the system and C_{cg} is the operating cost of a conventional thermal power unit. $U_i(t)$ is the start–stop state of the conventional thermal power unit i at time t. a_i, b_i, c_i are the coal consumption cost coefficients for the conventional thermal power unit i. $P_{cg,i}(t)$ is the output of the conventional thermal power unit i at time t, C_{cb} is the operating cost of the carbon capture unit, and $U_j(t)$ is the start–stop state of the carbon capture unit j at time t. a_j, b_j, c_j are the coal consumption cost coefficients of the carbon capture unit j and $P_{cb,j}$ is the output of the carbon capture unit j at time t. C_{aw} is the cost of wind abandonment. K_{aw} is the cost per unit of wind abandonment. $P_{wfore}(t)$ is the predicted output of wind power at time t and $P_w(t)$ is the planned day-ahead output value of wind power at time t. C_{nh} is the energy consumption cost of the carbon capture power plant, N_{cb} is the number of carbon capture units, $P_{Bj}(t)$ is the operating energy consumption of the carbon capture unit j at time t, and $P_{Dj}(t)$ is the fixed energy consumption of the carbon capture unit j. C_{zj} is the depreciation cost, N_{zj} is the depreciation period, and *alpha* is the discount rate for the carbon capture unit project. C_{tb} is the total cost of capture equipment for the carbon capture plant and V_{ry} is the cost per unit volume of solution memory. N_{ry} is the volume of the solution memory and N_{ry} is the solution memory depreciable life; C_{fc} is the total cost of sequestration of the carbon capture unit and K_{fc} is the cost per unit of CO_2 sequestration. C_{cb} is the capture cost of the carbon capture unit and $E_{cb,j}(t)$ is the total amount of CO_2 produced by the carbon capture unit j at time t. K_{cd} is the carbon emission intensity of the carbon capture unit. $P_{cb,j}(t)$ is the total output of the carbon capture unit j at time t. $E_{j,total-co,}t)$ is the total amount of CO_2 captured by the carbon capture unit j. β is the capture efficiency of carbon capture equipment and K_c is the unit cost of carbon emissions. C_{cgc} is the total cost of carbon emissions from conventional thermal power units.

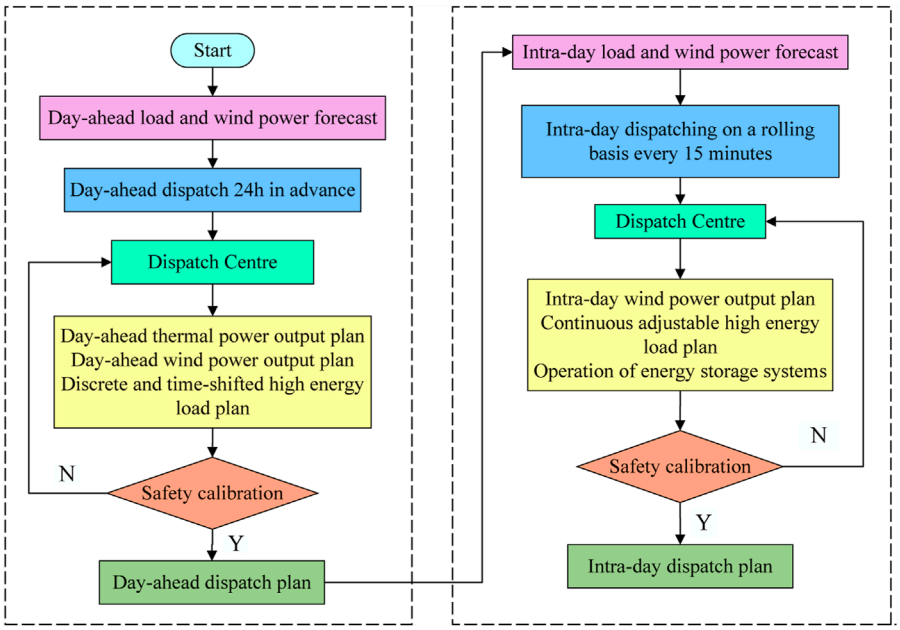

FIGURE 2
Flow chart of the two-stage scheduling method.

TABLE 3 Various adjustable energy-intensive load adjustment parameters.

Energy-intensive load	Base load/MW	Upward power adjustment/MW	Downward power adjustment/MW
Discrete	500	86	50
Continuous	150	10	10
Time-shifted	—	—	—

TABLE 4 Various adjustable energy-intensive load adjustment parameters.

Battery energy storage parameter	Parameter value
Battery storage capacity	200 MWh
Initial SOC of battery storage	0.25
Upper limit and lower limit of SOC	0.9/0.1
Energy storage charge and discharge efficiency	0.95
Upper/lower limit of energy storage charge and discharge power	50 MW/10 MW

The relevant constraints to be considered during the economic scheduling phase are as follows:

1) System power balance constraint:

$$\sum_{i=1}^{N_{cg}} P_{cg,i}(t) + \sum_{j=1}^{N_{cb}} P_{cb,j}(t) + P_w(t) = P_{cg}(t) + P_{lsh}(t) + P_{lxh}(t). \quad (21)$$

2) Wind power output constraint:

$$0 \le P_w(t) \le P_{wfore}(t). \quad (22)$$

3) Upper and lower output limit constraints for the conventional unit:

$$U_i(t) P_{cg,min,i} \le P_{cg}(t) \le U_i(t) P_{cg,max,i}. \quad (23)$$

4) Climbing constraints for the conventional unit:

$$\begin{cases} P_{cg,i}(t) - P_{cg,i}(t-1) \le U_i(t) R_i^{up}, \\ P_{cg,i}(t-1) - P_{cg,i}(t) \le U_i(t) R_i^{down}. \end{cases} \quad (24)$$

5) System rotation standby. The system rotation standby consists of conventional thermal and carbon capture units:

$$\begin{cases} \sum_{i=1}^{N_{cg}} P_{cg,i}(t) + \sum_{j=1}^{N_{cb}} P_{cb,j}(t) - \sum_{i=1}^{N_{cg}} P_{cgmin,i} - \sum_{j=1}^{N_{cb}} P_{cbmin,j} \ge R^{down}, \\ \sum_{i=1}^{N_{cg}} P_{cgmax,i} + \sum_{j=1}^{N_{cb}} P_{cbmax,j} - \sum_{i=1}^{N_{cg}} P_{cg,i}(t) - \sum_{j=1}^{N_{cb}} P_{cb,j}(t) \ge R^{up}. \end{cases} \quad (25)$$

6) Operational constraint on the carbon capture unit. According to the energy consumption characteristics of carbon capture units, the related constraints such as the flue gas diversion ratio constraint, carbon capture quantity constraint, and energy consumption of carbon capture equipment are considered. Among them, the energy consumption of carbon capture equipment is mainly composed of fixed and operational energy consumption. In addition, the output and climbing constraints of the carbon capture units are the same as those of the conventional units, which are not explained here. The mathematical model of carbon capture units is as follows:

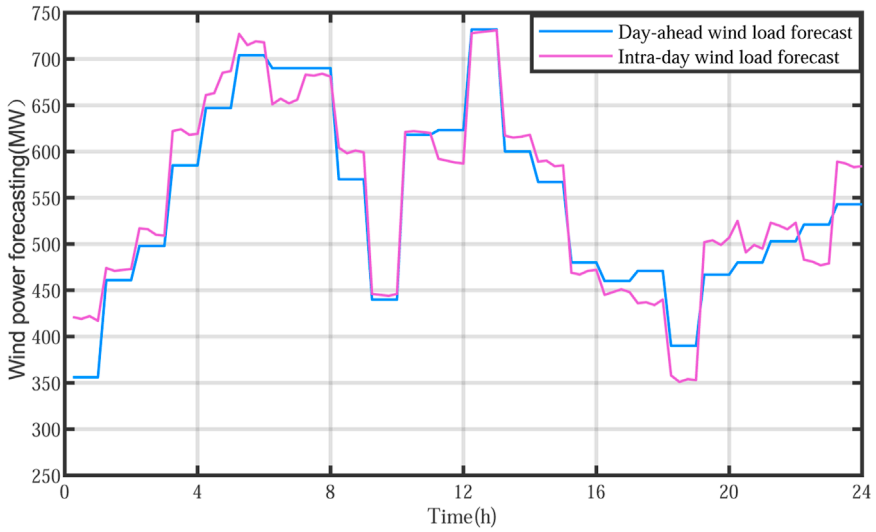

FIGURE 3
Forecast values of wind power (day-ahead and intra-day).

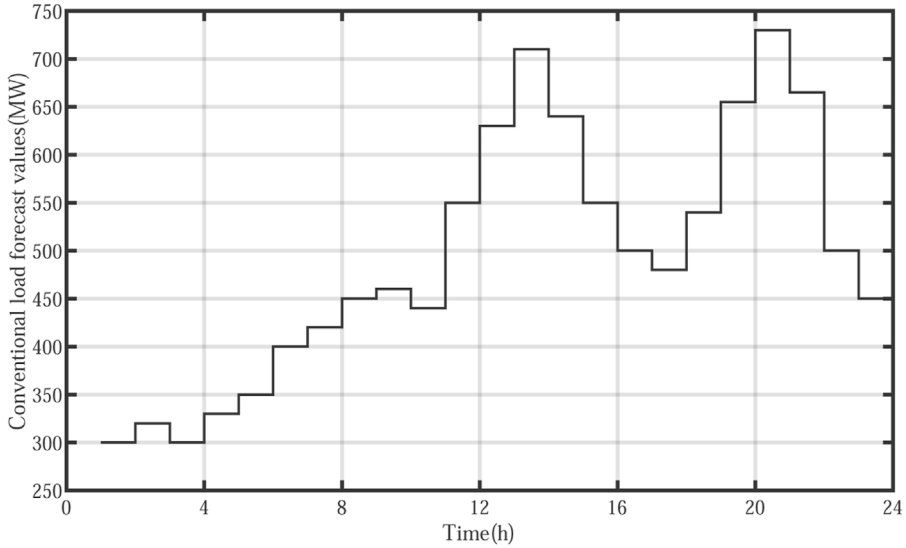

FIGURE 4
Conventional load forecasting values.

$$\begin{cases} 0 \le \theta_j \le 1, \\ 0 \le E_{j,\,\text{total},\,co_2}(t) \le \eta\beta K_{cd} P_{cbj,max}, \\ P_{Bj}(t) = \lambda E_{j,\text{total},co_2}(t), \\ P_{cb,j}(t) = P_{cj,j}(t) + P_{Bj}(t) + PDj(t), \end{cases} \tag{26}$$

where $P_{cg}(t)$ is the conventional load at time t, R_i^{up} is the climbing rate of unit i, and R_i^{down} is the downhill climbing rate of unit i; R^{down} is the negative rotation reserve of the system and R^{up} is a positive rotation standby for the system; K_{cd} is the carbon emission intensity of the carbon capture unit and $P_{cb,j}(t)$ is the total output of the carbon capture unit j at time t; and η is the maximum working state coefficient of carbon capture unit and $P_{cbj,\,max}$ is the maximum output of carbon capture unit j.

7) Solution memory operation constraint. Ethanolamine solution is used in the solution memory of the carbon capture unit, and the mass of CO_2 is calculated using the volume of the solution using the processing method, with the following relational formula:

$$C_{CAj}(t) = \frac{Q_{Gj}(t) M_{EA}}{M_{co_2} \theta_j C_R \rho_R}, \tag{27}$$

where $C_{CAj}(t)$ is the solution volume of CO_2 captured by the carbon capture unit j at time t, $Q_{Gj}(t)$ is the mass of CO_2 captured by the carbon capture unit j at time t, M_{EA} is the molar mass of ethanolamine solution, M_{co_2} is the molar mass of CO_2, C_R is the concentration of ethanolamine solution, and ρ_R is the density of the ethanolamine solution.

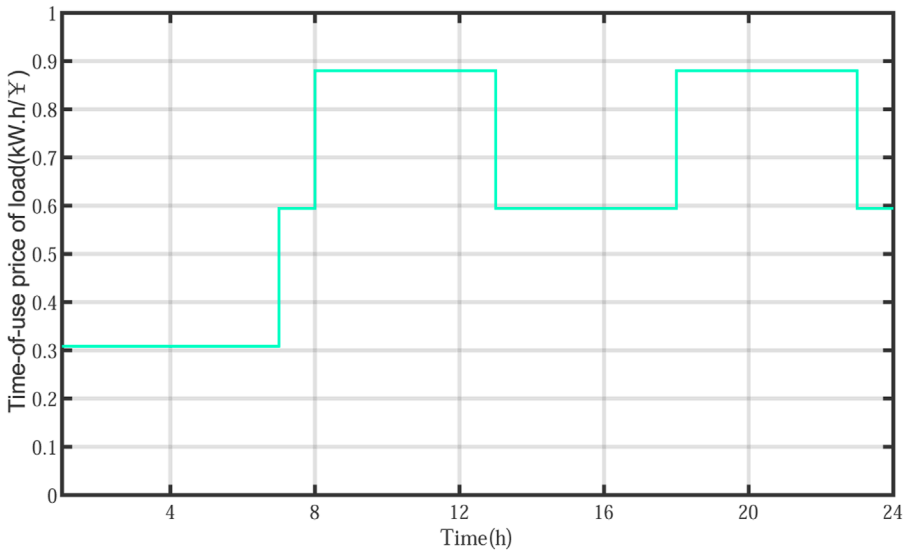

FIGURE 5
Time-of-use price of the load in the system.

TABLE 5 Operating costs for different scenarios.

	Scenario 1	Scenario 2	Scenario 3	Scenario 4
Conventional thermal power operation cost/¥	1,677,136	1,603,145	779,551	779,551
Carbon capture unit operation cost/¥	—	—	859,140	859,140
Load adjustment cost/¥	—	323,503	321,000	336,035
Wind curtailment cost/¥	1,317,400	836,149	642,950	517,300
Storage operation cost/¥	—	—	—	99,130
Carbon emission cost/¥	473,059	449,666	307,872	307,872
Total cost/¥	3,467,595	3,212,463	2,910,513	2,899,028

8) The solution storage operation constraints of the carbon capture unit are as follows:

$$\begin{cases} V_{Fj}(t) = V_{Fj}(t-1) - V_{CAj}(t-1), \\ V_{Pj}(t) = V_{Pj}(t-1) - V_{CAj}(t-1), \\ 0 \le V_{Fj}(t) \le V_{CAj}(t), \\ 0 \le V_{Pj}(t) \le V_{CAj}(t), \\ V_{Fj}(0) = V_{Fj}(24), \\ V_{Pj}(0) = V_{Pj}(24), \end{cases} \tag{28}$$

where $V_{Fj}(t)$ is the solution volume of the enriched liquid storage of the carbon capture unit j at t time, $V_{Pj}(t)$ is the solution volume of the carbon capture unit j lean liquid storage at t time, and $V_{CAj}(t)$ is the solution volume of the carbon capture unit j at t time.

9) Tie line power flow safety constraint:

$$\left|P_i - P_j\right| \le P_{\text{line,max}}, \tag{29}$$

where P_i and P_j are the injected power at neighboring nodes i and j, respectively. $P_{\text{line,max}}$ is the limit value of the transmitted power required for the safe operation of the system.

3.2 Intra-day scheduling model

In the intra-day phase, based on the day-ahead phase, the scheduling plan is changed every 15 min. The energy storage system with faster demand response and continuous adjustable energy-intensive load is used as regulation targets. Participation in intra-day system regulation is reasonably arranged according to the system wind abandonment situation and the impact of the time-of-use electricity price of the load. To ensure low-carbon economic safety of the system, the objective function is to minimize the system operating costs and the adverse effects of errors between the day-ahead wind power plan and the actual measured intra-day wind power values.

The intra-day scheduling model objective function is as follows:

$$F_2 = \min\left(C_{\text{cn}} + C_{\text{lx}} + C_{\Delta\text{aw}}\right), \tag{30}$$

$$\begin{cases} C_{\text{cn}} = K_{\text{cn}} \sum_{t=1}^{96} \left(P_{\text{cha}}(t) + P_{\text{dis}}(t)\right)/4, \\ C_{\Delta\text{aw}} = K_{\text{aw}} \sum_{t=1}^{96} \left(\Delta P_{\text{w1}}(t) - \Delta P_{\text{w}}(t)\right)/4, \end{cases} \tag{31}$$

where F_2 is the total operating cost of the system in the intra-day stage, C_{lx} is the continuous adjustable energy-intensive load

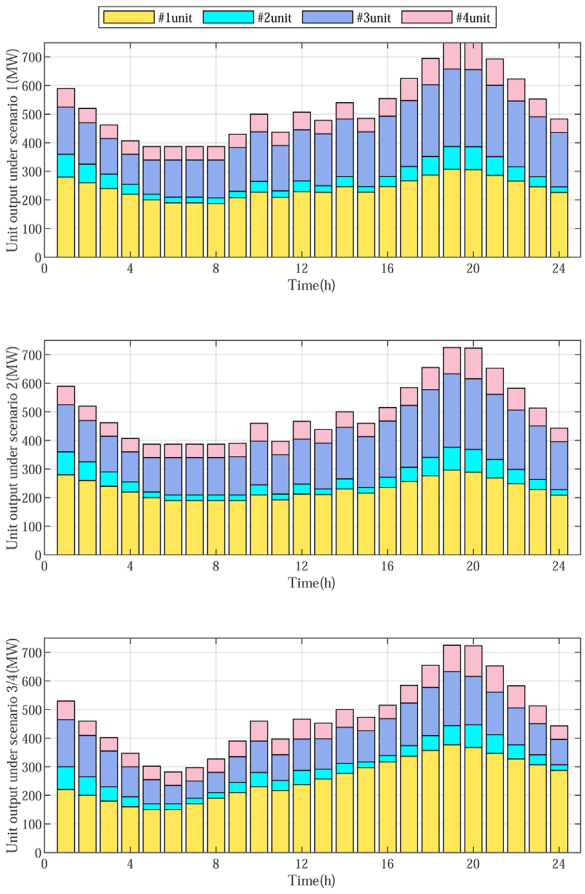

FIGURE 6
Output of each unit under different scenarios.

regulation cost, C_{cn} is the cost of operating the energy storage system, $C_{\Delta aw}$ is the cost of intra-day wind abandonment, and K_{cn} is the cost per unit of energy storage.

The continuous adjustable energy-intensive load operating constraints have been described previously and will not be repeated here.

1) Intra-day power regulation balance constraint:

$$\Delta P_w(t) = P_{lx-up}(t) - P_{lx-down}(t) + P_{cha}(t) - P_{dis}(t). \quad (32)$$

2) Energy storage system operating constraints:

To ensure the lifetime of the energy storage system, its charge state constraint and charge/discharge power constraint should be considered. The mathematical model is as follows:

The state of charge of the energy storage system and its formula:

$$\begin{cases} B_{soc} = (E_b/C_b) \times 100\%, \\ B_{soc,min} \le B_{soc}(t) \le B_{soc,max}, \end{cases} \quad (33)$$

$$B_{soc}(t+1) = \left(\frac{P_{cha}(t)\eta_{cha}\Delta t}{C_b} - \frac{P_{dis}(t)\Delta t}{C_b \eta_{dis}} \right) \times 100\% + B_{soc}(t). \quad (34)$$

Charging and discharging power constraints for the energy storage system:

$$\begin{cases} P_{cha,min} \le P_{cha}(t) \le P_{cha,max}, \\ P_{dis,min} \le P_{dis}(t) \le P_{dis,max}, \end{cases} \quad (35)$$

where $\Delta P_{w1}(t)$ is the difference between the predicted wind power output value during the day and the planned wind power output value before the day, $\Delta P_w(t)$is the intra-day wind power consumption, B_{soc} is the state of charge of the energy storage system, E_b is the current moment power of the energy storage system, and C_b is the total capacity of the energy storage system; $B_{soc,min}$ and $B_{soc,max}$ are the minimum and maximum values of the charge state of the energy storage system, respectively, and $B_{soc}(t)$ is the state of charge of the energy storage system at time t; $P_{cha}(t)$ is the charging power of the energy storage system at time t and η_{cha} is the charging efficiency; $P_{dis}(t)$ is the discharge power of the energy storage system at time t, η_{dis} is the discharge efficiency, and $P_{cha,min}$ and $P_{cha,max}$ are the upper and lower limits of the charging power of the energy storage system, respectively; and $P_{dis,min}$ and $P_{dis,max}$ are the upper and lower limits of the electrical power discharged from the energy storage system, respectively.

4 Case study

4.1 Overview of the case study

This paper presents a case analysis of the improved IEEE-39 node system. The system contains a 900 MW wind farm and four thermal power units, of which G1 is converted into a carbon capture unit, and the rest are conventional thermal units. The detailed parameters of the thermal units are shown in Table 2. Among the forms of MEL, the electro-melt magnesium load of the magnesia industry is taken as an example of the discrete adjustable energy-intensive load, and the ferroalloy load is taken as an example of the continuous adjustable energy-intensive load The regulation parameters are shown in Table 3, and the specific parameters are shown in Table 4 which shows that the system is equipped with 200 MWh energy storage system; the system day-ahead and intra-day wind power forecast values are shown in Figure 3; the conventional load forecast values are shown in Figure 4; and the load time-of-use price is shown in Figure 5. The problem studied in this paper is a mixed integer linear programming problem, which is solved using the optimization software CPLEX.

To verify the effectiveness of the proposed method, four different operational scenarios are set up for validation analysis:

1) Conventional scheduling: The power side participates in the regulation of the system, but the load side does not.
2) Coordinated power and load scheduling: All thermal units in the system are conventional units, with time-shifted adjustable energy-intensive and discrete adjustable energy-intensive loads participating in system regulation for day-ahead low-carbon economic scheduling.
3) Coordinated power and load scheduling considering low-carbon characteristics of carbon capture units: Power-side participation

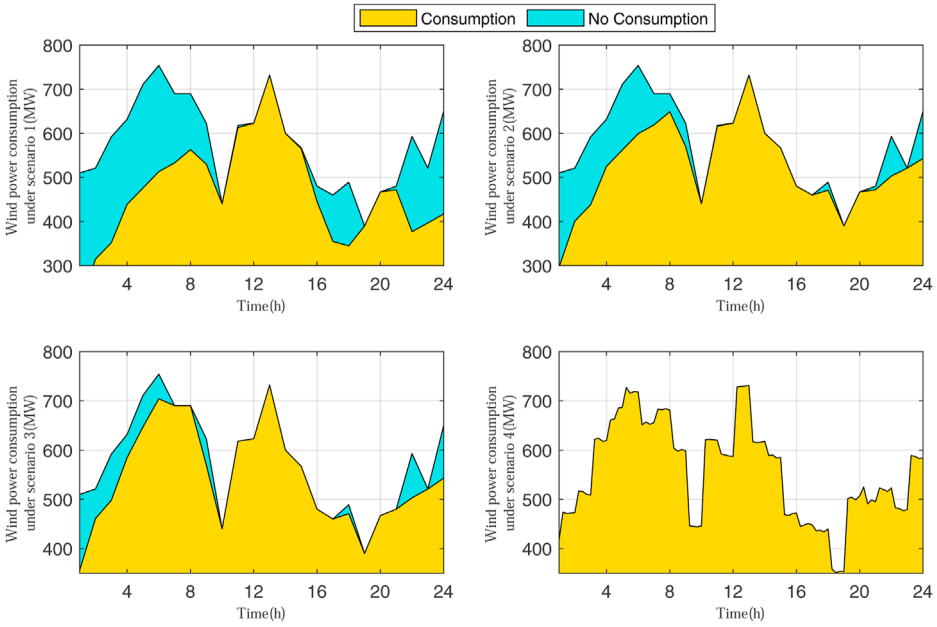

FIGURE 7
Wind power consumption under different scenarios.

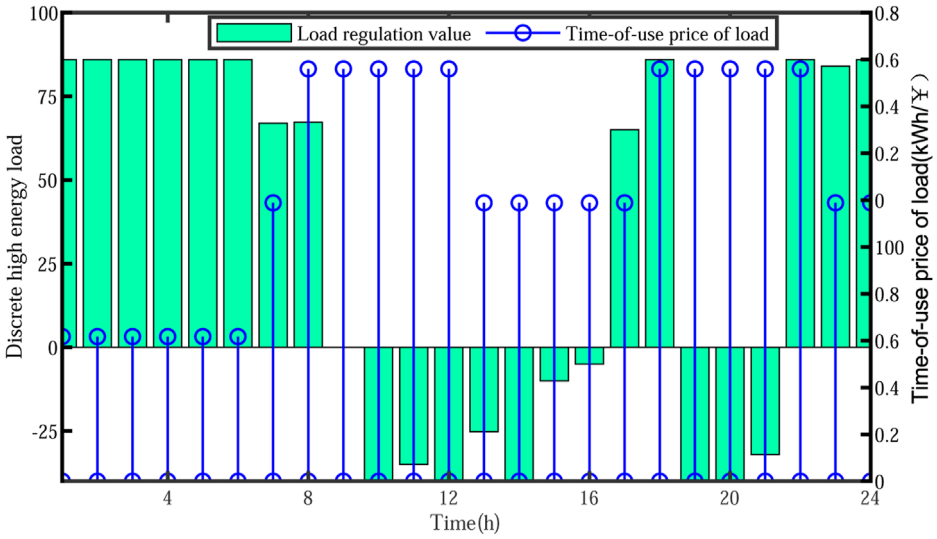

FIGURE 8
Regulation of the discrete adjustable energy-intensive load and time-of-use price.

in system regulation and conversion of one thermal power unit to a carbon capture unit, as well as time-shifted adjustable energy-intensive load and discrete adjustable energy-intensive load participation in system regulation for day-ahead economic scheduling.

4) Day-ahead and intra-day two-stage economic scheduling: Based on the aforementioned Scenario 3, continuous adjustable energy-intensive load in the system combined with an energy-storage system participates in system regulation for day-ahead and intra-day economic scheduling.

4.2 Result analysis

4.2.1 Comparative analysis of different operational scenarios

The system is analyzed according to the aforementioned scenarios, and the operating costs for each scenario are shown in Table 5.

A comparison of the costs of the systems in different scenarios shows that in Scenario 1, the conventional scheduling method of regulation results in the largest amount of abandoned wind, the most serious carbon emissions, and the highest operating

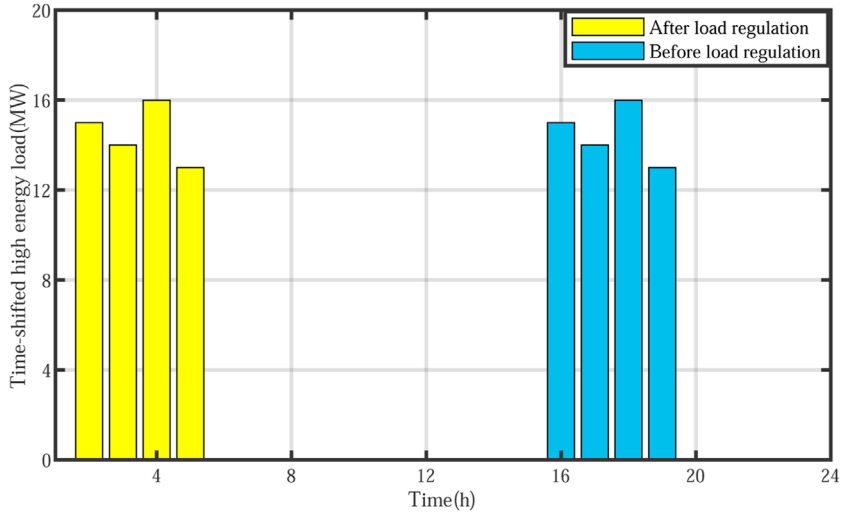

FIGURE 9
Regulation of the time-shifted adjustable energy-intensive load.

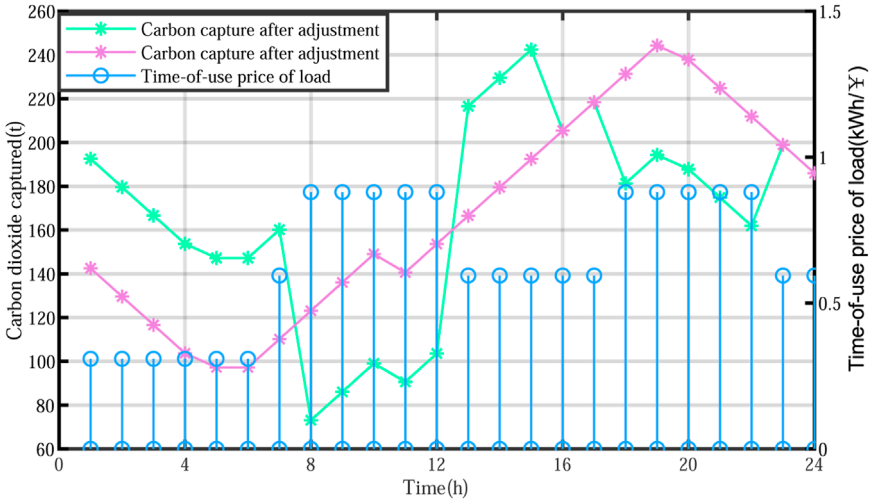

FIGURE 10
Carbon dioxide capture capacity of the carbon capture unit and time-of-use price.

costs. In Scenario 2, regulation is carried out using power–load coordination, involving time-shifted adjustable energy-intensive and discrete adjustable energy-intensive loads in the day-ahead phase of the system, resulting in a 7.36% reduction in total system costs, a 36.53% reduction in wind abandonment costs, and a 4.95% reduction in carbon emission costs compared to Scenario 1. Compared to Scenario 1, the advantages of co-coordinated power and load scheduling are demonstrated in Scenario 2. In Scenario 3, a carbon capture unit with low-carbon characteristics is introduced into the system. By using the scheduling method in Scenario 2, the operating cost of the unit increases, but there is a decrease in system adjustment and carbon emission costs. Overall, the total system cost is reduced by 9.39%, and the carbon emission cost is reduced by 31.53%. In Scenario 4, based on Scenario 3, continuous adjustable energy-intensive load and energy storage system are used as regulation resources to participate in the intra-day phase of system regulation, maximizing the elimination of the difference between the forecasted intra-day wind power output and the planned day-ahead wind power output. Using the method proposed in this paper, the operating cost of the system is reduced by 16.4% and the carbon emission cost is reduced by 34.92% compared to Scenario 1, proving the effectiveness of the method proposed in this paper, which ensures the safe operation of the system while taking into account the low-carbon and economic aspects of the system. The power output of each unit in each scenario is shown in Figure 6. In the conventional scheduling mode in Scenario 1, only the output of thermal units is regulated to cope with load and wind power, and there is greater pressure to regulate conventional thermal units.

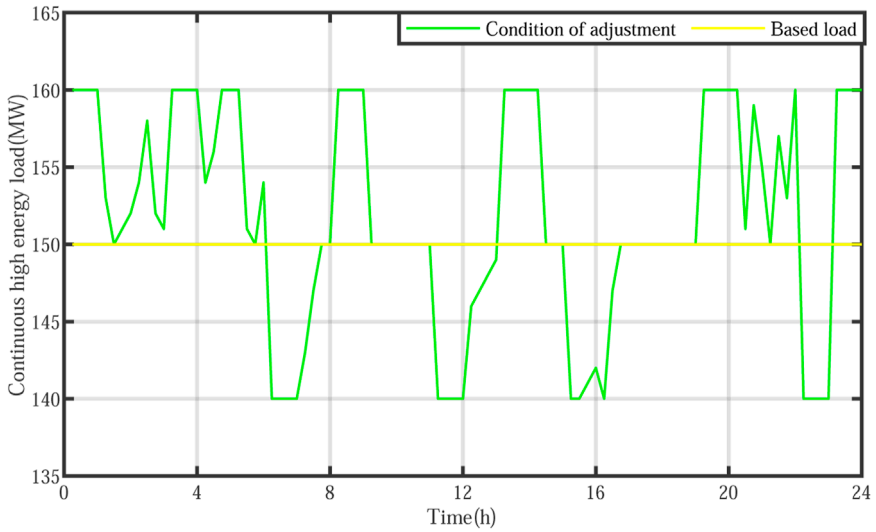

FIGURE 11
Regulation of the continuous adjustable energy-intensive load.

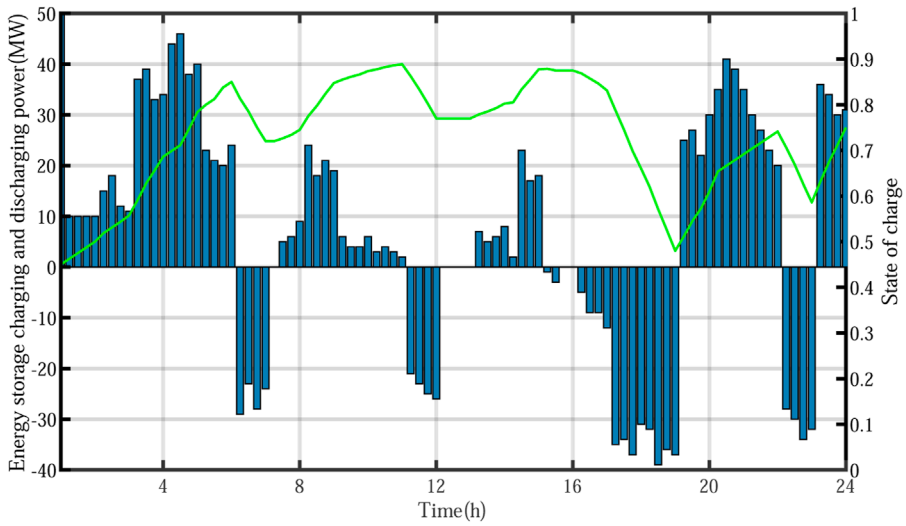

FIGURE 12
Operation of the energy storage system.

In Scenario 2, the regulation pressure on conventional thermal units is further reduced as the time-shifted and discrete adjustable energy-intensive loads on the supply side participate in the demand response; scenarios 3 and 4 show the same scheduling results. By converting unit 1 to a carbon capture unit, the output of unit 1 accounts for a larger proportion of the capacity than scenarios 1 and 2 due to the low-carbon and economic operation of the carbon capture unit, and the output of other high-carbon units is compressed, resulting in a further reduction in the carbon emissions and operating costs of the system.

The wind and power consumption in each scenario is shown in **Figure 7**. Under the traditional scheduling model of Scenario 1, only the power side participates in scheduling, while the lack of system regulation resources leads to serious wind power abandonment in the system. In Scenario 2, both sides of the power supply and load participate together as regulating resources in the scheduling, and system wind abandonment is mitigated. The conversion of the conventional unit 1 to a carbon capture unit in Scenario 3 further increases the flexibility on the source side of the system, thereby mitigating the system wind abandonment to some extent. Scenario 4 builds on Scenario 3 by considering the prediction errors of day-ahead and intra-day wind power, while adding two regulation resources, an energy-storage system, and continuous energy-intensive load, to the intra-day phase, resulting in a significant reduction in system wind abandonment and achieving the goal of low-carbon and economical system operation.

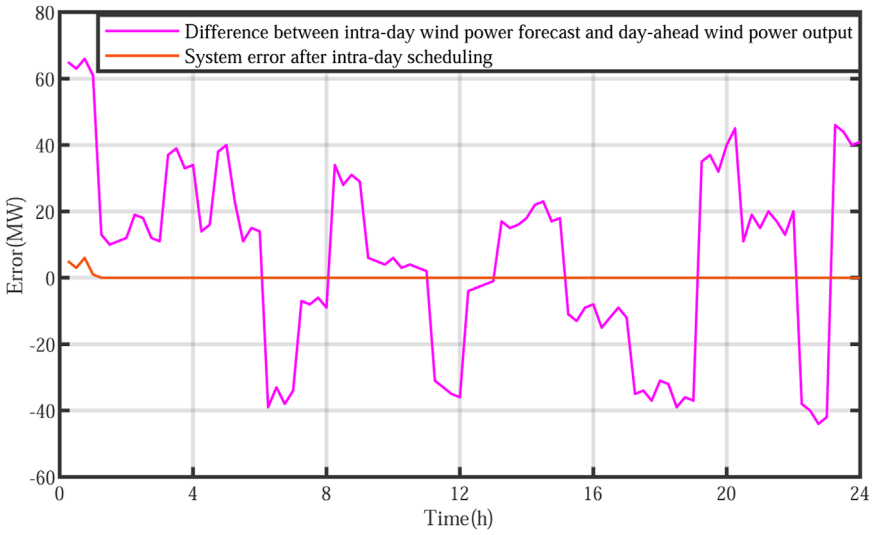

FIGURE 13
Dynamic adjustment of the system error.

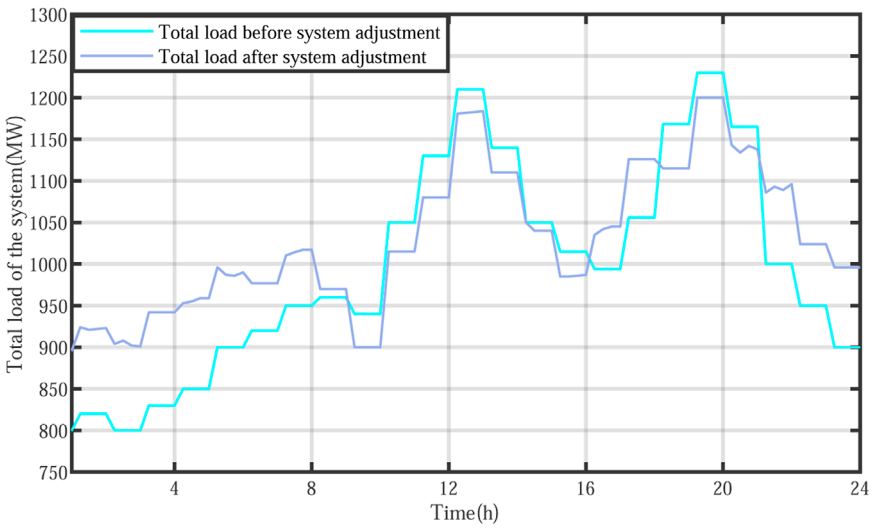

FIGURE 14
Comparison of load before and after scheduling.

4.2.2 Result analysis of the scheduling method proposed in this paper

To verify the effectiveness of the method proposed in this paper, the scheduling results are analyzed as follows:

The regulation of discrete adjustable energy-intensive and the time-shifted adjustable energy-intensive loads during the day-ahead economic scheduling phase is shown in **Figure 8** and **Figure 9**, respectively. During the day-ahead phase, the variation in discrete adjustable energy-intensive loads negatively correlates with the variation in electricity prices. In the adjustment process, the load is low at the stage of wind abandonment, and then the load is raised to absorb wind power; when there is no wind-abandoning load peak, the load is lowered to reduce the regulation pressure of conventional thermal power units. At the same time, by shifting the time-shifted adjustable high-energy peak hour load to the low-valley period, enterprises can make use of the peak–valley price differential for arbitrage based on their safe operation, making a profit of 24,856 CNY, thereby improving wind power consumption as well as reducing the cost of electricity for time-shifted high-energy enterprises.

The carbon capture unit CO_2 and time-of-use electricity price are shown in **Figure 10**. The carbon capture unit uses the solution memory for energy time shifting based on time-of-use electricity price and system wind abandonment. During low points, the price of electricity is lowered and the amount of carbon capture is increased; during peak hours, the price of electricity is raised and the amount of

carbon capture is lowered. Therefore, peak shaving and valley filling in energy consumption of carbon capture equipment are achieved, thus ensuring low-carbon capture units and economic operation of the carbon.

The continuous adjustable energy-intensive load and storage system operation during the intra-day economic scheduling phase are shown in **Figure 11** and **Figure 12**, respectively. In the intra-day phase, the error between the intra-day wind power forecast and the day-ahead wind power metered output value is minimized by dynamically adjusting the continuous adjustable energy-intensive load and the energy storage system, thus ensuring low-carbon and economic operation of the system by completely utilizing the flexibility of demand-side scheduling resources. The dynamic error adjustment is shown in **Figure 13**.

Figure 14 shows the comparison of the system load before and after scheduling. After scheduling by the method proposed in this paper, the system load increases during the wind abandonment hours (00:00–08:00 and 22:00–24:00) and decreases during the wind shortage hours; the daily peak-to-valley difference of the system load is reduced by 129.22 MW after scheduling. In summary, this paper makes full use of low-carbon characteristics of the complementary power and load sides and the flexibility of demand-side scheduling resources to ensure safe operation of the system, while taking into account the economy and low-carbon nature of the system.

To sum up, this paper mainly uses carbon capture technology at the source side and energy storage at the load side, supplemented by reasonable dispatching strategies and other technical means, ensuring the safe operation of the system. It fully exploits the flexibility and low-carbon nature of dispatching resources in the power system, improves the level of wind power consumption of the system, and takes into account the economy, low-carbon nature, and flexibility of system operation.

5 Conclusion

This article proposes a day-ahead and intra-day two-stage low-carbon economic dispatch method for wind power systems that consider MEL, and the following conclusions are drawn:

1) Based on classifying the differences in response characteristics of various adjustable MELs, this article provides a detailed analysis of the operational and regulatory characteristics of the adjustable MEL. It establishes a refined mathematical model that conforms to the actual operational characteristics of MEL.
2) This article introduces a carbon capture device with low-carbon characteristics into the system, which improves the low-carbon and economic performance of the system through proper scheduling. Simulation shows that compared to the situation without introducing carbon capture units, the total cost of the system is reduced by 9.39% and the carbon emission cost is reduced by 31.53%.
3) This article proposes a day-ahead and intra-day two-stage low-carbon economic dispatch method for wind power systems that consider MEL. Taking into account the low-carbon characteristics and flexibility of regulating resources on the source load storage sides as well as the differences in response characteristics of demand-side scheduling resources, the low-carbon and economic performance of the system has been improved through reasonable scheduling of regulating resources on each side. The simulation results show that compared with traditional scheduling methods, the system operation cost is reduced by 16.4% and the carbon emission cost is reduced by 34.92%.

Data availability statement

The raw data supporting the conclusion of this article will be made available by the authors, without undue reservation.

Author contributions

ZY and YW contributed to the conception and design of the study. ZY performed the statistical analysis. ZY wrote the first draft of the manuscript. ZY, YX, CL, WG, GC, JZ, AS, XL, and BL wrote sections of the manuscript. All authors contributed to manuscript revision and read and approved the submitted version.

Conflict of interest

WG was employed by State Grid Liaoning Electric Power Supply Co., Ltd. AS and XL were employed by Changchun Power Supply Company, State Grid Jilin Electric Power Co., Ltd. BL was employed by Jilin Thermal Power Plant of Guoneng Jilin Longhua Thermal Power Co., Ltd.

The remaining author declares that the research was conducted in the absence of any commercial or financial relationships that could be construed as a potential conflict of interest.

The reviewer MY declared a shared affiliation with the authors ZY, YX, CL, GC, and JZ at the time of the review.

Publisher's note

References

Afzalan, M., and Jazizadeh, F. (2020). Data-driven identification of consumers with deferrable loads for demand response programs. *IEEE Embed. Syst. Lett.* 12, 54–57. doi:10.1109/les.2019.2937834

Akbari-Dibavar, A., Mohammadi-Ivatloo, B., Zare, K., Khalili, T., and Bidram, A. (2021). Economic-emission dispatch problem in power systems with carbon capture power plants. *IEEE Trans. Industry Appl.* 57, 3341–3351. doi:10.1109/tia.2021.3079329

Bao, Y., Wang, B., Yang, L. I., and Yang, S. (2016). Rolling dispatch model considering wind penetration and multi-scale demand response resources. *Proc. Csee* 36 (19), 5103–5110.

Ge, X., Jin, Y., Fu, Y., Ma, Y., and Xia, S. (2019). Multiple-cut benders decomposition for wind-hydro-thermal optimal scheduling with quantifying various types of reserves. *IEEE Trans. Sustain. Energy* 1, 1358–1369. doi:10.1109/tste.2019.2925213

Guo, X., Lou, S., Wu, Y., and Wang, Y. (2022). Low-carbon operation of combined heat and power integrated plants based on solar-assisted carbon capture. *J. Mod. Power Syst. Clean Energy* 10, 1138–1151. doi:10.35833/mpce.2021.000046

Ji, Z., Kang, C., Chen, Q., Xia, Q., Jiang, C., Chen, Z., et al. (2013). Low-carbon power system dispatch incorporating carbon capture power plants. *IEEE Trans. Power Syst.* 28, 4615–4623. doi:10.1109/tpwrs.2013.2274176

Jia, Q., Chen, S., Yan, Z., and Li, Y. (2022). Optimal incentive strategy in cloud-edge integrated demand response framework for residential air conditioning loads. *IEEE Trans. cloud Comput.* 10, 31–42. doi:10.1109/tcc.2021.3118597

Jiaming, L. I., Wen, J., and Han, X. (2015). Low-carbon unit commitment with intensive wind power generation and carbon capture power plant. *J. Mod. Power Syst. Clean Energy* 3, 9.

Li, M., Hu, D., and Zhou, Y. (2016). "Research and practice of renewable energy local consumption mode in gansu province based on "double alternative" strategy," in *Power system technology*.

Li, X., Cao, X., Li, C., Yang, B., and Chen, D. (2019). A coordinated peak shaving strategy using neural network for discretely adjustable energy-intensive load and battery energy storage. *IEEE Access* 8, 5331–5338. doi:10.1109/ACCESS.2019.2962814

Liao, S., Jian, X., Sun, Y., Yi, B., and Tang, B. (2018). Control of energy-intensive load for power smoothing in wind power plants. *IEEE Trans. Power Syst.* 33, 6142–6154. doi:10.1109/TPWRS.2018.2834940

Liu, C., Liu, W., Wang, W., Zhu, D., Wen, J., and Meng, J. (2015). A quantitative method to pre-evaluate power grid's capability of accommodation for wind/photovoltaic power under participation of high-energy load. *Power Syst. Technol.* 76, 177–194.

Luo, J. B., Chen, Y. H., and Liu, Q. (2014). Overview of large-scale intermittent new energy grid-connected control technology. *Power Syst. Prot. Control* 42, 140–146.

Neubauer, J., and Simpson, M. (2013). *Optimal sizing of energy storage and photovoltaic power systems for demand charge mitigation*. Golden, Colorado: National Renewable Energy Laboratory (U.S.). (poster).

Peng, G., Jing, W., Zhu, D., Wang, W., and Liu, W. (2017). The coordination control strategy for large-scale wind power consumption based on source-load interactive. *Trans. China Electrotech. Soc.* 32, 1–9.

Shi, Z., Wang, W., Huang, Y., Li, P., and Dong, L. (2022). Simultaneous optimization of renewable energy and energy storage capacity with the hierarchical control. *CSEE J. Power Energy Syst.* 8, 95–104. doi:10.17775/CSEEJPES.2019.01470

Teng, F., Marko, A., Danny, P., and Goran, S. (2015). Benefits of demand-side response in providing frequency response service in the future gb power system. *Front. Energy Res.* 3, 36.

Tindemans, S. H., Trovato, V., and Strbac, G. (2015). Decentralized control of thermostatic loads for flexible demand response. *IEEE Trans. Control Syst. Technol.* 23, 1685–1700. doi:10.1109/tcst.2014.2381163

Yang, H., Yu, Q., Liu, J., Jia, Y., and Dong, Z. Y. (2020). Optimal wind-solar capacity allocation with coordination of dynamic regulation of hydropower and energy intensive controllable load. *IEEE Access* 8, 5331–5338. doi:10.1109/ACCESS.2019.2962814

frontiers | Frontiers in Energy Research

TYPE Original Research
PUBLISHED 01 June 2023
DOI 10.3389/fenrg.2023.1168768

OPEN ACCESS

EDITED BY
Yiyun Yao,
National Renewable Energy Laboratory (DOE), United States

REVIEWED BY
Zhiyi Li,
Zhejiang University, China
Zhenjie Li,
Northeast Forestry University, China

*CORRESPONDENCE
Rui Zhang,
njzhangrui@hit.edu.cn

RECEIVED 18 February 2023
ACCEPTED 22 May 2023
PUBLISHED 01 June 2023

CITATION
Zhang R and Yu J (2023), New urban power grid flexible load dispatching architecture and key technologies. *Front. Energy Res.* 11:1168768. doi: 10.3389/fenrg.2023.1168768

New urban power grid flexible load dispatching architecture and key technologies

Rui Zhang* and Jilai Yu

School of Electrical Engineering and Automation, Harbin Institute of Technology, Harbin, China

Towards the dual-carbon goals, the new urban power grid (NUPG) dominated by new energy has a low proportion of adjustable power generation units, resulting in insufficient scheduling flexibility. As a result, it becomes challenging to cope with the complex operating conditions of the NUPG. In this paper, after analyzing the new operational characteristics and challenges of the NUPG, a flexible load dispatching architecture and key technologies for the NUPG are proposed. These enhance the scheduling flexibility of the NUPG from the load side, which further provides support for the operation of the large power grid. Then, the types of scheduling objects, scheduling methods, scheduling tasks, and four essential dispatching technologies are introduced to provide a reference for building the NUPG flexible load dispatching system. Finally, the effectiveness of the NUPG flexible dispatching architecture and technologies is verified by simulation analysis of the IEEE39-bus system and the actual power grid in East China.

KEYWORDS

new urban power grid, flexible dispatch system, flexible resources, load dispatch, dispatching architecture

1 Introduction

Under the "3060"dual-carbon target, the future power system will be dominated by new energy (Han et al., 2021; Liu et al., 2022). The power supply of the urban power grid comes from the external power system (Sun et al., 2021; Yu et al., 2021). Therefore, the urban power grid will transform into a new urban power grid (NUPG) dominated by new energy. Due to the insufficient proportion of traditional adjustable hydro and thermal power units. NUPG will face the challenges of the changeable operation mode of the external new power system, the internal operation conflict between the source grid load storage, and the severe conflict of the internal and external operation mode to NUPG operation (Zhao et al., 2022). Therefore, it is urgent to improve the flexibility from the load side and respond to the internal and external operation requirements of NUPG. The new urban power grid is a new type of urban power system that primarily uses renewable energy for power supply, takes the load as the main dispatching object, and actively shares the dispatching tasks of the main grid.

The load-side of NUPG has many flexible resources: 1) The adjustable load has increased significantly. It is estimated that the number of electric vehicles in China's cities will exceed 50% of the total vehicles by 2050 (Zhengyou et al., 2020). The installed capacity of energy storage will exceed 200 GW (Liu et al., 2017). The proportion of air conditioning load in some cities in summer has exceeded 50% (Zhang, 2022). 2) The proportion of distributed new energy increased. At present, the installed proportion of distributed new energy in the total power generation capacity of the grid is more than 20%, which is expected to exceed

50% by 2050 (Energy Research Institute of National Development and Reform Commission, 2015), and the distributed new energy in the urban grid will also gradually increase (Bie et al., 2022). 3) Flexible DC has the regulation characteristics of good flexibility and fast regulation speed. Its application in the urban power grid has gradually increased in recent years, which can improve the flexibility of NUPG internal power regulation (Li et al., 2022). 4) In the future, NUPG will include a variety of flexible energy sources, such as steam, heat and hydrogen (Schulthoff et al., 2021), to jointly support NUPG operation.

Currently, the urban power grid is uniformly dispatched by the provincial large power grid and operates passively as a role of load. Reference (Yuan and Tang, 2021) evaluates the demand response capability of electric vehicles and utilizes them to reduce the voltage impact on the distribution network by constructing a road-electricity coupled network model. Reference (Wang et al., 2018) evaluates the ability of air conditioning load to participate in demand response. Reference (Kai et al., 2018) utilizes air conditioning load to participate in grid frequency regulation services. Reference (Wu et al., 2020) proposes combining electric vehicles and HVAC systems to increase flexibility and participate in ancillary services. Reference (Liu et al., 2019) utilizes a house energy management system to participate in peak shaving services for the power grid. Reference (Yang et al., 2015) proposed a specific implementation method for public buildings to participate in peak shaving services, dividing building management into building-level, terminal-level, communication-level, and primary station levels and managing it from bottom to top. Reference (Li W. et al., 2021) proposes an optimal incentive strategy for demand response participation based on electricity usage preferences of shiftable loads.

In summary, existing methods for addressing power grid operation issues still primarily focus on dispatching thermal and hydroelectric power, while load participation plays a supplementary role, and both the scale and capacity of dispatched loads remain relatively small. Moreover, in existing methods, load lacks unified control and management (Cai and Luo, 2023), and its flexibility has not yet been fully exploited (Yang C. et al., 2022). Therefore, in scenarios where the proportion of dispatchable thermal and hydroelectric power in the NUPG is insufficient, existing load control methods struggle to provide enough capacity to meet the operational needs of the NUPG. There is a need to study new dispatching models to schedule all adjustable loads within the NUPG, satisfying the operational demands of the power grid.

In this article, we propose NUPG's flexible load scheduling architecture and key technologies. The contribution of the proposed method is summarized as follows.

1) A flexible scheduling architecture for NUPG is constructed. This architecture enables NUPG to actively undertake scheduling tasks from the new power system, serving as a new large-scale dispatchable entity rather than passively operating as a traditional load role.
2) The main fundamental key technologies for NUPG's flexible scheduling are provided. Instead of making hydro and thermal power units the main scheduling object, and rather than small-scale participants as ancillary services, this technology makes load resources the main scheduling object.
3) The flexible load scheduling architecture and key technologies proposed in this paper mainly target the future dual-carbon goals, providing references for solving the bottleneck problems in the "3060"roadmap and future urban power grid operation modes.

The rest of this article is organized as follows: The characteristics and challenges of NUPG are described in Section 2. The NUPG flexible scheduling architecture is analyzed in Section 3. Section 4 introduced the key technologies of NUPG flexible scheduling. The simulation results are presented in Section 5. The article is concluded in Section 6.

2 Characteristics and challenges of NUPG

NUPG has eight main characteristics under the "3060"dual-carbon target, as shown in Figure 1.

1) New external power. The injection power of traditional urban power grid is mainly thermal power, which is relatively stable and less fluctuate. In the future, NUPG injection power will be dominated by new energy, and the fluctuation and uncertainty of injection power will increase significantly.
2) New grid structure. The traditional urban power grid is based on AC and a double-loop structure, and the coordination between partitions is not flexible enough. When some partitions have faults or power shortages, it is difficult for other partitions to support power in time. Flexible DC technology (Gomis-Bellmunt et al., 2019) will increase the power coordination capability of each partition in NUPG.
3) New dispatching mode. The dual-carbon target has impacted all links of power grid dispatching, increasing the difficulty of dispatching and requiring more subjects to participate. The new power system dispatching mode will change to coordination between large grid dispatching and NUPG dispatching. NUPG undertakes the task of large grid dispatching and reduces the pressure of large grids.
4) New dispatching environment. Under the dual-carbon goal, on the one hand, the power grid will conduct low-carbon dispatching to reduce carbon emissions. The cost of carbon emissions will distribute to users through the carbon trading market. On the other hand, the contracted electricity purchased by users through the electricity market needs to be transmitted through the internal tie line, which affects the capacity and regulation capacity of the tie line.
5) New dispatching requirements. NUPG injection power has more substantial fluctuation and a shorter period, which puts forward higher requirements for NUPG regulation: NUPG needs a shorter period and sustainable regulation ability to support real-time power balance.
6) New dispatching targets. On the one hand, NUPG needs to undertake the scheduling task of the external power grid. On the other hand, it is necessary to balance the fluctuating power injected by the external power grid to ensure operational stability. In addition, it is also essential to meet the power generation and consumption schedules of internal virtual

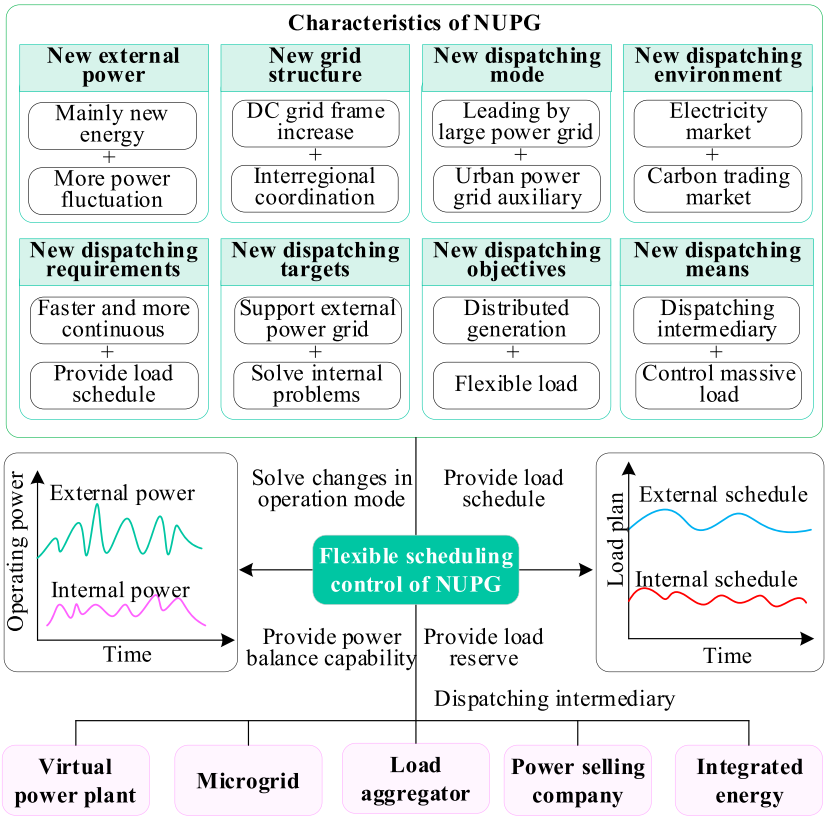

FIGURE 1
Characteristics of NUPG.

power plants, microgrids, and load aggregators, as well as the tie-line plans between different power grids and the intra-day correction plans.

7) New dispatching objectives. The traditional power grid dispatching object is mainly hydro and thermal power units, and the load is passive. The Jiangsu power-grid-load system only involves a small-large load, and the control cost is high. The NUPG dispatching objects are mainly loads and distributed power sources, such as massive electric vehicles, controllable air conditioners, and transferable loads.
8) New dispatching means. It is difficult for NUPG to directly control each air conditioner and each electric vehicle due to the control cost constraints and the impact of the control effect. It needs new control means as a medium, such as load aggregators, to control the massive controllable load.

Based on the above characteristics, NUPG operation will face the challenges of changing the external new power system operation mode, internal operation impact of source and load, and operation mode conflict between internal and external.

1) The challenge of changing the operation mode of an external new power system. The absolute value of power fluctuations will be immense based on the proportion of existing power fluctuations in new energy. It is challenging to balance power and electricity. The uncertainty of new energy power will bring about variable operation modes and challenge scheduling flexibility.
2) The challenge of internal operation conflict between source gird load. The first challenge is the role change of NUPG from passive load to active participation in scheduling. The second challenge is the conflict between internal massive distributed power generation, flexible load disorder operation and power grid stability. The third challenge is the expansion of scheduling objects, the application of new technologies, the introduction of the carbon trading market and the impact of new business development in the future.
3) The challenge of internal and external operation conflicts. The frequent change of operation mode is a challenge to adapt to the change of self-sufficiency, the change of external dependence, and the intertwined factors such as unplanned operation mode, power fluctuation, and internal and external faults. Unexpected operation mode challenges brought by uncertainties.

3 NUPG flexible load scheduling architecture

For the challenges faced by NUPG, under the existing unified scheduling and hierarchical management mode, this paper proposes a flexible load scheduling architecture for NUPG. This architecture can improve the flexibility of NUPG and support the internal and external operation of NUPG, as shown in Figure 2.

This architecture takes load aggregators, virtual power plants, integrated energy companies, and power retailers as dispatching

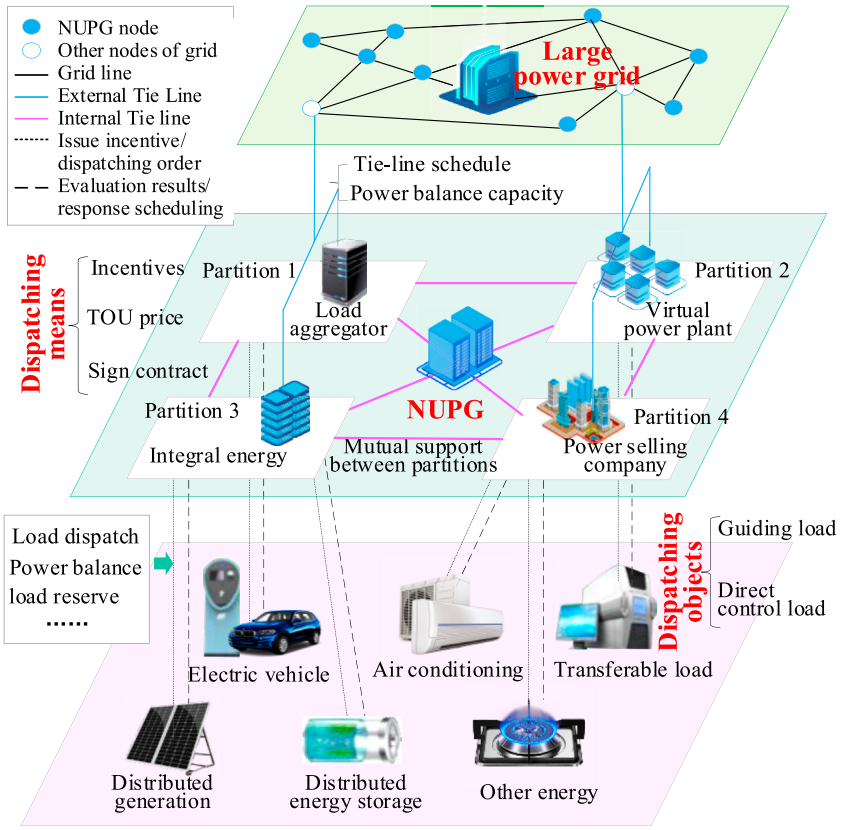

FIGURE 2
NUPG flexible load dispatching architecture.

entities, integrating massive controllable load resources through incentives, electricity prices, contracts, and other means. This feature endows NUPG with dual power supply and load attributes, enabling bi-directional power regulation. The dispatch entities in each partition may differ but have similar functions, all capable of increasing or decreasing power (Similar to the function of several large urban virtual pumped storage power stations). Internal tie lines enable mutual power support between different partitions. When a partition experiences a failure, other partitions can provide powerful support. This architecture serves the higher-level power grid dispatch, with the load as the main scheduling object (instead of the traditional power grid where hydro and thermal power units as the main scheduling object), proactively sharing the burden of power grid regulation tasks. It also serves the lower-level internal power grid operations, addressing internal issues within NUPG. We will introduce the architecture from three aspects: scheduling objects, scheduling means and scheduling tasks.

3.1 Scheduling object of NUPG

The load of NUPG consists of a basic load and an adjustable load. 1) The basic load mainly refers to the uncontrollable load that meets the basic living and production needs. When making the day-ahead load schedule, this part of the load is predicted by the conventional urban power grid load forecasting method (Xiao et al., 2021). 2) The term “adjustable load” refers to flexible resources that can be adjusted to meet production and daily needs, such as air conditioning loads that can be changed within the comfort interval (Fu et al., 2022), electric vehicle loads that can be charged and discharged flexibly without affecting the operational schedule (Yu et al., 2022), and transferable loads that can be independently selected during power consumption intervals (Yang et al., 2020). Distributed power generation is a kind of crucial flexible resource, mainly including the whole county/region photovoltaic (Qiu, 2022), distributed energy storage (Cai Z. et al., 2022), and distributed new energy around the city (Wang et al., 2023).

The adjustable load can be divided into guided and direct control loads according to the dispatching means. 1) Guided load refers to the flexible resources that participate in regulation through electricity price (Cai Q. et al., 2022), electricity market (Wang et al., 2021) and incentives (Wang et al., 2022). The response time scale varies from minute level to hour level. 2) Directly controlled load mainly refers to the load that is directly controlled by signing a contract with some high-quality users with a large adjustable capacity and fast response speed, as well as the distributed power supply that can be directly controlled. The response time scale is seconds and can be directly controlled in an emergency (Hu et al., 2022).

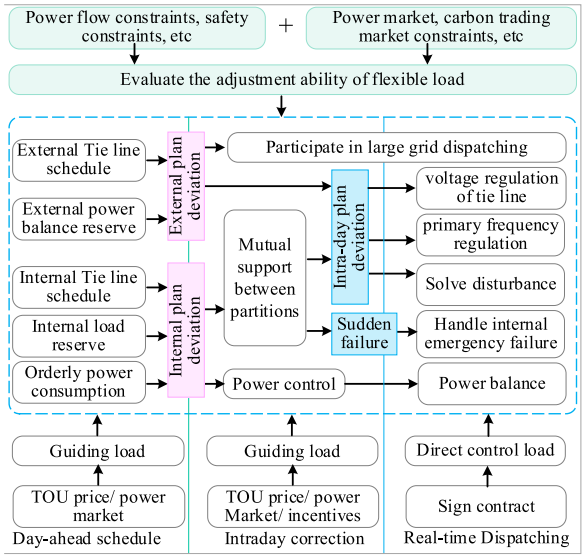

FIGURE 3
Multi-time scale dispatching task of NUPG.

With the development of technology, high energy consumption loads such as electric heating, electric molten magnesium, electrolytic aluminum, and gas and heat energy can participate in NUPG dispatching in the future.

3.2 Scheduling means of NUPG

On the one hand, the flexibility resources of NUPG are various, large in quantity, widely distributed, small in single regulation capacity, high indirect regulation communication cost, and limited in the computing resources of the control centre, which makes it difficult for NUPG to schedule a single load directly. On the other hand, most flexible resources have dual attributes of production and consumption, and the controllability is lower than that of the traditional generation units. Therefore, need new means to ensure the effectiveness of NUPG scheduling.

In this paper, load aggregators are used to controlling many flexible resources, and different means are selected according to different dispatching needs. For day-ahead dispatching, users can be guided through electricity prices to formulate day-ahead power use plans. For intra-day dispatching, users can be guided to participate in intra-day dispatching through electricity price or incentive means. For online scheduling, flexible resources can be controlled directly in an emergency by signing a contract with users.

Electricity price is one of the crucial means of NUPG dispatching. It controls power indirectly by influencing the power demand of users, mainly including time-of-use and real-time electricity prices. The time-of-use electricity price can be used for peak shaving and valley filling, and the real-time electricity price can be used for secondary power control. Secondary power control relates to peak shaving and valley filling, and peak shaving and valley filling can help reduce the pressure of secondary power control.

3.3 Multi-time scale scheduling task of NUPG

Under the constraints of power flow constraints, security constraints and the electricity market, the main dispatching tasks of NUPG are shown in Figure 3.

3.3.1 Make a day ahead scheduling task

Based on the results of the pre-day adjustment capability assessment of the load within the NUPG, and considering the impact of contract electricity on the capacity of internal tie lines, an internal tie line schedule is developed. This schedule reserves dispatching capacity for power support between different regions. Prepare an internal accident backup schedule to deal with internal accidents. Formulate an internal orderly power utilization schedule to deal with the internal power balance problem of NUPG in case of power shortage. An external tie-line schedule is established to provide some regulatory leeway for balancing fluctuations in renewable energy power in the larger grid, thereby reducing operational pressure on the larger grid. Develop an external power balance reserve schedule to support a large power grid's power balance or failure.

3.3.2 Rolling correction of intra-day scheduled tasks

The load shall be adjusted to revise the day-ahead power consumption schedule according to the deviation from NUPG's internal and external operation schedule. Because of the power balance deviation of the large power grid, the internal guiding load shall be mobilized to participate in the daily continuous peak shaving and continuous peak shaving tasks of the large power grid through electricity price or incentive means. Because of the internal power balance deviation, the guiding load shall be mobilized to participate in the secondary power control to achieve the power balance in the area through electricity price or incentive. Dispatch a load of the different regions through the internal tie line in the area, realize mutual power support in other locations, and improve the internal disturbance and fault handling capability.

3.3.3 Online real-time scheduling tasks

For intra-day schedule deviation or sudden failure, direct control load shall be mobilized to participate in the power grid's rapid peak shaving, primary frequency regulation, or internal emergency fault handling tasks to achieve power balance. In response to the voltage stability margin insufficiency problem caused by inadequate renewable energy supply capacity, which in turn results in insufficient reactive power support problem, load shedding is primarily used to maintain supply-demand balance and thus ensure voltage stability. Depending on different circumstances, either direct load control can be chosen, or electricity pricing/ incentives can be used to mobilize and guide the load in addressing voltage stability problems.

3.3.4 Market mechanism

When NUPG arranges the dispatching schedule, it should prioritize meeting the schedule of the market part (such as the

TABLE 1 Difference between NUPG and provincial large power grid dispatching.

Characteristics	NUPG dispatching	Provincial power grid dispatching
Dispatching objects	Flexible load, distributed generation	Mainly generator set
Main tasks	Provide power balance to a large power grid	Independently undertake power balance
The basis for planning (load side)	Base load forecasting, planned load assessment, distributed energy forecasting, etc	Base load forecast, regional new energy forecast, etc
Schedule scope	Only part of the load is planned (others are traditional load forecasting)	Schedule all power supplies
Dispatching boundary	Provide external tie line schedule upwards	Dispatch down to tie line channel
Server types	Load server	Power generation reserve
Power market processing	Evaluate the impact on regulatory capacity after the transaction	Do a security check after the transaction
Regulation of interval partitions	Interval partitions mutual assistance, power support	Interval partitions coordination, frequency regulation
Optimization of internal partitions	Internal automatic balancing, fault disturbance handling	Internal optimization and low-carbon economic dispatching

power purchase contract) and meeting the requirements of the grid security check. The corresponding market mechanism is needed to guide the load to participate in the response within the load aggregator. In addition, the related carbon trading mechanism is required because of the future low-carbon scheduling objectives, and the impact of carbon constraints is considered in the scheduling.

3.3.5 Difference between the provincial power grid and NUPG dispatching

NUPG and provincial large power grid dispatching work in close cooperation and division of labour, each undertaking part of the dispatching tasks. The specific characteristics are shown in Table 1.

4 Key technologies of NUPG flexible scheduling

Because of the new changes in the NUPG dispatching objects, tasks and objectives, the original dispatching mode with the participation of the primary power source and the small-scale participation of the load is difficult to adapt to the operational requirements of the new power system. With the reduction of the adjustable capacity of the power supply side, the load will become the main dispatching object (Hu et al., 2022). Therefore, the station re-examines the load-dispatching technology under the NUPG control objectives and tasks. In the future, there will be many key technologies for load-based participation in NUPG scheduling. With the development of new technologies such as big data and artificial intelligence, the technologies will continue to be updated. Due to the space limitations of this paper, we mainly discuss fundamental key scheduling technologies within the time scale of day-ahead, intra-day, and real-time scheduling for the primary grid. The fundamental dispatching key technologies involved mainly include load response capability assessment and distribution technology, load server configuration and load schedule formulation technology, load participation in frequency regulation/peak shaving/voltage regulation technology, and load-based internal and external fault handling technology. The above key technologies constitute the NUPG flexible dispatching technical architecture, as shown in Figure 4.

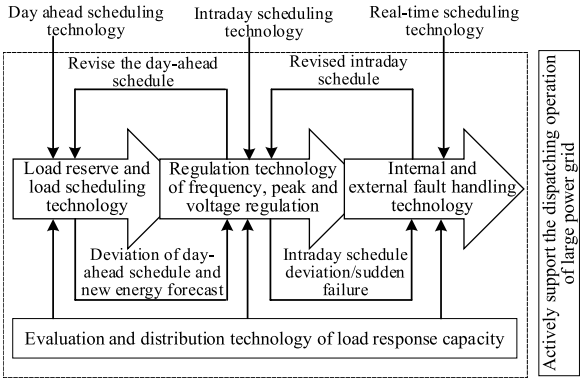

FIGURE 4
Key technology framework of NUPG flexible dispatching.

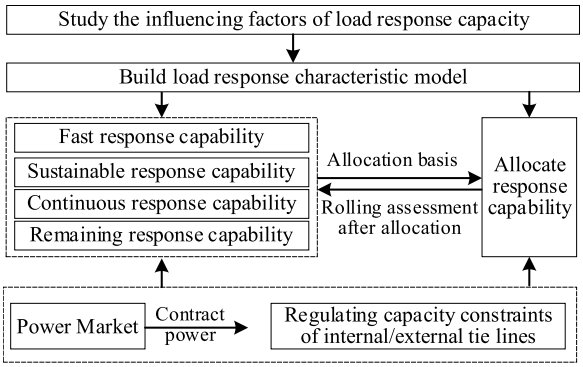

FIGURE 5
Load response capability evaluation and distribution technology.

4.1 Load response capacity assessment and distribution technology

In the new power system, the requirements for response capacity and response duration are different at different times and spaces. Therefore, to better support the operation of the new power system, it is necessary to evaluate the load response capability of NUPG with multiple time scales and dynamic updates. Furthermore, the evaluation and distribution technology of load response capability for NUPG dispatching is proposed. This technology aggregates massive loads through load aggregators to evaluate the responsiveness of NUPG, as shown in Figure 5.

It mainly includes three key technical issues: 1) Load response capability model construction technology. It fully considers the impact factors of different types of load response capability (economic, operational, environmental, and other factors), effectively reflecting the response characteristics of different loads and alleviating the uncertainty of load response. 2) Assessment technology for the response capability of different time scales supporting the large power grid. It mainly includes assessing rapid response capability online or emergency dispatching scenarios, sustainable response capability under fault disposal scenarios (The duration for which a certain power can sustain its response, such as how long 10 MW can be maintained sustainably), continuous response capability under continuous power fluctuation scenarios (The ability to continuously respond under continuous dispatch instructions), and residual capacity after response. 3) Responsiveness allocation technology. According to the scheduling requirements of different regions or scenarios, the response capability is allocated based on the user response characteristics, scheduling media revenue and the capacity constraints of tie line adjustment. After the allocation, the response capability is evaluated in a rolling manner.

Taking EBL (Electric Bus Load, EBL) as an example, the response ability assessment technique is introduced (Zhang and Yu, 2022). The online response ability assessment model of EBL is shown in Eq. 1.

$$\begin{cases} \Delta P_{zj}^{up} = \sum_{e=1}^{N_1} P_e^{up}(t) + \sum_{h=1}^{M_1} P_h^{up}(t) \\ \Delta P_{zj}^{dn} = \sum_{e=1}^{N_2} P_e^{dn}(t) + \sum_{h=1}^{M_2} P_h^{dn}(t) \end{cases} \tag{1}$$

Where ΔP_{zj}^{up} and ΔP_{zj}^{dn} are the rapid upward and downward adjustment capabilities of the load aggregation operator zj at time t. $P_e^{up}(t)$ and $P_e^{dn}(t)$ are the power that can be rapidly increased or decreased by EB (Electric Bus, EB) undercharging mode. N_1 and N_2 are the number of EB that can be rapidly increased or decreased, respectively. $P_h^{up}(t)$ and $P_h^{dn}(t)$ are the power that can be rapidly increased or decreased by battery h. M_1 and M_2 are the number of batteries that can be rapidly increased or decreased in power, respectively.

4.1.1 Power increase capability of Electric bus load

The EB can increase its power in charging mode as shown in Eq. 2. As for the EB in the discharging state, the response process is as follows: Discharging—>Stopping discharge—>Charging: the first step uprated capacity is $P_e^d(t)$, and the second step is $P_e^c(t)$. $S_e^{c\delta}(t)$ is the amount of electricity after the charging response of the EB; γ_e^c is the charging response threshold. $P^{jili}(t)$ is the excitation value at time t. $\xi_e^c(t)$ is the charging loss. $\delta_e(t)$ is the charging and discharging state of EB, and $\delta_e(t) = -1$ indicates that EB is in the discharging state. $\delta_e(t) = 1$ indicates that the EB is in a charging state. $\delta_e(t) = 0$ indicates that the EB is in an idle state.

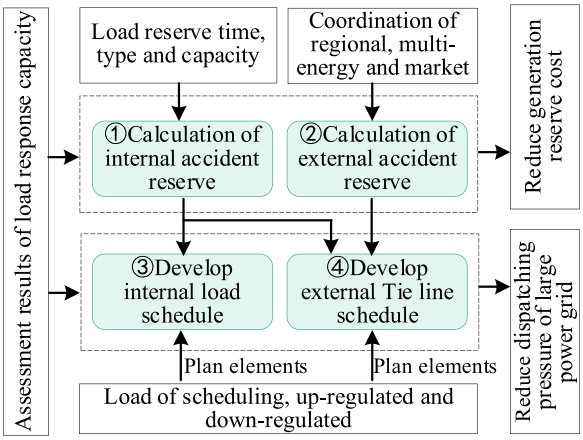

FIGURE 6
Load reserve configuration and power scheduling technology.

$$P_e^{up}(t) = \begin{cases} P_e^d(t) + P_e^c(t), \delta_e(t) = -1 \\ P_e^c(t), \delta_e(t) = 0 \end{cases} \tag{2}$$

The constraint conditions are:

$$\begin{cases} S_e^{c\delta}(t) < \gamma_e^c \\ P^{jili}(t) > \xi_e^c(t) \end{cases} \tag{3}$$

4.1.2 The power reduction capability of the Electric bus load

The EB can reduce its power output in charging mode as shown in Eq. 4. As for the EB in the charging state, the response process is as follows: Charging—>Stopping charging—>Discharging. The first step has a power reduction capability of $P_e^c(t)$, and the second step is equivalent to a power reduction capability of $P_e^d(t)$. $S_e^{dc\delta}(t)$ is the remaining electricity after the discharge response of the EB. γ_e^{dc} is the discharge response threshold. $\xi_e^{dc}(t)$ is the discharge loss.

$$P_e^{dn}(t) = \begin{cases} P_e^c(t) + P_e^d(t), \delta_e(t) = 1 \\ P_e^d(t), \delta_e(t) = 0 \end{cases} \tag{4}$$

The constraint conditions are:

$$\begin{cases} S_e^{dc\delta}(t) > \gamma_e^{dc} \\ P^{jili}(t) > \xi_e^{dc}(t) \end{cases} \tag{5}$$

The assessment of the up and down adjustment capability of the EB in battery swapping mode is similar to that in charging mode, but due to space constraints, which will not be described here.

4.2 Load reserve configuration and load scheduling technology

The load side resources of NUPG are various, large in scale, complex in the system and increase in business: on the one hand, it needs to expand the internal business to solve internal problems. On the other hand, it needs to undertake part of the task of a large power grid. Therefore, load scheduling is necessary to reduce uncertainty. This paper proposes the technology of load reserve configuration and power schedule formulation for NUPG dispatching. After reserving a certain proportion of NUPG internal load reserve, it provides load reserve for large power grids and reduces the cost of power generation reserve. In addition, the technology actively provides a NUPG load schedule to the large power grid to reduce the pressure on the large power grid, as shown in Figure 6.

The key technologies are as follows: 1) Internal emergency reserve configuration technology, mainly including the configuration technology of emergency reserve at different time scales; Emergency reserve configuration technology of different reserve types and reserve capacity optimization technology. 2) External emergency standby configuration technology. In addition to considering the reserved time, style, and capacity. It is necessary to study the emergency reserve mutual aid technology between NUPGs and different forms of emergency reserve coordination technology. 3) Internal load scheduling technology. Considering the evaluation results of response capability and accident reserve, the schedule of the NUPG internal liaison line is given to support internally coordinated operations. Formulate an orderly electricity use schedule to deal with the problem of how to balance the electricity in case of power shortage in a special period (long time, large range of no wind, no light). 4) External tie-line scheduling technology. Considering the internal and external emergency server configuration, the NUPG external tie-line schedule is formulated for the large power grid to reduce the dispatching pressure of the large power grid.

Taking the technology of formulating schedules based on load-based external tie lines as an example. Firstly, the load regulation margin model of NUPG partition k is constructed based on Eq. 1, as shown in Eqs. 6, (7).

$$P_k^{Z\,max}(t) = \begin{cases} \sum_{j=1}^{N_Z} \Delta P_{zj}^{up}(t) + P_k^{NL}(t), \sum_{j=1}^{N_Z} \Delta P_{zj}^{up}(t) < \Delta P_k^{lin}(t) \\ \Delta P_k^{lin}(t) + P_k^{NL}(t), \sum_{j=1}^{N_Z} \Delta P_{zj}^{up}(t) > \Delta P_k^{lin}(t) \end{cases} \tag{6}$$

$$P_k^{Z\,min}(t) = \sum_{j=1}^{N_Z} \Delta P_{zj}^{dn}(t) + P_k^{NL}(t) \tag{7}$$

$$\Delta P_k^{lin}(t) = P_k^{lin\,max}(t) - P_k^{NL}(t) - P_k^{con}(t) \tag{8}$$

Where $P_k^{Z\,max}(t)$ and $P_k^{Z\,min}(t)$ respectively represent the upper and lower limits of the load regulation margin for partition k. $\Delta P_k^{lin}(t)$ is the transmission capacity constraint of interconnection line k. $P_k^{lin\,max}(t)$ is the maximum transmission limit of partition interconnection line k. $P_k^{NL}(t)$ is the uncontrollable load forecast value of partition k. $P_k^{con}(t)$ is the contracted electric power value transmitted through interconnection line k. N_Z is the number of load aggregation merchants in partition k.

Based on the load regulation margin model of NUPG partition, the adjustable margin model of external tie lines of NUPG is constructed as shown in Eq. 9.

$$\begin{cases} P_G{}^{max}(t) = \sum_{k=1}^{N_q} P_k^{Z\,max}(t) - \sum_{j=1}^{N_g} P_j^n(t) \\ P_G{}^{min}(t) = \sum_{k=1}^{N_q} P_k^{Z\,min}(t) - \sum_{j=1}^{N_g} P_j^n(t) \end{cases} \tag{9}$$

Where $P_G{}^{max}(t)$ and $P_G{}^{min}(t)$ respectively represent the upper and lower limits of the adjustable margin for NUPG external interconnection lines. N_q is the number of partitions in NUPG. $P_j^n(t)$ and N_g respectively represent the total power and the number of internal power sources in NUPG.

According to Eq. 9, the power grid can establish the electricity schedule $P_{GY}(t)$ for NUPG external tie lines, as shown in Eq. 10 F_r is a random number function that can generate a random number in the range of (0,1).

$$\begin{cases} P_{GY}(t) = \sum_{k=1}^{N_Z} P_k^{NL}(t) + P_G{}^{min}(t)(1 - F_r) + P_G{}^{max}(t)F_r \\ P_G{}^{min}(t) < P_{GY}(t) < P_G{}^{max}(t) \end{cases} \tag{10}$$

Unlike the traditional approach of strictly adhering to load forecasting curves for creating electricity consumption schedules, our proposed method allows the grid to create a schedule within the adjustable capacity range of the external tie lines, which provides a more relaxed operational constraint for the power grid and reducing the pressure on its operation.

4.3 Load participation in frequency modulation/peak shaving/voltage regulation technology

In the new power system, the regulation capacity of the power supply side, such as the traditional hydro-thermal unit, is insufficient, so the load is required to participate in the power grid regulation. However, the load in the existing technology is only small-scale participation in grid operation (Zhang Y. J. et al., 2022), which is difficult to adapt to the demand of NUPG large-scale load participation in grid dispatching.

In addition, the load is the dual identity of production and marketing, which requires new technology to control effectively.

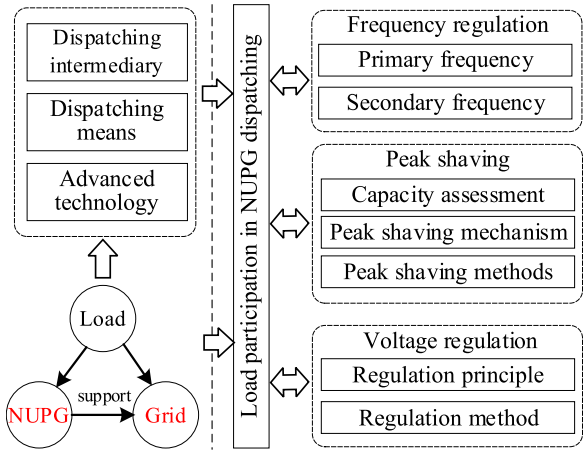

FIGURE 7
Load participation in frequency/peak shaving/voltage regulation technology of NUPG.

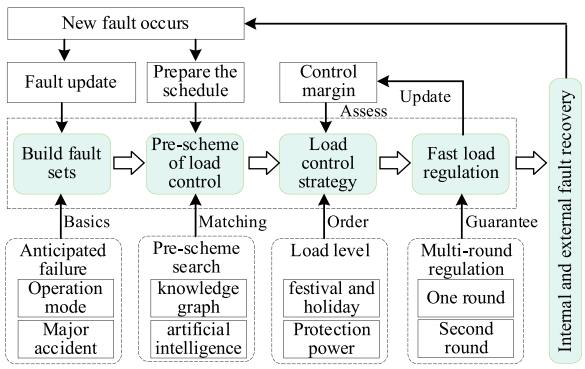

FIGURE 8
Internal and external fault handling technology based on load.

Therefore, it is necessary to study the power grid frequency regulation/peak regulation/voltage regulation technology for load participation in NUPG regulation objectives and tasks to meet the dispatching requirements of the new power system, as shown in Figure 7.

Specific key technologies include.

1) The load participates in NUPG frequency modulation technology. It mainly includes the load participating in the large power grid's primary frequency regulation mechanism, the NUPG secondary frequency regulation method to respond to the primary frequency regulation demand of the main external network, and the internal uncertainty disturbance. 2) The load participates in the peak-shaving technology of a large power grid. It mainly includes the capacity assessment of load participating in peak shaving, peak shaving mechanism and peak shaving method, etc., to fully mobilize load resources and respond to multi-timescale peak shaving demand. 3) Load participates in voltage regulation technology of large power grids. To solve the voltage stability problem, it is necessary to study the principle of load participating in the voltage regulation of a large power grid, establish the NUPG load voltage regulation mechanism, and study the method of load participating in the voltage regulation of a large power grid. In this way, NUPG can improve the large power grid's voltage security and stability level.

Take the sustainable peak-regulating capacity evaluation model under the peak-regulating command as an example. Set the peak-regulating command $R(t,\Delta t)=1$. When EB satisfies the condition in Eq. 11, EB can sustainably increase its power output. Here, t_{enT}^{F} refers to the time of the next departure after the response ends.

$$\begin{cases} t+\Delta t < t_{enT}^{F} \\ S_e^{dc\delta}(t+\Delta t) < \gamma_e^c \\ P^{jili}(t) > \xi_e^c(t) \end{cases} \tag{11}$$

When $\delta_e(t)=0$, it indicates that EB is in an idle state. The sustainable peak-regulating capacity evaluation model of EB is:

$$\begin{cases} P_e^{up}(t,\Delta t) = P_e^c(t) \\ S_e(t+\Delta t) = S_e(t) + \int_t^{t+\Delta t} P_e^c(t)dt \\ \delta_e(t\colon t+\Delta t) = 1 \end{cases} \tag{12}$$

Where $P_e^{up}(t,\Delta t)$ represents the power that can be sustainably increased for a duration of Δt. $S_e(t)$ represents the electricity quantity at time t. $S_e(t+\Delta t)$ represents the electricity quantity at time $(t+\Delta t)$. The sustainable peak-regulating capacity evaluation model of EB is:

$$\begin{cases} P_e^{up}(t,\Delta t) = P_e^c(t)+P_e^{dc}(t) \\ S_e(t+\Delta t) = S_e(t) + \int_t^{t+\Delta t} \left(P_e^c(t)+P_e^{dc}(t)\right)dt \\ \delta_e(t\colon t+\Delta t) = 1 \end{cases} \tag{13}$$

TABLE 2 NUPG scheduling basic key technology list.

Foundational key technologies	Specific technical sub-items
Load response capability assessment and allocation technology	Load response capability model construction technology
	Fine-grained load response capability assessment technology
	Load response capability allocation technology
Load reserve configuration and electricity usage schedule formulation technology	Internal contingency reserve configuration technology
	External contingency reserve configuration technology
	Internal electricity usage schedule formulation technology
	External interconnection schedule formulation technology
Load participation in grid frequency/peak/pressure regulation technology	Load participation in NUPG frequency regulation technology
	Load participation in power grid peak shaving technology
	Load participation in grid voltage regulation technology
The technology of load-based internal and external fault handling	NUPG internal and external fault set construction technology
	NUPG load control contingency schedule
	NUPG load control strategy
	Load fast shedding method

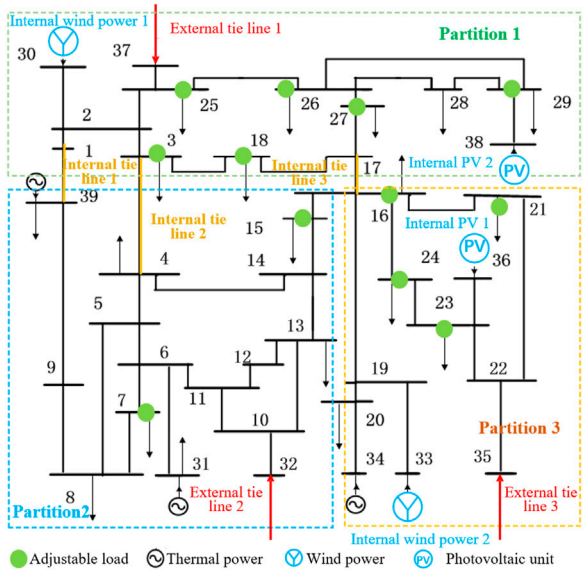

FIGURE 9
Improved IEEE 39 bus system.

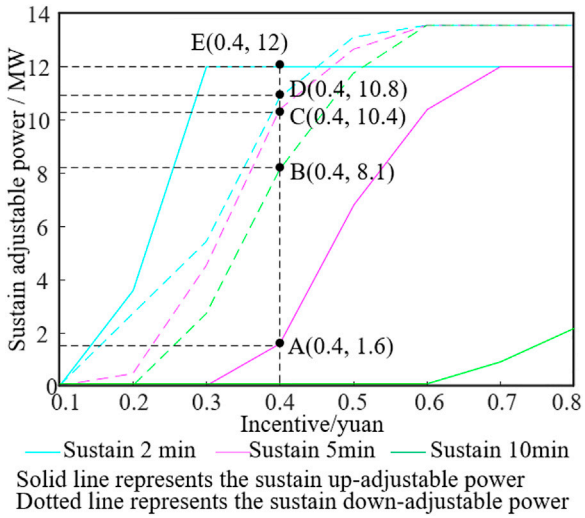

FIGURE 10
Assessment of the fast response capability of EBL in multiple time scales.

4.4 Internal and external fault handling technology based on load

Because of the insufficient regulating capacity of the power supply unit of the new power system, it is necessary to dispatch the NUPG load to deal with the faults (Yang Q. M. et al., 2022). Facing the MUPG control objectives and tasks, it is necessary to study the internal and external fault handling technology based on load resources, develop the system's load control schedule, handle the internal faults of NUPG, and actively support the large grid faults (Chen et al., 2023), as shown in Figure 8.

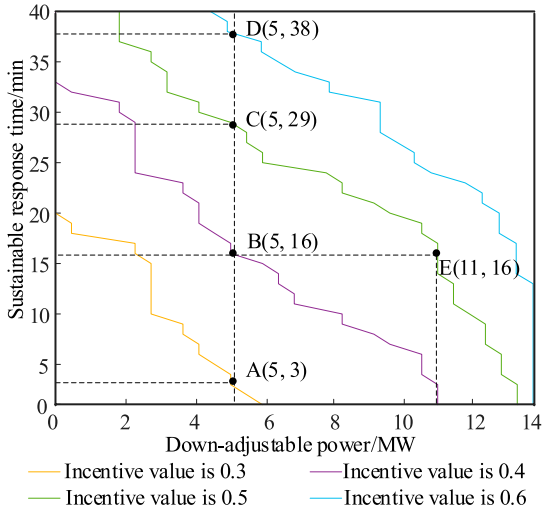

FIGURE 11
Sustainable response capability of EBL.

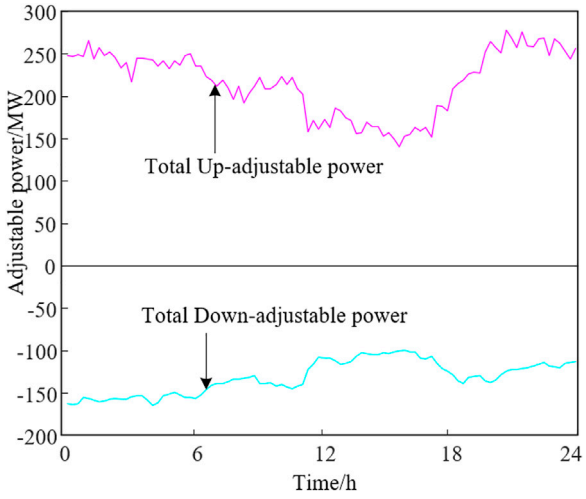

FIGURE 12
Adjustable capacity of each load.

Four key technologies are mainly studied: 1) NUPG internal and external fault set construction technology. It includes the construction technology of the expected fault set considering the changeable internal and external operation modes and major accidents, and the updated technology of the fault set for new faults. 2) NUPG load control schedule. It mainly includes the formulation of a load control schedule for a fault set, the formulation of an interval coordination schedule, and the search technology of a load control schedule based on a knowledge map or artificial intelligence. 3) NUPG load control strategy. It includes the classification of load levels, determination of control order and dynamic evaluation of control margin considering holidays and electricity conservation information. 4) Fast load removal method. It

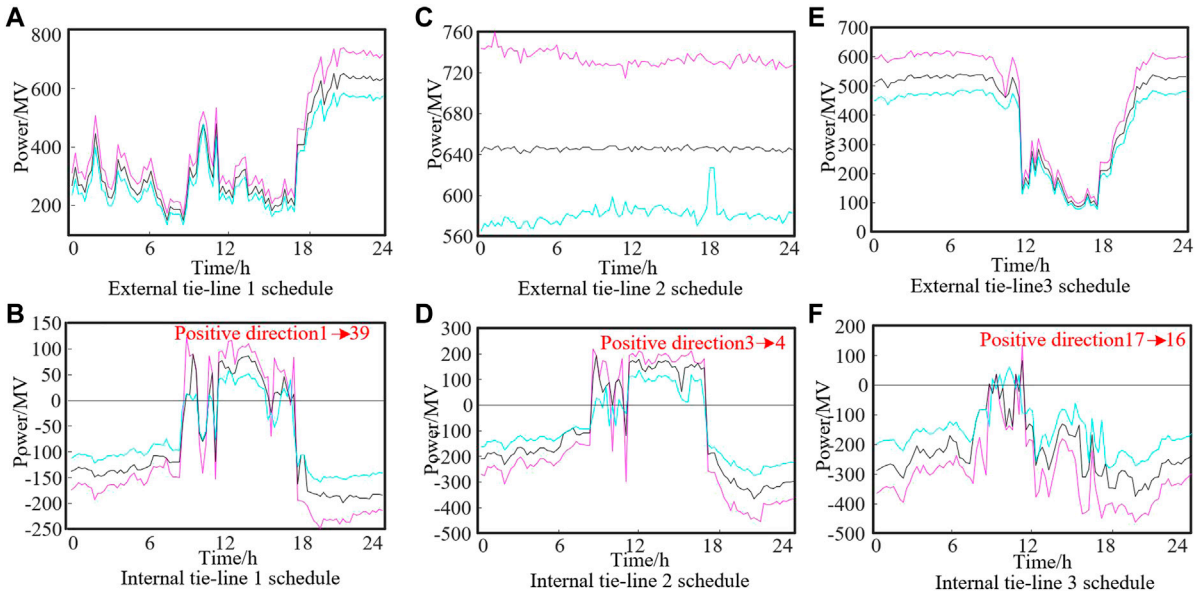

FIGURE 13
Internal and external tie line schedule of NUPG.

includes the first round fast cutting method of contract load and the second round cutting method of guiding load. After cutting off the load, the load control margin is updated.

We take the optimal control strategy for handling internal faults as an example. A load optimal control strategy considers user experience and economic efficiency, mobilizing the loads within the partition for fault handling, as shown in Eq. 14 The model aims to minimize the number of users involved, achieving cost-effective handling of internal faults.

$$min\left(\sum_{i=1}^{N_Z} P_{zj}^{exc} \cdot \Delta P_{zj}^{dn}(t,\Delta t) + h \cdot \varnothing\right)$$
$$\begin{cases} \Delta P_{ka}^{Z_{dn}}(t,\Delta t) = \sum_{i=1}^{N_Z} \Delta P_{zj}^{dn}(t,\Delta t) \\ k_i = 1, if\, \Delta P_{zj}^{dn}(t,\Delta t) > 0 \\ h = \sum k_i, \sum_{i=1}^{N_Z} P_{zj}^{exc} \le P_k^{prc} \end{cases} \quad (14)$$

Where P_{zj}^{exc} is the incentive cost of the jth load aggregator in partition k. h is the number of load aggregators participating in fault handling. $\varnothing$ is the action frequency penalty coefficient. P_k^{prc} is the incentive cost of partition k.

In summary, the following is a list of the fundamental new key technologies involved in this article as shown in Table 2.

5 Case studies

This section uses the IEEE-39 system and the actual system in East China to analyze some of the above key technologies (response capability assessment, load reserve and power utilization schedule formulation, and NUPG internal and external fault handling).

As shown in Figure 9, nodes 32, 35, and 37 are the connection points of external tie-line 1, 2, and 3, which are the actual wind farm data of East China Power Grid: SS wind farm, BY wind farm and SG wind farm. Nodes 30 and 33 are connected to the wind farm. Nodes 36 and 38 are connected to the photovoltaic power station. The green dot mark in the figure shows the adjustable load.

5.1 Refined assessment of load response capability

There are 8 lines connected to the electric bus station at node 7, 4 lines are in charge mode, 4 lines are in charge mode. The battery capacity of the charging line EB (electric bus, EB) is 220 kW·h, the battery capacity of the exchange line EB is 200 kW·h and the maximum charging and discharging power of the two types of single EB is 120 kW.

5.1.1 Load fast response ability with multiple time scales

Based on the response evaluation technology, the EB of node 7 is stimulated differently at 6:00 to evaluate its rapid response capability within 2, 5, and 10 min. The results are shown in Figure 10.

As shown in Figure 10, the same node has different rapid response capabilities under different demand durations. For example, when the incentive is 0.4-yuan, node 7 can rapidly increase the power by 12 MW in 2 min, while only 1.6 MW in 5 min. This is because some EBL (electric bus load, EBL) have finished charging at 6:00, and the remaining charging space is limited, so it can only participate in the power increase for a short time. The scheduling period of traditional methods is primarily 15 min (Cui et al., 2021). Traditional approaches fail to provide the load's quick response capacity at different time scales.

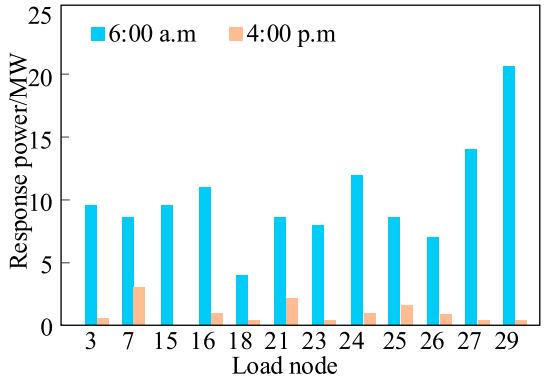

FIGURE 14
Actual response power value of the load at different time.

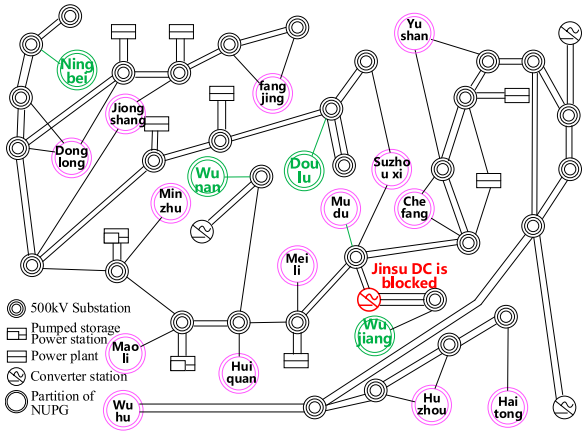

FIGURE 15
Fault handling of East China power grid supported by NUPG.

TABLE 3 Handling of faults within the partition.

Node No.		16	21	23	24	Total
Incentive unit price	Method 1/yuan	0	0.252	0.283	0.34	—
	Method 2/yuan	0.366	0.229	0.258	0.317	—
Response capacity	Method 1/MW	0	6.091	7.004	8.905	22
	Method 2/MW	3.423	5.411	6.032	7.134	22
Cost	Method 1/yaun	0	383	494	757	1634
	Method 2/yuan	313	309	388	565	1575
Response times	Method 1/times	0	1	1	1	3
	Method 2/times	1	1	1	1	4

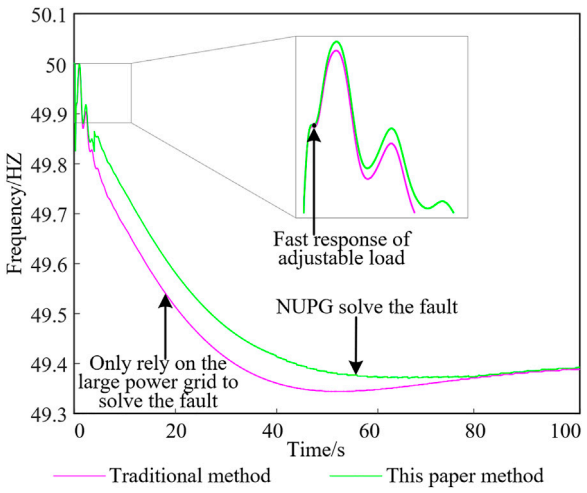

FIGURE 16
Frequency change curve of the large power grid during fault handling.

5.1.2 Assessment of loads' sustainable peak load shifting ability at multiple time scales

Based on the sustainable peak shaving capability evaluation model, the sustainable peak shaving capability of node 7 is evaluated under different incentive values, and the results are shown in Figure 11.

Figure 11 shows varying sustainable peak-shaving durations at the same node under different response powers. For instance, with an incentive value of 0.5 yuan, the maximum sustainable peak-shaving duration is 16 min at 11 MW power response and 29 min at 5 MW power response. At an incentive value of 0.4 yuan, the maximum sustainable peak-shaving duration is 16 min when responding to 5 MW power response. The traditional approach has a scheduling cycle of 15 min (Zhang H. et al., 2022), and can not provide sustainable load response capability at different time scales. The high proportion of power fluctuating in NUPG needs sustainable peak-shaving, but the traditional approach (Zhang H. et al., 2022) can not support this scene.

5.2 Load server configuration and load scheduling

According to the load response capability evaluation technology, the response capability of adjustable points in each partition is evaluated. The total amount of NUPG adjustable power up/down is obtained, as shown in Figure 12. Among them, partition 1 is connected with a controllable air conditioning load, partition 2 is connected with an electric vehicle load, and partition 3 is connected with the transferable load.

According to the adjustable load capacity, the NUPG internal and external tie lines schedule is calculated based on the load standby configuration and power scheduling technology, as shown in Figure 13.

According to Figure 13, the external tie line schedule mainly provides adjustable power upper and lower limits from NUPG to the large power grids. When formulating schedules, large power grids do not need to follow the traditional load forecasting curve strictly. Still, they can adjust within the upper and lower limits, which significantly loosens the constraints of large power grid operation schedules. The internal tie line schedule considers the impact of contract power on

TABLE 4 Adjustable capacity of NUPG tie line.

Tie line	Up-adjustable capacity/MW	Down-adjustable capacity/MW	Actual participation/MW
Nanjing - Ningbei	122	145	136
Cangzhou - Wunan	110	130	118
Wuxi - Doulu	225	200	180
Suzhou - Wujiang	213	220	206

TABLE 5 Frequency drop and power increase amount.

Method	Traditional method	This paper method
Minimum frequency drop value/HZ	49.35	49.4
Power increase amount of the power grid/MW	2660	2020

the regulating capacity of the inner interconnection line and supports inter-regional power support and fault handling.

5.3 Internal and external fault handling of NUPG

5.3.1 Internal fault handling of NUPG

5.3.1.1 Fault handling under different load spatial distributions

Faults were set at the external tie line at 6:00 a.m. and 16: 00 respectively, and the power of the tie line was 220 MW. Calculate the power value of the actual response of each adjustable load, as shown in Figure 14.

Figure 14 shows that when the same fault occurs at different times, the actual response of the load is different. This is because at 6:00 a.m. and 4:00 p.m., the NUPG load has different spatial load distribution, and the adjustable amount of each load is also different, resulting in a different actual response. Take load node seven as an example. Node 7 is the aggregated load of the electric bus station. At 6:00 in the morning, most buses are charging, which can respond to power reduction. At 4:00 p.m., most buses are in a state of operation, and the online charging load is less, which can respond to the load.

5.3.1.2 partition-level fault handling considering the impact on users

At 3:00, a fault occurred within Partition 3, requiring the shedding load for 22 MW. Partition 3 has a load aggregator on nodes 16, 21, 23, and 24 respectively, each of them controlling 100 controllable users. Based on the optimal load control strategy for handling internal faults, load aggregators were invoked to deal with the fault, and the results are shown in Table 3.

In Table 3, method 1 represents this paper method, while method 2 represents the traditional method that does not consider the number of user response times (Li L. W. et al., 2021). When shedding the 22 MW load, method 1 incurred a cost of 1634 yuan with three response times, while method 2 incurred a cost of 1575 yuan with four response times. Compared to Method 2, Method 1 had a higher cost of 3.7% and reduced user response times by 25%, significantly minimizing the impact on user electricity consumption.

5.3.2 External fault handling of NUPG

East China Power Grid has four NUPGs, like Nanjing, Changzhou, Wuxi, and Suzhou. These four NUPGs support the operation of the East China Power Grid through transmission lines, namely, Ningbei, Wunan, Doulou, and Mudu, as shown in Figure 15.

Jinsu HVDC system experienced a blocking fault, resulting in a loss of 2600 MW of power. The fault was dealt with using both the method proposed in this article and traditional methods. The changes in the power grid frequency curve after fault handling are shown in Figure 16.

According to Figure 16, the NUPG load can respond quickly after a fault and improve the grid frequency. NUPG load participating in the grid fault handling is more conducive to the recovery of the grid frequency than relying on the main grid itself, which can effectively improve the stable operation level of the large grid.

The adjustable capacity and actual participation capacity of each tie line are shown in Table 4.

The effect of NUPG's participation in the power grid fault handling is shown in Table 5.

In the method proposed in this article, the power increase amount of the power grid is 2020MW, which is 640 MW less than the traditional method (Wang et al., 2015), reducing the operating pressure of the power grid. The minimum frequency drop value of the power grid in this method is 49.4HZ, which is higher than the traditional method and is more conducive to the stable operation of the power grid. In addition, this method can effectively reduce the power grid reserve resources and save the backup cost of the power grid.

6 Conclusion

The impact of the low-carbon development of the external power grid and the diversification of internal load under the dual-carbon goal forces the transformation of the urban power grid to NUPG. This paper constructs a NUPG flexible dispatching architecture to share the dispatching pressure of a large power grid and improve the operational flexibility of NUPG.

1) NUPG has new features in external calls, power grid structure, dispatching mode, dispatching environment, dispatching demand, dispatching target, dispatching object, dispatching means, etc. NUPG face the challenges of internal operation, external operation and internal and external operation conflicts.
2) NUPG mainly dispatches flexible internal resources through load aggregators, integrated energy, virtual power plants and other media, with the help of electricity prices, incentives, power markets and other means. Undertake some large power grid and internal dispatching tasks, provide power balance and power consumption schedule, and support internal and external operations.
3) NUPG dispatches flexible internal load downward to meet internal operation requirements. Provide the ability of external tie line scheduling, peak shaving, frequency modulation, voltage regulation, load standby, fault handling, etc. to alleviate the dispatching pressure of a large power grid.
4) Facing the NUPG flexible dispatching architecture, it is necessary to focus on four basic key technologies: load response capability assessment and distribution technology, load standby configuration and power plan formulation technology, load participation in grid frequency regulation/peak shaving/voltage regulation technology, and internal and external fault handling technology based on load resources.

Data availability statement

The original contributions presented in the study are included in the article/Supplementary Material, further inquiries can be directed to the corresponding author.

Author contributions

RZ: conceptualization, methodology, software, writing—original draft; data curation, formal analysis, visualization, investigation. JY: conceptualization, methodology, resources, supervision. All authors contributed to the article and approved the submitted version.

Funding

This work was supported by the National Natural Science Foundation of China (51877049).

Conflict of interest

The authors declare that the research was conducted in the absence of any commercial or financial relationships that could be construed as a potential conflict of interest.

Publisher's note

All claims expressed in this article are solely those of the authors and do not necessarily represent those of their affiliated organizations, or those of the publisher, the editors and the reviewers. Any product that may be evaluated in this article, or claim that may be made by its manufacturer, is not guaranteed or endorsed by the publisher.

References

Bie, Z. H., Ren, Y. Z., and Li, G. F. (2022). Morphological structure and development path of urban energy system for carbon emission peak and carbon neutrality. *Automation Electr. Power Syst.* 46 (17), 3–15. doi:10.7500/AEPS20220601006

Cai, Q., Chen, H., Xiang, K., Lin, C., and Wu, W. (2022). Evaluation on the impact of general industrial and commercial electricity price reduction—a case study of fujian province. *Front. Energy Res.* 376, 1–12. doi:10.3389/fenrg.2022.871681

Cai, Y., and Luo, W. (2023). Coordinated active and reactive power operation of multiple dispersed resources for flexibility improvement. *Front. Energy Res.* 11, 9. doi:10.3389/fenrg.2023.1133768

Cai, Z., Yang, K., Chen, Y., Yang, R., Gu, Y., Zeng, Y., et al. (2022). Multistage bilevel planning model of energy storage system in urban power grid considering network reconfiguration. *Front. Energy Res.* 10, 952684. doi:10.3389/fenrg.2022.952684

Chen, H. Y., Tan, B. F., and Wu, L. A. (2023). Operation and control of the new power systems based on hierarchical clusters. *Proc. CSEE* 43 (2), 581–595. doi:10.13334/j.0258-8013.pcsee.213324

Cui, Y. F., Li, Z. G., Jia, Q. Q., Ren, M., and Yang, J. (2021). Dynamic evaluation of response potential of thermostatically controlled load based on parameter identification and state estimation. *Automation Electr. Power Syst.* 45 (1), 150–158. doi:10.7500/AEPS20200629009

Energy Research Institute of National Development and Reform Commission (2015). *Research on the scenario and roadmap of high proportion renewable energy development in China 2050*. Beijing: Energy Research Institute of National Development and Reform Commission.

Fu, Y., O'Neill, Z., Wen, J., Pertzborn, A., and Bushby, S. T. (2022). Utilizing commercial heating, ventilating, and air conditioning systems to provide grid services: A review. *Appl. Energy* 307, 118133. doi:10.1016/j.apenergy.2021.118133

Gomis-Bellmunt, O., Sau-Bassols, J., Prieto-Araujo, E., and Cheah-Mane, M. (2019). Flexible converters for meshed HVDC grids: From flexible AC transmission systems (FACTS) to flexible DC grids. *IEEE Trans. Power Deliv.* 35 (1), 2–15. doi:10.1109/TPWRD.2019.2939588

Han, X., Li, T., Zhang, D., and Zhou, X. (2021). New issues and key technologies of new power system planning under double carbon goals. *High. Volt. Eng.* 47 (9), 3036–3046. doi:10.13336/j.1003-6520.hve.20210809

Hu, G., Yan, Y. S., and Wu, H. (2022). Emergency load control strategy and terminal implementation for distribution network based on collaboration of main grid and distribution network. *Automation Electr. Power Syst.* 46 (2), 180–187. doi:10.7500/AEPS20200617004

Kai, M., Yuan, C. L., Xu, X., Yang, J., and Liu, Z. (2018). Optimizing regulation of aggregated thermostatically controlled loads based on multi-swarm PSO. IET Generation. *Transm. Distribution* 12 (10), 2340–2346. doi:10.1049/iet-gtd.2016.1847www.ietdl.org

Li, L., Sun, K., Liu, Z., Wang, W., Li, K. J., Qin, S. S., et al. (2022). The complete chloroplast genome of *Scoparia dulcis* (Plantaginaceae). *Front. Energy Res.* 10, 118–119. doi:10.1080/23802359.2021.2011449

Li, L. W., Wang, L., and Shi, J. W. (2021). Research on the technology of provincial dispatching load batch control based on IEC104 protocol. *Distribution Util.* 35 (10), 37–43. doi:10.19421/j.cnki.1006-6357.2018.10.007

Li, W., Han, R. D., Sun, C. J., Yang, H., Jin, J., Zhu, Y., et al. (2021). Diagnosis of pulmonary nodules by DNA methylation analysis in bronchoalveolar lavage fluids. *Proc. CSEE* 41 (1), 185–193. doi:10.1186/s13148-021-01163-w

Liu, G. D., Ollis, T. B., Xiao, B., Zhang, X., and Tomsovic, K. (2019). Distributed energy management for community microgrids considering phase balancing and peak shaving. *IET Generation, Transm. Distribution* 13 (9), 1612–1620. doi:10.1049/iet-gtd.2018.5881

Liu, X., Yue, Y., Huang, X., Xu, W., and Lu, X. (2022). A review of wind energy output simulation for new power system planning. *Front. Energy Res.* 932 (10), 1–8. doi:10.3389/fenrg.2022.942450

Liu, Y. J., Liu, C., and Wang, W. (2017). Analysis of development status and trend of energy storage technology. *Sino-Global Energy* 22 (4), 80–88.

Qiu, Y. (2022). *"Promoting the whole county" enables the new development of distributed photovoltaic [N]*. Beijing, China: China Electricity News.

Schulthoff, M., Rudnick, I., Bose, A., and Gençer, E. (2021). Role of hydrogen in a low-carbon electric power system: A case study. *Front. Energy Res.* 8, 585461. doi:10.3389/fenrg.2020.585461

Sun, K., Xiao, H., Pan, J., and Liu, Y. (2021). VSC-HVDC interties for urban power grid enhancement. *IEEE Trans. Power Syst.* 36 (5), 4745–4753. doi:10.1109/TPWRS.2021.3067199

Wang, D., Lan, Y., Jia, H. J., Myakala, K., Dobrinskikh, E., Rosenberg, A. Z., et al. (2018). FXR/TGR5 dual agonist prevents progression of nephropathy in diabetes and obesity. *Automation Electr. power Syst.* 42 (22), 118–137. doi:10.1681/ASN.2017020222

Wang, J., Wu, Z., Zhao, Y., Sun, Q., and Wang, F. (2023). A robust flexibility evaluation method for distributed multi-energy microgrid in supporting power distribution system. *Front. Energy Res.* 1530, 1021627. doi:10.3389/fenrg.2022.1021627

Wang, S., Zang, Y., Ge, W., Wang, A., Li, D., and Tang, J. (2021). Data-driven real-time pricing strategy and coordinated optimization of economic load dispatch in electricity market. *Front. Energy Res.* 9, 714951. doi:10.3389/fenrg.2021.714951

Wang, Y. C., Zhang, Z., and Lu, F. (2022). Stepwise incentive mechanism of demand response considering uncertainty of user behaviors. *Automation Electr. Power Syst.* 46 (20), 64–73. doi:10.7500/AEPS20210907006

Wang, Y., Liu, B., Liu, T. B., and Sun, H. (2015). Coordinated optimal dispatching of emergency power support among provinces after UHVDC transmission system block fault. *Proc. CSEE* 35 (11), 2695–2702. doi:10.13334/j.0258-8013.pcsee.2015.11.007

Wu, J. C., Ai, X., and Hu, J. J. (2020). Methods for characterizing flexibilities from demand-side resources and their applications in the day-ahead optimal scheduling. *Trans. China Electrotech. Soc.* 35 (9), 1973–1984. doi:10.19595/j.cnki.1000-6753.tces.190400

Xiao, B., Zhang, X. N., and Jiang, Z. (2021). Spatial load forecasting considering acceptability of standard cell and influence of load of adjacent cells[J]. *Automation Electr. Power Syst.* 45 (12), 57–64. doi:10.7500/AEPS20201107002

Yang, C., Sun, W., Han, D., and Yin, X. (2022). Research on power system flexibility considering uncertainties. *Front. Energy Res.* 1343, 967220. doi:10.3389/fenrg.2022.967220

Yang, Q. M., Li, G. F., and Bie, Z. H. (2022). Vehicle-to-Grid based resilience promotion strategy for urban distribution network under typhoon disaster. *Automation Electr. Power Syst.* 46 (12), 130–139. doi:10.7500/AEPS20211027007

Yang, Y. B., Yan, Q. G., Xu, S. M., Xiao, W., and Xue, M. (2015). Thinking of public building air-conditioning load participating in grid with virtual peak clipping. *Automation Electr. Power Syst.* 39 (17), 103–107. doi:10.7500/AEPS20150331023

Yang, Z., Yu, K., and Dong, Y. (2020). "Research on the optimal operating time of family transferable load," in 2020 IEEE/IAS Industrial and Commercial Power System Asia (I&CPS Asia), Weihai, China, July 13-16, 2020 (IEEE), 1592–1598.

Yu, K., Cen, Z., Chen, X., Liang, C., Zhou, Z., Dong, Z., et al. (2021). Optimization of urban multi-energy flow systems considering seasonal peak shaving of natural gas. *CSEE J. Power Energy Syst.* 8 (4), 1183–1193. doi:10.17775/CSEEJPES.2020.03740

Yu, S., Du, Z., and Chen, L. (2022). Optimal regulation strategy of electric vehicle charging and discharging based on dynamic regional dispatching price. *Front. Energy Res.* 10, 880825074. doi:10.3389/fenrg.2022.873262

Yuan, Q., and Tang, Yi. (2021). Electric vehicle demand response technology based on traffic-grid coupling networks. *Proc. CSEE* 41 (5), 1627–1637. doi:10.13334/j.0258-8013.pcsee.200097

Zhang, H. L. (2022). *Research on adjustable capability characterization and response strategy of flexible load group for power peak regulation*. Jilin: Jilin: Northeast Electric Power University.

Zhang, H., Zhang, L., Sun, C. L., Cai, G. W., Wu, J., Su, X., et al. (2022). Oxygen-defect-rich 3D porous cobalt-gallium layered double hydroxide for high-performance supercapacitor application. *Proc. CSEE* 42 (5), 1837–1845. doi:10.1016/j.jcis.2021.10.109

Zhang, R., and Yu, J. L. (2022). Capacity evaluation of electric bus load participating in peak shaving of new urban power grid. *Proc. CSEE* 42, 82–94. doi:10.13334/j.0258-8013.pcsee.221015

Zhang, Y. J., Yi, Y. Q., and Li, L. C. (2022). Characteristics, key problems and technology prospect of new type low-voltage distribution system. *Automation Electr. Power Syst.* 1 (1), 1–12. doi:10.7500/AEPS20210922006

Zhao, M., Hengxu, Z., Mengran, Z., Mengxue, W., Yuanyuan, S., Kaiqi, S., et al. (2022). New mission and challenge of power distribution and consumption system under dual carbon target. *Proc. CSEE*, 42 (19), 6931–6944. doi:10.13334/j.0258-8013.pcsee.213091

Zhengyou, H. E., Bo, L. I., and Kai, L. I. A. O. (2020). Key technologies for protection and control of novel urban power grids. *Proc. CSEE* 40 (19), 6193–6207. doi:10.13334/j.0258-8013.pcsee.200458

frontiers | Frontiers in Energy Research

TYPE Original Research
PUBLISHED 13 June 2023
DOI 10.3389/fenrg.2023.1202054

OPEN ACCESS

EDITED BY
Mingfei Ban,
Northeast Forestry University, China

REVIEWED BY
Yu Chen,
Shandong University of Technology, China
Wang Yufei,
State Grid Smart Grid Research Institute, China

*CORRESPONDENCE
Jiaming Weng,
wrzx_5@sjtu.edu.cn

RECEIVED 07 April 2023
ACCEPTED 02 June 2023
PUBLISHED 13 June 2023

CITATION
Liao W, Weng J, Liu D and Wu Y (2023), Optimal allocation of distributed renewable generations in low-carbon distribution system considering impact of natural disasters.
Front. Energy Res. 11:1202054.
doi: 10.3389/fenrg.2023.1202054

Optimal allocation of distributed renewable generations in low-carbon distribution system considering impact of natural disasters

Wang Liao, Jiaming Weng*, Dong Liu and Yufeng Wu

Key Laboratory of Control of Power Transmission and Conversion, The School of Electronic Information and Electrical Engineering, Shanghai Jiao Tong University, Shanghai, China

With global climate change, increasingly frequent natural disasters have brought great challenges to the safe and reliable power supply and low-carbon transition of power distribution systems. Most of the existing researches on the distribution system under the impact of natural disasters only focus on the improvement of power supply reliability, but have not consider the impact of disaster severity and disaster response measures on carbon emissions. In order to juggle the load restoration and carbon emission mitigation of distribution system under natural disasters, this paper proposes an optimal allocation method of distributed renewable generations (DRGs) considering carbon emission for multi-scenario natural disasters based on the framework of cyber-physical-social system in energy (CPSSE), and establishes a three-stage optimization model of pre-disaster prevention-disaster attack-post-disaster restoration. For the purpose of ensuring the practicability and robustness of the allocation results, the disaster scenario is modeled and the selection method of the worst fault scenario under disaster is proposed. The progressive hedging algorithm (PHA) is adopted to solve the proposed multi-scenario optimization problem. Finally, the simulation results indicate that the proposed method can restore more lost load at a lower cost of carbon emissions.

KEYWORDS

distribution system, natural disaster, carbon emission, optimal allocation, network reconfiguration

1 Introduction

The power industry is the main battlefield for achieving carbon peaking and carbon neutrality targets. It is of great strategic significance to build a modern power system with renewable energy as the main part and realize the low-carbon transition of the power system (FERNÁNDEZ-GUILLAMÓN et al., 2019; Wen et al., 2020; Zhuo et al., 2020). However, the realization of low-carbon transition of power system is a complex systematic project, which requires decision analysis of system development in the context of many new difficulties and new technologies. In recent years, with the increase of global carbon emissions, climate change has intensified (Wang et al., 2016; IPCC, 2019), and increasingly frequent natural disasters have brought great challenges to the safe and reliable power supply of power distribution systems. The distribution system is located at the end of the power grid and is directly connected to the power consumers. Due to its own characteristics, the distribution

system is extremely vulnerable to natural disasters (Li et al., 2014), which seriously affects people's production and life, causing huge losses (Chen et al., 2017). Thus, it is one of the primary tasks to construct a modern distribution system by formulating corresponding prevention and restoration strategies to improve the response capability for disasters and power supply reliability of the distribution system (Xue et al., 2013; Shen et al., 2020).

A large number of existing studies focus on the resilience improvement of distribution systems and the restoration of power supply under the impact of natural disasters. The measures taken can be divided into two categories: pre-disaster prevention and post-disaster restoration.

Pre-disaster prevention measures usually optimize the allocation and deployment of infrastructure or disaster prevention resources in advance to alleviate the damage and impact of disasters on the distribution system. In order to improve the resilience of the distribution system against hurricanes, the pre-disaster optimal placement model for the depots of the repair teams is proposed in the references (Khomami and Sepasian, 2018; Arif et al., 2020), so as to realize the rapid repair of the post disaster poles and lines. In the reference (Gan et al., 2022), considering the coupling of distribution system and transportation system, a planning model is proposed to improve the resilience of coupled network under disaster. The model includes the capacity expansion of power lines, roads and charging stations and the hardening of roads and power lines. In the reference (Barnes et al., 2019), the transmission capacity of the line is guaranteed by configuring additional lines, circuit breakers and transformers. According to the prediction of possible fault scenarios, the locations of the gathering point of the mobile emergency generators are selected in the reference (Lei et al., 2018) to minimize the system load loss. In the references (Lin and Bie, 2018; Ma et al., 2018), the weak lines are identified and hardened before disasters to improve the resistance of the lines to the disaster. In the references (Alguacil et al., 2014; Yuan et al., 2016; Wang et al., 2019a; Wu et al., 2019), a typical three-layer optimization strategy of defender-attacker-defender (DAD) is proposed. In the first layer, the system planning layer (acting as a defender) determines the optimal installation location of distributed generation or energy storage under specified budget constraints. In the second layer, the natural disaster (attacker) maximizes the system load loss under the specified number of line faults. In the third layer, the system operation layer minimizes the system load loss through the restoration strategy.

Post-disaster restoration measures are mainly to restore load power as quickly and as much as possible by formulating operation strategies after the disaster caused damage to the distribution systems. In the reference (Zhang et al., 2023), the characteristics of AC/DC hybrid distribution system are studied, and a topology search strategy and fault restoration model with DC lines as the core are proposed to realize the restoration of multiple power sources and key loads. In the references (Yao et al., 2019; Li et al., 2021), the real-time post-disaster dispatching strategies for transportable energy storage are proposed in view of the power outages caused by disasters. The efficient dispatching strategies of maintenance crews and restoration crews are developed restore electricity customers after the disasters (Zhang et al., 2020a; Sun et al., 2023). In the reference (Hafiz et al., 2019), load restoration is combined with direct load control and demand response to improve system resilience through the flexibility provided by load. In the references (Lin and Bie, 2018; Ghasemi et al., 2021), the network reconfiguration (NR) method is used to divide the island, so as to minimize the load loss in the fault scenario. In the reference (Hao et al., 2022), a two-layer decision support framework is designed for the post-disaster restoration of distribution systems. The upper layer generates a pre-adjustment scheme through load transfer and topology partition, and the lower layer optimizes the restoration scheme of each partition.

In summary, the existing research on the distribution system under disasters is mainly carried out from the perspective of improving the reliability of power supply, but the impact of disasters on carbon emissions is ignored. It is pointed out in the references (Yu and Xue, 2016; Xue and Yu, 2017) that the power system is gradually developing into a CPSSE that combines multiple fields and interdisciplinary. Under the CPSSE framework, the previous methods for analyzing disaster issues in power distribution systems have been unable to meet the requirements of the new research paradigm under the social issue of low-carbon transition, and an integration of holistic thinking and reductive thinking should be applied for research and analysis (Mulej, 2007). Moreover, addressing the impact of natural disasters is also a challenge that needs to be overcome in the development of low-carbon power systems. Based on such a background and methodological guidance, research on the impact of disasters should not only focus on the power balance, but also on the change of carbon emissions. From a long-term perspective, with the sudden and frequent occurrence of disasters, the cumulative effect will lead to the deviation of carbon emission trajectory from the expected path, which will hinder the realization of low-carbon transition goals. Accordingly, the study of the resilience of distribution systems under disasters should not be separated from carbon emission factors. Additionally, in the process of actual disaster prevention and power supply restoration, some measures are often taken to maximize the benefits of power supply reliability at the expense of high carbon emissions. However, from a low-carbon perspective, these prevention and response measures for disasters still have room for improvement.

To fill the gaps in the previous research, this paper proposes an optimal allocation method for DRGs considering carbon emissions under multi-scenario disasters. The main contributions can be summarized as follows:

- A DAD optimization model under multi-scenario natural disasters with consideration of carbon emissions is proposed, in which the DRGs are optimally allocated before the disaster and the NR method is adopted after the disaster to achieve disaster prevention and post-disaster restoration.
- The load loss emission ratio (LER) is established as the evaluation index of disaster prevention and response scheme.
- The line fault model under disaster scenarios is modeled, the fault constraints are given, and the selection method of the worst fault scenario is proposed.
- The PHA is adopted to solve the proposed multi-scenario optimization model.

The rest of the paper is organized as follows: In Section 2, the influence of natural disasters on the change of carbon emissions of

distribution system is analyzed. In Section 3, the mathematical formulation of the DAD optimization model is developed. In Section 4, the disaster scenario is modeled and the worst fault scenario selection process is proposed. In Section 5, the solution method to solve the multi-scenario optimization model is presented. Case studies are performed in Section 6. The paper is concluded in Section 7.

2 Carbon emission increment analysis of distribution system under natural disasters

Extreme events such as natural disasters can cause changes in the trajectory of carbon emissions and carbon sinks, bringing risks to achieving carbon neutrality target (Jiang et al., 2022). From the perspective of natural ecosystems, disasters will lead to a series of consequences of reducing carbon sinks and increasing carbon emissions, such as vegetation destruction and fire burning. From the perspective of power system, disasters will directly or indirectly affect the carbon emission. The carbon emission increment caused by natural disasters in the distribution system can be analyzed from the following aspects (Zhang et al., 2022):

1) Natural disasters lead to the functional failure of some equipment, and additional carbon emissions are caused by the replacement of redundant equipment. For example, the destruction of low-carbon power generation resources or the damage of lines lead to the blockage of low-carbon power transmission. In order to ensure the demand of power load, high-carbon power supply is used for replacement, resulting in an increase in carbon emissions.
2) Due to the lack of power supply caused by natural disasters, the increase of carbon emissions can be caused by other power substitution on the power consumer side. After some functions of the distribution system fail, the capacity of redundant equipment can be insufficient, which may lead to consumer-side power outages. For some unstoppable energy supply in production and life, such as many enterprises use self-provided power generation, some commercial or residential electric heating using gas instead, and electrified transportation using fuel oil instead, it means replacing low-carbon power with high-carbon power to meet demand.
3) The reference (Dou et al., 2022) pointed out that natural disasters can reduce carbon emissions to a certain extent, because natural disasters inhibit power consumption. However, in fact, for some production rigid loads, even if the load is reduced due to loss of power supply during the disaster, the production plan will be postponed until the fault is removed, so this part of the carbon emissions is not reduced. Therefore, although this part of the load transfer caused by the disaster itself does not bring excess carbon emissions, it cannot be ignored when calculating the carbon emissions of the power system after the disaster.

The additional carbon emissions of the distribution system under natural disasters may also include: the reduction of carbon sinks caused by the outage of artificial carbon reduction engineering equipment such as carbon capture, utilization and storage (CCUS), and the additional carbon emissions generated during the physical damage removal and fault repair of the distribution system. These are not considered in this paper.

3 Optimal allocation model of DRGs considering carbon emissions

Natural disasters can cause component damage, partial load loss of power supply, and also lead to the risk of additional carbon emissions in the distribution system. In order to improve the resilience to the impact of extreme disasters and reduce the negative impact of extreme disasters on the load loss and carbon emissions of the distribution system, appropriate disaster prevention and response measures need to be developed according to the different vital stages of the disaster effects. In this paper, the occurrence of natural disasters is regarded as an attack on the power grid, and a DAD three-stage model is proposed. The first stage is that the power grid operator acts as the defender to deploy the optimal allocation scheme of the distribution system before the disasters. The second stage is that the disasters act as the attacker to implement the attack behavior. The third stage is to develop a post disaster dispatching plan for the defender to reduce the impact of disasters. The schematic diagram of the three-stage model proposed in this paper is shown in Figure 1.

From the perspective of power grid decision makers, the optimal allocation model proposed in this paper can be divided into two levels: planning investment level and simulated operation level. The objective function can be written in the form of min-max-min as follows:

$$\min_{\boldsymbol{x}} \ \{C^{\text{inv}} + \max_{\boldsymbol{\alpha}} \ \min_{\boldsymbol{y},\boldsymbol{z}} C^{\text{op}}\} \tag{1}$$

where C^{inv} denotes the investment and construction cost of wind turbines (WTs) and PV units; C^{op} denotes the typical daily scenario minimum operating cost; $\boldsymbol{x}$ is the decision-making variable of DRGs optimal allocation, which is a binary variable; $\boldsymbol{\alpha}$ denotes disaster attack scenario; $\boldsymbol{y}$ and $\boldsymbol{z}$ are continuous decision variables and integer decision variables at the operation level.

3.1 Planning investment level model

The model at the planning investment level is to solve the optimal DRGs allocation scheme under the disaster attack scenario. The objective function consider both the investment and construction cost. The objective function is as follows:

$$C^{\text{inv}} = \sum_{n\in\Omega_N} \left(c^{\text{pv}} x_n^{\text{pv}} + c^{\text{wt}} x_n^{\text{wt}}\right) \tag{2}$$

where c^{pv} and c^{wt} are the cost coefficients of PV units and WTs, respectively; x_n^{pv} and x_n^{wt} are the decision variables for optimal allocation at node n; Ω_N the set of nodes in the system.

The constraints at the planning investment level are mainly the allocation budget constraints of DRGs, including the cardinality budget and the monetary budget. The mathematical form of the constraints is as follows:

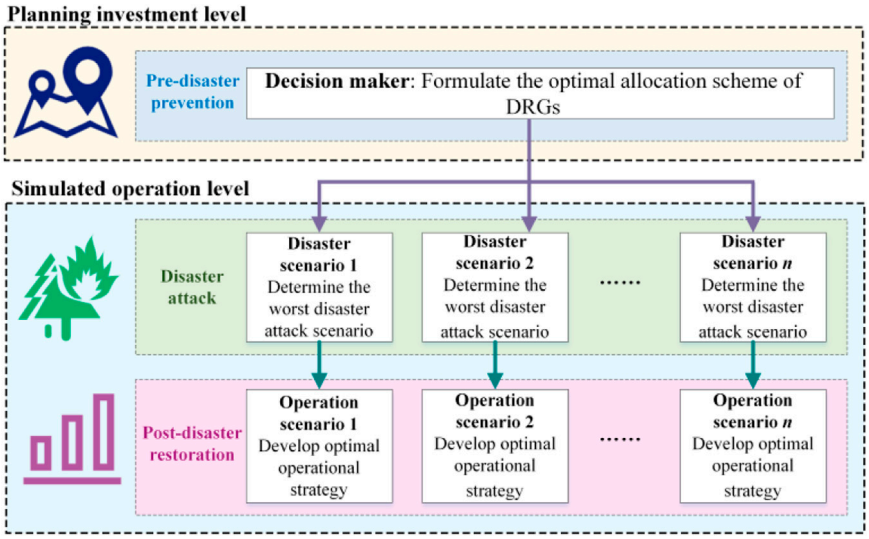

FIGURE 1
Three-stage model diagram.

$$\begin{cases} \sum\limits_{n\in\Omega_N} x_n^{\mathrm{pv}} \le G^{\mathrm{pv}}, \sum\limits_{n\in\Omega_N} x_n^{\mathrm{wt}} \le G^{\mathrm{wt}} \\ \sum\limits_{n\in\Omega_N} \left(c^{\mathrm{pv}} x_n^{\mathrm{pv}} + c^{\mathrm{wt}} x_n^{\mathrm{wt}}\right) \le C^{\mathrm{budget}} \end{cases} \tag{3}$$

where G^{pv} and G^{wt} denote the available number of PV units and WTs respectively; C^{budget} is the budget cost.

3.2 Simulated operation level

An ideal DRGs allocation scheme can not only reduce the output of carbon-emitting units and improve the low-carbon performance of the system operation, but also effectively prevent the risk of insufficient power supply and increased carbon emissions caused by disaster scenarios. Under a given allocation scheme and determined scenario conditions, the model at the simulated operation level minimizes the load loss in the disaster scenarios by means of NR, while also considering the economic efficiency and carbon emission mitigation. Therefore, the optimization objective includes the operation cost $C_{\mathrm{ECO}}^{\mathrm{op}}$ and the degree of load loss $C_{\mathrm{LS}}^{\mathrm{op}}$ under the multi-scenario disasters. In addition, the optimal allocation scheme should be able to mitigate the additional carbon emissions caused by disasters, so the optimization objective also includes the carbon emission cost $C_{\mathrm{CO2}}^{\mathrm{op}}$. The objective function is as follows;

$$C^{\mathrm{op}} = C_{\mathrm{LS}}^{\mathrm{op}} + C_{\mathrm{ECO}}^{\mathrm{op}} + C_{\mathrm{CO2}}^{\mathrm{op}} \tag{4}$$

$$C_{\mathrm{LS}}^{\mathrm{op}} = \sum_{s\in\Phi} \varphi_s \sum_{t\in T} \sum_{l\in\Gamma} VoLL_l \left(L_{l,t,s}^{\mathrm{pre}} - L_{l,t,s}\right) \tag{5}$$

$$C_{\mathrm{ECO}}^{\mathrm{op}} = \sum_{s\in\Phi} \varphi_s \left(C_s^{\mathrm{G}} + C_s^{\mathrm{RE}}\right) \tag{6}$$

$$C_s^{\mathrm{G}} = \sum_{t\in T} \sum_{g\in N_{\mathrm{G}}} \left(a_g P_{g,t,s} + b_g\right) \tag{7}$$

$$C_s^{\mathrm{RE}} = \sum_{t\in T} \sum_{m\in N_{\mathrm{RE}}} \lambda_{\mathrm{RE}} P_{m,t,s} \tag{8}$$

$$C_{\mathrm{CO2}}^{\mathrm{op}} = \sum_{s\in\Phi} \varphi_s \cdot p_{\mathrm{CO_2}} \sum_{t\in T} \left(\sum_{g\in N_{\mathrm{G}}} \delta_g P_{g,t,s} + \sum_{l\in\Gamma} \delta_l^{\mathrm{sub}} L_{l,t,s}^{\mathrm{sub}} \right) \tag{9}$$

where Φ denotes the set of disaster scenarios; φ_s is the probability of occurrence for disaster scenario s; N_{G}, N_{RE} and Γ are the set of carbon emission units, DRGs and loads respectively; C_s^{G} and C_s^{RE} denote the output cost of carbon emission units and the operation and maintenance cost of DRGs in the scenario s respectively; a_g and b_g are the cost coefficients; $VoLL_l$ is the value of lost load (VoLL) l; $L_{l,t,s}^{\mathrm{pre}}$ is the expected load value of load l during period t in the disaster scenario s; $L_{l,t,s}$ is the actual load value of load l during period t in the disaster scenario s; $P_{m,t,s}$ is the output of DRGs; $P_{g,t,s}$ is the output power of carbon emission units; λ_{RE} is the operation and maintenance cost coefficient of DRGs; $p_{\mathrm{CO_2}}$ is the penalty cost per unit mass of CO2; δ_g is the emission coefficient of carbon emission units; $L_{l,t,s}^{\mathrm{sub}}$ is the output of power substitution on the consumer side; δ_l^{sub} is the emission coefficient of energy substitution.

The constraints of the above model are as follows:

3.2.1 Power balance and power flow constraints

The DC power flow model is adopted for modeling, and the following constraints should be met for all scenarios $s \in \Phi$:

$$\boldsymbol{A}_g \boldsymbol{P}_{g,t,s} + \boldsymbol{A}_m \boldsymbol{P}_{m,t,s} = \boldsymbol{A}_l \boldsymbol{L}_{l,t,s} + \boldsymbol{A}_{b,s} \boldsymbol{P}_{b,t,s} + \boldsymbol{A}_{sw} \boldsymbol{P}_{sw,t,s} \tag{10}$$

$$\left| PL_{ij,t,s} - B_{ij}\left(\theta_{i,t}^s - \theta_{j,t}^s\right) \right| \le M\left(1 - z_{ij}^s\right), i, j \in \Omega_N \tag{11}$$

$$PL_{ij}^{\min} \le PL_{ij,t,s} \le PL_{ij}^{\max}, i, j \in \Omega_N \tag{12}$$

$$\theta_i^{\min} \le \theta_{i,t}^s \le \theta_i^{\max}, i \in \Omega_N \tag{13}$$

where $\boldsymbol{A}_g$, $\boldsymbol{A}_m$, $\boldsymbol{A}_l$, $\boldsymbol{A}_{b,s}$ and $\boldsymbol{A}_{sw}$ are the incidence matrices of carbon emission units, DRGs, loads, lines and reconfiguration switches respectively; $P_{b,t,s}$ and $P_{sw,t,s}$ are the power flow through the branches and the reconfiguration switches; $PL_{ij,t,s}$ is the power flow from node i to node j; B_{ij} denotes the line admittance; $\theta_{i,t}^s$

and $\theta_{j,t}^{s}$ denote the phase angle; M is a big number; z_{ij}^{s} is the operating status of line i-j ; $PL_{ij}{}^{\max}$ and $PL_{ij}{}^{\min}$ are the upper and lower limits of line transmission capacity.

3.2.2 Reconfiguration switch constraint

Under the disaster scenario, the distribution system adjusts the state of the reconfiguration switches by means of NR, so as to change the operation mode, which can effectively reduce the load loss, mitigate the impact of disasters and improve the ability to cope with natural disasters. The reconfiguration switch constraint is as follows:

$$z_{sw}^{s}P_{sw}^{\min} \le P_{sw,t,s} \le z_{sw}^{s}P_{sw}^{\max}, sw \in N_{\mathrm{sw}} \tag{14}$$

where z_{sw}^{s} denotes the final state of the line controlled by the reconfiguration switch; $P_{sw}^{\max}$ and $P_{sw}^{\min}$ are the upper and lower limits of reconfiguration switch transmission capacity; N_{SW} is the set of the reconfiguration switches.

3.2.3 Power output constraints

The power sources in the distribution system mainly include controllable distributed generators (DG) and renewable power generation. In addition, the injection power of the upstream power grid is also regarded as the power output, and the output cost mainly considers the purchase cost of the upstream power grid.

$$P_{g}^{\min} \le P_{g,t,s} \le P_{g}^{\max}, g \in N_{\mathrm{G}}, s \in \Phi \tag{15}$$

$$0 \le P_{m,t,s} \le P_{m,t,s}^{\max}, m \in N_{\mathrm{RE}}, s \in \Phi \tag{16}$$

where $P_{g}{}^{\max}$ and $P_{g}{}^{\min}$ are the maximum and minimum power output of non-renewable power generations; $P_{m,t,s}{}^{\max}$ is the maximum power output of DRGs.

3.2.4 Load shedding constraint

In order to maintain power balance, part of the load can be disconnected from the grid by load shedding when the distribution system fails due to disasters. The load shedding cannot exceed the expected load, so the constraint can be expressed as follows:

$$0 \le L_{l,t,s}^{\mathrm{pre}} - L_{l,t,s} \le L_{l,t,s}^{\mathrm{pre}}, s \in \Phi \tag{17}$$

3.2.5 Topological constraints

After natural disasters, the distribution system can realize island partition through NR and improve the reliability of power supply. To prevent the occurrence of ring and node isolation after NR, the radiality of the distribution system and the connectivity of the islands should be guaranteed. The reconstructed grid topology under the fault scenario should meet the following two necessary and sufficient conditions (Balakrishnan and Ranganathan, 2012).

Condition 1. The number of closed branches is equal to the total number of nodes minus the number of partitions.

Condition 2. Each partition should ensure its connectivity.

The key to satisfy the first condition is to determine the number of partitions. In the reference (Lavorato et al., 2012), the number of DGs is taken as the number of partitions when partitioning islands. However, in fact, there may be multi-power island and load island. In this regard, this paper assumes that each partition has only one dominant node, and the number of dominant nodes determines the number of partitions. Then the constraints corresponding to Condition 1 can be expressed as follows:

$$\sum_{(i,j)\in\Omega_B} z_{ij} = N_{\mathrm{bus}} - \sum_{i\in\Omega_N} r_{i}^{s} \tag{18}$$

where Ω_B is the set of branches; N_{bus} is the total number of nodes; r_{i}^{s} denotes whether node i is selected as the dominant node of the partition under scenario s.

According to the safe operation regulations, the distribution system performs topology transformation after the fault occurs. Usually, only the substation node and some controllable DG can be used as the black-start power supply for the islanded partition. Therefore, the substation node and the controllable DG node can be used as alternatives to the dominant node. It is assumed that the DRGs allocated in this paper are equipped with self-organizing inverters (Du et al., 2022), which can be selected as the dominant point of islanded partitions. In addition, due to the possibility of load island, the associated nodes of the fault line can also be used as the dominant nodes. Since there must be at least one dominant node in the distribution system, the following constraints should be met:

$$\sum_{i\in\Omega_N} r_{i}^{s} \ge 1 \tag{19}$$

For Condition 2, this paper uses the single commodity flow method to describe the connectivity constraints of the partition. For each partition, its only dominant node is set as a fictitious source, and other non-dominant nodes are set as fictitious loads (the load value can be valued as 1). In order to ensure connectivity, all non-dominant nodes should be connected to the dominant node, and the following fictitious flow constraints need to be met (Ding et al., 2017a; Ding et al., 2017b; Zhang et al., 2020b):

$$\begin{cases} \sum_{j\in\sigma(i)} F_{ij}^{s} - \sum_{j\in\pi(i)} F_{ji}^{s} \ge -1 - M\cdot r_{i}^{s}\cdot\left(x_{i}^{g}+x_{i}^{f}\right) \\ \sum_{j\in\sigma(i)} F_{ij}^{s} - \sum_{j\in\pi(i)} F_{ji}^{s} \le -1 + M\cdot r_{i}^{s}\cdot\left(x_{i}^{g}+x_{i}^{f}\right) \\ \sum_{j\in\sigma(i)} F_{ij}^{s} - \sum_{j\in\pi(i)} F_{ji}^{s} \ge W_{i}^{s} - M\cdot\left(1-r_{i}^{s}\right) \\ \sum_{j\in\sigma(i)} F_{ij}^{s} - \sum_{j\in\pi(i)} F_{ji}^{s} \le W_{i}^{s} + M\cdot\left(1-r_{i}^{s}\right) \\ -M\cdot z_{ij} \le F_{ij}^{s} \le M\cdot z_{ij} \\ W_{i} \ge 0 \end{cases} \tag{20}$$

where F_{ij}^{s} is the fictitious flow on line i-j under scenario s; x_{i}^{g} indicates whether there is a power generation unit at node i; x_{i}^{f} indicates whether node i is associated with a fault line; W_{i}^{s} denotes the output of the fictitious source at node i. Since the fault line may appear at the end node of the distribution system, forming a single node island, the minimum value of W_{i}^{s} must be 0.

If the above fictitious flow constraints can be met, it means that there is at least one path from the fictitious source node to the fictitious load node. Since the fictitious flow constraints have the same topology as the original distribution system, the connectivity of the partition can be guaranteed. In Eq. 20, $(x_{i}^{g}+x_{i}^{f})$ denotes whether node i can be chosen as the dominant node. The dominant node should meet the following constraint:

$$r_{i}^{s} \le \left(x_{i}^{g}+x_{i}^{f}\right) \tag{21}$$

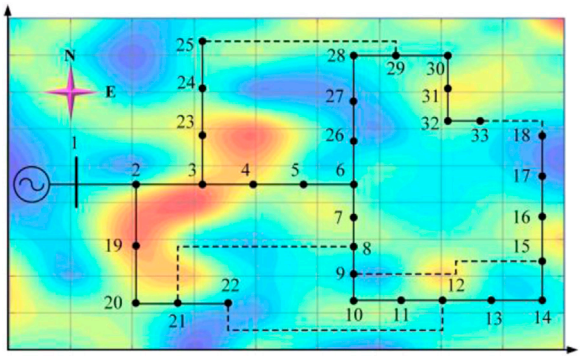

FIGURE 2
GIS-based disaster frequency heat map in distribution system.

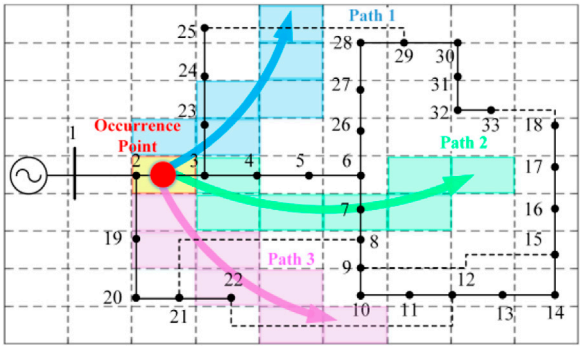

FIGURE 3
Disaster development path in distribution system.

3.3 Evaluation index

In order to evaluate the impact of the response scheme on the carbon emissions of the disaster-stricken distribution system, this paper first defines the total carbon emission (TCE) as an evaluation index to evaluate the carbon emission of the system under a given scheme. As previously analyzed, carbon emissions from rigid loads with production plan postponement need to be considered in post-disaster carbon accounting, so the TCE calculation formula is as follows:

$$TCE = D\sum_{s\in\Phi}\varphi_s\sum_{t\in T}\left(\sum_{g\in N_G}\delta_g P_{g,t,s} + \sum_{l\in\Gamma}\delta_l^{\text{sub}} L_{l,t,s}^{\text{sub}} + \sum_{l\in\Gamma}\delta_g L_{l,t,s}^{\text{trans}}\right) \quad (22)$$

where D is the frequency of disasters in a year; $L_{l,t,s}^{\text{trans}}$ denotes the loss of rigid load with production plan postponement. This paper considers that the transfer load is powered by the substation after disaster restoration, so its carbon emission coefficient is δ_g.

On this basis, in order to comprehensively consider the impact of disaster response schemes on power supply reliability and carbon emissions, a load loss emission ratio (LER) is defined to characterize the effect of disaster response measures. The smaller the value is, the smaller the load loss value corresponding to the unit carbon emission under the scheme is. That is, more loads are restored at the cost of smaller carbon emissions. The calculation formula of LER is as follows:

$$LER_{\boldsymbol{x}} = \frac{\sum_{s\in\Phi}\sum_{t\in T}\sum_{l\in\Gamma} D\left(L_{l,t,s}^{\text{pre}} - L_{l,t,s}\right)}{TCE_{\boldsymbol{x}}} \quad (23)$$

where $TCE_{\boldsymbol{x}}$ is the total carbon emissions under response scheme $\boldsymbol{x}$. It is worth noting that the value of LER is not the smaller the better. It is also necessary to comprehensively evaluate the scheme according to the actual load loss value and the total carbon emission.

4 Modeling and analysis of disaster scenarios

4.1 Disaster development model

The occurrence and development of natural disasters have certain regional and directional characteristics, and as a form of attack, its impact on the distribution system has certain uncertainty. Therefore, when analyzing the impact of natural disaster damage on the distribution system, it is necessary to fully consider the spatial and temporal characteristics of natural disaster development, clarify the disaster path in the distribution system, determine the scope of disaster impact on the distribution system, and evaluate the severity of disaster impact on the components in the distribution system.

Due to the strong correlation between the occurrence of natural disasters and geographical location, this paper combines the topology with the geographical information system (GIS), divides the system into square grids based on geographical areas (9), and draws a disaster frequency heat map as shown in Figure 2 based on the historical data of disasters. The red area in Figure 2 represents the disaster-prone area, and the deeper the red color, the higher the frequency of disasters, while the blue area represents the area where rare disasters occur. It can be seen from Figure 2 that the distribution system in the red area is more vulnerable to natural disasters and damage, resulting in fault.

According to the disaster frequency heat map, the average frequency of a certain type of disaster in each square grid can be calculated, so as to obtain the high frequency occurrence square grid of such disaster in the grid area. The occurrence and development of disasters usually have certain dynamic spatial and temporal distribution characteristics, so it is necessary to consider the impact of disaster development path. This paper assumes that the disaster moves geographically along the development path and affects the distribution system along the way, causing the power line on the moving path to fail. Figure 3 shows the path of disaster development in the distribution system. The disaster moves along different paths from the occurrence point, and the lines in the square grid on the path will be affected by the disaster. Because the square grids on the disaster path are in different geographical areas, the degree of disaster impact is not the same. This paper assumes that in the square grid near the disaster point, the power grid is more seriously affected, while the grid far away from the disaster point is relatively less affected by the disaster (18). According to the disaster path and the disaster intensity in the square grid, the fault probability curve can be used to calculate the fault probability of the line in the grid. The fault probability curve can usually be expressed as (Panteli et al., 2017):

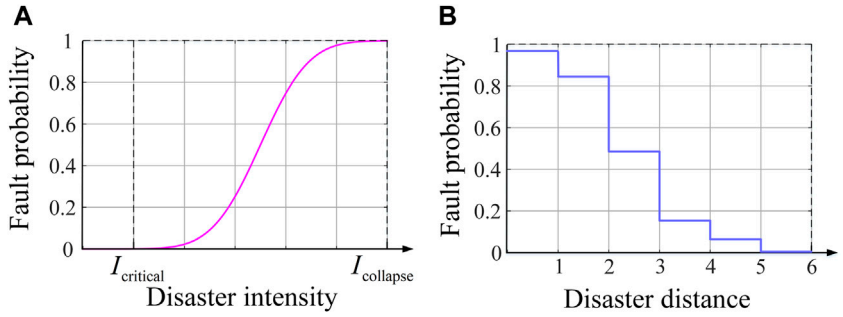

FIGURE 4
(A) Line fault probability under the variety of disaster intensity; **(B)** Line fault probability under the variety of disaster distance.

$$\mathbb{P}^s = \begin{cases} 0, & I < I_{\text{critical}} \\ \mathbb{P}^s(I), & I_{\text{critical}} \le I < I_{\text{collapse}} \\ 1, & I \ge I_{\text{collapse}} \end{cases} \tag{24}$$

where $\mathbb{P}^s$ denotes the line fault probability in the grid related to the disaster intensity in scenario s; I denotes the intensity of disaster; I_{critical} is the critical disaster intensity that causes the line to fail; I_{collapse} is the intensity of the disaster that makes the line certain fault. Figure 4A shows the line fault probability curve under the variety of disaster intensity.

Because it is difficult to accurately measure and calculate the disaster intensity, in order to simplify the model and facilitate the solution, this paper uses the distance between the square grid on the disaster path and the disaster occurrence point to replace the disaster intensity as the input of the fault probability curve, and sets the line fault probability in each square grid to be the same. Therefore, the fault probability curve is discretized, and the discretized curve is shown in Figure 4B. In the figure, the disaster distance of the abscissa is represented by the square grid order along the disaster path.

4.2 Disaster scenario constraints

The distribution system itself has a certain degree of resistance to natural disasters, which determines that the damage of disasters to the power system is not without an upper limit. Therefore, this should be taken into account when generating line fault constraints in disaster scenarios. The disaster scenario is modelled by using the line fault set considering the budget of disaster attack. For a certain type of disaster scenario, the following constraints should be met:

$$\sum_{(i,j)\in\Omega_R} u_{ij}^s \le K_{\text{budget}} \tag{25}$$

where u_{ij}^s indicates whether line i-j is affected by disasters and has faults. Ω_R denotes the set of lines on the disaster path; K_{budget} is the budget of disaster attack, the maximum number of fault lines under the disaster. Ignoring the sequence of the impact of disasters on the line, the model can be regarded as a typical N-K fault problem. The constraint Eq. 25 can be rewritten as follows:

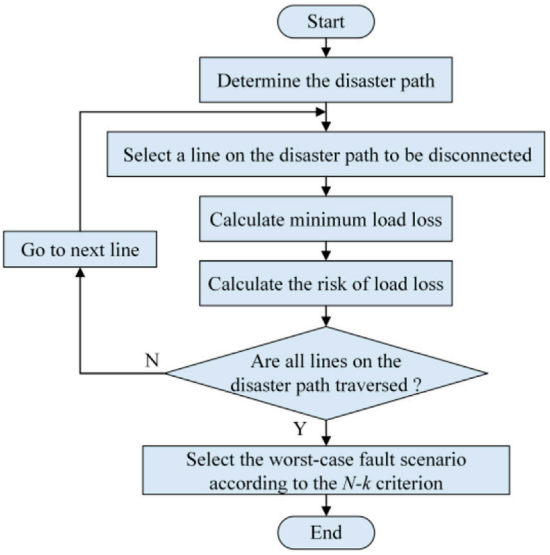

FIGURE 5
Flowchart of worst-case fault scenario selection.

$$\sum_{(i,j)\in\Omega_B} \left(1 - u_{ij}^s\right) \ge N_{\text{brch}} - K_{\text{budget}} \tag{26}$$

where N_{brch} is the total number of the branches in the system, containing the branches where the reconfiguration switches are located.

After considering the impact of disasters and NR, the final state of the line in the distribution system can be expressed as:

$$z_{ij}^s = \left(z_{ij}^0 + U_{sw}^s\right) \cdot \left(1 - u_{ij}^s\right) \tag{27}$$

where z_{ij}^0 is the initial state of the line in the distribution system; U_{sw}^s is the state variable of the reconfiguration switch; It should be noted that when the line controlled by the reconfiguration switch is on the path affected by the disaster, if the disaster causes damage to the line, the line cannot operate normally even if the reconfiguration switch is closed.

4.3 Selection method of worst-case fault scenario

For the DAD model proposed in this paper, in order to ensure the robustness of the allocation results, the most severe impact of natural disasters as attackers on the distribution system should be considered. Based on the *N-K* criterion, a method for selecting the worst-case fault scenario considering the line fault probability is proposed. This method evaluates the severity of the impact of a line fault on the distribution system by solving the risk of load loss (Nikkhah et al., 2018). The worst-case fault scenario selection process is shown in Figure 5.

The calculation formula of the risk of load loss (RoLL) mentioned in the above process is as follow:

$$RoLL_l = C_{\mathrm{LS}}^{\mathrm{op}} \cdot \mathbb{P}_l^s \tag{28}$$

where $RoLL_l$ denotes the load loss risk value of line l; $C_{\mathrm{LS}}^{\mathrm{op}}$ denotes the load loss after line l fault; $\mathbb{P}_l^s$ denotes the fault probability of line l under disaster scenario s.

5 Solution algorithm

5.1 Model linearization

After obtaining disaster information and related data, using the aforementioned disaster scenario modeling and worst-case fault scenario selection methods, it is possible to determine the specific attack scenario $\boldsymbol{\alpha}$ in which the disaster acts as an attacker in the distribution system, corresponding to the second stage of the DAD model proposed in Section 3. Therefore, the min-max-min problem in this paper can be transformed into a mixed integer programming (MIP) optimization problem with both inner and outer layers in the form of min, so that it can be combined into a single-layer optimization model, which can be written as follow:

$$\begin{cases} \min\limits_{\boldsymbol{x},\boldsymbol{y}_s,\boldsymbol{z}_s} \ \boldsymbol{c}^{\mathrm{T}}\boldsymbol{x} + \sum\limits_{s\in\Phi} \varphi_s \boldsymbol{d}^{\mathrm{T}}\boldsymbol{y}_s \\ \text{s.t. } \boldsymbol{G}\boldsymbol{x} \geq \boldsymbol{g} \\ \boldsymbol{K}_s\boldsymbol{y}_s \geq \boldsymbol{h}_s \\ \boldsymbol{F}_s\boldsymbol{z}_s \geq \boldsymbol{m}_s \\ \boldsymbol{Q}_s\boldsymbol{z}_s = \boldsymbol{r}_s \\ \boldsymbol{I}_s\boldsymbol{y}_s + \boldsymbol{J}_s\boldsymbol{z}_s \geq \boldsymbol{l}_s \\ \boldsymbol{U}_s\boldsymbol{y}_s + \boldsymbol{T}\boldsymbol{x}\boldsymbol{y}_s = \boldsymbol{v}_s \end{cases} \tag{29}$$

where he specific expression of the optimization decision variables are:

$$\begin{cases} \boldsymbol{x} = \left[x_n^{\mathrm{pv}}, x_n^{\mathrm{wt}}\right]^{\mathrm{T}} \\ \boldsymbol{y}_s = \left[L_{l,t,s}, P_{g,t,s}, P_{m,t,s}, P_{b,t,s}, P_{sw,t,s}, \theta_{i,t,s}, F_{ij}^s, W_i^s\right]^{\mathrm{T}} \\ \boldsymbol{z}_s = \left[U_{sw}^s, r_i^s\right]^{\mathrm{T}} \end{cases} \tag{30}$$

The first row of constraints in Eq. 29 corresponds to Eq. 3; the second row corresponds to the last row of Eqs 12, 13, 15, 17, 20; the third row corresponds to Eqs 19, 21; the fourth row corresponds to Eqs 18, 27; the fifth row corresponds to Eqs 11, 14, and the first five rows of Eq. 20; and the sixth row corresponds to Eq. 10.

It can be seen that there is a case where integer decision variables are multiplied by continuous decision variables in constraint Eq. 10, and it is difficult to solve this nonlinear constraint. Therefore, the following linear equivalent transformation is conducted for this constraint:

First, define the auxiliary variable w_s, let:

$$w_s = \boldsymbol{A}_m P_{m,t,s} \tag{31}$$

Then, the following auxiliary constraints are introduced:

$$\begin{cases} w_s \leq P_{m,t,s} \\ w_s \geq P_{m,t,s} - (\boldsymbol{E} - \boldsymbol{A}_m) P_{m,t,s}^{\max} \\ 0 \leq w_s \leq \boldsymbol{A}_m P_{m,t,s}^{\max} \end{cases} \tag{32}$$

Finally, the constraint Eq. 10 becomes:

$$\boldsymbol{A}_g P_{g,t,s} + w_s = \boldsymbol{A}_l L_{l,t,s} + \boldsymbol{A}_{b,s} P_{b,t,s} + \boldsymbol{A}_{sw} P_{sw,t,s} \tag{33}$$

5.2 Solution method of PHA

As can be seen from Eq. 29, the model is a hierarchical multi-scenario optimization problem. The investment level decision variable a is an ex-ante decision variable that is independent of the scenario, while the operation level decision variables b and c are related to the scenario and need to be calculated based on the specific disaster scenario. For the multi-scenario optimization problem, the progressive hedging algorithm (Rockafellar and Wets, 1991) is employed to solve it. PHA is a decomposition algorithm for multi-scenario optimization problems. Its main idea is to use orthogonal projection and augmented Lagrange multiplier method to decompose the original problem into sub-problems in multiple scenarios for iterative solution. The advantage of PHA is that it exhibits global convergence when dealing with convex optimization problems. For the optimization problem shown in Eq. 29, the PHA iteration steps are as follows:

1) Initialization. Set $k = 0$, $\boldsymbol{\omega}_s^{(k)} = 0$.
2) For all scenario $s \in \Phi$, solve the following optimization problems:

$$\boldsymbol{x}_s^{(k)}: \ = \operatorname{argmin}\left\{\boldsymbol{c}^{\mathrm{T}}\boldsymbol{x} + \boldsymbol{d}^{\mathrm{T}}\boldsymbol{y}_s\right\} \tag{34}$$

3) Update the parameters.

$$\bar{\boldsymbol{x}}^{(k)} = \sum_{s\in\Phi} \varphi_s \boldsymbol{x}_s^{(k)} \tag{35}$$

$$\boldsymbol{\omega}_s^{(k+1)} = \boldsymbol{\omega}_s^{(k)} + \rho\left(\boldsymbol{x}_s^{(k)} - \bar{\boldsymbol{x}}^{(k)}\right) \tag{36}$$

4) Set $k = k + 1$. And solve augmented Lagrange form optimization problems for all scenario $s \in \Phi$.

$$\boldsymbol{x}_s^{(k)}: \ = \operatorname{argmin}\left\{\begin{array}{c} \boldsymbol{c}^{\mathrm{T}}\boldsymbol{x} + \boldsymbol{d}^{\mathrm{T}}\boldsymbol{y}_s \\ +\boldsymbol{\omega}_s^{(k-1)}\boldsymbol{x} + \dfrac{\rho}{2}\left\|\boldsymbol{x} - \bar{\boldsymbol{x}}^{(k-1)}\right\|^2 \end{array}\right\} \tag{37}$$

5) Update the parameters according to Eqs 35, 36 and calculate the convergence index.

$$\gamma^{(k)} = \sum_{s\in\Phi} \varphi_s \left\|\boldsymbol{x}_s^{(k)} - \bar{\boldsymbol{x}}^{(k)}\right\| \tag{38}$$

If $\gamma^{(k)} < \varepsilon$, the iteration is terminated and then take $\boldsymbol{x}^* = [\bar{\boldsymbol{x}}^{(k)} + 0.5\boldsymbol{I}_{\mathrm{E}}]$; otherwise return to step 4.

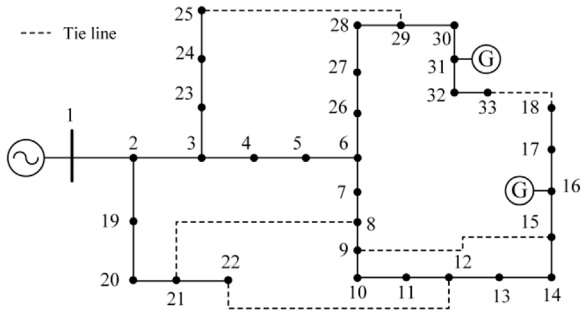

FIGURE 6
Modified IEEE 33-node system diagram.

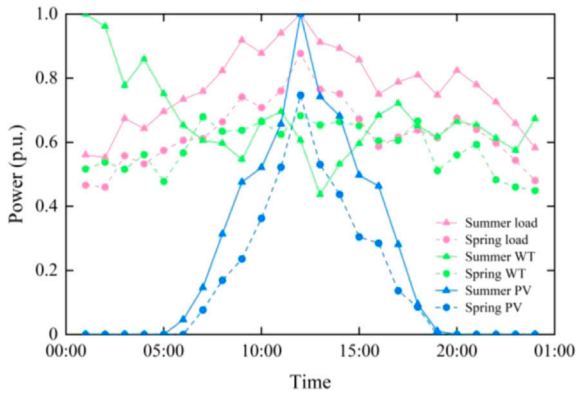

FIGURE 7
Curve of wind power, photovoltaic power and load under different disaster scenarios.

In the above iteration process, k denotes the number of iterations. $\boldsymbol{\omega}_s^{(k)}$ denotes the auxiliary multiplier of the k-th iteration under the scenario s. $\boldsymbol{x}_s^{(k)}$ denotes the investment level solution of the sub-problem solved by the k-th iteration under scenario s. $\bar{\boldsymbol{x}}^{(k)}$ is the weighted average of the solutions of the investment level under all scenario $s \in \Phi$ after the k-th iteration. ρ is a penalty parameter, and the value can refer to the reference (Watson and Woodruff, 2011). $\boldsymbol{x}^*$ denotes the optimal solution of investment level. $\boldsymbol{I}_E$ is a column vector whose elements are all 1. $[\cdot]$ denotes the rounding operation for matrix elements.

6 Case study

6.1 Case description

The modified IEEE 33-node distribution system is used for case study, as shown in Figure 6. In the system, node 16 and node 31 are connected with a micro turbine (MT) respectively. In addition, there are power substitutions at nodes 14, 22, and 24, and rigid load with load transfer at nodes 10, 17, and 27. The disaster scenario data and disaster geographic information are derived from the actual statistical data of a disaster-prone year in a city in China. Using the method proposed in Section 4.1 to process disaster data can obtain typical disaster scenario probabilities, disaster paths, and line fault probabilities on disaster paths, as shown in Table 1. Due to the obvious seasonal characteristics of the occurrence of disasters, the k-means clustering method is used to process the historical data of wind power, photovoltaic and load in the disaster-prone seasons. This paper mainly focuses on the summer with frequent floods and the spring with frequent wildfires, and obtains the typical intraday curves of wind power, photovoltaic and load under disaster scenarios, as shown in Figure 7. The VoLL of each node of the test system is shown in Table 2. The allocation budget of DRGs includes 2 photovoltaic units and 1 WT with a capacity of 400 kW, and the power generation costs are 0.35¥/(kW·h) and 0.28¥/(kW·h) respectively. The cost of purchasing power from the upstream power grid is 0.78¥/(kW·h), and other parameters are shown in Table 3. In this paper, the duration of a single disaster is considered to be 24 h, so the simulation time scale is set to 24 h.

6.2 Selection of worst-case fault scenario

In order to obtain the most severe line faults combination in the disaster scenario, traverse each line on the disaster path, set the line disconnected and calculate the RoLL value, and the results shown in Table 4 can be obtained. Set the disaster attack budget value K_{budget}, and based on the results in Table 4, select the same number of lines with large RoLL values in the scenario as the worst-case fault scenario for the disaster scenario.

6.3 Operation and allocation results under multi-scenario disasters

In order to verify the effectiveness of the model and disaster response measures proposed in this paper, five schemes are set up for comparison. The scheme settings are shown in Table 5. Set the disaster attack budget K_{budget} to 2, and according to Table 4, the worst-case fault scenarios are: lines 5–6 and 7–8 (in scenario 1); lines 31–32 and 23–24 (in scenario 2); lines 6–7 and 26–27 (in scenario 3); lines 3–4 and 19–20 (in scenario 4). The results

TABLE 1 Description of typical disaster scenarios.

Disaster type	Scenario number	Scenario probability φ_s	Disaster path and fault probability of lines (line, probability)
Flood	1	0.2	(12–13, 0.82) (11–12, 0.78) (7–8, 0.42) (6–7, 0.22) (5–6, 0.18) (3–23, 0.12)
	2	0.2	(17–18, 0.65) (31–32, 0.60) (30–31, 0.45) (27–28, 0.32) (23–24, 0.22)
Wildfire	3	0.3	(29–30, 0.78) (26–27, 0.71) (6–26, 0.55) (6–7, 0.23) (7–8, 0.18)
	4	0.3	(20–21, 0.75) (19–20, 0.67) (2–19, 0.43) (3–4, 0.32) (3–23, 0.24) (23–24, 0.19)

TABLE 2 Value of lost load of buses.

Node	*VoLL* [¥/(kW·h)]	Node	*VoLL* [¥/(kW·h)]	Node	*VoLL* [¥/(kW·h)]	Node	*VoLL* [¥/(kW·h)]
2	2.18	10	3.64	18	3.788	26	3.38
3	2.93	11	1.79	19	4.02	27	1.49
4	4.08	12	2.58	20	3.30	28	2.18
5	4.10	13	3.96	21	3.52	29	1.53
6	1.84	14	3.62	22	3.48	30	1.67
7	4.11	15	4.09	23	2.50	31	3.70
8	4.09	16	3.24	24	3.24	32	3.35
9	2.76	17	1.50	25	1.88	33	2.29

TABLE 3 Parameter settings.

Parameter	Value
a_g/b_g [¥/(kW·h)]	0.67/0
p_{CO2} (¥/t)	100
δ_g [t/(MW·h)]	1.2
δ_l^{sub} [t/(MW·h)]	1.5
$P_{sw}^{\min}/P_{sw}^{\max}$ (kW)	−1,000/1,000
$P_g^{\min}/P_g^{\max}$ (kW)	0/800
D (d)	10

TABLE 4 RoLL of lines under different disaster scenarios.

Scenario 1		Scenario 2		Scenario 3		Scenario 4	
Line	*RoLL*	Line	*RoLL*	Line	*RoLL*	Line	*RoLL*
12–13	0.2429	17–18	8.1782	29–30	1.3026	20–21	14.3070
11–12	1.3789	31–32	18.6481	26–27	7.6033	19–20	18.8049
7–8	14.7783	30–31	0.0412	6–26	7.5696	2–19	16.7722
6–7	13.7682	27–28	5.4579	6–7	8.7538	3–4	20.4341
5–6	15.0902	23–24	17.4896	7–8	3.1352	3–23	17.2386
3–23	10.5382	—	—	—	—	23–24	12.3542

solved under the five different disaster response schemes are shown in Table 6.

By comparing the results of the scheme 1 and scheme 2, it can be seen that by adopting the NR, the load loss caused by the distribution system failure under the disaster is reduced by 81.94%, and the total operation cost is reduced by 5.34×10^4¥. This indicates that NR can effectively restore most of the power supply after a distribution system failure, ensuring power supply reliability. Due to the NR restoring a large amount of load, resulting in an increase in the output of carbon emission units, the carbon emissions in scheme 2 have significantly increased compared to scheme 1. From the LER value, it can be seen that scheme 2 is superior to scheme 1.

TABLE 5 Scheme settings.

Scheme	Optimal allocation	Random allocation	NR
1	×	×	×
2	×	×	√
3	×	√	×
4	√	×	×
5	√	×	√

From the results of scheme 3 and scheme 4, it can be concluded that compared with scheme 1, after the allocation of PV unit and WT, the load loss under disasters is reduced by 5,171.12 and 6,978.41 kW·h respectively, and the total carbon emission is reduced by 5.28% and 6.68% respectively. This is due to the fact that the output of DRGs has restored the lost load in some load islands, and the total carbon emission has decreased due to the replacement of the output of MT and upstream power grid. This indicates that the allocation of DRGs in the pre-disaster prevention stage can effectively improve the load restoration capability and reduce the carbon emissions. Compared with the result under random allocation, the optimal allocation of DRGs can further reduce the load loss of 1,807.29 kW·h and the total carbon emission of 1.40% under disaster scenarios. The LER value of scheme 4 is less than that of scheme 3, and it can be concluded that the optimal allocation effect of scheme 4 is better than that of scheme 3.

As can be seen from Table 6, scheme 5 can significantly reduce the load loss caused by disasters and greatly reduce the total cost by optimizing the allocation of DRGs before disasters and adopting NR after disasters. Compared with operation scheme 2, scheme 5 further reduces the total carbon emissions. However, compared with schemes 3 and 4, the total carbon emissions increase. The reason is that NR leads to the restoration of power supply for a large number of loads, and the output of carbon emission units increases. According to the LER value, scheme 5 is the optimal scheme.

TABLE 6 Results under different schemes.

Scheme	Total cost (10^4 ¥)	Load loss (kW·h)	*TCE* (t)	*LER*	Allocation node [(PV), (WT)]
1	16.49	35,034.27	1,194.87	293.21	—
2	11.15	6,325.80	1,408.38	44.92	—
3	14.68	29,863.15	1,131.81	263.85	(7, 26), (20)
4	14.04	28,055.86	1,115.06	251.61	(9, 33), (21)
5	10.28	3,334.78	1,322.82	25.21	(7, 25), (30)

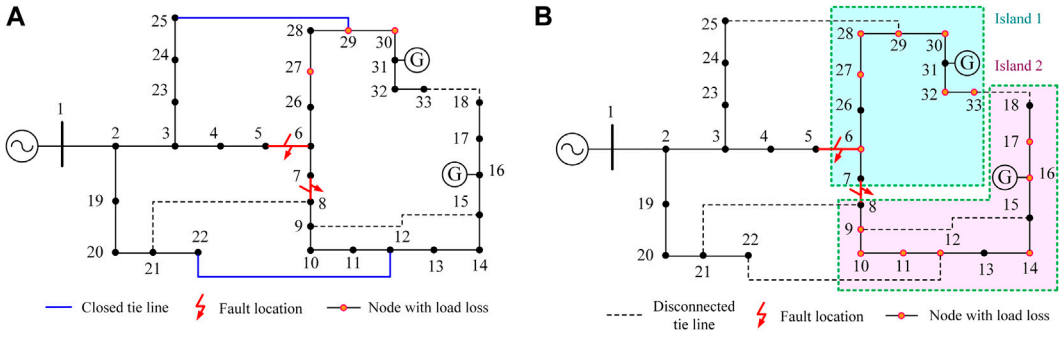

FIGURE 8
(A) Operation without NR; **(B)** Operation with NR.

TABLE 7 Results in different case 1 and case 2 under disaster scenario 1.

Fault line	NR line	Total cost (10^4¥)	Load loss (kW·h)	*TCE* (t)	*LER*
5–6, 7–8	—	17.04	37,650.70	1,292.65	291.27
5–6, 7–8	12–21, 25–29	12.14	2,997.12	1,627.83	18.41

6.4 Effectiveness of NR

In order to demonstrate the effect of NR on restoring lost load, calculation and analysis are carried out under a single disaster scenario. Based on disaster scenario 1, the test is carried out under scheme 1 and scheme 2 respectively. The results are shown in Figure 8 and Table 7. Comparing Figures 8A, B, it can be seen that without NR, two load islands are generated in the distribution system due to line faults. Although the islands are equipped with corresponding black-start power supplies, due to the limited capacity of the unit, most nodes still have load loss, and the reliability of power supply is low. After adopting the network reconstruction method, the switches between the tie line 12–22 and 25–29 is closed, so that the entire distribution system maintains a radial complete connection state, avoiding the generation of load islands. In this case, the load loss of the entire power grid is reduced. Although due to the transmission capacity limit of tie lines, the lost load has not been fully restored, compared to the case where NR is not taken, the load loss has been reduced by 92.04%, and the fault restoration ability of the distribution system has been greatly improved. From the LER value, adopting NR can restore more power at a lower cost of carbon emissions.

6.5 Effectiveness of different allocation scheme

In order to compare the effects of different allocation schemes, the calculation under a single disaster scenario is performed based on disaster scenario 4, and the results under three different allocation schemes are obtained, as shown in Figure 9 and Table 8.

As can be seen from Figure 9A, when allocation scheme 1 is adopted, there are four DGs in island 1 for load restoration. However, because there is only one power dividing point of node 7, the PV units located at node 7 and node 26 cannot deliver power to node 27 and its downstream nodes. In fact, the total load of nodes 31 and 32 at the end of the branch is heavy, and the VoLL of the load is large. Therefore, under this allocation scheme, the renewable energy is not fully utilized, and the important load is not sufficiently

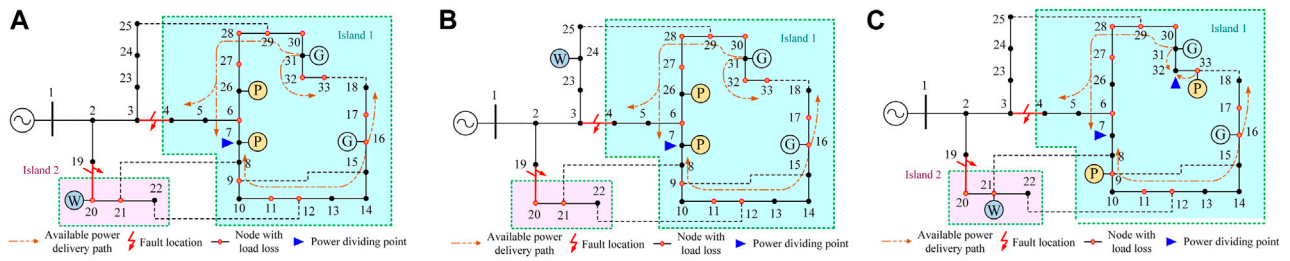

FIGURE 9
(A) Random allocation scheme 1; **(B)** Random allocation scheme 2; **(C)** Optimal allocation scheme.

TABLE 8 Results under different allocation scheme.

Allocation scheme	Fault line	Allocation node [(PV), (WT)]	Total cost (10^4¥)	Load loss (kW·h)	*TCE* (t)	*LER*
1	3–4, 19–20	(7, 26), (20)	14.62	30,268.90	984.87	307.34
2	3–4, 19–20	(7, 26), (24)	14.27	34,310.34	924.78	371.01
3	3–4, 19–20	(9, 33), (21)	12.78	28,712.36	943.90	304.19

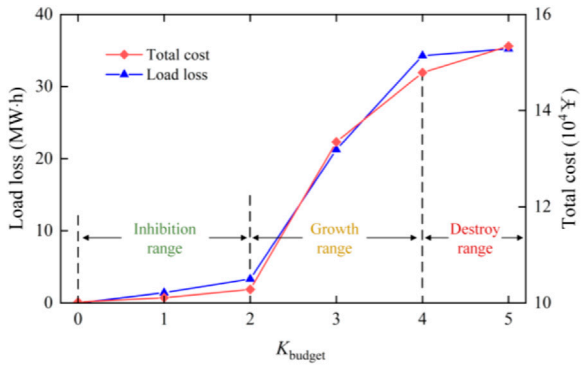

FIGURE 10
Load loss and total cost under different disaster severity.

TABLE 9 Results under different placement scheme.

K_{budget}	Allocation node [(PV), (WT)]	*TCE* (t)	*LER*
0	(18, 24), (33)	1,353.08	0
1	(11, 32), (33)	1,346.79	10.58
2	(7, 25), (30)	1,322.82	25.21
3	(26, 33), (7)	1,139.64	186.63
4	(18, 26), (7)	1,000.75	342.66
5	(7, 26), (7)	1,034.02	340.63

powered, resulting in more load loss and higher total carbon emissions.

In Figure 9B, compared with scheme 1, scheme 2 changes the allocation position of WT from node 20 to node 24. Because the output of WT is not blocked by the fault line, it can replace part of the output of the upstream power grid. From Table 8, it can be found that the total carbon emission under allocation scheme 2 is lower than that under allocation scheme 1. Although the change in the location of the WT has little impact on island 1, it has caused island 2 to lose the power source for restoration, leading to island 2 becoming a load island. The load loss of the scheme is greatly increased compared with the allocation scheme 1, and the LER value is the largest among the three schemes, which shows that the scheme is not desirable.

The optimal allocation scheme is adopted in Figure 9C, so that there are two power dividing points of node 7 and node 32 in different periods of a day in island 1. It can be seen from the figure that the scheme has more diverse power delivery paths than the first two allocation schemes. During periods when the load of nodes 31 and 32 is small, the PV unit located at node 33 can bypass node 32 to provide power supply to other loads, and at this time node 32 does not act as a power dividing point. When the load at the end of the branch is large, node 32 becomes a power dividing point, and is powered by the power supplies on both sides. This means that under this scheme, PV units are allocated more reasonably and the load power supply mode is more flexible. It can be seen from the results in Table 8 that the optimal allocation scheme has smaller load loss than the first two schemes, and its total carbon emissions are relatively low, and the LER value is the smallest, which is an ideal scheme.

6.6 Influence of disaster severity

For a given disaster response scheme, changes in disaster severity will lead to differences in disaster response effects. On the basis of scheme 5, the results under the multi-scenario disasters can be obtained by changing the disaster attack budget K_{budget}, as shown in Figure 10 and Table 9. It can be seen from Figure 10 that as the severity of the disaster increases, the load loss and operating costs continue to increase. From Table 9, it can be

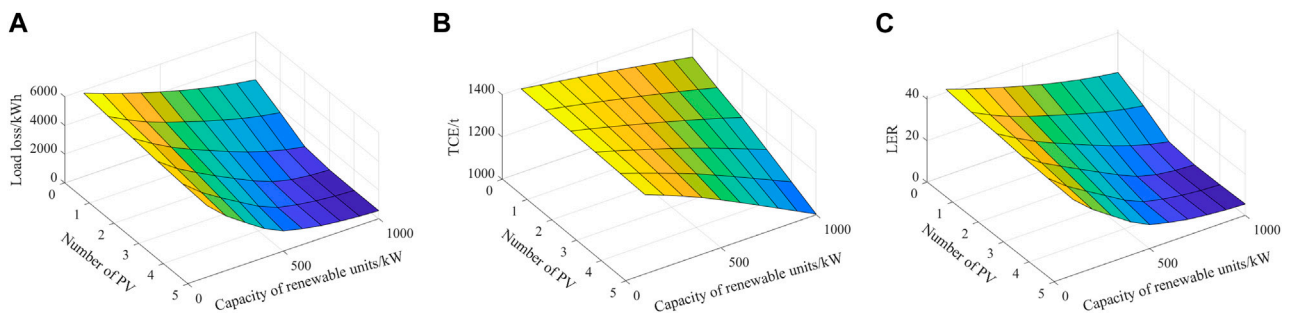

FIGURE 11
Influence of allocation budget on **(A)** Load loss; **(B)** TCE; **(C)** LER.

seen that the total carbon emissions show a downward trend, indicating that disasters have a certain inhibitory effect on the carbon emissions. However, this inhibitory effect is at the expense of load loss. From Table 9, it can also be found that the LER value is at a high level when the disaster severity is high, which means that the load lost for each unit of carbon emissions generated is large. When the value of K_{budget} is not greater than 2, the load loss and total cost of the system are relatively low, and the LER value is also small, indicating that the disaster response scheme at this time has a good effect. When the value is greater than 2, the load loss and total cost rise rapidly, and the LER value increases sharply, indicating that the disaster is severe enough that current allocation budget and operational methods have gradually failed to meet the disaster response requirements. Therefore, it is necessary to increase the allocation budget or take more effective measures [such as line hardening (Wang et al., 2019b), etc.] to cope with more severe disaster scenarios. When the value is greater than 4, the load loss and total cost growth slow down, indicating that the marginal benefit of disaster attacks has decreased, and the system is suffering the most severe disaster damage.

According to the impact of the severity of the disaster on the distribution system, it can be divided into three ranges. When $K_{\text{budget}} \in [0, 2]$, it is called the inhibition interval, within which the existing disaster prevention and response measures play an effective role in inhibiting the disaster. When $K_{\text{budget}} \in [2, 4]$, it was called a growth range, and the existing disaster prevention and response measures within this range gradually failed to meet the disaster response requirements. Therefore, the impact of disaster increased sharply with the severity of the disaster. When $K_{\text{budget}} \in [4, 5]$, it is called the destroy range. In this range, the damage degree of the disaster on the distribution system tends to be maximized, and existing disaster prevention and response measures have little effectiveness.

6.7 Influence of allocation budget

The allocation budget mainly includes the number and capacity of allocated units. On the basis of the scheme 5, taking the value of K_{budget} as 2, changing the capacity of the allocated units and the number of PV units, the results shown in Figure 11 can be obtained. It can be seen from the figure that with the increase of unit capacity and allocation number, the load loss and carbon emissions of the system have significantly decreased, and the LER value also decreases. It is worth noting that with the increase in unit capacity and number, the downward trend of load loss and LER values becomes slower. This result shows that the marginal benefits of disaster prevention and response brought about by the increase in the allocation budget are decreasing. When making disaster prevention and response decisions in practical, it is necessary to take into account the severity of the disaster and the risk tolerance level of the distribution system, while weighing the marginal benefits and allocation costs, and comprehensively formulate an appropriate allocation scheme.

7 Conclusion

Natural disasters will not only lead to load loss caused by line faults in distribution systems, but also affect carbon emissions. In order to improve the load restoration capability of the distribution system under disasters and mitigate the additional carbon emissions during the load restoration process, this paper proposes a multi-scenario DAD model considering carbon emission based on the CPSSE framework. The model pre-allocates the DRG units before the disaster and implements NR after the disaster to restore the power supply of the distribution system. To describe the impact of disasters, this paper models the line fault probability under disasters, gives the fault constraints under disasters, and proposes a method for selecting the worst-case fault scenario. Finally, the PHA algorithm is adopted to solve the multi-scenario problem. Through the case analysis, the following conclusions can be drawn:

1) Natural disasters can cause a large amount of load losses in the distribution system. Adopting NR can avoid the generation of isolated islands, ensure the integrity of the distribution system topology, and reduce load loss by 92.04%.
2) The proposed optimal allocation model comprehensively considers the impact of disasters on load restoration and carbon emissions of the distribution system, and is suitable for multi-scenario disasters. It can improve the flexibility of load restoration in islands under disasters, and restore more lost load with less carbon emissions.
3) As the severity of disasters increases, the impact of disasters on distribution system can be divided into three ranges: inhibition

range, growth range, and destroy range. When the disaster attack budget is greater than 2, existing disaster prevention and response measures will gradually lose their effectiveness.

4) With the increase of the allocation budget, the effect of the optimal allocation shows a diminishing marginal benefit. Therefore, the allocation effect and budget should be weighed simultaneously when making allocation decisions.

Due to space limitations, this paper only focuses on the impact of disasters on the distribution system, and has not considered the impact of disasters on carbon sinks. Future research will consider the changes of carbon emissions and carbon sinks in the transmission and distribution system under the impact of disasters simultaneously, and formulate more comprehensive disaster prevention and emission mitigation measures to better achieve carbon neutrality.

Data availability statement

The original contributions presented in the study are included in the article/supplementary material, further inquiries can be directed to the corresponding author.

Author contributions

WL: Methodology, software, validation, investigation, writing—original draft. JW: Conceptualization, supervision, writing—review and editing. DL: Conceptualization, supervision, data collection, writing—review and editing. YW: Validation, investigation, visualization. All authors contributed to the article and approved the submitted version.

Funding

This work was supported by the National Natural Science Foundation of China—Key Program of Joint Fund in Smart Grid (U2166210).

Conflict of interest

The authors declare that the research was conducted in the absence of any commercial or financial relationships that could be construed as a potential conflict of interest.

Publisher's note

All claims expressed in this article are solely those of the authors and do not necessarily represent those of their affiliated organizations, or those of the publisher, the editors and the reviewers. Any product that may be evaluated in this article, or claim that may be made by its manufacturer, is not guaranteed or endorsed by the publisher.

References

Alguacil, N., Delgadillo, A., and Arroyo, J. (2014). A trilevel programming approach for electric grid defense planning. *Comput. Oper. Res.* 41, 282–290. doi:10.1016/j.cor.2013.06.009

Arif, A., Wang, Z., Chen, C., and Chen, B. (2020). A Stochastic Multi-commodity logistic model for disaster preparation in distribution systems. *IEEE Trans. Smart Grid* 11 (1), 565–576. doi:10.1109/TSG.2019.2925620

Balakrishnan, R., and Ranganathan, K. (2012). *A textbook of graph theory*. Berlin, Germany: Springer.

Barnes, A., Nagarajan, H., Yamangil, E., Bent, R., and Backhaus, S. (2019). Resilient design of large-scale distribution feeders with networked microgrids. *Electr. Power Syst. Res.* 171, 150–157. doi:10.1016/j.epsr.2019.02.012

Chen, C., Wang, J., and Ton, D. (2017). Modernizing distribution system restoration to achieve grid resiliency against extreme weather events: An integrated solution. *Proc. IEEE* 105 (7), 1267–1288. doi:10.1109/JPROC.2017.2684780

Ding, T., Lin, Y., Bie, Z., and Chen, C. (2017a). A resilient microgrid formation strategy for load restoration considering master-slave distributed generators and topology reconfiguration. *Appl. Energy* 199, 205–216. doi:10.1016/j.apenergy.2017.05.012

Ding, T., Lin, Y., Li, G., and Bie, Z. (2017b). A new model for resilient distribution systems by microgrids formation. *IEEE Trans. Power Syst.* 32 (5), 4145–4147. doi:10.1109/TPWRS.2017.2650779

Dou, Y., Shahbaz, M., Dong, K., and Dong, X. (2022). How natural disasters affect carbon emissions: The global case. *Nat. Hazards* 113 (3), 1875–1901. doi:10.1007/s11069-022-05374-z

Du, Y., Tu, H., Lu, X., Wang, J., and Lukic, S. (2022). Black-start and service restoration in resilient distribution systems with dynamic microgrids. *IEEE J. Emerg. Sel. Top. Power Electron.* 10 (4), 3975–3986. doi:10.1109/JESTPE.2021.3071765

Fernández-Guillamón, A., Gómez-Lázaro, E., Muljadi, E., and Molina-Garcia, A. (2019). Power systems with high renewable energy sources: A review of inertia and frequency control strategies over time. *Renew. Sustain. Energy Rev.* 115, 109369. doi:10.1016/j.rser.2019.109369

Gan, W., Shahidehpour, M., Guo, J., Yao, W., Pandey, S., Paaso, A., et al. (2022). A tri-level planning approach to resilient expansion and hardening of coupled power distribution and transportation systems. *IEEE Trans. Power Syst.* 37 (2), 1495–1507. doi:10.1109/TPWRS.2021.3107402

Ghasemi, M., Kazemi, A., Gilani, M., and Shafie-Khah, M. (2021). A stochastic planning model for improving resilience of distribution system considering master-slave distributed generators and network reconfiguration. *IEEE Access* 9, 78859–78872. doi:10.1109/ACCESS.2021.3083698

Hafiz, F., Chen, B., Chen, C., de Queiroz, A., and Husain, I. (2019). Utilising demand response for distribution service restoration to achieve grid resiliency against natural disasters. *IET Gener. Transm. Distrib.* 13 (14), 2942–2950. doi:10.1049/iet-gtd.2018.6866

Hao, L., Xue, Y., Li, Z., Wang, H., and Xu, Q. (2022). Decision support system for adaptive restoration control of distribution system. *J. Mod. Power Syst. Clean. Energy* 10 (5), 1256–1273. doi:10.35833/MPCE.2021.000528

IPCC (2019). IPCC special report: Global warming of 1.5 °C. Avialable at: https://www.ipcc.ch/sr15/.

Jiang, L., Hu, X., Zhang, G., Chen, Y., Zhong, H., and Shi, P. (2022). Carbon emission risk and governance. *Int. J. Disaster Risk Sci.* 13 (2), 249–260. doi:10.1007/s13753-022-00411-8

Khomami, M., and Sepasian, M. (2018). Pre-hurricane optimal placement model of repair teams to improve distribution network resilience. *Electr. Power Syst. Res.* 165, 1–8. doi:10.1016/j.epsr.2018.08.016

Lavorato, M., Franco, J., Rider, M., and Romero, R. (2012). Imposing radiality constraints in distribution system optimization problems. *IEEE Trans. Power Syst.* 27 (1), 172–180. doi:10.1109/TPWRS.2011.2161349

Lei, S., Wang, J., Chen, C., and Hou, Y. (2018). Mobile emergency generator pre-positioning and real-time allocation for resilient response to natural disasters. *IEEE Trans. Smart Grid* 9 (3), 1–2041. doi:10.1109/TSG.2016.2605692

Li, B., Chen, Y., Wei, W., Huang, S., and Mei, S. (2021). Resilient restoration of distribution systems in coordination with electric bus scheduling. *IEEE Trans. Smart Grid* 12 (4), 3314–3325. doi:10.1109/TSG.2021.3060801

Li, G., Zhang, P., Luh, P. B., Li, W., Bie, Z., Serna, C., et al. (2014). Risk analysis for distribution systems in the northeast U.S. under wind storms. *IEEE Trans. Power Syst.* 29 (2), 889–898. doi:10.1109/TPWRS.2013.2286171

Lin, Z., and Bie, Z. (2018). Tri-level optimal hardening plan for a resilient distribution system considering reconfiguration and DG islanding. *Appl. Energy* 210, 1266–1279. doi:10.1016/j.apenergy.2017.06.059

Ma, S., Chen, B., and Wang, Z. (2018). Resilience enhancement strategy for distribution systems under extreme weather events. *IEEE Trans. Smart Grid* 9 (2), 1442–1451. doi:10.1109/TSG.2016.2591885

Mulej, M. (2007). Systems theory: A worldview and/or a methodology aimed at requisite holism/realism of humans' thinking, decisions and action. *Syst. Res. Behav. Sci.* 24 (3), 347–357. doi:10.1002/sres.810

Nikkhah, S., Jalilpoor, K., Kianmehr, E., and Gharehpetian, G. (2018). Optimal wind turbine allocation and network reconfiguration for enhancing resiliency of system after major faults caused by natural disaster considering uncertainty. *IET Renew. Power Gener.* 12 (12), 1413–1423. doi:10.1049/iet-rpg.2018.5237

Panteli, M., Mancarella, P., Trakas, D., Kyriakides, E., and Hatziargyriou, N. (2017). Metrics and quantification of operational and infrastructure resilience in power systems. *IEEE Trans. Power Syst.* 32 (6), 4732–4742. doi:10.1109/TPWRS.2017.2664141

Rockafellar, R., and Wets, R. (1991). Scenarios and policy aggregation in optimization under uncertainty. *Math. Oper. Res.* 16 (1), 119–147. doi:10.1287/moor.16.1.119

Shen, F., Wu, Q., and Xue, Y. (2020). Review of service restoration for distribution networks. *J. Mod. Power Syst. Clean. Energy* 8 (1), 1–14. doi:10.35833/MPCE.2018.000782

Sun, X., Chen, J., Zhao, H., Zhang, Wen., and Zhang, Y. (2023). Sequential disaster recovery strategy for resilient distribution network based on cyber-physical collaborative optimization. *IEEE Trans. Smart Grid* 14 (2), 1173–1187. doi:10.1109/TSG.2022.3198696

Wang, X., Li, Z., Shahidehpour, M., and Jiang, C. (2019b). Robust line hardening strategies for improving the resilience of distribution systems with variable renewable resources. *IEEE Trans. Sustain. Energy* 10 (1), 386–395. doi:10.1109/TSTE.2017.2788041

Wang, X., Shahidehpour, M., Jiang, C., and Li, Z. (2019a). Resilience enhancement strategies for power distribution network coupled with urban transportation system. *IEEE Trans. Smart Grid* 10 (4), 4068–4079. doi:10.1109/TSG.2018.2848970

Wang, Y., Chen, C., Wang, J., and Baldick, R. (2016). Research on resilience of power systems under natural disasters—A review. *IEEE Trans. Power Syst.* 31 (2), 1604–1613. doi:10.1109/TPWRS.2015.2429656

Watson, J. P., and Woodruff, D. L. (2011). Progressive hedging innovations for a class of stochastic mixed-integer resource allocation problems. *Comput. Manag. Sci.* 8 (4), 355–370. doi:10.1007/s10287-010-0125-4

Wen, Y., Cai, B., Yang, X., and Xue, Y. (2020). Quantitative analysis of China's low-carbon energy transition. *Int. J. Electr. Power Energy Syst.* 119, 105854. doi:10.1016/j.ijepes.2020.105854

Wu, X., Wang, Z., Ding, T., Wang, X., Li, Z., and Li, F. (2019). Microgrid planning considering the resilience against contingencies. *IET Gener. Transm. Distrib.* 13 (16), 3534–3548. doi:10.1049/iet-gtd.2018.6816

Xue, Y., Wu, Y., Xie, Y., Wen, F., Dong, Z., Zhao, J., et al. (2013). Extension of blackout defense scheme to natural disasters early-warning. *Automation Electr. Power Syst.* 37 (16), 18–26. (in Chinese). doi:10.7500/AEPS20130606010

Xue, Y., and Yu, X. (2017). Beyond smart grid—Cyber–physical–social system in energy future [point of view]. *Proc. IEEE* 105 (12), 2290–2292. doi:10.1109/JPROC.2017.2768698

Yao, S., Wang, P., and Zhao, T. (2019). Transportable energy storage for more resilient distribution systems with multiple microgrids. *IEEE Trans. Smart Grid* 10 (3), 3331–3341. doi:10.1109/TSG.2018.2824820

Yu, X., and Xue, Y. (2016). Smart grids: A cyber–physical systems perspective:a cyber-physical systems perspective. *Proc. IEEE* 104 (5), 1058–1070. doi:10.1109/JPROC.2015.2503119

Yuan, W., Wang, J., Qiu, F., Chen, C., Kang, C., and Zeng, B. (2016). Robust optimization-based resilient distribution network planning against natural disasters. *IEEE Trans. Smart Grid* 7 (6), 2817–2826. doi:10.1109/TSG.2015.2513048

Zhang, G., Zhang, F., Zhang, X., Wu, Q., and Meng, K. (2020b). A multi-disaster-scenario distributionally robust planning model for enhancing the resilience of distribution systems. *Int. J. Electr. Power Energy Syst.* 122, 106161. doi:10.1016/j.ijepes.2020.106161

Zhang, G., Zhang, G., Zhang, X., Meng, K., and Dong, Z. (2020a). Sequential disaster recovery model for distribution systems with co-optimization of maintenance and restoration crew dispatch. *IEEE Trans. Smart Grid* 11 (6), 4700–4713. doi:10.1109/TSG.2020.2994111

Zhang, J., Wang, Y., Chang, K., Xue, F., and Xue, Y. (2022). *Bayesian network modeling for new power system carbon emission with natural disaster chain and carbon change estimation. Proceedings of the 7th PURPLE MOUNTAIN FORUM on Smart Grid Protection and Control (PMF2022). PMF 2022.* Singapore: Springer. doi:10.1007/978-981-99-0063-3_31

Zhang, L., Wang, C., Liang, J., Wu, M., Zhang, B., and Tang, W. (2023). A coordinated restoration method of hybrid AC/DC distribution network for resilience enhancement. *IEEE Trans. Smart Grid* 14 (1), 112–125. doi:10.1109/TSG.2022.3192910

Zhuo, Z., Du, E., Zhang, N., Kang, C., Xia, Q., and Wang, Z. (2020). Incorporating massive scenarios in transmission expansion planning with high renewable energy penetration. *IEEE Trans. Power Syst.* 35 (2), 1061–1074. doi:10.1109/TPWRS.2019.2938618

frontiers | Frontiers in Energy Research

TYPE Original Research
PUBLISHED 04 July 2023
DOI 10.3389/fenrg.2023.1194595

OPEN ACCESS

EDITED BY
Mingfei Ban,
Northeast Forestry University, China

REVIEWED BY
Zhihua Zhang,
China University of Petroleum, China
Wei Tang,
China Agricultural University, China
Yibo Wang,
Northeast Dianli University, China

*CORRESPONDENCE
Xiaoyi Qian,
qianxiaoyi123@163.com

RECEIVED 27 March 2023
ACCEPTED 31 May 2023
PUBLISHED 04 July 2023

CITATION
Zhang X, Lu M, Li H, Gao F, Zhong C and Qian X (2023), Flexibility resource planning of a power system considering a flexible supply–demand ratio.
Front. Energy Res. 11:1194595.
doi: 10.3389/fenrg.2023.1194595

Flexibility resource planning of a power system considering a flexible supply–demand ratio

Xiaotian Zhang[1], Mingxuan Lu[1], Hua Li[1], Fengxi Gao[1], Chongfei Zhong[1] and Xiaoyi Qian[2]*

[1]State Grid Liaoning Economic Research Institute, Shenyang, China, [2]Shenyang Institute of Engineering, Shenyang, China

Aiming at the problems of insufficient power system regulation capacity and lack of flexible resources caused by source-load uncertainty, the flexible resource planning of power systems is studied with the goal of improving flexibility. Uncertainty and flexibility are combined in this article, and a probability index of an insufficiently flexible supply-demand ratio is proposed based on the probability characteristics of flexibility. A bi-level programming model of power system flexibility resources considering the probability of an insufficiently flexible supply demand ratio is constructed. Optimal economics is used as the objective function of the planning layer, and the proposed minimum probability index of the flexible supply-demand ratio is used as the objective function of the operations layer. Economics and flexibility are studied, taking the power system in a certain area in Northeast China as the research object. A flexible resource planning scheme that meets different flexibility expectations is obtained, and the scheme is discussed in detail from the aspects of system flexibility, economic cost, and new energy consumption capacity. The effectiveness of quantitative indicators and planning methods are verified.

KEYWORDS

power system, uncertainty, flexibility, bi-level programming Problem, supply–demand ratio

Introduction

Under the global low-carbon goal, the penetration of new energy generation is increasing in power systems worldwide (International Energy Agency, 2009). Affected by natural factors, wind and solar power generation bring uncertainty to the system operations, while the load side indeterminacy arises due to the massive access to distributed new energy (State Grid Energy, 2020; Zhang et al., 2020; Guo, 2021). Posed by the requirement of responding to the system uncertainties, flexibility has become one of the most important performance indicators of current and future power systems (Ding et al., 2018; National Development and Reform Commission and the National Energy, 2018). Therefore, to improve the flexibility of power systems, the flexibility quantification method under uncertainty and its application in related planning have become important research directions.

There are many studies on flexibility. The North American Electric Reliability Cooperation (2011) defines the flexibility of power systems as the ability to make full use of system resources to respond to load fluctuations. In International Energy Agency (2008), flexibility is defined as the ability of power systems to respond quickly to foreseeable and unforeseen changes and emergencies in a specific economic operation. Flexibility can be

summarized as the ability of the system to respond to uncertain factors, which involves the actual operations and investment planning of a power system. The selection and application of quantitative flexibility indicators are also different for different research objects and research fields. Indicators applicable to the planning problem include the technical flexibility index (T_USFI), the technical and economic flexibility index (TE_USFI), the expected loss of load (LOLE), and the expected energy not supplied (EENS) (Capasso et al., 2005; Li and Wang, 2020; Zhao et al., 2021). It can be seen that the application of system flexibility indicators in power system planning focuses on economics. The indicators applicable to operational problems include the insufficient ramping resource expectation (IRRE), the operational flexibility index (UlBig A), and the expected value of up–down flexibility shortage (Lannoye et al., 2012; Ul Big and Andersson, 2012; Li et al., 2015). In Lu and LiQiao (2018), flexibility is quantified from the demand and the supply side. System uncertainty leads to an increase in demand for flexibility. It is proposed that there are some connections between flexibility and source–load uncertainty. Guo (2020) shows that flexibility quantification has a certain guiding significance for power system flexibility resource planning with large-scale new energy access. The aforementioned quantitative flexibility indicators are mostly focused on the application of traditional power system planning, operations, and other scenarios. Few studies examine the quantitative flexibility indicators that consider uncertainty, and those indicators are not often applied to power systems with increased proportions of new energy sources and dual source–load uncertainty.

For power systems with a large proportion of new energy, there is a mutual restraint relationship between flexibility and economics (Xiao, 2015). There have been some achievements in system planning research considering flexibility. In Yang et al. (2022), a bi-level programming model is adopted. The upper layer is the planning layer, and the lower layer is the operations layer. The planning result is economically optimal, and the flexibility margin is considered the planning layer constraint to participate in the planning. In Li et al. (2021), a transmission network planning model based on flexibility and economics is proposed using a multi-objective programming method, aiming at the optimal investment cost, operating cost, renewable energy abandonment, and flexibility. The optimal solution is obtained by adding the weights of multiple objectives. The lowest flexibility weight does not highlight the system's requirement for flexibility. In Xu et al. (2019), flexibility adjusts the decision variables in the form of indicators and selects the scheme with the least cost through iteration. Compared with the (k-1)th iteration, in the kth iteration process, when the cost increases, the unit new investment is selected to improve the flexibility index. Cui and Zhang (2018) established a multi-time scale economic dispatch model of photovoltaic units to optimize the flexibility of climbing. In Lu et al. (2019), a wind turbine planning method considering system flexibility and new energy consumption capacity was constructed to maximize the system's adjustability and enhance the ability to accept new energy.

In summary, the current research on flexibility mostly focuses on the establishment of quantitative flexibility indicators considering economics and proposes evaluation methods, while less research examines quantitative flexibility indicators that consider uncertainty and the application of flexibility indicators in power system planning. In terms of application, most studies are based on the planning and design of the power supply side based on power flexibility, while there are few studies on the planning of flexible resources (Zi, 2018; Yu et al., 2022).

In view of the aforementioned problems, this paper will research quantifying flexibility under uncertainty and propose a probability index of an insufficiently flexible supply–demand ratio based on the probability characteristics of flexibility. A bi-level programming model of power system flexible resources considering the probability of an insufficiently flexible supply–demand ratio is constructed. Optimal economics is used as the objective function of the planning layer, and the proposed minimum probability index of the flexible supply–demand ratio is used as the objective function of the operations layer. Economics and flexibility are studied, taking the power system in a certain area in Northeast China as the research object and verifying the effectiveness of the proposed indicators and models.

Flexibility quantification under system uncertainty

The flexibility of a new power system is its response ability to deal with uncertainty. It is necessary to consider the uncertainty factor in the flexibility index. System uncertainty is frequently neglected in the study of the flexibility quantification index. To strengthen the connection between them, a flexible supply–demand ratio index is proposed by characterizing the adjustment ability of the system to the source–load uncertainties at multiple scales (15 mins, 1 h, 1 day). Based on this, a quantitative index based on the flexibility probability characteristics is defined and named the probability index of an insufficiently flexible supply–demand ratio. The expressions are as follows:

The flexible supply–demand ratio R_{fsd} characterizes the quantitative relationship between flexible supply and demand in a certain time range. The expression is as follows:

$$R_{fsd,i,t} = \frac{\sum_{a\in S} X_{a,t}}{\sum_{b\in D} Y_{b,t}} = \frac{\sum_{a\in S} X_{a,t}}{P_{NL,t}},$$

where $R_{fsd,t}$ is the supply–demand ratio of the system in t period under a certain time scale i, S represents the set of flexible supply sources, and $X_{a,t}$ represents the supply of the ath flexible resource at a certain time scale (MW/t), D represents a collection of flexibility requirements, $Y_{b,t}$ denotes the bth flexibility demand in t period under a certain time scale (MW/t), and $P_{NL,t}$ is the net load value of t period under a certain time scale, not less than zero (MW/t). When the supply–demand ratio is equal to 1, the system reaches the balance of supply and demand. If the flexibility margin is considered, the supply–demand ratio must be greater than 1.

The amount of flexibility supply is the sum of the flexibility provided by various flexibility resources of the system at this time. Common flexibility resources include traditional generator sets, new energy generator sets, power-to-hydrogen, and electric vehicles. The number of flexibility requirements is equal to the net load of the system at this time. The net load represents the ability of the system to cope with the insufficient power supply caused by the uncertainty

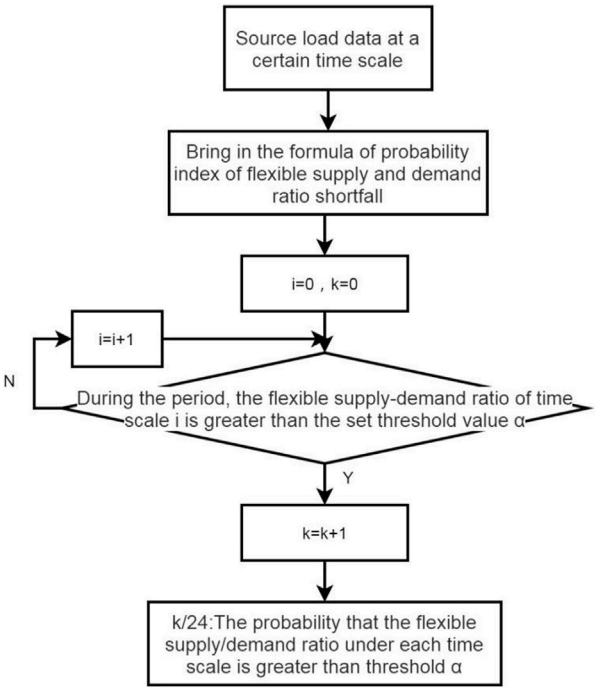

FIGURE 1
The proposed solving process.

of wind–solar electric field output and the uncertainty of load demand at a certain time scale *i*. That is, the expression of the system flexibility demand in the *t*th period is

$$P_{NL,i,t} = \sum_{i\in I}\left(P_{L,i,t} - P_{W,i,t} - P_{S,i,t}\right),$$

where time period *t* contains *i* time scales and is the load size in the *i* time scale. $P_{L,t}$ is the wind turbine output at the *i* time scale. $P_{W,t}$ is the photovoltaic generator output at the *i* time scale. The probability of an insufficiently flexible supply–demand ratio (P_{IFSR}-α) is used to characterize the probability that the system flexibility is in short supply. The threshold α represents the flexibility expectation; its physical meaning is the target value set by the system. In the ideal state, the threshold $\alpha = 1$ indicates that the supply and demand balance is satisfied. The specific expression is as follows:

$$P_{IFSR} - \alpha = PR\left(R_{fsd} < \alpha\right) = PR\left(\frac{\sum_{a\in S} X_{a,t}}{\sum_{i\in I}\left(P_{L,i,t} - P_{W,i,t} - P_{S,i,t}\right)} < \alpha\right).$$

The process of solving this index is shown in Figure 1. Compared with traditional indicators, its advantages include: 1) Simplifying the quantization process. The initial data processing is simple, and the convolution and volume differences of random variable functions are replaced by the ratio of total supply and demand. 2) Strengthening the link between uncertainty and flexibility. The uncertainty of wind power directly affects the flexibility demand of the system, thus affecting the index value. The threshold value directly represents the ability of the system to deal with uncertain factors. 3) The index can be used to evaluate the flexibility of new power systems under multiple time scales. It can obtain the index through the historical operations data in a short time, check the flexibility of the system immediately, and evaluate the flexibility of the long-term operations of the system using a year's historical data.

Dynamic mathematic model of flexible resources

The adjustment methods used to address the system volatility and uncertainty factors can be used as flexibility resources. Common flexibility resources include traditional generator sets, energy storage, power-to-hydrogen, and electric vehicles. In this paper, three common dynamic response models of flexible resources are established that can be used to calculate the flexibility index or participate in flexible resource planning as the constraint part of the planning model.

Traditional generation units

Traditional flexible resources include thermal power, hydropower, and nuclear power, which account for a large proportion of the overall power structure. Traditional flexible power supply is mainly from thermal power units; the flexibility they provide is as follows:

$$\begin{cases} F_{ga,u,t} = \min\left\{r_{ga,u}T_0, P_{ga,\max} - P_{ga,t}\right\}, \\ F_{ga,d,t} = \min\left\{r_{ga,d}T_0, P_{ga,t} - P_{ga,\min}\right\}, \\ P_{ga,\min} \le P_{ga,t} \le P_{ga,\max}, \\ P_{ga,\min} = 0.31P_{ga,\max}, \end{cases}$$

where $F_{ga,u,t}$ and $F_{ga,d,t}$ are the flexibility of upregulation and downregulation provided by the thermal power units at time t, $r_{ga,u}$ and $r_{ga,d}$ are the upward climbing rate and downward climbing rate of the thermal power units, T_0 is the scheduling time of the thermal power units, $P_{ga,max}$ and $P_{ga,min}$ are the maximum technical power output and the minimum technical power output of the thermal power units, respectively, and $P_{ga,t}$ is the active power output of the thermal power units at time t. In order to ensure that flue gas emissions meet the standard, thermal power units should operate stably at more than 31% of their rated capacity.

Power to hydrogen

Power to hydrogen (P2H) is used to consume unbalanced power during low load periods, which is one of the important means of converting power to gas. Compared with the process of power to (natural) gas (P2G), P2H can avoid the energy loss of the methanation reaction. P2H uses redundant new wind and solar energy to generate electricity and then uses that electricity to decompose water into hydrogen and oxygen, which not only avoids the environmental pollution caused by traditional fossil fuel hydrogen production but also alleviates the waste of abandoned wind and light energy. The expression of P2H is as follows:

10.3389/fenrg.2023.1194595

$$V_{P_{2H,t}} = \frac{P_{elc,t} \cdot \Delta t}{\mu_h},$$

where $V_{P2H,t}$ is the volume of hydrogen produced by the electrolytic cell in t period, $P_{elc,t}$ is the average power consumption of the electrolysis cell in t period, Δt is the length of time period t, and μ_h is electrolysis cell unit power consumption, generally taken as 4.50–5.04 ($kw \bullet h/N \bullet m^3$). The expressions of flexibility and related constraints provided by P2H are as follows:

$$\begin{cases} S_t = S_{t-1} + P_t^{ch} \cdot \eta^{ch} - \dfrac{P_t^{dis}}{\eta^{dis}} - O_t, \\ S^{\min} \le S_t \le S^{\max}, \\ F_{P2H,u,t} = P_t^{ch}, \\ F_{P2H,d,t} = P_t^{dis}, \\ I_t^{ch} \cdot P^{ch,\min} \le P_t^{ch} \le I_t^{ch} \cdot P^{ch,\max}, \\ I_t^{dis} \cdot P^{dis,\min} \le P_t^{dis} \le I_t^{dis} \cdot P^{dis,\max}, \\ 0 \le I_t^{ch} + I_t^{dis} \le 1, \end{cases}$$

where S_t is the hydrogen storage energy of the hydrogen storage tank in the P2H system during the t period (MWh); $F_{P2H,u,t}$ and $F_{P2H,d,t}$ are, respectively, the upward adjustment flexibility and downward adjustment flexibility provided by the P2H system at time t; P_t^{ch} and P_t^{dis} are the charging power and discharging power of hydrogen energy storage in t period, corresponding to the power of hydrogen production by electrolysis of water and the power of hydrogen power generation in t period, respectively (in MW); η_t^{ch} and η_t^{dis} are the charging efficiency and discharging efficiency of the system, corresponding to the efficiency of water electrolysis and hydrogen power generation; O_t is the power of hydrogen sold to the hydrogen trading market for other hydrogen industries in period t (MW); S^{max} and S^{min} are the upper and lower energy storage limits of the P2H system (in MWh); $P^{ch,max}$ and $P^{ch,min}$ are the operating power upper and lower limits of the water electrolysis hydrogen production device (in MW); $P^{dis,max}$ and $P^{dis,min}$ are the upper and lower operating power limits of the hydrogen power generation device, respectively (in MW); I_t^{ch} and I_t^{dis} are the charge–discharge state of the electric-to-hydrogen system in the t period and are binary variables; $I_t^{ch} = 1$ indicates that the power-to-hydrogen system is in a charged state during t period; and $I_t^{dis} = 0$ is the discharge status.

The economic benefit of hydrogen production is that hydrogen can be sold directly after it is produced using excess wind power. Therefore, the profit value of P2H as a system flexibility resource is considered here, and its expression is as follows:

$$C_{elc} = \sum_{t=1}^{T} \lambda_{H_2} \frac{P_{elc,t} \cdot \Delta t}{\mu_h},$$

where C_{elc} is the economic benefit of selling hydrogen and λ_{H_2} is the selling price of hydrogen per unit volume (2.7 yuan/Nm^3).

Energy storage

The charging and discharging response time of energy storage technology is short, usually in seconds. It can provide bilateral flexibility for the power system, such as providing power when the power generation is less than the load or consuming the remaining electricity when the power generation is greater than the load. Energy storage can effectively improve the utilization rate of new energy. The expressions of flexibility and related constraints provided by energy storage are as follows:

$$\begin{cases} F_{ESS,u,t} = P_{ESS,d,t}, \\ F_{ESS,d,t} = P_{ESS,d,t}, \\ S_{ESS,\min} \le S_{ESS,t} \le S_{ESS,\max}, \\ P_{ESS,d,\min} \le P_{ESS,d,t} \le P_{ESS,d,\max}, \\ P_{ESS,c,\min} \le P_{ESS,c,t} \le P_{ESS,c,\max}, \end{cases}$$

where $F_{ESS,u,t}$ and $F_{ESS,d,t}$ are the upward and downward adjustment flexibilities provided by the energy storage system to the system at time t; $P_{ESS,d,t}$ and $P_{ESS,c,t}$ are the discharge and charging power of the energy storage system at time t; and $P_{ESS,d,\max}$ and $P_{ESS,d,\min}$ are the maximum and minimum discharge power of the energy storage system, respectively. $P_{ESS,c,\max}$ and $P_{ESS,c,\min}$ are the maximum and minimum charging power for the energy storage system. $S_{ESS,t}$ is the state of charge of the energy storage system.

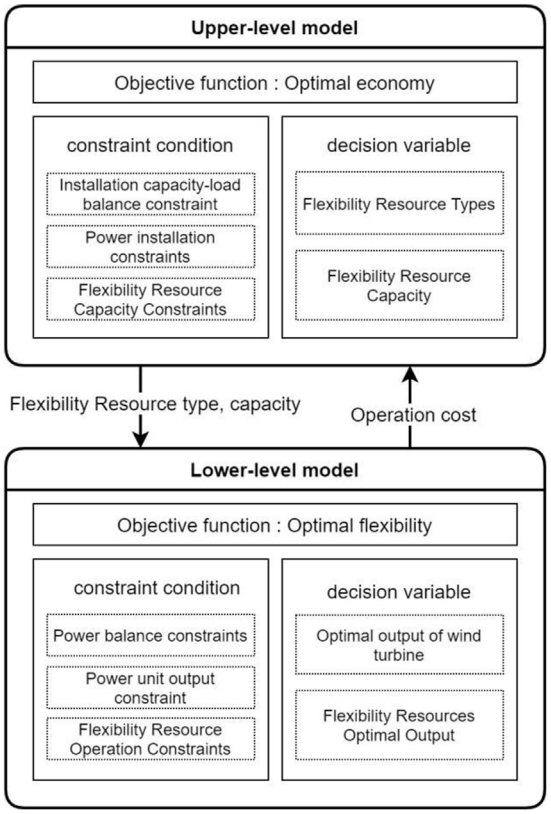

FIGURE 2
The bi-level programming model relationship.

Flexible resource planning model considering a flexible supply–demand ratio

In order to make full use of the value of flexible resources in the power system while considering the economics of the system, a bi-

level programming model of power system flexible resources based on the quantitative index of flexibility under uncertainty is proposed by referring to the probability index of an insufficiently flexible supply–demand ratio (P_{IFSR}-α) proposed previously. The selection scheme of the upper-level decision variables determines the optimization process of the lower-level optimization model. The lower-level optimization model will feed the optimal value to the upper-level optimization model, and the upper level will then calculate the global optimal planning results based on the obtained lower-level optimal value. The bi-level programming model relationship shown in Figure 2 consists of a planning layer model and an operations layer model.

Upper-level programming model

The upper-level programming model takes optimal economics as the goal and the type and capacity of flexible resources as the decision variables. On the basis of satisfying the balance of power and electricity, carbon emission constraints, and flexibility margin constraints, collaborative optimization is carried out with the goal of minimizing the construction cost of new resources and the surplus value of existing resources, and the planning decision scheme is obtained.

Upper programming objective function

The upper-level programming objective function is the most economical; that is, it has the lowest economic cost. The objective function is expressed as follows:

$$\min f_1 = \min\left(C_{new} + C_{elc} + C_{Fm} + C_{Om} + C_{Fu} + C_{Curt}\right),$$

where f_1 is the cost of resource investment decision-making stage, C_{new} is the cost of new unit investment decision-making stage, C_{elc} is the profit value cost of new resources, the sum of C_{Fm} and C_{Om} is the maintenance cost, C_{Fu} is the fuel cost, and C_{Curt} is the penalty cost of wind abandonment.

New resources investment construction cost

The construction cost of new resources is the construction cost of flexible resources, which is expressed as follows:

$$C_{\text{new}} = \sum_{t=1}^{T}\left(\sum_{n\in N} x_{n,t} I_{n,t} P_{n,t}\right) CRF,$$

where $x_{n,t}$ determines whether the flexibility resource is constructed as a 0/1 variable; $P_{n,t}$ and I_n are the new investment capacity and unit investment cost of the flexible resource n in the fourth year, respectively; N represents the collection of flexibility resources, including flexibility part, energy storage, power-to-hydrogen, and electric vehicles provided by conventional thermal power units; and T is the planning cycle.

$$CRF = \frac{\sigma(1+\sigma)^d}{(1+\sigma)^d - 1},$$

where CRF is the investment cost recovery coefficient, d represents the conversion days of various active resources, and σ represents the discount rate; this paper uses 5%.

Maintenance cost

The maintenance cost can be divided into the fixed equipment maintenance cost and variable operations maintenance cost. The equipment maintenance cost is related to the type and capacity of flexible resources and can be expressed by a certain proportion of the investment cost. The fixed maintenance cost is shown as follows:

$$C_{Fm} = \beta C_f^{new},$$

where the ratio of the fixed maintenance cost to initial investment cost is 0.03.

$$C_{\text{Om}} = \sum_{t=1}^{T}\sum_{k\in K} P_{k,t}\beta_k^{Om},$$

where $P_{k,t}$ is the power consumption of each flexible resource at time t and β_k^{Om} is the operations maintenance cost of each flexible resource per unit of power consumption.

Fuel costs

The fuel cost only considers the coal cost of thermal power units.

$$C_{Fu} = C_{coal}\sum_{t=1}^{T} f_{g,t},$$

where C_{coal} is the unit coal consumption cost of the thermal power unit. $f_{g,t}$ is the coal consumption of the thermal power unit at time t, which can be expressed as the secondary form of power generation:

$$f_{g,t} = a\cdot\left(P_{g,t}\right)^2 + b\cdot P_{g,t} + c,$$

where a, b, and c are the coal consumption coefficients of thermal power units, and $P_{g,t}$ is the power generation of the thermal power unit at the moment.

Wind curtailment penalty cost

The penalty cost of wind curtailment is added to the target to increase the consumption rate of wind power:

$$C_{Curt} = C_w^{curt}\sum_{t=1}^{T} P_{w,t}^{curt},$$

where C_{Curt} is the unit wind abandonment penalty cost and $P_{w,t}^{curt}$ is the abandoned wind volume of the wind turbine at the moment, which is equal to the predicted power generation of wind power minus the actual power generation of wind power.

Upper planning constraints

Installation capacity–load balance constraint

$$\sum_{m=1}^{M}\Delta P_{m,t} + \sum_{n=1}^{N}\Delta P_{n,t} \geq L_t\left(1+R_t\right),$$

where $P_{m,t}$ is the installed capacity of the various power sources in the t year, $P_{n,t}$ is the installed capacity of the various flexible resources in year t, L_t is the maximum load of the system in year t, and R_t is the capacity reserve coefficient.

Power installation constraints

$$\begin{cases} P_{m,t} \geq 0, \\ P_{m,t}^{\min} \leq P_{m,t} \leq P_{m,t}^{\max}, \end{cases}$$

where $P_{m,t}^{\min}$ and $P_{m,t}^{\max}$ are the minimum and maximum installed capacities of various types of hydropower and nuclear power, respectively.

Flexibility resource capacity constraints

$$\begin{cases} P_{n,t} \geq 0, \\ P_{n,t}^{\min} \leq P_{n,t} \leq P_{n,t}^{\max}, \end{cases}$$

where $P_{n,t}^{\min}$ and $P_{n,t}^{\max}$ are the lower and upper limits of the installation capacity of various flexible resources in year t, respectively, and are selected according to the actual situation.

Lower-level programming model

The lower-level programming model solves the flexibility problem under uncertainty in the new power system. In upper-level programming, the unit capacity is selected as the decision variable with the goal of economic optimization, the optimal output of various flexible resources satisfying the optimal goal of system flexibility is obtained, and the optimal output curve is obtained as the decision variable of the upper-level programming.

Lower-level programming objective function, aiming at optimal flexibility

$$\min f_2 = \min P_{IFSR},$$

where f_2 indicates that the objective function of the lower-level programming model is optimal flexibility. For the flexible supply and demand ratio, P_{IFSR} is used to characterize the system's ability to adjust supply to meet the demand.

Lower planning constraints

Power balance constraints

$$P_{g,t} + P_{w,t} + P_{s,t} + P_{n,t} + P_{h,t} + P_{l,t} = L_t + P_{loss} + P_{f,t},$$

where $P_{g,t}, P_{w,t}, P_{s,t}, P_{n,t}, P_{h,t}, P_{l,t}, P_{loss}, L_t, P_{f,t}$ are the thermal power units, wind turbines, photovoltaic units, nuclear power units, hydropower units, tie lines, network losses, loads, and flexible resource absorption power in the simulated operating period t, respectively.

Power unit output constraints

$$\lambda_m^{\min} P_{m,t} \leq P_{m,t} \leq \lambda_m^{\max} P_{m,t},$$

where $\lambda_m^{\min}, \lambda_m^{\max}$, and $P_{m,t}$ represent the minimum and maximum output coefficients of each power unit and the output of the unit at each moment in the operations simulation, respectively.

Flexibility resource operations constraints

$$0 \leq P_{n,t} \leq P_{n,t}^{\max},$$

where $P_{n,t}^{\max}$ is the maximum flexibility provided by each type of flexibility resource in the t period.

Insufficiently flexible supply–demand ratio probability constraint

In order to ensure sufficient flexibility, the index constraints of the system to meet the flexibility are given.

$$P_{IFSR} - \alpha = PR(R_{\text{fsd}} < \alpha) \leq P_{IFSR_{\max}},$$

where $P_{IFSR_{\max}}$ is the flexibility evaluation index value when the system flexibility is the worst (1), which indicates that the flexible system supply cannot meet the demand at any time. α is the flexibility expectation that is numerically equal to the flexible supply and demand ratio target value.

System simulation analysis

Base data

The example of this paper takes the power system in a certain area of Northeast China as the research object. The upper layer applies the genetic algorithm; the lower layer calls the fmincon function and uses MATLAB to write a program to solve the model. The new power system includes a total capacity of 1.49456 million kilowatts of thermal power units, 43.5 million kilowatts of wind turbines, 19.1 million kilowatts of photovoltaic units, 12.196 million kilowatts of hydropower units, and 22.3 million kilowatts of nuclear power units. The economic parameters involved in the example are shown in Table 1. The planning layer considers the annual planning cost, the optimization cycle of the operations layer is 24 h, and the time scale is 1 h, ignoring the influence of the unit ramp. The target value of the flexible supply and demand ratio (flexibility expectation α) ranges from 0.6 to 0.9.

Through the Latin hypercube sampling scene generation and K-means clustering scene reduction method, the uncertainty of the wind power load is processed, and typical days of large wind power–small load, large wind power–large load, small wind power–large load, and small wind power–small load are generated. After clustering, the weights of each typical daily scenario are 0.148, 0.18, 0.219, and 0.677, respectively. The wind abandonment situation is observed on a typical large wind power–small load day. The output and load curve of the system unit is shown in Figure 3. The new energy power generation accounts for approximately 40%, and there is obvious wind abandonment.

Analysis of simulation results

Through simulation, the optimal flexibility resource planning capacity is obtained when the system meets different flexibility expectations (α) under different uncertainties, taking into account economics and flexibility. The results are shown in Table 2.

TABLE 1 Flexibility economic parameters for resource planning.

Unit capacity cost of P2H (yuan per kW)	Fixed maintenance cost coefficient of P2H (β)	Unit operating cost of P2H (yuan per Nm^3)	Power consumption per unit of P2H (kWh per Nm^3)
3500	0.03	1.7	5
P2H operating efficiency	Service life of P2H equipment (years)	coal price (yuan per ton)	Unit wind abandonment penalty cost (yuan per MW)
0.95	20	330	500

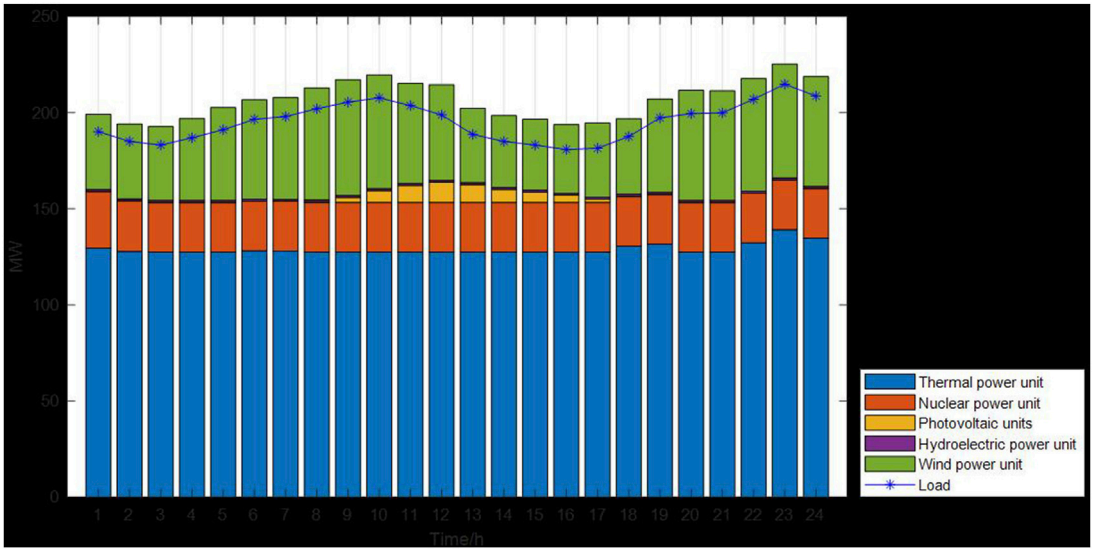

FIGURE 3
The output and load curve of the system unit.

TABLE 2 Flexibility resource planning results under different flexibility expectations.

	Flexibility expectation (α)	Optimal P2H capacity (MW)		Flexibility expectation (α)	Optimal P2H capacity (MW)
1	0.6	51.1464	9	0.76	18.4322
2	0.62	30.9346	10	0.78	30.526
3	0.64	40.3906	11	0.8	64.3299
4	0.66	39.1352	12	0.82	52.5487
5	0.68	33.4069	13	0.84	46.4750
6	0.7	26.4324	14	0.86	41.1390
7	0.72	58.4769	15	0.88	44.8224
8	0.74	32.3377	16	0.90	45.5781

The aforementioned table shows the planning results of the flexibility resource power-to-hydrogen when the system flexibility expectation threshold is 0.6–0.9. That is, when the system flexibility supply can meet the flexibility demand of 60%–90% as the planning target, considering the economics and flexibility, the optimal power-to-hydrogen capacity is planned. It can be seen that there is no direct linear or non-linear relationship between the capacity of flexibility resources and the expected value of flexibility due to the consideration of economics.

Flexibility analysis

Taking the typical large wind power–small load day as an example, the system flexibility under the planning is analyzed. As shown in Figure 4, under the optimal planning capacity,

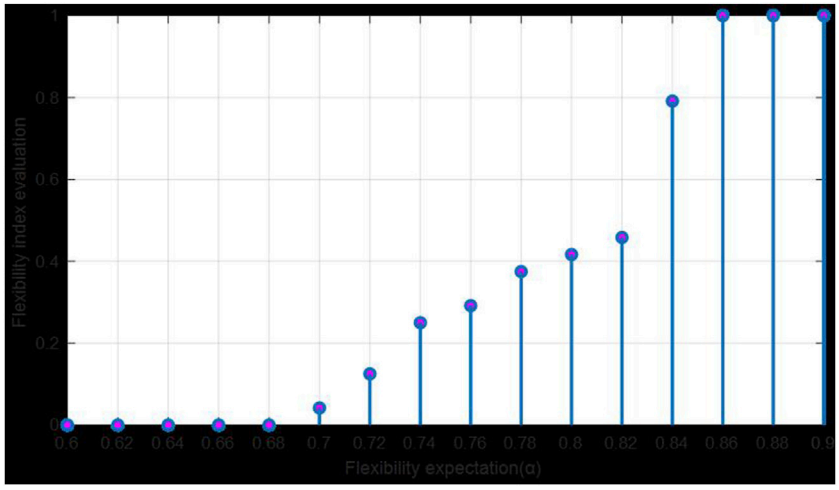

FIGURE 4
The system flexibility under the planning.

TABLE 3 Annual planning cost and flexibility index evaluation.

Flexibility expectation (α)	Total cost of P2H planning (10,000 yuan per year)	Probability of an insufficiently flexible supply–demand ratio (P_{IFSR}-α)	Flexibility expectation (α)	Total cost of P2H planning (10,000 yuan per year)	Probability of an insufficiently flexible supply–demand ratio (P_{IFSR}-α)
0.6	5177.3549	0	0.76	5285.7115	0.6458
0.62	5297.3501	0	0.78	5579.9154	0.6875
0.64	5551.3645	0	0.80	5266.6917	0.7083
0.66	5321.8229	0	0.82	5051.6129	0.7291
0.68	5302.6341	0.0833	0.84	5087.7608	0.8958
0.7	5055.7378	0.375	0.86	5282.6961	1
0.72	5510.0464	0.5625	0.88	5292.0086	1
0.74	5163.2797	0.625	0.90	5395.1604	1

when the supply-demand ratio of the system is required to be less than 0.68, the probability of an insufficiently flexible supply–demand ratio is 0; that is, the flexibility supply meets the flexibility demand of 68% at any time in the cycle, and the system can fully respond to the flexibility demand caused by uncertainty. When the demand–supply ratio of the system is greater than 0.86, the probability of insufficiently flexible supply and demand is 1; that is, the flexibility supply cannot meet the 86% flexibility demand at any time, and the system does not have the ability to respond to uncertainty. When the threshold is set to 0.7, that is, when the expected system meets 70% flexibility, the flexibility supply–demand ratio is 0.0417; that is, the probability that the system meets the flexibility supply to meet the 70% flexibility demand in the cycle is 4.17%. Compared with the large wind power–small load scenario, the flexibility index is reduced.

Financial analysis

The simulation data of system planning cost and corresponding flexibility index are shown in Table 3.

In the scenario of large wind power–small load, when the system flexibility is sufficient, that is, in the planning with the probability index of an insufficiently flexible supply and demand ratio of 0, if the optimal economic cost is expected to be the lowest, the power-to-hydrogen planning capacity with the expected flexible supply and demand ratio of 0.6 is selected according to Table 3. In order to achieve optimal flexibility, the corresponding power-to-hydrogen capacity is selected when the flexible supply–demand ratio is 0.66, and the total planned cost is 532.18229 million yuan.

Analysis of new energy consumption

In the large wind power–small load scenario, the P2H capacity with 66% responsiveness of the system to system uncertainty is selected for

TABLE 4 P2H power consumption in MW/h for different targets.

Time (h)	Flexibility as a single objective	Economic-flexibility bi-level programming objective	Time (h)	Flexibility as a single objective	Economic-flexibility bi-level programming objective
1	16.0049	16.0560	13	15.6287	15.6798
2	15.8273	15.8784	14	14.3022	14.3533
3	15.3317	15.3828	15	13.8770	13.9281
4	19.6115	19.6626	16	12.6930	12.7441
5	25.2840	25.3351	17	15.5728	15.6239
6	28.6792	28.7303	18	16.1361	16.1872
7	29.8793	29.9304	19	25.5846	25.6357
8	35.2407	35.2918	20	34.1931	34.2442
9	37.0734	37.1245	21	33.9351	33.9862
10	36.1552	36.2063	22	35.5900	35.6411
11	29.0025	29.0536	23	36.1818	36.2329
12	26.7020	26.7531	24	35.4118	35.3643

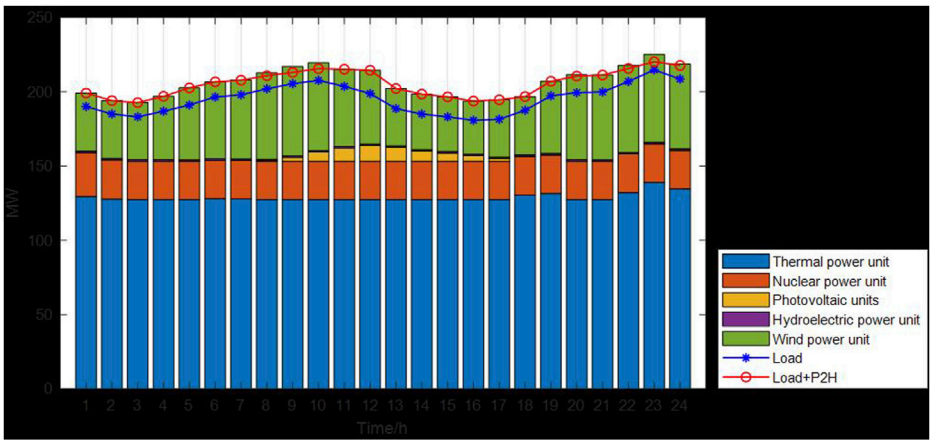

FIGURE 5
The system diagram after flexible resource planning.

wind abandonment analysis. From Tables 2, 3, it can be seen that when the expected system flexibility supply meets the 66% flexibility demand at any time, the power-to-hydrogen capacity is 39.1352 MW, and the total planned cost is 53.218229 million yuan per year.

The P2H output during the lower-level operations optimization with flexibility as the only goal and the electricity-to-hydrogen power consumption after the economic flexibility bi-level programming are shown in Table 4. It can be seen from the data in the table that when the flexibility optimization is carried out separately, the total P2H power consumption is 603.8982 MW. After considering the economics and flexibility, the power consumption of P2H increases to 605.0252 MW.

This paper only considers "green hydrogen"; that is, the conversion of electricity to hydrogen made from wind curtailment is green hydrogen, and its power consumption is equivalent to the consumption of wind curtailment. The system diagram after flexible resource planning is shown in Figure 5.

It can be seen intuitively from Figure 5 that flexible resource planning has the benefit of accommodating new energy. After calculation, the typical daily wind abandonment penalty cost before planning is 319,730 yuan. When only considering the flexibility of the system, the wind abandonment penalty cost is reduced to 34,998.3 yuan. After the economic flexibility bi-level planning, it is reduced to 17,217.4 yuan. At the same time, flexible resource planning reduces the operating cost of the new power system and improves the economics of the system.

Conclusion

Aiming at the insufficient response ability and flexibility resources problem caused by uncertainties in both the supply and load sides, research is carried out on improving system flexibility while making full

use of the flexible resources in the power system while considering the economics of the system. A probability index of an insufficiently flexible supply–demand ratio with flexibility probability characteristics is proposed to guide flexibility resource planning. A bi-level programming model of power system flexibility resources considering the probability of an insufficiently flexible supply–demand ratio is constructed, taking the power system in a certain area in Northeast China as the research object. The conclusions are as follows.

1) A probability index of an insufficiently flexible supply–demand ratio is proposed. Compared with the traditional flexibility index, it can effectively quantify the flexibility of the power system under the uncertainty of both the power supply side and the load side, strengthen the connection between uncertainty and flexibility, and describe the relationship between flexible supply and demand.
2) A resource planning model of the power system considering a flexible supply and demand relationship is constructed that takes into account economics and flexibility. By using the probability index of an insufficiently flexible supply–demand ratio, the flexibility expectation of the planning scheme can be selected, and the optimal scheme can be obtained by combining the evaluation results of planning cost and flexibility index. This scheme will not lead to poor economics in order to ensure ultra-high flexibility, nor will it force the system to not respond to operational risks in order to achieve optimal economics. The planning results can safely and effectively improve the new energy consumption capacity of the system.

Data availability statement

The original contributions presented in the study are included in the article/Supplementary Material; further inquiries can be directed to the corresponding author.

Author contributions

Conceptualization, XZ and ML; methodology, HL; software, FG; validation, CZ, XZ, and ML; resources, HL; data curation, FG; writing—original draft preparation, CZ; writing—review and editing, XZ; visualization, ML; supervision, HL. All authors contributed to the article and approved the submitted version.

Funding

This work was supported by the Science and Technology Project of State Grid Liaoning Electric Power Co., Ltd. (No. 2022YF-62).

Acknowledgments

The authors would like to thank the School of Electric Power, Shenyang Institute of Engineering, for helpful discussions on topics related to this work.

Conflict of interest

Authors XZ, ML, HL, FG, and CZ were employed by State Grid Liaoning Economic Research Institute.

The remaining author declare that the research was conducted in the absence of any commercial or financial relationships that could be construed as a potential conflict of interest.

The authors declare that this study received funding from the Science and Technology Project of State Grid Liaoning Electric Power Co., Ltd. (No.2022YF-62). The funder was involved in the study design, collection and analysis.

Publisher's note

References

Capasso, A., Falvo, M. C., and Lamedica, R. (2005). "A new methodology for power systems flexibility evaluation[C]," in 2005 IEEE Russia Power Tech Conference, St. Petersburg, Russia, 27-30 June 2005 (IEEE), 27–30.

Cui, M., and Zhang, J. (2018). Estimating ramping requirements with solar-friendly flexible ramping product in multi-timescale power system operations. *Appl. Energy* 225 (1), 27–41. doi:10.1016/j.apenergy.2018.05.031

Ding, Y., Shao, C., and Yan, J. (2018). Economical flexibility options for integrating fluctuating wind energy in power systems: The case of China. *Appl. Energy* 228, 426–436. doi:10.1016/j.apenergy.2018.06.066

Guo, J. B. (2021). Challenges faced by new power systems and thinking on related mechanisms[J]. *China Power Enterp. Manag.* 25, 8–11. doi:10.3969/j.issn.1671-735X.2021.12.028

Guo, T. (2020). *Power system flexibility evaluation and flexibility transformation planning research[D]*. Beijing: North China Electric Power University.

International Energy Agency (2008). *Empowering variable renewables-options for flexible electricity flexible electricity systems[R]*. Internatio Energy Agency.

International Energy Agency (2009). Empowering Variable Renewables—Options for Flexible Electricity Systems: (Complete Edition)[J]. *OECD Energy* 23, 1—36.

Lannoye, E., Flynn, D., and O'Malley, M. (2012). "Assessment of power system flexibility: A high-level approach[C]," in 2012 IEEE Power and Energy Society General Meeting, San Diego, CA, USA, 22-26 July 2012 (IEEE).

Li, H., Lu, Z., and Qiao, Y. (2015). Evaluation of power system operation flexibility with large-scale wind power integration[J]. *Power grid Technol.* 39 (6), 1672–1678. doi:10.13335/j.1000-3673.pst.2015.06.032

Li, L. F., Chen, Z. P., Hu, Y., Tai, N. L., Gao, M. P., and Zhu, T. (2021). Renewable energy power system expansion planning based on flexibility and economy[J]. *J. Shanghai Jiao Tong Univ.* 55 (07), 791–801. doi:10.16183/j.cnki.jsjtu.2020.024

Li, W. N., and Wang, Q. (2020). Stochastic production simulation for generating capacity reliability evaluation in power systems with high renewable penetration. *Energy Convers. Econ.* 1 (3), 210–220. doi:10.1049/enc2.12016

Lu, Y., WuChen, S. Y. J. Z., Liu, J., and Kang, C. Q. (2019). A planning method for wind power and photovoltaic absorption considering flexible resources[J]. *Distrib. Energy* 4 (05), 10–16. doi:10.16513/j.2096-2185.DE.191089

Lu, Z., and LiQiao, H. Y. (2018). Probabilistic flexibility evaluation for power system planning considering its association with renewable power curtailment. *IEEE Trans. Power Syst.* 33 (03), 3285–3295. doi:10.1109/tpwrs.2018.2810091

National Development and Reform Commission and the National Energy (2018). Guidance on improving the regulation capacity of power system. *Energy Res. Util.* 10, 3.

North American Electric Reliability Cooperation (2011). North American Electric Reliability Corporation 1, hereby submits this Notice of Filing of[J].

State Grid Energy (2020). *Research Institute Co Ltd [M]*.Beijing: China Electric Power Press.

Ul Big, A., and Andersson, G. (2012). "On operational flexibility in power systems [C]," in Proceedings of the Power and Energy Society General Meeting, San Diego California, USA, 22-26 July 2012 (IEEE), 22–26.

Xiao, D. Y. (2015). *Research on flexibility evaluation index and optimization of power system with large-scale renewable energy[D]*. Shanghai: Shanghai Jiaotong University.

Xu, T. H., Lu, Z. X., Qiao, Y., and An, J. (2019). Source-load-storage multi-type flexible resource coordinated high-proportion renewable energy power planning[J]. *Glob. Energy Internet* 2 (01), 27–34.

Yang, J., Li, F. T., and Zhang, G. H. (2022). New energy high permeability system planning method considering flexibility requirements[J]. *Power Grid Technol.* 46 (06), 2171–2182. doi:10.13335/j.1000-3673.pst.2021.0943

Yu, D., Guo, Y. H., Wu, J., Li, J. T., and Wang, C. M. (2022). Flexibility improvement planning and evaluation of regional integrated energy system considering uncertainty [J]. *Power Supply* 39 (04), 84–92. doi:10.19421/j.cnki.1006-6357.2022.04.012

Zhang, Y. Z., Dai, H. C., and Zhang, N. (2020). *The low-carbon transformation of power system needs ' multi-line attack ' [N]*. Beijing: China Energy News.

Zhao, S., Xu, M., and Zhou, W. (2021). Simulation of sequential operation of multi-energy power system considering section constraints[J]. *Electr. Power Autom. Equip.* 41 (07), 1–6. doi:10.16081/j.epae.202104011

Zi, P. L. (2018). An extreme scenario method for robust transmission expansion planning with wind power uncertainty[J]. *Energies* 11, 8. doi:10.3390/en11082116

frontiers | Frontiers in Energy Research

TYPE Original Research
PUBLISHED 17 July 2023
DOI 10.3389/fenrg.2023.1209875

OPEN ACCESS

EDITED BY
Mingfei Ban,
Northeast Forestry University, China

REVIEWED BY
Shuan Dong,
National Renewable Energy Laboratory (DOE), United States
Jiyu Wang,
National Renewable Energy Laboratory (DOE), United States

*CORRESPONDENCE
Yajuan Guan,
ygu@energy.aau.dk

RECEIVED 21 April 2023
ACCEPTED 26 June 2023
PUBLISHED 17 July 2023

CITATION
Kang W, Guan Y, Danang Wijaya F, Kondorura Bawan E, Priyo Perdana A, Vasquez JC and M. Guerrero J (2023), Community microgrid planning in Lombok Island: an Indonesian case study.
Front. Energy Res. 11:1209875.
doi: 10.3389/fenrg.2023.1209875

Community microgrid planning in Lombok Island: an Indonesian case study

Wenfa Kang[1], Yajuan Guan[1]*, Fransisco Danang Wijaya[2], Elias Kondorura Bawan[2], Adam Priyo Perdana[2], Juan C. Vasquez[1] and Josep M. Guerrero[1]

[1]AAU Energy, Aalborg University, Aalborg, Denmark, [2]Department of Electrical Engineering and Information Technology, Universitas Gadjah Mada, Yogyakarta, Indonesia

Rural electrification, diesel generator replacement, and resilient electrification systems against natural disasters are among the main targets for Perusahaan Listrik Negara (PLN) in Indonesia to achieve a universally accessible, resilient, and environment-friendly electricity supply. Microgrids, therefore, become a popular and available way to achieve the aforementioned targets due to their flexibility and resiliency. This paper aims to provide a resilience-oriented planning strategy for community microgrids in Lombok Island, Indonesia. A mixed-integer linear program, implemented in the distributed energy resources customer adoption model (DER-CAM), is presented in this paper to find the optimal technology portfolio, placement, capacity, and optimal dispatch in a community microgrid. The multinode model is adopted for the planning, and hence, power flow constraints, N-1 contingency, and technology constraints are considered. The results show that the placement of photovoltaic (PV) arrays, battery energy storage systems (BESSs), and diesel generators (DGs) as backup sources in multi-node community microgrids lead to multiple benefits, including 100% rural electrification, over 25% cost savings, as well as over 22%, in particular CO_2 emission reduction in multinode community microgrids.

KEYWORDS

community microgrid planning, resilience, CO_2 reduction, rural electrification, distributed energy resources

1 Introduction

Over recent years, about 80% of the world's primary energy is being provided by fossil fuels, and the energy consumption rate has increased at 2.3% per year from 2015 to 2040, which inevitably increases the CO_2 levels in the atmosphere (Martinez-Frias et al., 2008). High level of CO_2 in the atmosphere causes the rise of average global temperature, which leads to adverse effects on global climates. Moreover, the burning of fossil fuels to gain electrical energy causes global warming and produces environmental pollutants such as NOx, SOx, and other volatile organic compounds. Therefore, the feasible way to shift to a lower carbon society is to impose carbon taxes and carbon trading polices (Chu et al., 2017).

However, for remote areas without access to the existing electricity grid, locally available resources, such as renewable energy resources (RESs), are promising to support local loads by using microgrid technologies due to their flexibility endowed by advanced control technologies and energy storage systems. In addition, the least cost electrification program in Indonesia is the off-grid generation. In other words, solar battery-based

microgrids/min–microgrids are the most suitable and cost-effective options for achieving universal access to electricity (ESCAP, 2020). Furthermore, in some extreme cases, for example, utility black outages or natural disasters, microgrids can work in islanded mode to support the local critical loads and to assist the electricity recovery of adjacent areas, which enables the power distribution network to be more resilient and reliable (Wang and Lu, 2020). Based on the aforementioned arguments, the optimal planning of microgrids is the very first essential step to achieve universal access to electricity, energy transition of Indonesia, and CO_2 emission reduction. This is also in line with the government's commitment to convert conventional power plants to renewable energy generators (PLN, 2021) and Sustainable Development Goals (SDGs) number 7 (IEA and IRENA, 2021).

The optimal portfolio, sizing, and placement of renewable energy resources form a complicated problem because of the features of renewable energy resources; stochastic load demand; and large numbers of continuous and discrete variables, integers, and parameters considered during the design of microgrids. Hence, the optimal planning method can decrease the investment cost with full use of technology components.

Several techno-economic studies have investigated the planning of community microgrids with the RES and energy storage systems (ESSs) (Mizani and Amirnaser, 2009; Hafez and Bhattacharya, 2012; Hittinger et al., 2015; Schittekatte et al., 2016; Madathil et al., 2017; Cao et al., 2019; Borghei and Ghassemi, 2021). Hafez and Bhattacharya (2012); Hittinger et al. (2015) designed microgrid planning models based on the Hybrid Optimization of Multiple Energy Resources (HOMER) software, where life cycle cost and environmental emissions are considered. In Stadler et al. (2013), Stadler et al. (2016), Prathapaneni and Detroja (2019), Borghei and Ghassemi (2021), microgrid planning is modeled into a mixed-integer linear programming (MILP) problem, where binary integers are usually considered to find the locations of various energy carriers. The model of power flow constraints, BESS model, and operation costs in these references are linearized. For the non-linear model of power flow equation, BESS model, and operation costs, Wang et al. (2021), Wu et al. (2023) provide mixed-integer non-linear programming (MINLP) models to solve the proposed problems. These solutions are more accurate than solutions obtained from MILP, but are much more time-consuming.

Aside from providing planning models, several software tools are also designed and compared to analyze the electrical, economical, and environmental performance of microgrids with the RES and ESS, which can be seen in Mendes et al. (2011), Bahramara et al. (2016), Khare et al. (2016), Siddaiah and Saini (2016), Jung and Villaran (2017), Cardoso et al. (2019). Although HOMER is one of the popular software tools, this paper adopts the Distributed Energy Resources Customer Adoption Model (DER-CAM) not only due to the flexible and robust optimization algorithms, hourly time step, and scale considerations but also due to the successful applications with modeling microgrids (Lee et al., 2015; Jung and Villaran, 2017). The DER-CAM tool was designed by Lawrence Berkeley National Laboratory (LBNL) to provide optimal planning and operation of distributed energy generation (DER) either in a distribution system or in microgrids (Stadler et al., 2014). The optimization objective in the DER-CAM contains annual costs and CO_2 emissions.

Normally, the key inputs of the model are load profiles, solar radiation, wind speed, water speed, tariff and fuel prices, and user-defined lists of preferred investment of technologies. The outputs of the DER-CAM include optimal portfolios, placements, sizing of DER and ESS, energy dispatch, CO_2 emissions, and fuel consumption. With the development, the DER-CAM tool has two basic models, namely, single node and multi-node planning model. In the multi-node planning model, the power flow constraints are integrated. In addition, N-1 contingency and ancillary services are considered (Cardoso et al., 2017; MadathilChalil et al., 2017; Mashayekh et al., 2018). The contribution of this work lines in the modeling of multi-node community microgrids for the Lombok Island based on the native practical data, also in providing strategies for rural electrification in Indonesia. Compared with the HOMER-based strategies, the provided strategy includes the power line flow in the planning. In addition, the sensitivity analysis demonstrates that the proposed planning model is robust to capital cost variations.

This paper presents a technique for optimal planning and operation of microgrids with the RES and ESS in the multi-node model in the context of Lombok Island, Indonesia. The rest of the paper is organized as follows. Section 2 introduces the model of a multi-node microgrid. Section 3 proposes the planning objectives and constraints for community microgrids. Data inputs and parameter setup are presented in Section 4. Section 5 introduces the planning results for multi-node (networked) microgrids. The conclusion of the paper is presented in Section 6.

2 The model of community microgrids

Figure 1 shows the model of a multi-node microgrid. The microgrid has two operation modes—islanded mode and grid-connected mode. Each node is composed of various loads, including electricity loads (household electricity equipment, air conditioner, washing machine, and refrigerator). The objective function of planning is to determine the capacity and placement of various DER technologies with minimized cost and carbon dioxide (CO_2) emissions subject to constraints such as capacity constraints and operation constraints (electricity and thermal) of various technologies.

3 Planning model of community microgrid headings

3.1 Objective function

Three typical load profiles are adopted in the planning, namely, weekday profile, weekend day profile, and peak day profile. For a typical year characterized by the three load profiles, the time step equals the Number of Months × Hours × Types of load profile, which is $12 \times 24 \times 3 = 864$.

The objective function of planning is to minimize the overall microgrid investment and operation cost including emission cost in the typical year aforementioned. The objective function is formulated as follows (Eq. 1):

$$C = C_{Inv} + C_{Pur} + C_{De} + C_{Ex} + C_G + C_{FM} + C_{CO2} + C_{Cur}, \quad (1)$$

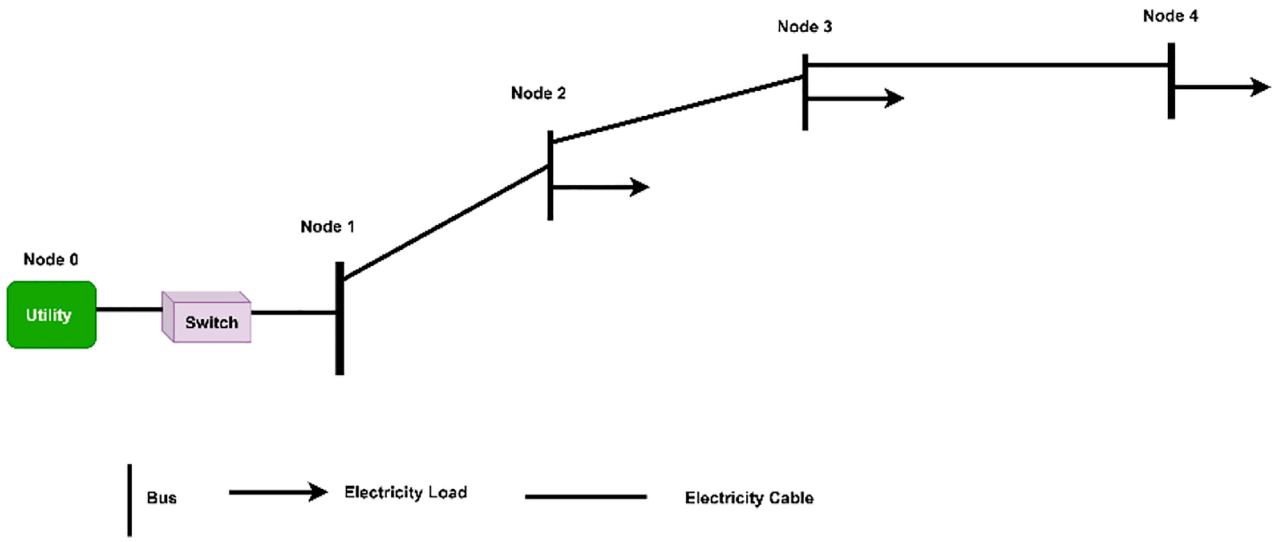

FIGURE 1
Multi-node community microgrids.

where C_{Inv} is the annualized investment cost of various technologies, C_{Pur} is the total cost of electricity purchase with CO_2 taxation, C_{De} is the demand charge fee, C_{Ex} is the electricity export revenue, C_G is the generation cost of various technologies including variable maintenance costs, C_{FM} is the fixed maintenance cost, C_{CO2} is the CO_2 taxation on local generations, and C_{Cur} is the load curtailment costs.

The annualized investment cost, including the capital cost of discrete technology (Diesel Generator, DG) and capital cost of continuous technology (BESS and PV), is formulated as follows:

$$C_{Inv} = \sum_{n,g} Inv_{n,g} \cdot P_{Rate,g} \cdot C_{Turn,g} \cdot r_{Ann,g} + \sum_{n,k} \left(C_{FX,k} \cdot Pur_{n,k} + C_{Var,k} \cdot Cap_{n,k} \right) \cdot r_{Ann,k}, \quad (2)$$

where $\boldsymbol{Inv_{n,g}}$ is the integer units of discrete generation technology g at node n, $P_{Rate,g}$ is the power rating of discrete generation technology g (kW), and $C_{Turn,g}$ is the turnkey capital cost of discrete generation technology g ($/kW). $C_{FX,k}$ is the fixed capital cost of continuous technology k ($), $C_{var,k}$ is the variable capital cost of continuous technology k ($/kW), $\boldsymbol{Pur_{n,k}}$ is the binary installation decision for continuous technology k, $\boldsymbol{Cap_{n,k}}$ is the installed capacity of continuous technology k at node n, and $r_{Ann,i}$ is the annuity rate for the technology i at node n. As observed, the investment costs are decided by the investment decisions of technology, which are $\boldsymbol{Inv_{n,g}}$, $\boldsymbol{Pur_{n,k}}$ and the installed capacity $\boldsymbol{Cap_{n,k}}$.

The purchase cost of microgrids is shown in (Eq. 3)

$$C_{Pur} = \sum_{n,t} Put_{n,t} \cdot \left(P_{g_t} + C_{Tax} \cdot MCRT_t \right), \quad (3)$$

where P_{gt} is the utility electricity purchasing price at time t, C_{Tax} is the tax on CO_2 emissions, $MCRT_t$ is the marginal carbon emissions from marketplace generation, and $\boldsymbol{Put_{n,t}}$ is the electricity purchased from the utility.

The demand charge cost is as follows:

$$C_{De} = \sum_{n,m,p} DRt_{m,p} \cdot MPur_{n,m,p}, \quad (4)$$

where $DRt_{m,p}$ is the power demand charge for month m and period p, ($/kW) and $\boldsymbol{MPur_{n,m,p}}$ is the maximal electricity purchased from the utility during period p of month m at node n.

The electricity export revenues are as follows:

$$C_{Ex} = -\sum_{n,t} ExRt_t \cdot ExP_{n,t}, \quad (5)$$

where $ExRt_t$ is the energy rate for electricity export ($/kWh) and $\boldsymbol{ExP_{n,t}}$ is the electricity exported to the utility at node n.

$$C_G = \sum_{n,j,t} Gen_{n,j,t} \left(GCst_j + M_{var,j} \right), \quad (6)$$

where $\boldsymbol{Gen_{n,j,t}}$ is the output of technology j to meet energy use u at node n and $GCst_j$ and $M_{var,j}$ are the generation cost of technology j ($/kWh) and variable annual operation and maintenance cost of technology j ($/kWh), respectively.

$$C_{FM} = \sum_{n,g} Inv_{n,g} \cdot P_{Rate,g} \cdot MF_g + \sum_{n,k} Cap_{n,k} \cdot MF_k, \quad (7)$$

where MF_g is the fixed annual operation and maintenance cost of technology g, $/kW capacity.

In addition, the carbon taxation on local generation is formulated as follows:

$$C_{CO2} = \sum_{n,j,t} Gen_{n,j,t} \cdot \frac{1}{\eta_j} \cdot GCRt_j \cdot C_{Tax}, \quad (8)$$

where $GCRt_j$ is the carbon emission rate from generation technology j (kg/kWh) and η_j is the electrical efficiency of generation technology j.

$$C_{Cur} = \sum_{n,u,t} PLcur_{n,u,t} \cdot CurPr_{n,u}, \quad (9)$$

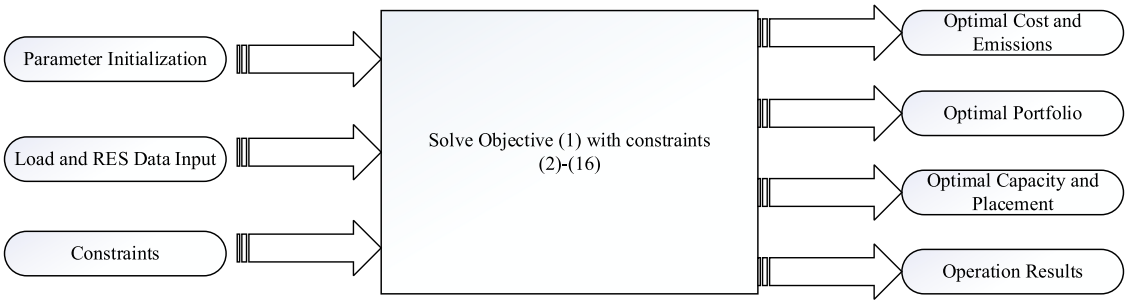

FIGURE 2
Diagram of the planning of community microgrids.

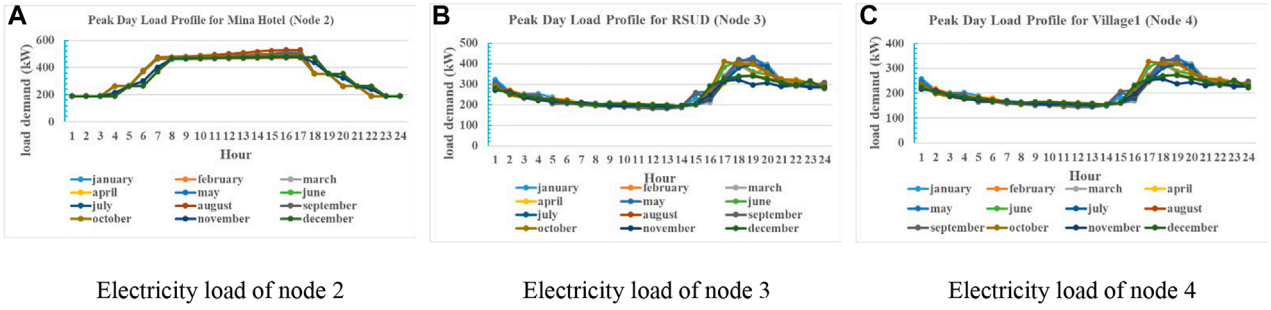

FIGURE 3
Load profiles of community microgrids in 2020. **(A)** Electricity load of node 2, **(B)** electricity load of node 3, and **(C)** electricity load of node 4.

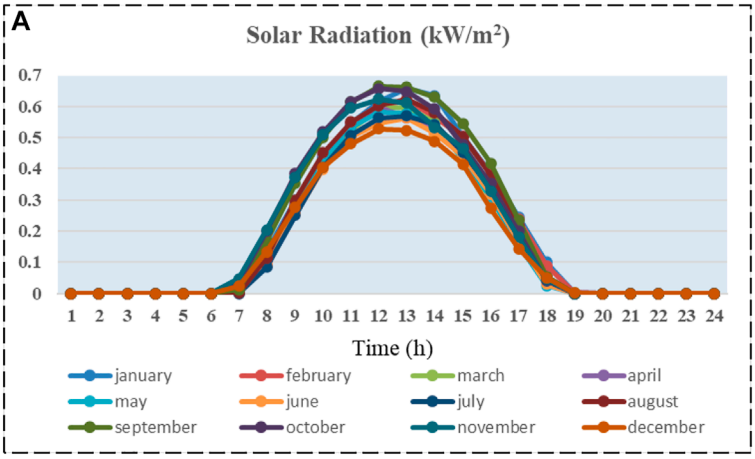

B

	Hours	1	2	3	4	5	6	7	8	9	10	11	12	13	14	15	16	17	18	19	20	21	22	23	24
Summer	peak	3	3	3	3	3	3	3	3	2	2	2	1	1	1	1	1	1	1	2	2	2	2	3	3
Summer	week	3	3	3	3	3	3	3	3	2	2	2	1	1	1	1	1	1	1	2	2	2	2	3	3
Summer	weekend	3	3	3	3	3	3	3	3	3	3	3	3	3	3	3	3	3	3	3	3	3	3	3	3
Winter	peak	3	3	3	3	3	3	3	3	3	3	3	3	3	3	3	3	3	3	3	3	3	3	3	3
Winter	week	3	3	3	3	3	3	3	3	2	2	2	2	2	2	2	2	2	2	2	2	2	2	3	3
Winter	weekend	3	3	3	3	3	3	3	3	3	3	3	3	3	3	3	3	3	3	3	3	3	3	3	3

1	On-peak	0.4 $/kWh
2	Mid-peak	0.2 $/kWh
3	Off-peak	0.11 $/kWh

	Januar	Februa	March	April	May	June	July	August	Septem	Octobe	Novem	December
Winter	1	1	1	1	0	0	0	0	0	0	1	1
Summe	0	0	0	0	1	1	1	1	1	1	0	0

ToU rates and Hours

FIGURE 4
PV radiations and Time-of-Use (ToU) rates for community microgrids. **(A)** Solar radiations and **(B)** ToU rates and hours.

TABLE 1 Parameters of battery energy storage systems (lithium-ion batteries).

η_{ch}/η_{dis}	Decay rate	Discharge rate	$SoC_{\min}$ (%)	Temperature (°C)	Maximum number of cycles
0.9	0.001	0.3	30	25	200

TABLE 2 Unit of items such as maxp (kW), lifetime (year), efficiency (%), and ramp rate (%).

Technology	maxp	maxS	Lifetime	Cap cost	NOxRate	Efficiency	Ramp rate
DGTech01	65	65	15	6,440	0.0001	0.0073	65
DGTech02	75	75	15	5761.407	0.0068	0.0128	75
DGTech03	200	200	15	6,300	0.0001	0.0085	200

TABLE 3 Costs of load-shedding for the multi-node microgrids.

		Variable costs	Max-curtailment	Max-hours
Node 2	LowCR	0.15	0.2	24
Node 4	LowCR	0.15	0.2	24

where $\boldsymbol{PLcur}_{n,u,t}$ is the customer load not met in energy consumption u at node n (kW) and $Cur\mathrm{Pr}_{n,u}$ is the load curtailment cost for energy use u at node n ($/kWh).

As described in Eqs 2–9, the total cost objective function includes 1) annualized investment costs of discrete and continuous technologies; 2) total cost of electricity purchase inclusive of carbon taxation; 3) demand charges; 4) electricity export revenues; 5) generation cost for electrical, heating, or cooling technologies inclusive of their variable maintenance costs; 6) fixed maintenance cost of discrete and continuous technologies; 7) carbon taxation on local generation; and 8) load curtailment costs. The optimization variables include $X = [Inv_{\mathrm{n,g}}, \mathrm{Pur}_{\mathrm{n,k}}, \mathrm{Cap}_{\mathrm{n,k}}, Put_{n,t}, MPur_{n,m,p}, ExP_{n,t}, Gen_{\mathrm{n,j,t}}$, and $PLcur_{n,u,t}]$, which are composed of continuous and binary variables. Parameter $Y = [\mathrm{P}_{\mathrm{Rate,g}}, \mathrm{C}_{\mathrm{Turn,g}}, \mathrm{C}_{\mathrm{FX,k}}, \mathrm{C}_{\mathrm{var,k}}, \mathrm{r}_{\mathrm{Ann,i}}, \mathrm{P}_{\mathrm{gt}}, \mathrm{C}_{\mathrm{Tax}}, \mathrm{MCRT}_{\mathrm{t}}, DRt_{m,p}, ExRt_{t}, GCst_{j}, \mathrm{MF}_{\mathrm{g}}, \mathrm{GCRt}_{\mathrm{j}}, \eta_{j}$, and $Cur\mathrm{Pr}_{n,u}]$ is the constant associated with the planning, which should be determined before solving the optimization objective.

The constraints include energy balance constraints, power flow constraints, storage constraints, cable current constraints, and energy import/export constraints.

The power flow constraints include current and voltage constraints for multi-node microgrids. However, for single-node microgrids, power flow constraints can be ignored. In this paper, a linear power flow model is considered for a balanced multi-node microgrid. It is assumed that the slack bus of microgrids is denoted by N, which means that the voltage of node N is $V_N = V_0 \angle 0$.

3.2 Electricity balance constraints

The power flow is represented as follows:

$$\begin{aligned} Pg_{\mathrm{n,t}} = {} & Put_{\mathrm{n,t}} - ExP_{\mathrm{n,t}} + \sum_{\mathrm{j}\in\{\mathrm{PV,ICE,MT,FC,WT}\}} Gen_{\mathrm{n,j,t}} \\ & - \left(PL_{\mathrm{n,u=EL,t}} - PLcur_{\mathrm{n,u=EL,t}}\right) + P_{\mathrm{dis,n,s=ES,t}} \cdot \eta_{\mathrm{di,s=ES}} \\ & - \frac{1}{\eta_{\mathrm{ch,s=ES}}} \cdot P_{\mathrm{ch,n,S=ES,t}} - \frac{1}{co_1} \cdot Gen_{\mathrm{n,c=EC,t}}, \end{aligned} \tag{10}$$

$$Qg_{n,t} = Pg_{n,t} \cdot \tan(\operatorname{acos} \phi); \quad n \neq N, \tag{11}$$

$$\begin{cases} \mathrm{re}V_{\mathrm{n,t}} = \mathrm{V}_0 + \dfrac{1}{\mathrm{V}_0} \sum \left(\mathrm{Zr}_{\mathrm{n},n'} \cdot Pg_{\mathrm{n,t}} + \mathrm{Zi}_{\mathrm{n},n'} \cdot Qg_{\mathrm{n,t}}\right); & \mathrm{n},n' \neq \mathrm{N} \\ \mathrm{Im}V_{n,t} = V_0 + \dfrac{1}{V_0} \sum \left(\mathrm{Zin}_{n,n'} \cdot Pg_{n,t} - Zr_{n,n'} \cdot Qg_{n,t}\right); & n,n' \neq N \\ \mathrm{re}V_{n,t} = V_0, \mathrm{Im}V_{n,t} = 0; & n = N, \end{cases} \tag{12}$$

$$\begin{cases} \mathrm{Ploss_t} = \dfrac{1}{2} \sum\limits_{\mathrm{n},n'} \mathrm{r}_{\mathrm{n},n'} \cdot \left(|Ir_{\mathrm{n},n',\mathrm{t}}|^2 + |Ii_{\mathrm{n},n',\mathrm{t}}|^2\right) \approx \dfrac{1}{2} \sum\limits_{\mathrm{n},\mathrm{n}'} \mathrm{r}_{\mathrm{n},n'} \cdot \left(eIr_{\mathrm{n},n',\mathrm{t}} + eIi_{\mathrm{n},n',\mathrm{t}}\right) \\ \mathrm{Qloss_t} = \dfrac{1}{2} \sum\limits_{\mathrm{n},n'} \mathrm{x}_{\mathrm{n},n'} \cdot \left(|Ir_{\mathrm{n},n',\mathrm{t}}|^2 + |Ii_{\mathrm{n},n',\mathrm{t}}|^2\right) \approx \dfrac{1}{2} \sum\limits_{\mathrm{n},\mathrm{n}'} \mathrm{x}_{\mathrm{n},n'} \cdot \left(eIr_{\mathrm{n},n',\mathrm{t}} + eIi_{\mathrm{n},n',\mathrm{t}}\right), \end{cases} \tag{13}$$

where active power outputs from node n $Pg_{n,t}$ are related to the exported/imported power to/from the utility, power generated from the installed energy resources (PV, DG, FC, and WT), load demand and curtailed loads, consumed power by electric chiller, and the discharged/charged power from energy storage systems. Parameter co_1 is the coefficient of the electric chiller, and η_{dis}/η_{ch} is the discharge/charge efficiency of BESSs. Moreover, each node has the constant power factor ϕ. The nodal voltages $V_{n,t}$ shown in Eqs 11, 12 are calculated by the nodal active/reactive power injection and network impedance matrix $\boldsymbol{Z}$ without the slack bus row and column. Equation 13 is the power loss of the network, which is used to decide the placements of DERs. In addition, $r_{\mathrm{n},n'}$ and $x_{\mathrm{n},n'}$ are the resistance and inductance of line impedance between nodes n and n', respectively; $eIr_{n,n't}$ and $eIi_{n,n't}$ are the linearized real current Ir^2 and image current Ii^2 of line (n, n') (Mashayekh et al., 2017), respectively; and $\mathrm{re}V\mathrm{n,t}$ and $\mathrm{Im}V\mathrm{n,t}$ are the real and imaginary part of the voltage amplitude of node n at time t, respectively.

3.3 Operational constraints

The operation constraints contain the nodal voltage constraints, generation capacity constraints, storage constraints, and energy import/export constraints. The constraints of energy storage are formulated as follows:

$$\begin{cases} SoC_{\mathrm{n,s,t}} = \left(1 - \phi_{\mathrm{s}}\right) \cdot SoC_{\mathrm{n,t-t}} + P_{ch,\mathrm{n,s,t}} - P_{dis,\mathrm{n,s,t}} \\ SoC_{\min} \leq SoC_{\mathrm{n,s,t}} \leq SoC_{\max} \\ P_{ch,\mathrm{n,s,t}} \leq P_{ch,\max,n,s} \\ P_{dis,\mathrm{n,s,t}} \leq P_{dis,\max,n,s}. \end{cases} \tag{14}$$

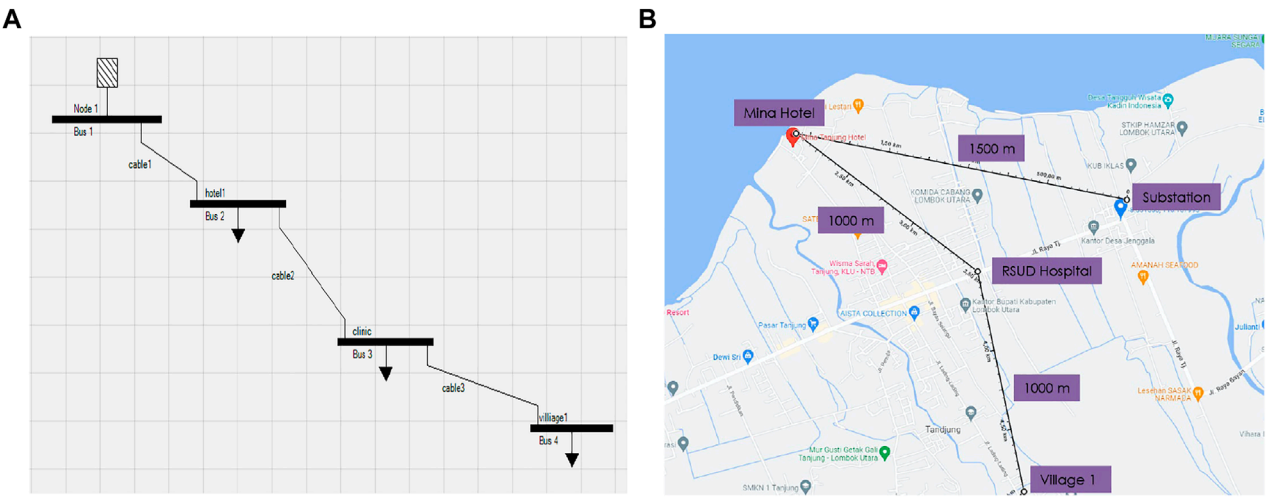

FIGURE 5
Topology of the four-node community microgrid (MG). **(A)** Topology of four-node MG in the DER-CAM and **(B)** geographical topology of the MG.

TABLE 4 Planning results of multi-node MG.

Node	Optimized value	Reference value	Total savings (%)
Total annual energy costs (k$)	789	1,013	22.12
Total annual CO_2 emissions (tons)	1,420	1,900	25.25

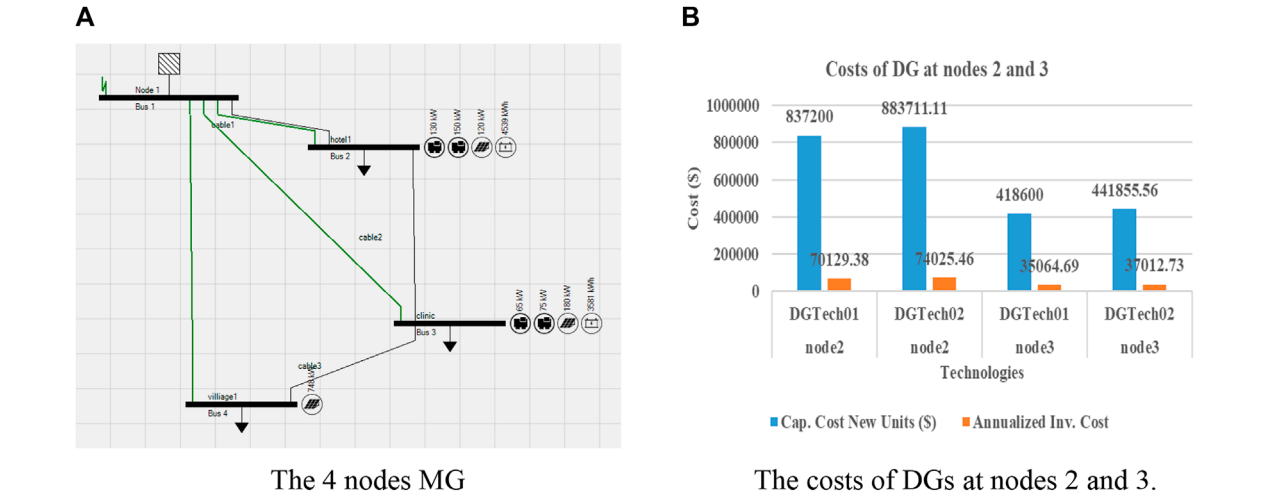

FIGURE 6
Four-node community MG with installed PV and BESS. **(A)** Four-node MG and **(B)** costs of DGs at nodes 2 and 3.

The generation constraints are formulated as follows

$$\begin{cases} Gen_{n,c,t} \leqslant Cap_{n,c} \cdot \eta_{eff} \cdot Solar_t; \quad c \in \{PV, ST\} \\ Gen_{n,g,t} \leqslant Inv_{n,g} \cdot P_{Rate,g} \\ Cap_{n,k} \leqslant Pur_{\mathbf{n,k}} \cdot M \\ Gen_{n,c,t} \leqslant Cap_{n,c}, \end{cases} \tag{15}$$

where η_{eff} is the solar radiation conversion efficiency of generation technology $c \in$ (PV, ST), $Solar_t$ is the average fraction of maximum solar insolation received during time t (%), and $Pur_{n,k}$ is the binary purchase decision for continuous technology k at node n. M is a very large positive constant which decides the upper limits of the capacity of the continuous technology. $Gen_{n,g,t}$ is the DG power generation of node n at time t. $Gen_{n,c,t}$ is the power generation of continuous

technology of node n at time t. $Cap_{n,k}$ is the capacity of technology k of node n.

For the gird-connected mode, microgrids may import or export energy from/to the utility by the point of common coupling (PCC) node. However, the energy transferred by the PCC node is normally limited, which is as follows:

$$\begin{cases} Put_{n,t} \leqslant psb_{n,t} \cdot grd \cdot M, \mathrm{n} = \mathrm{N}, (\text{slack bus}) \\ ExP_{n,t} \leqslant (1 - psb_{n,t}) \cdot grd \cdot mExP, \mathrm{n} = \mathrm{N}\ (\text{slack bus}), \end{cases} \tag{16}$$

where $psb_{n,t}$ is the binary electricity purchase/sell decision at node n, M is the maximal energy purchased from the utility, and $mExP$ is the maximal energy exported to the grid.

4 Planning configuration

4.1 Diagram of community microgrid planning

The planning model of community microgrids is described by Eqs 1–16, where the total investment cost, operation cost, emission cost, energy balance, and operation constraints are introduced. The aforementioned optimization problem is a mixed-integer linear optimization problem, which is an NP-hard problem, but can be solved by mature optimization solvers such as Gurobi and Cplex. Before solving the planning problem, one should first initialize the parameters of the problem, such as to define the value of vector Y = [$P_{Rate,g}$, $C_{Turn,g}$, $C_{FX,k}$, $C_{var,k}$, $r_{Ann,i}$, P_{gt}, C_{Tax}, $MCRT_t$, $DRt_{m,p}$, $ExRt_t$, $GCst_j$, MF_g, $GCRt_j$, η_j, and $CurPr_{n,u}$] according to the demand, energy policy, specific technologies, and tariffs.

Second, the basic load profile of the microgrids should be collected and input into the optimization problem. In addition, solar radiations and wind speed data should also be collected for the planning. Then, with the given parameters and data input, the proposed optimization problem can be solved. In addition, the optimization variables $\boldsymbol{X}$ = [$\boldsymbol{Inv}_{n,g}$, $\mathbf{Pur}_{n,k}$, $\mathbf{Cap}_{n,k}$, $\boldsymbol{Put}_{n,t}$, $\boldsymbol{MPur}_{n,m,p}$, $\boldsymbol{ExP}_{n,t}$, $\boldsymbol{Gen}_{n,j,t}$, and $\boldsymbol{PLcur}_{n,u,t}$] will be obtained. Finally, with the optimal solutions, the capacities and placements of energy resources will be given. The diagram of the planning of community microgrids is illustrated in Figure 2.

4.1 Data input

The basic data needed for the planning include the load demand for peak day, solar radiations, and electricity rates. The yearly load profiles for nodes 2, 3, and 4 are shown in Figures 3A–C, which are based on the real measured load profile of community microgrids (MGs) in Lombok, Indonesia. Figure 3 shows that the load demand varies from about 200–550 kW from 0 h to 24th hour for node 2. In addition, the load valley is around noon. For node 3, the load peak appears at 18:00, reaching 430 kW for node 3, and the load valley is about 180 kW. For village 1, the load peak comes at 18–19:00, reaching 330 kW. These load profiles are obtained by transferring the practical 5-min loads into a yearly load profile using the DER-CAM. It can be seen the maximal load deviation among months is larger than 100 kW for each node. However, the basic load profiles

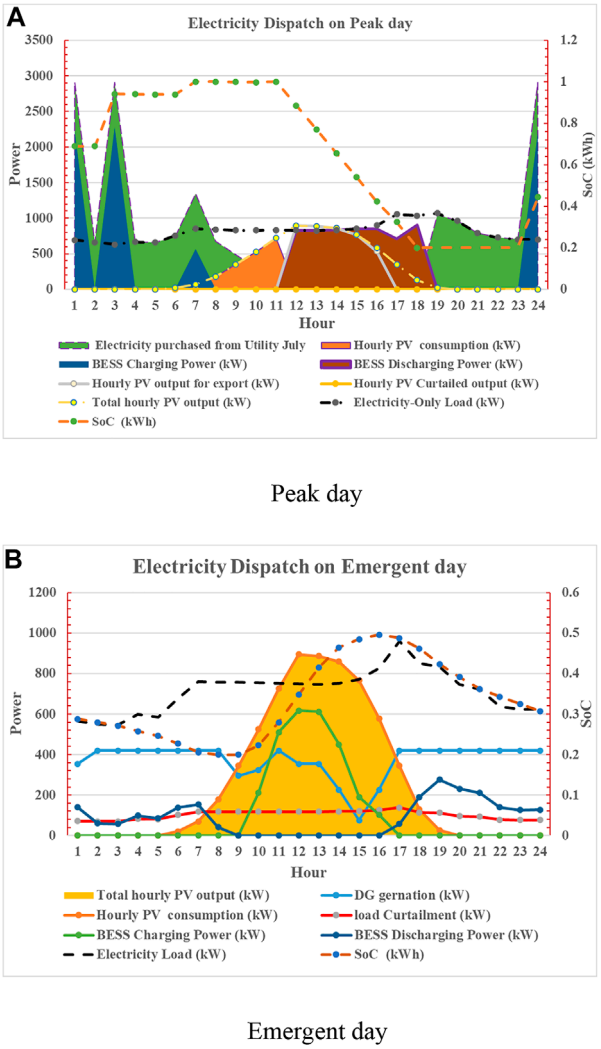

FIGURE 7
Electricity dispatch of the four-node community MG (July). **(A)** Peak day and **(B)** emergent day.

are similar because Indonesia's climate is almost entirely tropical, and the temperatures do not vary much from season to season.

The solar radiation data of Lombok (Indonesia) Island are obtained from the photovoltaic geographical information system. The solar radiation is shown in Figure 4A, from which it can be observed that the maximal power generated is about 0.68 kW/m^2. Generally, the PV power output is higher in summer days than in winter days. The electricity price of community microgrids, estimated by the real price in Indonesia, is shown in Figure 4B, where the peak price is 0.4 $/kWh and off-peak price is 0.11 $/kWh. The hours of Time of Use (ToU) rates for summer days are from 12:00 to 18:00 during a day. The PV power sale price is the same as the purchase price in the planning parameter setup.

4.2 System parameters

For the single-node case, the power flow equation is not considered; therefore, the corresponding constraints, such as current

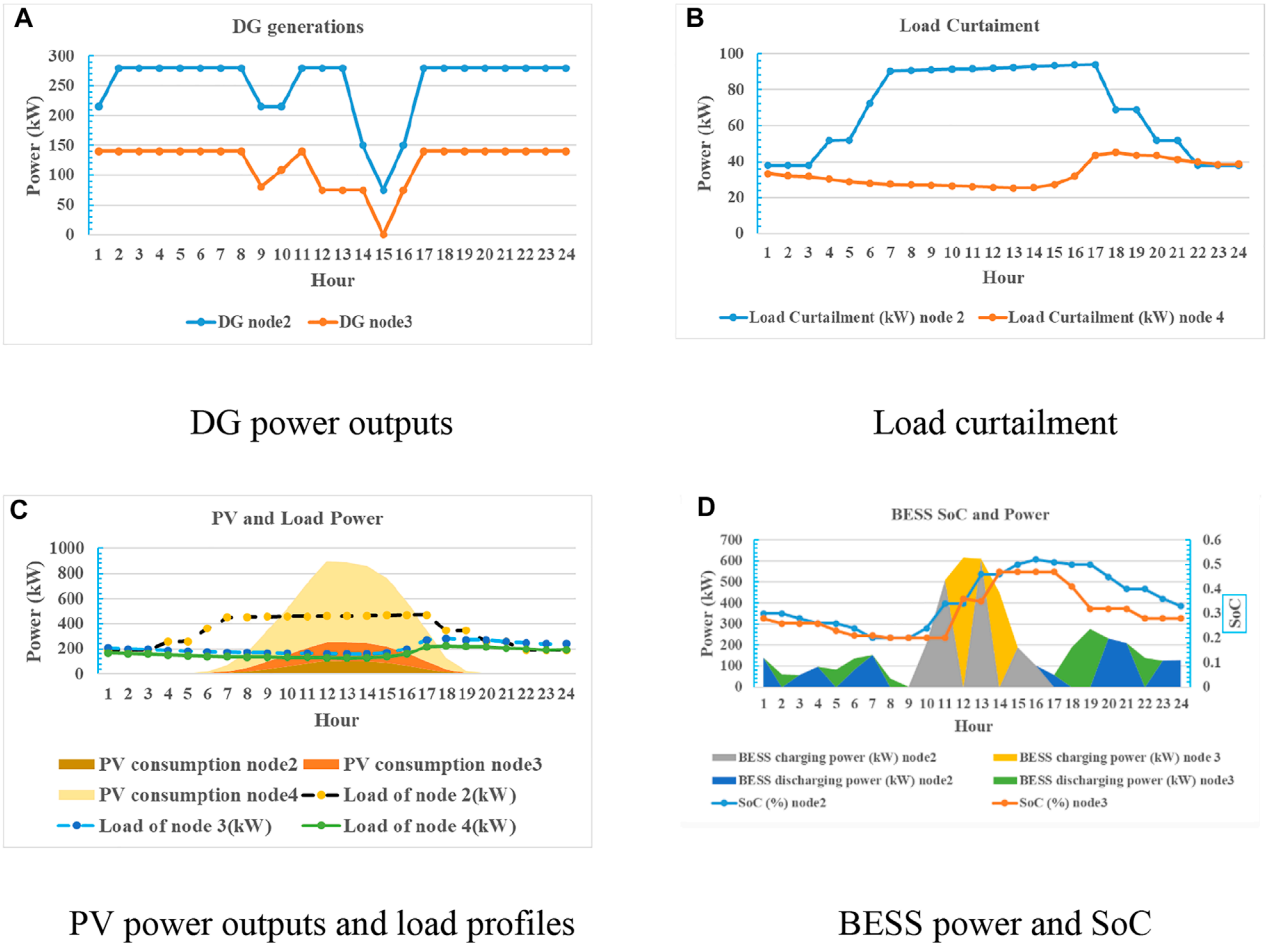

FIGURE 8
Electricity dispatch for each node in the four-node community MG. **(A)** DG power outputs, **(B)** load curtailment, **(C)** PV power outputs and load profiles, and **(D)** BESS power and SoC.

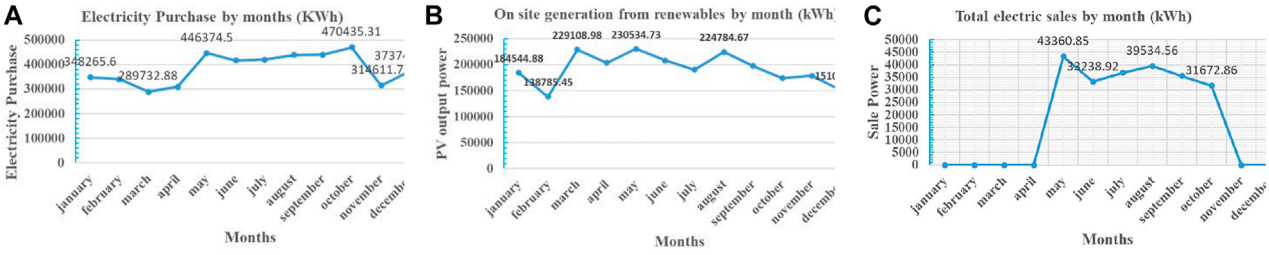

FIGURE 9
Electricity in the four-node MG. **(A)** Monthly electricity purchase from the utility; **(B)** monthly PV generation; **(C)** monthly electricity sales from PV generation.

constraints and voltage constraints, are neglected in the planning. However, for multiple-node microgrids, the power constraints need to be considered. The planning objectives contain cost minimization and CO_2 emission reduction with the same weights, namely, equal to 0.5. The discount rate is set as 3%, and the maximal payback period of microgrids is 20 years. The voltage level is 12 kV, and the maximal capacity of the transformer connected to the upper grid is set as 5 MVA.

The investment cost of PV systems includes fixed investment cost, variable cost, maintenance cost, and inverter cost. In this work, the fixed cost is 2,500 $, and the variable cost is 2,500 $/kW. The lifetime is assumed to be 30 years, and the maintenance cost is 0.005 $/(kW × month). The inverter cost is 500 $/kW-cap for an inverter with a capacity of 100 kW. The investment cost of the BESS includes the fixed cost, variable cost, maintenance cost, and inverter cost. The investment cost is estimated according to the following equation:

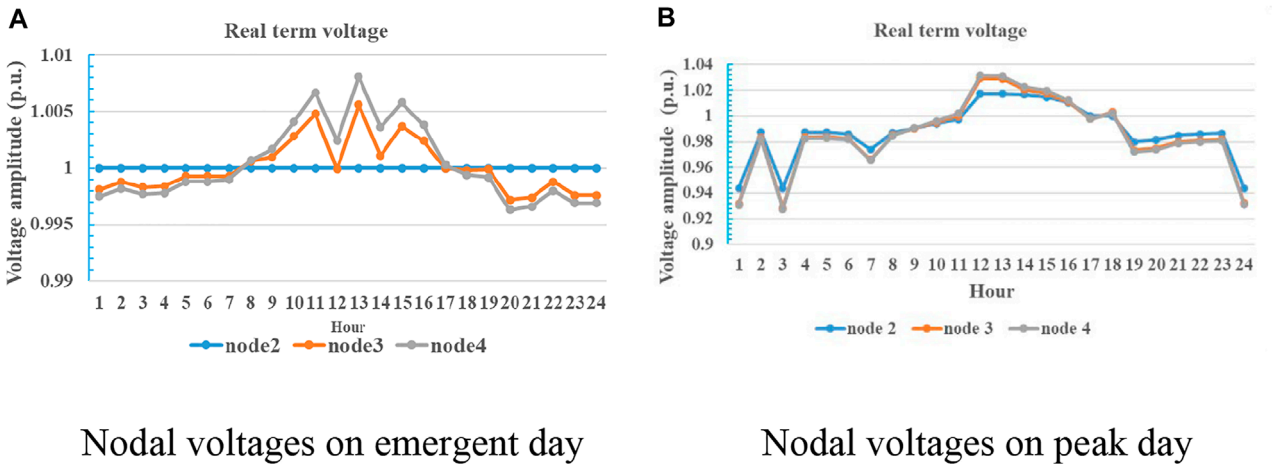

FIGURE 10
Nodal voltages on the emergent day. **(A)** Nodal voltages on the emergent day and **(B)** nodal voltages on the peak day.

Investment Cost = (FixedCost + VariableCost × Capacity) × Investment Decision. In this study, the fixed cost is set as 500 $, variable cost is set as 300 $/kW-cap, and variable maintenance cost is set as 0.005 $/(kW × month). The inverter cost of the BESS is set as 200 $/kW-cap for the 100 kVA capacity. The lifetime of the BESS is set as 15 years, while the lifetime of the inverter is 20 years. The battery degradation parameters are shown in Table 1. The cost of diesel generators includes the variable cost and maintenance cost. The variable cost is set as 5761.4074 $/kW. The variable maintenance cost is set as 0.0128 $/kWh, which is dependent on its energy production. Its maximal capacity is 75 kW, with efficiency 0.0238. The other two kinds of DGs are listed in Table 2. The NoXRate is 0.0001 kgNOx/kWh, where NOx emissions are resulted from fuel usage. Its maximum ramp up and ramp down rate is 0.5. The starting time is 20 min, and the time needed to ramp up the generation facility to full capacity is 10 min, which are default parameters in DER-CAM software (Phase, 2018; Heleno et al., 2017).

The utility outages contain scheduled outages for scheduled maintenance and unscheduled outages caused by natural disasters or faults. The scheduled outage is defined to occur on the peak day of June of each year, and its duration is 24 h. The unscheduled outage is assumed to occur on the weekdays of December for 24 h. There are three types of loads for load shedding. The first type is low critical loads, which can be cut down for 20% of total loads for 24 h with the cost 0.15 $/kWh. The second type is the middle critical load. In the planning part, middle critical and high critical loads are not chosen to be cut down. The costs of curtailing load are shown in Table 3.

5 Planning of multi-node networked microgrids

5.1 Costs and capacities

This case study focuses on the multi-node community MG, in which the topology constraints, namely, the power flow equations, are considered. In this case, the community MG has four nodes. Node 1 is Tanjung station, node 2 is Mina Hotel, node 3 is RSUD (hospital), and node 4 is a village nearby. The topology of this community MG is shown in Figure 5, Figure 5A shows the topology in the DER-CAM, and Figure 5B shows the geographical positions of various nodes.

This case study aims to investigate the capacities and locations of DER for the four-node community MG. The main procedure of this planning work is similar with that of the single-node community MG. The difference between the single-node MG and the multi-node MG planning is that in the multi-node MG planning, the power flow equations and the constraints of voltage and current magnitudes should be considered. During the planning, the N-1 contingency is also considered.

The utility outages for multi-node MG include scheduled outages for scheduled maintenance and unscheduled outages caused by natural disasters or faults. The scheduled outage is defined to occur on the weekdays of July of each year. Its duration is 24 h. In addition, the unscheduled outage occurs on the weekends of December for 24 h. There are three types of loads for load shedding in the DER-CAM. The first type is low critical loads, which can be cut down by 20% of the total consumption for 24 h and the cost is 0.15 $/kWh. The second type is the middle critical load. In the planning part, middle critical and high critical loads are not chosen to be cut down.

With the input data and system setup, the planning results can be obtained with the optimized capacities and locations of various energy sources, costs and revenues, and CO_2 emissions. Table 4 shows the costs of four-node community MG. With the installation of the PV, DG, and BESS, the total annual energy cost for the MG is 789 k$, which means that the MG earns money by selling energy to the utility each year. Compared with the original case (reference case), the total savings are 22.12%. The CO_2 emissions decreased to 1,420 tons per year, with a reduction rate of 25.25%.

The optimal placement and combination of technologies are shown in Figure 6A, where node 2 installs two kinds of DG with capacities being 130 and 150 kW, respectively, and one PV with 120 kW capacity, as well as a BESS with 4,539 kWh. For node 3,

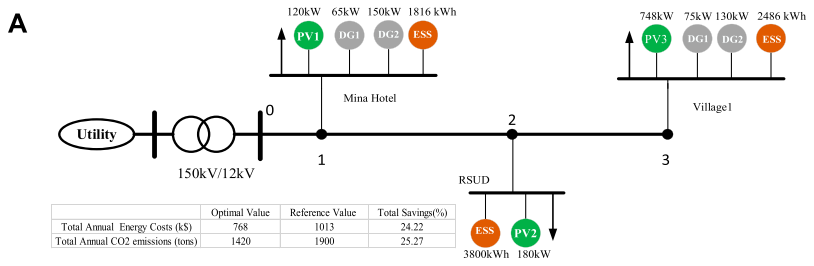

Sensitivity Analysis with Discrete Tech. Capital Cost variations (-10%)

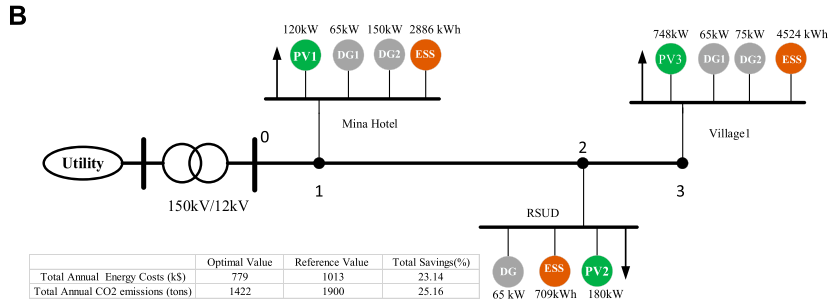

Sensitivity Analysis with Discrete Tech. Capital Cost variations (-5%)

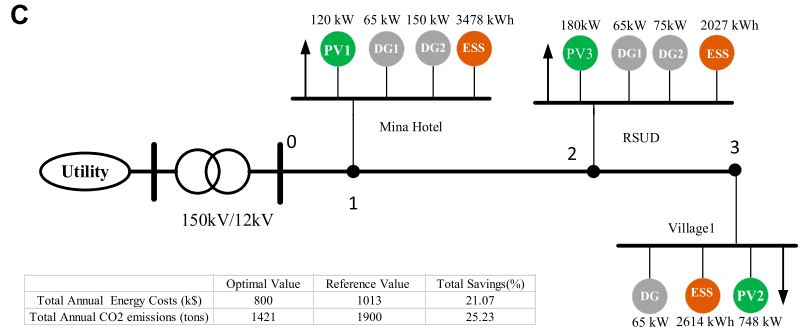

Sensitivity Analysis with Discrete Tech. Capital Cost variations (5%)

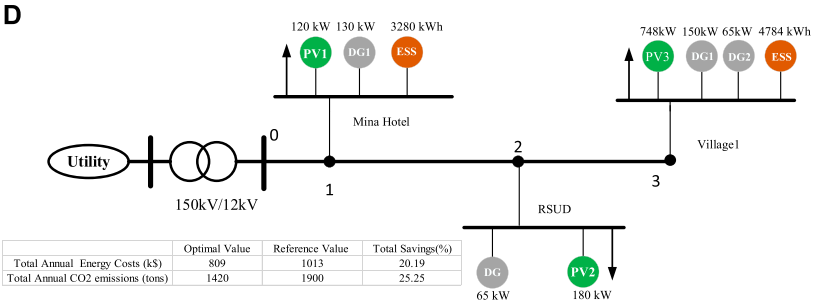

Sensitivity Analysis with Discrete Tech. Capital Cost variations (10%)

FIGURE 11
Sensitivity analysis with various interest rates. **(A)** Sensitivity analysis with discrete technology capital cost variations (–10%), **(B)** sensitivity analysis with discrete technology capital cost variations (–5%), **(C)** sensitivity analysis with discrete technology capital cost variations (5%), and **(D)** Sensitivity analysis with discrete technology capital cost variations (10%).

two DGs with capacities being 65 and 75 kW and 180 kW PV and 3,581 kWh BESS are installed, respectively. Meanwhile, for node 4, only a PV with capacity 748 kW is installed. In the planning, the area constraints for installing PV panels are considered for each node, which are, respectively, 800, 1,200, and 5,000 m^2. Therefore, node 2 connects only 120 kW PV. The capital and annualized investment costs of two kinds of DGs are shown in Figure 6B for various capacities.

5.2 Energy dispatch

The electricity dispatch in July of each year is obtained in Figure 7, where on a peak day, the surplus PV power is exported to the utility, as shown by a gray curve in Figure 7A. In addition, the BESS also discharges during the daylight, shown by dark red area, and during the nights, the BESS is charged by the utility, shown by blue areas. Because during the daylight (from 12:00 to 18:00), the utility price is using on-peak price, shown in Figure 4B, PV sells power to the utility to gain the revenue. In addition, the BESS discharges for local load consumption and during the night, when electricity price is low, the BESS purchases power from utility. During utility outages, the PV and BESS can also provide electricity to the local consumers, as shown in Figure 7B. At most 20% of low critical loads are curtailed in order to keep the system power balance during the utility outages, shown by a red curve.

For the electricity power interaction among nodes in July on the emergent day, the results are shown in Figure 8. From Figure 8A, it can be observed that the DGs at nodes 2 and 3 start generating power to the MG during the utility outages, where the maximal DG output power at nodes 2 and 3 is 280 and 130 kW, and the minimal output power at nodes 2 and 3 is 75 and 0 kW, respectively. The low critical loads at nodes 2 and 4 also curtail their demand during the outages. The maximal curtailed power of nodes 2 and 4 is 95 and 43 kW, respectively, shown in Figure 8B. The PV outputs and load demands are shown in Figure 8C, where PV power outputs are all consumed by local loads. The BESSs at nodes 2 and 3 provide power to the MG when the PV radiation is low (nights) and absorb power from the MG when the PV output power is high, which is shown in Figure 8D.

Figure 9A shows the electricity purchased from the utility during the normal operation, where the peak electricity purchase happens in October and that of valley electricity in March. The difference between peak and valley value is 180,703 kWh. In summer days, solar radiation is high such that the peak PV power is in May, reaching 230,534 kWh/month, while the valley PV power is in February in winter days, shown in Figure 9B. Accordingly, as shown in Figure 9C, during summer days, the PV sources sell power to the utility according to the ToU price illustrated in Figure 4.

The nodal voltages of community MG during the utility outages are shown in Figure 10A. With the power flow constraints, the nodal voltages are all varying in the normal range, i.e., [0.95 1.05] p.u., even with the fluctuation of PV power generation and outages. In the planning, node 2 becomes the slack bus providing voltage support. However, during the peak day, the nodal voltages are varying in the normal time, most of the time, except in conditions of heavy load demand. However, the nodal voltages are very close to the lower voltage limit. In the planning, only the active power dispatch is considered, and the voltage will be recovered into the normal range if reactive power dispatch is taken into account.

5.3 Sensitivity analysis

This section elaborates on the sensitivity analysis when different discrete capital costs are considered. As shown in Figure 11, the optimal operation costs vary from 768 to 800 k$, and the total annual CO_2 reduction emission costs vary from 1,420 to 1,422 tons with the variation of capital costs. In addition, the total cost saving is at least above 20% and CO_2 emission reduction is at least above 25%. Even with the variation of capital costs, the capacity of PV panels remains unchanged as 1,048 kW. However, the total DER capacity of each node varies due to different combinations of technologies. Interestingly, the total capacity of the BESS varies in a very small range, e.g., from 8,102 to 8,119 kWh. The total capacity of DG remains unchanged (420 kW) even with the variation of capital costs because the discrete technology is insensitive to the planning results.

6 Conclusion

This paper investigated the optimal planning and operation of community MGs with the RES and ESS for Lombok Island of Indonesia as a response to the rural electrification program. First, the optimization and constraints for MG planning are presented, which are integrated into the DER-CAM. This study also analyzes the economic benefits and environmental emissions of the optimal sizing and location of the RES and ESS within the MGs. The results of the analyses validate that the DER-CAM can provide the optimal capacities, type, location of various technologies, and optimal energy dispatch for multi-node MGs with optimized total annual costs and total annual CO_2 emissions. The planning results demonstrate that the MGs with the RES and ESS contribute to the rural electrification and energy transition of Indonesia, leading to over 100% electrification, 20% cost savings, and 25% CO_2 reduction, with interest rates varying from −10% to 10%.

Data availability statement

The original contributions presented in the study are included in the article/Supplementary Material, further inquiries can be directed to the corresponding author.

Author contributions

WK and YG conceived and designed the software simulations. WK and YG performed the simulations. FD, AP, JV, and JM analyzed the data. FD, EK, JV, and JM contributed to the analysis. WK and YG wrote the paper. All authors contributed to the article and approved the submitted version.

Funding

This work was supported by the Tech-IN project (Granted by Danish Ministry for foreign affairs and supported by Danida Fellowship Centre under grant #20-M06-AAU); www.energy.aau.dk/tech-in.

Conflict of interest

The authors declare that the research was conducted in the absence of any commercial or financial relationships that could be construed as a potential conflict of interest.

Publisher's note

References

Bahramara, S., Parsa Moghaddam, M., and Haghifam, M. R. (2016). Optimal planning of hybrid renewable energy systems using HOMER: A review. *Renew. Sust. Energ. Rev.* 62, 609–620. doi:10.1016/j.rser.2016.05.039

Borghei, M., and Ghassemi, M. (2021). Optimal planning of microgrids for resilient distribution networks. *Int. J. Electr. Power & Energy Syst.* 128 (2021), 106682. doi:10.1016/j.ijepes.2020.106682

Cao, X., Wang, J., Wang, J., and Zeng, B. (2019). A risk-averse conic model for networked microgrids planning with reconfiguration and reorganizations. *IEEE Trans. Smart Grid* 11 (1), 696–709. doi:10.1109/tsg.2019.2927833

Cardoso, G., Heleno, M., and DeForest, N. (2019). *Remote off-grid microgrid design support tool (ROMDST)-an optimal design support tool for remote, resilient, and reliable microgrids (Phase II, Final Report)*. Berkeley, CA (United States): Lawrence Berkeley National Lab.

Cardoso, G., Stadler, M., Mashayekh, S., and Hartvigsson, E. (2017). The impact of ancillary services in optimal DER investment decisions. *Energy130* 130, 99–112. doi:10.1016/j.energy.2017.04.124

Chu, S., Cui, Y., and Liu, N. (2017). The path towards sustainable energy. *Nat. Mater* 16, 16–22. doi:10.1038/nmat4834

ESCAP (2020). *Energy transition pathways for the 2030 agenda: SDG7 roadmap for Indonesia*. Bangkok, Thailand: United Nations Economic and Social Commission for Asia and the Pacific.

Hafez, O., and Bhattacharya, K. (2012). Optimal planning and design of a renewable energy based supply system for microgrids. *Renew. Energy* 45, 7–15. doi:10.1016/j.renene.2012.01.087

Heleno, M., et al. (2017). "Optimal sizing and placement of distributed generation: MILP vs PSO comparison in a real microgrid application," in Proceedings of the 19th International Conference on Intelligent System Application to Power Systems, San Antonio, TX, USA, September 2017.

Hittinger, E., Wiley, T., Kluza, J., and Whitacre, J. (2015). Evaluating the value of batteries in microgrid electricity systems using an improved Energy Systems Model. *Energy Convers. Manag.* 89, 458–472. doi:10.1016/j.enconman.2014.10.011

Iea, W., and Irena, U. N. S. D. (2021). *Tracking SDG 7: The energy progress report 2021*. Washington DC: World Bank, 234.

Jung, J., and Villaran, M. (2017). Optimal planning and design of hybrid renewable energy systems for microgrids. *Renew. Sustain. Energy Rev.* 75, 180–191. doi:10.1016/j.rser.2016.10.061

Khare, V., Nema, S., and Baredar, P. (2016). Solar–wind hybrid renewable energy system: A review. *Renew. Sustain. Energy Rev.* 58, 23–33. doi:10.1016/j.rser.2015.12.223

Lee, E. S., Gehbauer, C., Coffey, B. E., McNeil, A., Stadler, M., and Marnay, C. (2015). Integrated control of dynamic facades and distributed energy resources for energy cost minimization in commercial buildings. *Sol. Energy* 122, 1384–1397. doi:10.1016/j.solener.2015.11.003

Madathil Chalil, S., et al. (2017). Resilient off-grid microgrids: Capacity planning and N-1 security. *IEEE Trans. Smart Grid* 9 6, 6511–6521.

Madathil, S. C., Yamangil, E., Nagarajan, H., Barnes, A., Bent, R., Backhaus, S., et al. (2017). Resilient off-grid microgrids: Capacity planning and N-1 security. *IEEE Trans. Smart Grid* 9 (6), 6511–6521. doi:10.1109/TSG.2017.2715074

Martinez-Frias, J., Aceves, S. M., Ray Smith, J., and Brandt, H. (2008). A coal-fired power plant with zero-atmospheric emissions. *J. Eng. gas turbines power* 130 (2). doi:10.1115/1.2771255

Mashayekh, S., Stadler, M., Cardoso, G., and Heleno, M. (2017). A mixed integer linear programming approach for optimal DER portfolio, sizing, and placement in multi-energy microgrids. *Appl. Energy* 187, 154–168. doi:10.1016/j.apenergy.2016.11.020

Mashayekh, S., Stadler, M., Cardoso, G., Heleno, M., Madathil, S. C., Nagarajan, H., et al. (2018). Security-constrained design of isolated multi-energy microgrids. *IEEE Trans. Power Syst.* 33 (3), 2452–2462. doi:10.1109/TPWRS.2017.2748060

Mendes, G., Ioakimidis, C., and Ferrão, P. (2011). On the planning and analysis of integrated community energy systems: A review and survey of available tools. *Renew. Sustain. Energy Rev.* 15.9, 4836–4854. doi:10.1016/j.rser.2011.07.067

Mizani, S., and Amirnaser, Y. (2009). "Design and operation of a remote microgrid," in Proceedings of the 2009 35th Annual Conference of IEEE Industrial Electronics, Porto, Portugal, November 2009 (IEEE).

Phase, I. I. (2018). *Remote off-grid microgrid design support tool (ROMDST)-An optimal design support tool for remote, resilient, and reliable microgrids*.

PLN (2021). *Rencana usaha penyediaan tenaga Listrik (RUPTL) PT PLN (persero) 2021-2030*. Jakarta: RUPTL.

Prathapaneni, D. R., and Detroja, K. P. (2019). An integrated framework for optimal planning and operation schedule of microgrid under uncertainty. *Sustain. Energy, Grids Netw.* 19, 100232. doi:10.1016/j.segan.2019.100232

Schittekatte, T., Stadler, M., Cardoso, G., Mashayekh, S., and Sankar, N. (2016). The impact of short-term stochastic variability in solar irradiance on optimal microgrid design. *IEEE Trans. Smart Grid* 9 (3), 1647–1656. doi:10.1109/tsg.2016.2596709

Siddaiah, R., and Saini, R. P. (2016). A review on planning, configurations, modeling and optimization techniques of hybrid renewable energy systems for off grid applications. *Renew. Sustain. Energy Rev.* 58, 376–396. doi:10.1016/j.rser.2015.12.281

Stadler, M., Groissbock, M., Cardoso, G., and Marnay, C. (2014). Optimizing distributed energy resources and building retrofits with the strategic DER-CAModel. *Appl. Energy* 132, 557–567. doi:10.1016/j.apenergy.2014.07.041

Stadler, M., Cardoso, G., Mashayekh, S., and Sankar, N. (2016). The impact of short-term stochastic variability in solar irradiance on optimal microgrid design. *IEEE Trans. Smart Grid* 9 (3), 1647–1656.

Stadler, M., Kloess, M., Groissböck, M., Cardoso, G., Sharma, R., Bozchalui, M., et al. (2013). Electric storage in California's commercial buildings. *Appl. Energy* 104, 711–722. doi:10.1016/j.apenergy.2012.11.033

Wang, J., and Lu, X. (2020). Sustainable and resilient distribution systems with networked microgrids [point of view]. *Proc. IEEE* 108 (2), 238–241. doi:10.1109/jproc.2019.2963605

Wang, Y., Rousis, A. O., and Strbac, G. (2021). A three-level planning model for optimal sizing of networked microgrids considering a trade-off between resilience and cost. *IEEE Trans. Power Syst.* 36 (6), 5657–5669, Nov. doi:10.1109/TPWRS.2021.3076128

Wu, Q., Xue, F., Lu, S., Jiang, L., Huang, T., Wang, X., et al. (2023). Integrated network partitioning and DERs allocation for planning of Virtual Microgrids. *Electr. Power Syst. Res.* 216 (2023), 109024. doi:10.1016/j.epsr.2022.109024

frontiers | Frontiers in Energy Research

TYPE Original Research
PUBLISHED 20 July 2023
DOI 10.3389/fenrg.2023.1230878

OPEN ACCESS

EDITED BY
Mingfei Ban,
Northeast Forestry University, China

REVIEWED BY
Daniele Groppi,
Sapienza University of Rome, Italy
Hongxun Hui,
University of Macau, China

*CORRESPONDENCE
Jiaming Weng,
wrzx_5@sjtu.edu.cn

RECEIVED 29 May 2023
ACCEPTED 03 July 2023
PUBLISHED 20 July 2023

CITATION
Fan Q, Weng J and Liu D (2023), Low-carbon economic operation of integrated energy systems in consideration of demand-side management and carbon trading. *Front. Energy Res.* 11:1230878. doi: 10.3389/fenrg.2023.1230878

Low-carbon economic operation of integrated energy systems in consideration of demand-side management and carbon trading

Qiang Fan, Jiaming Weng* and Dong Liu

Key Laboratory of Control of Power Transmission and Conversion, Ministry of Education, School of Electronic Information and Electrical Engineering, Shanghai Jiao Tong University, Shanghai, China

Under the background of carbon emission abatement worldwide, carbon trading is becoming an important carbon financing policy to promote emission mitigation. Aiming at the emerging coupling among various energy sectors, this paper proposes a bi-level scheduling model to investigate the low-carbon operation of the electricity and natural gas integrated energy systems (IES). Firstly, an optimal energy flow model considering carbon trading is formulated at the upper level, in which carbon emission flow model is employed to track the carbon flows accompanying energy flows and identify the emission responsibility from the consumption-based perspective, and the locational marginal price is determined at the same time. Then at the lower level, a developed demand-side management strategy is introduced, which can manage demands in response to both the dynamic energy prices and the nodal carbon intensities, enabling the user side to participate in the joint energy and carbon trading. The bi-level model is solved iteratively and reaches an equilibrium. Finally, case studies based on the IEEE 39-bus system and the Belgium 20-node system illustrate the effectiveness of the proposed method in reducing carbon emissions and improving consumer surplus.

KEYWORDS

integrated energy system, carbon trading, demand-side management, carbon emission flow, bi-level optimization

1 Introduction

With the increasingly severe energy crisis and environmental problems, energy conservation and emission reduction have become the consensus of all countries for sustainable development. According to the statistics provided by the International Energy Agency (IEA), electricity and heat industry accounts for more than 40% of the global CO_2 emissions in 2021 (IEA, 2022). Therefore, developing low-carbon electricity is of great significance to the control of carbon emissions.

The emerging integrated energy system (IES), as a carrier of multi-energy coupling, has been recognized as an efficient method to promote the consumption of renewable energy and reduce carbon emissions. A lot of efforts have been made on the coordinated optimization and market operation of the electricity and natural gas IES at present. In literature (Jiang et al., 2022), a bi-level strategic bidding model was proposed to study the market behaviors of the gas-fired units in interdependent electricity and natural gas markets. In literature (Chen et al., 2020), the operational equilibria of electric and natural gas systems

was obtained under different levels of temporal and spatial granularity. A mixed-integer linear programming (MILP) approach was addressed to solve the security-constrained joint expansion planning problems of natural gas and electricity transmission systems in literature (Zhang et al., 2018). Besides the transmission level, the energy hub (EH), which integrates multiple energy sources at the distribution level, plays an important role in energy production, transmission, conversion, and storage (Geidl and Andersson, 2007). The modeling (Wang et al., 2019), planning (Huang et al., 2019), and operation (Paudyal et al., 2015) of IES with EHs have also attracted extensive attention. However, the natural gas flow equation is nonlinear and nonconvex, which will bring great challenges to solve the IES operation problem. In literature (Zhang et al., 2018), piecewise linearization method was applied to convert the Weymouth equation into the MILP form, but the solution accuracy and efficiency were affected by the number of 0–1 variables. A second-order cone (SOC) relaxation method was proposed in literature (Borraz-Sánchez et al., 2016) for model convexification, while the relaxation would cause an optimality gap due to the expansion of the feasible region. How to solve the natural gas flow equation accurately and efficiently still needs to be studied in IES research.

Meanwhile, when considering the low-carbon operation of IES, low-carbon factors can be embedded into the problems with emission constraints (Olsen et al., 2019; Gu et al., 2020) or objective functions including environmental costs (Li et al., 2018). Moreover, the rise of carbon emission trading provides a market solution for carbon abatement and regulation, in which the cap-and-trade scheme has been proven as one of the most effective mechanisms in real-world implementations such as Europe (EMBER, 2021) and China (Fang et al., 2019). In the process of carbon cap-and-trade scheme, the government issues a set amount of permits to companies that comprise a cap on allowed CO_2 emissions, and companies that surpass the cap are taxed, while companies that cut their emissions may sell or trade the unused credits. In this context, the coordination of carbon trading and energy trading has become a common concern. Existing research has been conducted on how to develop a joint energy and carbon market scheme. An IES co-trading market including electricity, natural gas, and carbon trading was proposed in literature (Sun et al., 2022), where an improved Multi-agent Deep Deterministic Policy Gradient algorithm was applied to achieve fair trade and entity privacy protection. Literature (Liu, 2022) analyzed the characteristics of the carbon-electricity integrated market and constructed a carbon-electricity integrated optimal bidding model for the virtual power plant (VPP) with the consideration of multiple uncertainties. To promote local decarbonization, a peer-to-peer (P2P) joint electricity and carbon trading model to co-optimize the energy and carbon permit transactions considering the trading preferences in the distribution network was proposed in literature (Lu et al., 2023), in which a carbon-aware distribution locational marginal pricing was formulated to guide the P2P transactions among prosumers.

However, the works above normally focus on the "observed" emission and attribute the emission responsibility to the generation side. But it is a fact that end-users create the need for the combustion of fossil fuels and are the underlying driving force of emissions, the intuitive generation-based settlement cannot clarify the emission responsibility of the demand side, which may result in uneven incentives (Wang et al., 2020). Therefore, it is important to track the carbon emission path and identify emission amount from the perspective of energy users. A demand-side management (DSM) approach aiming at carbon footprint control was proposed in literature (Pourakbari-Kasmaei et al., 2020), which was proven fairer and superior compared to existing policies. The concept of carbon emission flow (CEF) was introduced in literature (Kang et al., 2015), where CEF was regarded as a virtual attachment to the power flow and accumulated at the demand side. On this basis, the CEF model was extended to the multiple energy systems (MESs) in literature (Cheng et al., 2019). The low-carbon operation of MESs by coordinating the transmission-level and distribution-level via the energy-carbon integrated prices was studied in literature (Cheng et al., 2020), in which the carbon emissions of different energy systems are uniformly priced using the CEF model. Although the CEF model provides a more accurate method for carbon accounting and a fairer way for emission responsibility clarification, the literatures mentioned above have not involved user-side participation in the joint energy and carbon trading process.

Accordingly, this paper proposes a bi-level economic operation model for the electricity and natural gas IES with the consideration of DSM and carbon trading. The proposed method relies on CEF model to obtain the overall carbon flow distribution, and guides demand response through the nodal carbon intensities (NCIs) and the locational marginal prices (LMPs), realizing the IES low-carbon economic dispatch with the participation of user side. The main contributions are summarized as follows.

1) The carbon-constrained locational electricity marginal price (LMEP) and locational marginal gas price (LMGP) are formulated to describe the impacts of carbon trading scheme to the demand side, where the sequential cone programming (SCP) method is applied to guarantee the strictness of the relaxation of natural gas flow equation.
2) A developed demand response model is introduced. Our model can manage energy users to adjust their demands by means of transfer or substitution in response to both the carbon emission intensities and the locational marginal prices.
3) A bi-level scheduling model is proposed to investigate the low-carbon economic operation of the IES. An optimal energy flow model aiming at minimizing the negative social welfare considering carbon trading is formulated at the upper level, and demands on the user side are managed to maximize the consumer surplus at the lower level. The two levels interact iteratively to reach an equilibrium.

The rest of this paper is organized as follows. Section 2 provides the formulations of the proposed model. The linearization method and iterative procedure are presented in Section 3. Section 4 provides case study results based on an actual IES. Finally, conclusions are drawn in Section 5.

2 Model formulations

2.1 Problem statement

Before building the mathematical model, we need to make the following assumptions:

1) Since the carbon emissions in the electricity network are mainly related to active power and rarely affected by reactive power, both power flow and carbon flow analyses of the electricity network in this paper use the DC power flow model, and carbon and network losses are ignored.
2) A simplified steady-state gas flow model without considering line-pack is adopted in this paper. The power system and natural gas system are coupled via gas-turbine units at the transmission level.
3) The electricity and gas supply and consumption are paid at LMEPs and LMGPs, which are determined by the independent system operator (ISO) and natural gas market operator (GMO) in the market clearing process, respectively.
4) Carbon trading exists not only on the generation side but also on the demand side. Energy users calculate their carbon emissions via the CEF model, and the carbon emission allowances for users are pre-determined.

On this basis, the proposed framework can be modeled as a hierarchical problem which contains two levels, as shown in Figure 1. The upper level is formulated as an optimal power flow problem to minimize the negative social welfare, including the power generation cost and the carbon trading cost at the generation side. Meanwhile, the carbon emission intensities of each bus in the IES and LMPs can be obtained at the upper level and transmitted to the lower level. At the lower level, energy users make a response to the indicators passed from the upper level to maximize their consumer surplus. In this process, energy users would be motivated to cut demands with high carbon emission intensities to get benefits in the carbon trading market at the demand side. Afterward, the updated electricity and gas demands are sent back to the upper level to reschedule the power output. This bi-level interaction procedure iterates until equilibrium is reached.

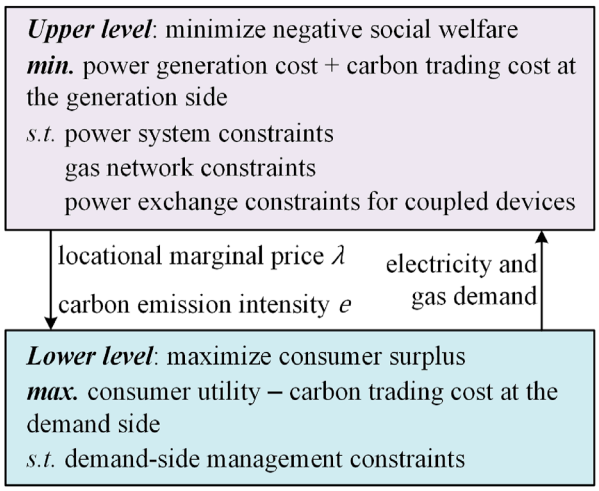

FIGURE 1
The framework of the proposed bi-level model.

2.2 Carbon emission model

Although CO_2 is directly emitted by generators, consumers are the main driving force of emissions due to energy use. Clarification of the emission responsibility is essential to mitigate carbon emissions. The CEF model can be used to trace the carbon emissions from the generation side to the demand side. In the CEF model, carbon emission intensity is one of the key indicators, which denotes the accompanying carbon emissions per unit of energy flow. In this paper, nodal carbon emission intensity (NCI) and branch carbon emission intensity (BCI) are mainly considered.

In the electricity network, for a given node n, its NCI can be represented as,

$$e_{n,t}^{EN} = \frac{\sum_{k:(k,n)\in\Omega_n^{EN+}} \left|f_{kn,t}\right| \cdot \rho_{kn,t}^{line} + \sum_{i\in\Omega_n^{TU}\cup\Omega_n^{GT}} P_{Gi,t} \cdot e_{Gi}}{\sum_{k:(k,n)\in\Omega_n^{EN+}} \left|f_{kn,t}\right| + \sum_{i\in\Omega_n^{TU}\cup\Omega_n^{GT}} P_{Gi,t}} \tag{1}$$

where Ω_n^{EN+}, Ω_n^{TU}, and Ω_n^{GT} denote the set of transmission lines that inject power into node n, the set of coal-fired thermal units connected to node n, and the set of gas-turbine units connected to node n, respectively. $f_{kn,t}$ and $\rho_{kn,t}^{line}$ are the power flow and the BCI of transmission line kn, respectively. $P_{Gi,t}$ and e_{Gi} are the injected power and the carbon emission intensity of generator i, respectively.

And the BCI of the transmission line kn can be expressed as,

$$\rho_{kn,t}^{line} = \begin{cases} e_{k,t}^{EN}, if\, f_{kn,t} \geq 0 \\ e_{n,t}^{EN}, if\, f_{kn,t} < 0 \end{cases} \tag{2}$$

Based on the results of NCI and BCI, the emission accounting can be implemented in a fairer way. Specifically, for the supply side, the carbon emission amount $E_{Gi,t}$ of generator i can be calculated as follows,

$$E_{Gi,t} = P_{Gi,t} \cdot e_{Gi} \cdot \Delta t, \forall i \in \Omega_n^{TU} \cup \Omega_n^{GT}, t \tag{3}$$

where Δt is the time interval. Note here we treat e_{Gi} as a time-independent known parameter since for a single generator, its carbon emission intensity, which is also known as the generation carbon intensity (GCI), can be determined by the carbon emission factor of fuel and its fuel consumption rate, and we consider it to be an inherent generator parameter similar to the generation cost coefficient (i.e. a, b, c).

For the demand side, the "virtual" carbon emission amount $E_{Dn,t}$ due to the nodal power consumption $P_{Dn,t}$ can be obtained in the same way,

$$E_{Dn,t} = P_{Dn,t} \cdot e_{n,t}^{EN} \cdot \Delta t, \forall n \in \Omega_D^{EN}, t \tag{4}$$

where Ω_D^{EN} is the set of demand buses in the electricity network.

Similarly, for the gas network, the NCI of a node m depends on the injected gas flow and the connected gas source. Mathematically,

$$e_{m,t}^{GN} = \frac{\sum_{b:(b,m)\in\Omega_m^{GN+}} \left|w_{bm,t}\right| \cdot \rho_{bm,t}^{pipe} + \sum_{j\in\Omega_m^{GW}} g_{j,t} \cdot e_j}{\sum_{b:(b,m)\in\Omega_m^{GN+}} \left|w_{bm,t}\right| + \sum_{j\in\Omega_m^{GW}} g_{j,t}} \tag{5}$$

$$\rho_{bm,t}^{pipe} = \begin{cases} e_{b,t}^{GN}, if\, w_{bm,t} \geq 0 \\ e_{m,t}^{GN}, if\, w_{bm,t} < 0 \end{cases} \tag{6}$$

where Ω_m^{GN+} and Ω_m^{GW} denote the set of gas pipelines that inject natural gas into node m and the set of gas sources connected to

node m, respectively. $w_{bm,t}$ and $\rho_{bm,t}^{pipe}$ are the gas flow and the BCI of gas pipeline bm, respectively. $g_{j,t}$ and e_j are respectively the injected natural gas and the carbon emission intensity of gas source j, where e_j equals the emission factor of natural gas as methane contains carbon. The typical value of e_j is 0.20tCO$_2$/(MWh) (Cheng et al., 2019).

2.3 Upper-level model

The upper level is formulated as an objective function that minimizes the negative social welfare in the energy market and the carbon trading market, which can be presented as,

$$min\sum_t\left(\sum_{i\in\Omega^{TU}}C(P_{Gi,t})+\sum_{j\in\Omega^{GW}}\gamma_{j,t}\cdot g_{j,t}+C_{car}\right) \tag{7}$$

$$C(P_{Gi,t})=a_i\cdot(P_{Gi,t})^2+b_i\cdot P_{Gi,t}+c_i,\forall i\in\Omega^{TU},t \tag{8}$$

The first term in (7) denotes the generation cost of coal-fired thermal units i, which is a quadratic function of the electricity production $P_{Gi,t}$ as in (8) and can be piecewise linearized. The second term in (7) denotes the natural gas production cost of gas source j, with the production price $\gamma_{j,t}$. The third term in (7) denotes the carbon trading cost, specifically,

$$C_{car}=\kappa\cdot\left(\sum_{i\in\Omega^{TU}\cup\Omega^{GT}}\left(E_{Gi,t}-E_{Gi}^{cap}\right)+\sum_{j\in\Omega^{GW}}\left(E_{Gj,t}-E_{Gj}^{cap}\right)\right) \tag{9}$$

where κ denotes the carbon trading price, E_{Gi}^{cap} and E_{Gj}^{cap} denote the allocated carbon allowances of generator i and gas source j, respectively.

2.3.1 Power system constraints

$$\sum_{i\in\Omega_n^{TU}\cup\Omega_n^{GT}}P_{Gi,t}+\sum_{r\in\Omega_n^{WG}}P_{r,t}^{WG}+\sum_{k:(k,n)\in\Omega_n^{EN}}f_{kn,t}-P_{Dn,t}=0,\forall n\in\Omega^{EN},t:\lambda_{n,t}^{EN} \tag{10}$$

$$-F_{kn}^{max}\le f_{kn,t}=(\theta_{k,t}-\theta_{n,t})/x_{kn}\le F_{kn}^{max},\forall(k,n)\in\Omega^{EN},t \tag{11}$$

$$P_{Gi}^{min}\le P_{Gi,t}\le P_{Gi}^{max},\forall i\in\Omega^{TU}\cup\Omega^{GT},t \tag{12}$$

$$\begin{cases}P_{Gi,t}-P_{Gi,t-1}\le R_{Gi}^{up},if P_{Gi,t}\ge P_{Gi,t-1}\\P_{Gi,t-1}-P_{Gi,t}\le R_{Gi}^{down},if P_{Gi,t-1}\ge P_{Gi,t}\end{cases},\forall i\in\Omega^{TU}\cup\Omega^{GT},t \tag{13}$$

Where Ω^{EN} denotes the set of buses in electricity network, Ω_n^{WG} denotes the set of renewable energy sources connected to node n, and its power output is $P_{r,t}^{WG}$. x_{kn} denotes the impedance of transmission line kn. $\theta_{k,t}$ and $\theta_{n,t}$ are the nodal phase angle of the two end nodes of line kn at time t. F_{kn}^{max} is the transmission capacity of line kn. P_{Gi}^{min} and P_{Gi}^{max} are the minimum and maximum power limits of generator i. R_{Gi}^{up} and R_{Gi}^{down} are the ramp-up and ramp-down limits of generator i, respectively.

Constraint (10) guarantees the power balance at each bus of the electricity network. Constraint (11) enforces the transmission capacity limits. Constraints about generators are imposed in (12), (13), which are generation limits and ramping up/down limits respectively.

2.3.2 Gas system constraints

$$\sum_{j\in\Omega_m^{GW}}g_{j,t}+\sum_{b:(b,m)\in\Omega_m^{GN}}w_{bm,t}-Q_{Dm,t}-\sum_{i\in\Omega_m^{GT}}Q_{i,t}^{GT}-\sum_{s\in\Omega_m^{com}}Q_{s,t}^{com}=0,\forall m\in\Omega^{GN},t:\lambda_{m,t}^{GN} \tag{14}$$

$$Q_{i,t}^{GT}=\alpha_i+\beta_iP_{Gi,t}+\gamma_i(P_{Gi,t})^2,\forall i\in\Omega^{GT},t \tag{15}$$

$$g_j^{min}\le g_{j,t}\le g_j^{max},\forall j\in\Omega^{GW},t \tag{16}$$

$$w_{bm,t}=C_{bm}sgn(\delta_{b,t},\delta_{m,t})\sqrt{\left|\delta_{b,t}^2-\delta_{m,t}^2\right|},\forall(b,m)\in\Omega^{GN},t \tag{17}$$

$$-w_{bm}^{max}\le w_{bm,t}\le w_{bm}^{max},\forall(b,m)\in\Omega^{GN},t \tag{18}$$

$$\delta_m^{min}\le\delta_{m,t}\le\delta_m^{max},\forall m\in\Omega^{GN},t \tag{19}$$

$$Q_{s,t}^{com}=B_sw_{s,t}^{com}\left((\delta_{b,t}/\delta_{m,t})^{Z_s}-1\right) \tag{20}$$

Where Ω^{GN} denotes the set of nodes in gas network, Ω_m^{GT} and Ω_m^{com} denote the set of gas-turbine units and compressors connected to node m. Constraint (14) guarantees the nodal gas balance, where $Q_{Dm,t}$ is the gas demand at node m, $Q_{i,t}^{GT}$ is the natural gas consumption of gas-turbine units i, which can be expressed as the quadratic function of $P_{Gi,t}$ as in (15). $Q_{s,t}^{com}$ is the gas flow consumed by compressor s, which is shown in (20), where B_s and Z_s are constants related to the temperature and efficiency of compressor s, $w_{s,t}^{com}$ is the inflow gas of compressor s. g_j^{min} and g_j^{max} are the minimum and maximum production limits of gas source j, respectively. Constraint (17) applies the Weymouth equation to calculate the pipeline gas flow (Zlotnik et al., 2017), where $w_{bm,t}$ is determined by the pressure difference between the two end nodes b and m. C_{bm} is a constant parameter related to the physical characteristics of pipeline bm. $\delta_{b,t}$ and $\delta_{m,t}$ are the pressure of node b and node m. The sign function $sgn(\cdot)$ indicates the gas flow direction, i.e., $sgn(\delta_{b,t},\delta_{m,t})=1$ when $\delta_{b,t}\ge\delta_{m,t}$ and -1 otherwise. Constraint (18) is the gas flow constraint of pipelines where w_{bm}^{max} is the capacity limit of pipeline bm. Constraint (19) enforces the nodal pressure limits for the gas network, where δ_m^{min} and δ_m^{max} are the minimum and maximum bounds of the nodal pressure, respectively.

2.4 Lower-level model

After running the optimal energy flow at the upper level, the NCI and LMP of each node can be obtained, where the LMEP and LMGP are equal to the dual variables of the energy pricing model, i.e., $\lambda_{n,t}^{EN}$ and $\lambda_{m,t}^{GN}$. Then at the lower level, energy users would respond to these two indicators. In this paper, we assume that users can be divided into traditional users and energy hubs. Traditional users have a fixed energy consumption form, and their demand response is normally price-based, that is, users spontaneously transfer their energy consumption periods according to the price signals. While energy hubs can choose different forms of energy to meet the demand of end-users with the same quality. This kind of substitution between electricity and natural gas can help improve the flexibility of the system effectively. Note that since there is no load shedding, demand response compensation for users is not considered in this paper. On this premise, the lower level can be formulated

to maximize the end users' surplus, which can be expressed as,

$$max \sum_t \sum_{n\in\Omega_D^{EN}} \left(U\left(P'_{Dn,t}\right) - \lambda_{n,t}^{EN} P'_{Dn,t} - \kappa\left(E'_{Dn,t} - E_{Dn}^{cap}\right)\right) + \sum_t \sum_{m\in\Omega_D^{GN}} \left(U\left(Q'_{Dm,t}\right) - \lambda_{m,t}^{GN} Q'_{Dm,t} - \kappa\left(E'_{Dm,t} - E_{Dm}^{cap}\right)\right) \quad (21)$$

$$P'_{Dn,t} = P_{Dn,t} + \Delta P_{Dn,t}^{tran} + \Delta P_{Dn,t}^{sub} \quad (22)$$

$$Q'_{Dm,t} = Q_{Dm,t} + \Delta Q_{Dm,t}^{tran} + \Delta Q_{Dm,t}^{sub} \quad (23)$$

Where $P'_{Dn,t}$ and $Q'_{Dm,t}$ are respectively the electricity load and gas load after demand response, and they can be expressed as in (22) and (23), in which superscripts "tran" and "sub" represent the demand response amount for transfer and substitution respectively. E_{Dn}^{cap} and E_{Dm}^{cap} denote the carbon allowances of the demand.

Function $U(\cdot)$ denotes the consumer utility which describes the satisfaction of consumers' consumption of electricity and natural gas, in this paper, we use a piecewise function to model this relationship. In the first step, consumer utility grows with the increase of energy consumption, but the uptrend gradually slows down. In the second step, consumer utility reaches the maximum and increasing energy consumption does not make a change. Take the electricity consumers as example, the overall utility function can be formulated as,

$$U\left(P_{Dn,t}\right) = \begin{cases} k_1 P_{Dn,t} - k_2 (P_{Dn,t})^2, P_{Dn,t} < k_1/2k_2 \\ (k_1)^2/4k_2, P_{Dn,t} \geq k_1/2k_2 \end{cases} \quad (24)$$

where k_1 and k_2 are coefficients of the utility function.

The objective function (21) is subjected to

$$\begin{cases} \sum_t \Delta P_{Dn,t}^{tran} = 0, -\Delta P_{Dn,t}^{tran,max} \leq \Delta P_{Dn,t}^{tran} \leq \Delta P_{Dn,t}^{tran,max}, \forall n \in \Omega_D^{EN}, t \\ \sum_t \Delta Q_{Dm,t}^{tran} = 0, -Q_{Dm,t}^{tran,max} \leq \Delta Q_{Dm,t}^{tran} \leq Q_{Dm,t}^{tran,max}, \forall m \in \Omega_D^{GN}, t \end{cases} \quad (25)$$

$$\begin{cases} \Delta P_{Dn,t}^{sub} = -\varphi \Delta Q_{Dm,t}^{sub} \\ \Delta P_{Dn,t}^{sub,min} \leq \Delta P_{Dn,t}^{sub} \leq \Delta P_{Dn,t}^{sub,max} \\ \Delta Q_{Dm,t}^{sub,min} \leq \Delta Q_{Dm,t}^{sub} \leq \Delta Q_{Dm,t}^{sub,max} \end{cases} \quad (26)$$

Constraint (25) indicates that the total amount of transferable demand remains unchanged in a scheduling cycle. Constraint (26) shows the substitution relationship between electricity and gas demand, where φ is the energy conversion coefficient, here we adopt $\varphi = 0.06MW/kcf\left(1kcf = 28.317m^3\right)$. Other expressions in (25) and (26) set the upper and lower bounds on the demand response amount.

3 Solution method

3.1 Model linearization

Nonlinear constraints (15) and (17) make the optimal energy flow model at the upper level nonconvex and hard to solve. SOC reformulation is an effective method for convexification, however, there may be optimality gap since the feasible region of the original problem will be expanded during the reformulation process.

Specifically, constraint (15) can be directly converted into the following SOC form, which is always tight and there is no need for relaxation gap detection because unnecessary gas consumption will increase operating costs and carbon emission costs.

$$Q_{i,t}^{GT} \geq \alpha_i + \beta_i P_{Gi,t} + \gamma_i (P_{Gi,t})^2, \forall i \in \Omega^{GT}, t \quad (27)$$

For pipeline flow constraint (17), it can be firstly converted into a mixed-integer nonlinear programming (MINLP) form as follows,

$$\left(I_{bm}^{+} - I_{bm}^{-}\right)\left(\pi_{b,t} - \pi_{m,t}\right) = \left(1/C_{bm}\right)^2 \left(w_{bm,t}\right)^2 \quad (28)$$

$$-\left(1 - I_{bm}^{+}\right) w_{bm}^{max} \leq w_{bm,t} \leq \left(1 - I_{bm}^{-}\right) w_{bm}^{max} \quad (29)$$

$$I_{bm}^{+} + I_{bm}^{-} = 1 \quad (30)$$

$$\pi_m^{min} \leq \pi_m \leq \pi_m^{max} \quad (31)$$

where $\pi_{b,t}$ and $\pi_{m,t}$ denote the squared nodal pressure, binary variables I_{bm}^{+} and I_{bm}^{-} indicate the gas flow direction in pipeline bm. Further, (28) can be relaxed and transformed into a mixed-integer second-order cone programming (MISOCP) problem,

$$Y_{bm,t} \geq \left(1/C_{bm}\right)^2 \left(w_{bm,t}\right)^2 \quad (32)$$

$$Y_{bm,t} \geq \pi_{m,t} - \pi_{b,t} + \left(I_{bm}^{+} - I_{bm}^{-} + 1\right)\left(\pi_b^{min} - \pi_m^{max}\right) \quad (33)$$

$$Y_{bm,t} \geq \pi_{b,t} - \pi_{m,t} + \left(I_{bm}^{+} - I_{bm}^{-} - 1\right)\left(\pi_b^{max} - \pi_m^{min}\right) \quad (34)$$

$$Y_{bm,t} \leq \pi_{m,t} - \pi_{b,t} + \left(I_{bm}^{+} - I_{bm}^{-} + 1\right)\left(\pi_b^{max} - \pi_m^{min}\right) \quad (35)$$

$$Y_{bm,t} \leq \pi_{b,t} - \pi_{m,t} + \left(I_{bm}^{+} - I_{bm}^{-} - 1\right)\left(\pi_b^{min} - \pi_m^{max}\right) \quad (36)$$

where $Y_{bm,t}$ is the auxiliary variable for SOC relaxation. Note that constraints (32-36) are equivalent to primal constraint (28) only when (32) is tight. Therefore, the relaxation process causes a relaxation gap, making the optimized solution infeasible to the primal model. To this end, a concave constraint (37) is firstly introduced to ensure (32) is tight, then the SCP method (Yan et al., 2021) is applied here to solve the MISOCP with concave constraints. The detailed steps are as follows.

$$Y_{bm,t} - \left(1/C_{bm}\right)^2 \left(w_{bm,t}\right)^2 \leq 0 \quad (37)$$

Step 1: Parameter initialization. Set gas flow starting value $w_{bm,t}^0$, penalty factor χ^0, maximum penalty factor χ^{max}, growth factor $\nu > 1$, SCP residuals tolerances ε^z, ε^s, and iteration index $k = 1$.

Step 2: Introduce non-negative auxiliary variables $s_{bm,t}^k$ and linearize (37) into (38) using the first-order Taylor expansion with respect to $w_{bm,t}^{k-1}$ obtained in the last iteration,

$$Y_{bm,t}^k - \left(1/C_{bm}\right)^2 \left[\left(w_{bm,t}^{k-1}\right)^2 + 2 w_{bm,t}^{k-1} \cdot \left(w_{bm,t}^k - w_{bm,t}^{k-1}\right)\right] \leq s_{bm,t}^k \quad (38)$$

Step 3: Convert the primal upper-level nonlinear nonconvex problem into the following MISOCP problem,

$$\begin{cases} min\, z^k = min\,(7) + \sum_{bm,t} \chi^k \cdot s^k_{bm,t} \\ s.t.(1)-(3),(5)-(6),(8)-(14),(16), \\ (18)-(20),(27),(29)-(36),(38) \end{cases} \tag{39}$$

Step 4: Calculate the SCP residuals and check if they are within the tolerances,

$$\begin{cases} gap^z = z^k - z^{k-1} \le \varepsilon^z \\ gap^s = \sum s^k_{bm,t} \le \varepsilon^s \end{cases} \tag{40}$$

If (40) is satisfied, then terminate the iteration. Otherwise, update penalty factor χ^k by

$$\chi^k = min\left(v\chi^{k-1}, \chi^{max}\right) \tag{41}$$

Step 5: Update $k = k + 1$, and repeat Step 2 to Step 4 until (40) is satisfied, that is, convergence.

3.2 Bi-level interaction procedure

In the proposed model, the upper level and lower level interact and iteratively optimize to reach an equilibrium. At the upper level, both the nodal carbon intensities and the energy prices are decided with fixed demand amount. At the lower level, the nodal carbon intensities and the energy prices are used as parameters to update the demand amount. These demands are then transferred to the upper level for the next iteration. From the game theoretical point of view, it can be regarded as a single-leader multi-follower Stackelberg game. The bi-level interaction terminates until the convergence criteria are met, i.e.,

$$\begin{cases} \left|P^{(s)}_{Dn,t} - P^{(s-1)}_{Dn,t}\right| / P^{(s)}_{Dn,t} \le \xi, \forall n \in \Omega^{EN}_D, t \\ \left|Q^{(s)}_{Dm,t} - Q^{(s-1)}_{Dm,t}\right| / Q^{(s)}_{Dm,t} \le \xi, \forall m \in \Omega^{GN}_D, t \end{cases} \tag{42}$$

where ξ is the tolerance and s is the bi-level iteration index. The flowchart of the bi-level interaction procedure is shown inFigure 2.

4 Case studies

4.1 System description

The proposed method is tested on an IES consisting of a modified IEEE 39-bus system and a modified Belgian 20-node natural gas system, as shown in Figure 3. The detailed network parameters can be found in (Jiang et al., 2018). The system includes eleven generators (five coal-fired thermal units, three gas-turbine units, two hydro plants with total capacity of 75MW, and one wind farm), four gas wells, and two compressors. The parameters of these facilities are provided in Tables 1–4. Nodes 1, 9, and 14 of the natural gas network are connected to buses 26, 32, and 36 of the electricity network via gas-turbine units, respectively. In addition, the carbon trading price is set as 30$/ton, the carbon emission allowances per unit of active power output is set as 0.648tCO_2/(MWh). The coefficients of utility function are adopted as $k_1 = 2000$/(MWh) and $k_2 = 10$/(MWh)^2. SCP parameters are shown in Table 5. The 24-h electricity load, gas load, and wind power output profiles are shown in Figure 4. The proposed bi-level model is verified using the following three cases:

Case 1: Traditional power scheduling in the IES without carbon trading and DSM.

Case 2: Power scheduling considering carbon trading but without demand response on the user side.

Case 3: Proposed bi-level scheduling model with carbon trading policy and DSM.

4.2 Results of carbon emission intensity and LMP

In this paper, we mainly focus on the power scheduling of the electricity system. The NCIs of the 39 buses in the electricity network under two typical hours, peak hour and valley hour, are illustrated in Figure 5.

It can be observed that the average value of carbon emission intensities in peak hour is higher than those in valley hour. It is mainly because, in valley hour, wind power output is larger, and clean energy accounts for a higher proportion in the system, reducing the NCIs at the overall level. In both typical hours, Case 1 has the highest carbon intensities, followed by Case 2 and Case 3. This indicates the proposed carbon trading and DSM strategies can effectively reduce the carbon emission intensities. It should be noted that there are nodes with zero carbon intensities in the system, such as buses 35, 37 in peak hour and buses 1, 9, 39 in valley hour. This is because that they are either directly connected to zero-carbon units or their demands can be fully met by clean energy.

In peak hour, the carbon intensities in Case 2 are generally lower than those of Case 1. However, several buses, such as 21, 22, 23, 25, and 26, have higher carbon intensities than Case 1. This is due to the carbon trading in Case 2, which forces the coal-fired thermal units to reduce their output and turn to gas-turbine units with lower carbon emission intensities for power supply. As a result, although the overall carbon intensities of the system decrease, the carbon intensities of the buses near gas-turbine units increase. Compared with Case 2, the NCIs in Case 3 decrease, in which buses originally with higher carbon emissions have greater changes, like the carbon intensity of bus 8 decreases from 0.73 to 0.66. This is because the buses with higher carbon emissions would have larger adjustment of energy users' demands through DSM, making the carbon intensity curve smoother. In valley hour, the wind power is more active, resulting in the carbon intensities of nearby buses (bus 1 and 9) remain zero in all three cases. For bus 22, due to the limited capacity of hydro power, the output increase of gas-turbine unit at bus 36 in Case 2 would change the power flow direction between bus 22 and bus 23, and there would be "carbon embedded" power flow injected to bus 22, thus improving the carbon intensity from 0 in Case 1 to 0.2 in Case 2.

The dynamic electricity prices of bus 15 in three cases are examined in this paper, as shown in Figure 6. Compared with Case 1, it is clear to see the electricity prices are raised due to the consideration of carbon emissions in Case 2. The price differences

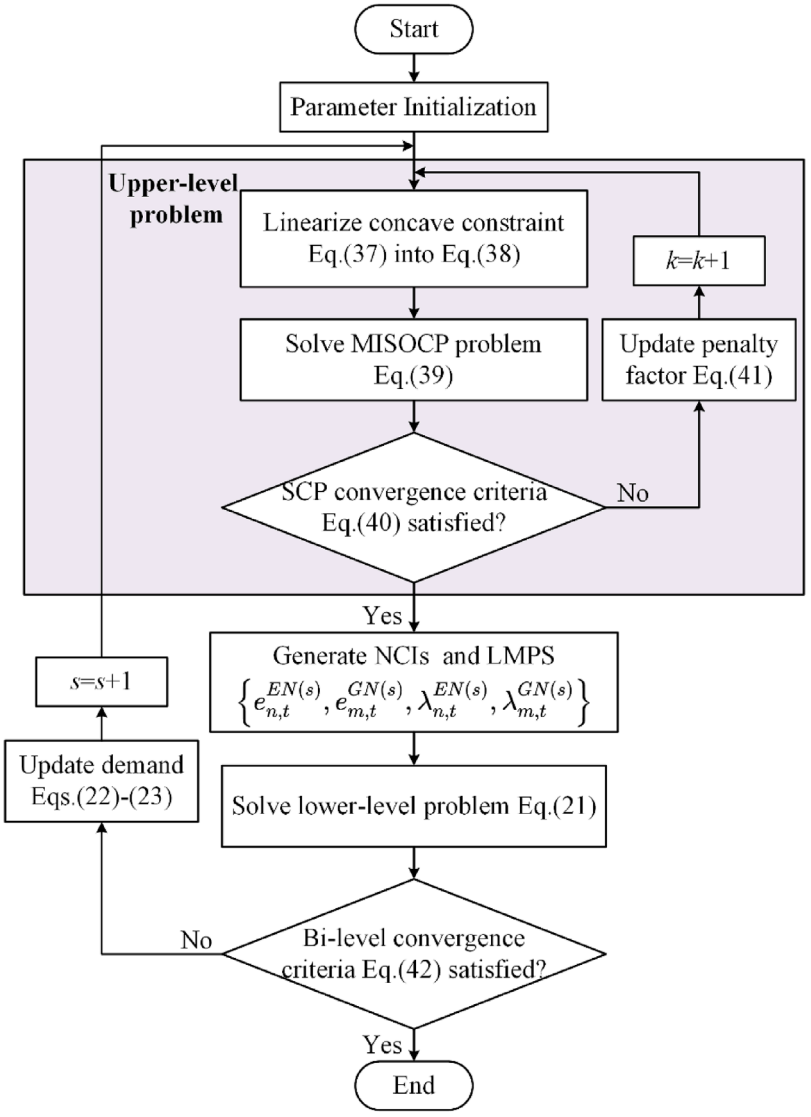

FIGURE 2
Flowchart of the bi-level interaction procedure.

between the two cases are relatively larger in the periods when the NCI of bus 15 is high (periods 8, 18). The different LMEPs among three cases, on the other hand, can reflect the distinct NCIs in different periods. For Case 3 with the proposed DSM strategy, it can be observed that the fluctuations of price become smoother, and prices stay at around 55$/MWh.

4.3 Results of optimal scheduling

As mentioned in the case setting, in case 1, the objective function is to minimize the generation cost and the gas production cost of IES, and in case 2, carbon trading cost is added to the objective function, as shown in Eq. 7. Both case 1 and case 2 do not consider DSM, so the electricity and gas loads in these two cases will not change and we model them as single-level, which can be solved easily by the off-the -shelf commercial solver. While case 3 presents the proposed bi-level scheduling model considering carbon trading and DSM, and we can solve it through the methods shown in Section 3.

The details of the total carbon emissions and the financial conditions are shown in Table 6, where the total carbon emissions are derived from Eq. 3, the generation cost refers to $\sum_t(\sum_{i\in\Omega^{TU}}C(P_{Gi,t})+\sum_{j\in\Omega^{GW}}\gamma_{j,t}\cdot g_{j,t})$, the consumer utility and carbon trading cost can be calculated according to Eq. 24 and Eq. 9, respectively. As can be seen, cases considering carbon trading have a decided advantage in carbon emission mitigation, the total carbon emission amount in Case 2 is 19.4% lower than that of Case 1. DSM strategies can also help reduce carbon emissions, the total carbon emission amount in Case 3 is reduced by 7.7% compared to Case 2. However, the generation cost in Case 2 and Case 3 increase because more gas-turbine units with lower carbon intensities are being used, which are more expensive than coal-fired thermal units. It should be noted that the consumer utility in Case 3 has a 5.75% decrease. This

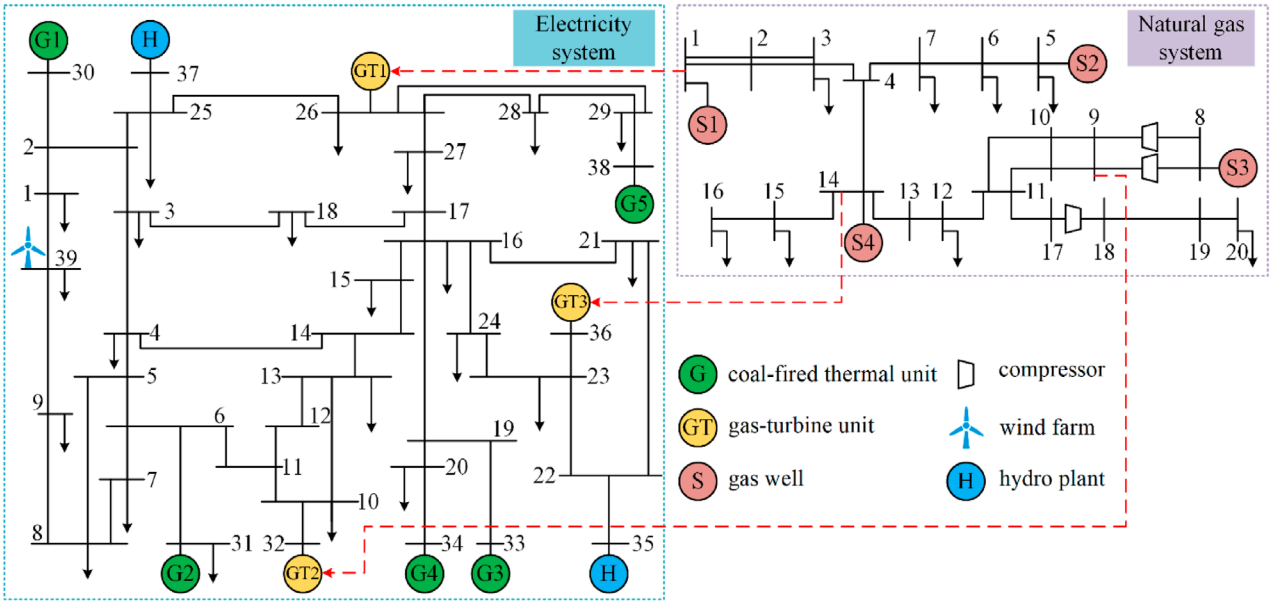

FIGURE 3
Diagram of the integrated energy system.

TABLE 1 Parameters of the coal-fired thermal units.

Parameter	G1	G2	G3	G4	G5
Capacity/MW	90	120	140	140	150
Emission intensity/(tCO_2/MWh)	0.80	0.85	0.875	0.875	0.90
a/($/MWh^2)	0.077	0.009	0.030	0.077	0.077
b($/MWh)	19.71	21.02	20.31	24.02	19.71
c/$	89	110	94	55	100

TABLE 2 Parameters of the gas-turbine units.

Parameter	GT1	GT2	GT3
Capacity/MW	160	160	200
Emission intensity/(tCO_2/MWh)	0.5	0.5	0.5
α/(km^3/h)	45.28	53.46	45.28
β/(km^3/MWh)	19.71	25.34	19.71
γ/(km^3/MW^{2}h)	0.003	0.006	0.003

TABLE 3 Parameters of gas wells.

Parameter	S1	S2	S3	S4
Maximum gas production/(km^3/h)	6.5	3.6	5.5	4.6
Minimum gas production/(km^3/h)	0	0	0	0
Gas production cost/($/m^3)	0.25	0.25	0.42	0.42

TABLE 4 Parameters of compressors.

Compress No.	Start node	End node	Compression ratio	B_s	Z_s
1	8	9	1.1	124.74	0.2334
2	17	18	1.2	124.74	0.2334

TABLE 5 Parameters of the SCP algorithm.

χ^0	χ^{max}	N	ε^z	ε^s
0.1	1,000	2	0.1	0.01

is because the DSM strategy in Case 3 would motivate energy users to cut demands with high emission intensities to seek the maximum consumer surplus, which might reduce the consumer utility to some extent.

Moreover, Case 2 has the highest carbon trading cost, while the carbon trading cost in Case 3 is decreased by 77.1%. The reason for this result is twofold. Firstly, there is fewer carbon emissions in Case 3, which means more carbon sources are below their emission caps so that the extra allowances that generators need to purchase are fewer. Secondly, due to the DSM, energy users in Case 3 can also sell carbon allowances to earn extra revenues in certain periods. It is obvious that whether users can obtain profits is dependent on the emission allowances allocation. When the emission allocation on the demand side is loose, the benefits of selling emission allowances would stimulate end users to participate in DSM to reduce the total carbon emissions.

The optimal scheduling results of the electricity system for all three cases on a typical day are shown in Figure 7. The hydro power remains constant in three cases because we assume that the hydro power plants are operating at their maximum power. It is evident that there is a significant reduction in the output of coal-fired thermal units from Case 1 to Case 3. The power produced by coal holds almost 54.2% of the total power generation in Case 1, and this value

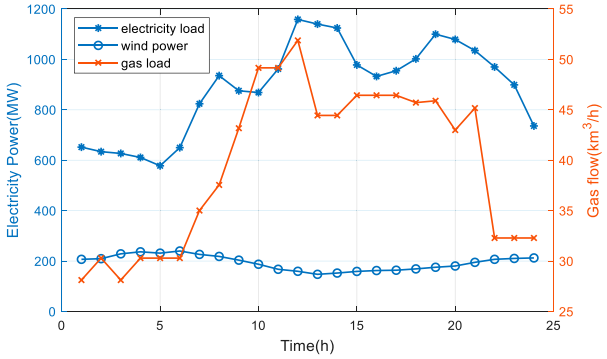

FIGURE 4
Profiles of 24-h electricity load, gas load and wind power output.

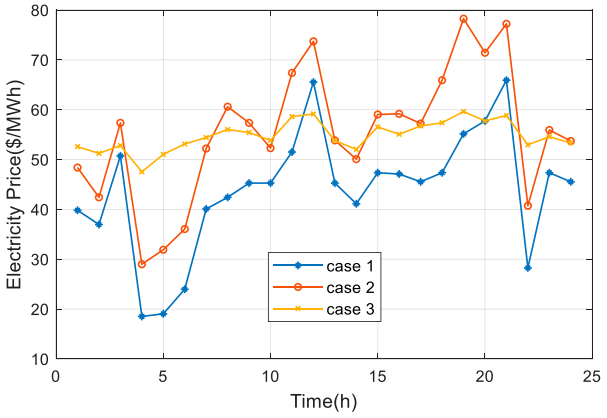

FIGURE 6
LMEPs of bus 15 in three cases.

changes to about 50.4% in Case 2% and 44.5% in Case 3. On the contrary, the output of gas-turbine units is increasing gradually, which means under the effect of carbon trading, more GTs with lower emissions are put into use to replace the coal-fired units. The area between the generation cost and the consumer utility curves in Figure 7 represents the negative social welfare. By comparing Case 2 and Case 3, it can be seen that the proposed model has a remarkable effect on reducing the negative social welfare.

In addition, the scheduling results of the natural gas system of Case 1 and Case 3 are shown in Figure 8. Compared with Case 1, the increase of the gas-turbine units output and gas load adjustments in Case 3 result in a 17.68% increase of the gas well output, and so do the corresponding carbon emissions of the natural gas system. And the load adjustment results after DSM in Case 3 are illustrated in Figure 9. It can be observed that the electricity users tend to cut their demands in the peak hours and transfer them to the valley hours, because in valley hours, the LMEPs and NCIs are relatively low, and the demand transfer can help electricity users to optimize their cost. While the natural gas loads show the opposite trend. This is mainly because the lower level is built as a linear programming problem, when the electricity loads decrease, the natural gas users would increase their demands to raise their consumer utility, thus maximizing the whole consumer surplus.

Finally, the convergence process of SCP algorithm is presented in Figure 10. Constraint violations are significant at the beginning and decrease dramatically as the penalty factor grows. Solution with SCP is found after 6 iterations, which is feasible for the primal problem. Besides, the convergence of the bi-level interaction is illustrated in Figure 11. The demand response amount of bus 15 in the electricity network and bus 12 in the natural gas network at 13:00 in each iteration are investigated. The optimization in Case 3 can finally converge to equilibrium with 20 iterations, and the total computation time is 430s. This result verifies the feasibility of the adopted bi-level optimization model.

4.4 Impact of the carbon trading price and gas production

The carbon trading price κ can represent the weight of the low-carbon objective in the proposed model, and the change of

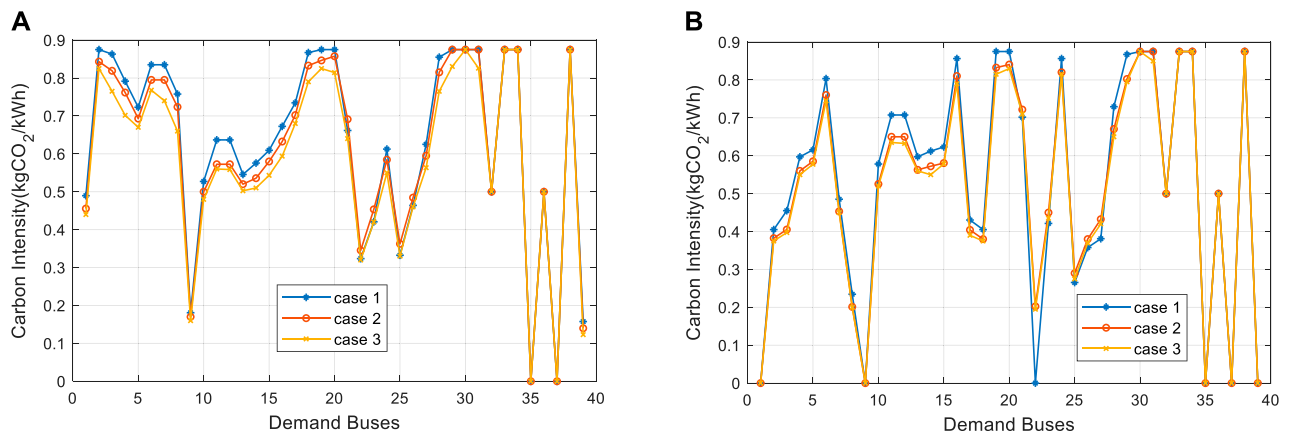

FIGURE 5
NCIs of 39 buses in **(A)** peak hour and **(B)** valley hour.

carbon trading price will affect the operating state of the system. The impact of the carbon trading price on total carbon emissions and carbon trading cost in Case 3 is shown in Figure 12. Initially, when the carbon trading price is below 15$/ton, the total carbon emissions remain almost unchanged, and the carbon trading cost increases steadily with the increase of carbon trading price. In such a case, the carbon trading cost plays a minor role in the integrated objective function, and coal-fired units account for the major parts of power generation because of their cheapness. When the carbon trading price rises to 20$/ton, gas-turbine units become competitive, especially during peak hours. As a result, the total carbon emissions begin to decline significantly, and so does the cost of carbon trading. When the carbon trading price increases to around 32.5$/ton, the carbon trading cost drops to 0, which means the carbon emissions of the system is equal to the carbon allowances allocation at this point, and then environmental profits would be generated, making the carbon emissions drop rapidly. The total carbon emissions can be reduced by 40.5% with a carbon trading price of 40$/ton. However, a further increase of the carbon trading price has a slight impact on the carbon emissions when the carbon trading price is up to 45$/ton, since the output of gas-turbine units nears the maximum level, and the carbon trading cost declines slowly in proportion to the carbon trading price. This result indicates that the operating state of the IES is sensitive to the fluctuation of the carbon trading cost.

TABLE 6 Carbon emissions and system cost comparison for all three cases.

Cases	1	2	3
Total carbon emissions/ton	6,510	5,245	4,839
Generation cost/k$	787.16	1,032.47	941.37
Consumer utility/k$	231.46	231.46	218.15
Carbon trading cost/k$	0	56.22	12.88

Similar to the carbon trading price, the gas production cost also affects carbon emissions and carbon trading cost. It is evident that when the gas production cost is relatively low, the carbon emission is low as well and there would be earnings from carbon trading. The carbon emissions and carbon trading cost would rise with the gas production cost increases. It should be noted that the carbon trading price where environmental profits are generated (32.5$/ton in this paper) is closely related to the gas production cost. The higher the gas production cost is, the higher the carbon trading price is to obtain carbon income. Thus, the regulators can set appropriate carbon trading prices according to the gas production cost to stimulate more low-carbon energy utilization to obtain environmental revenues from both the generation side and the demand side.

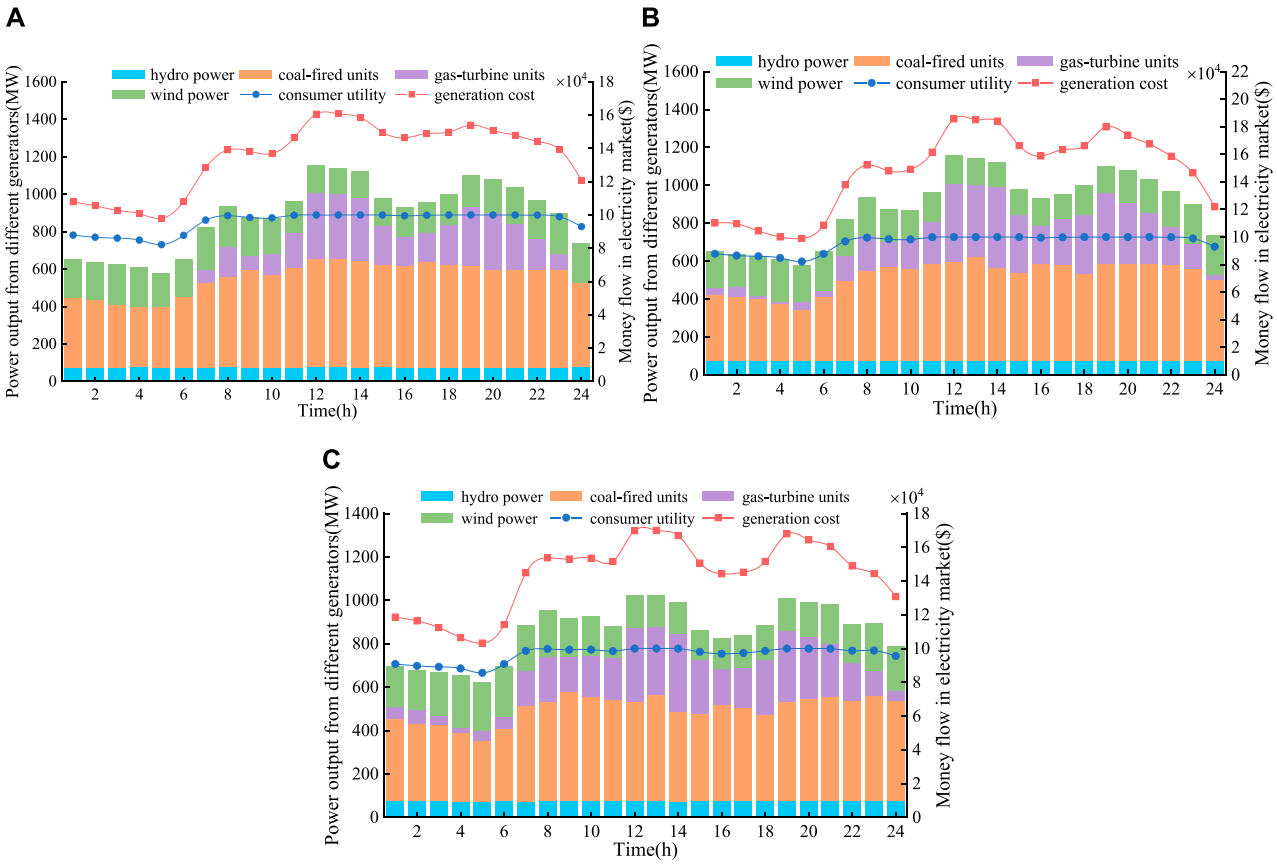

FIGURE 7
Optimal scheduling results of **(A)** Case 1 **(B)** Case 2 and **(C)** Case 3.

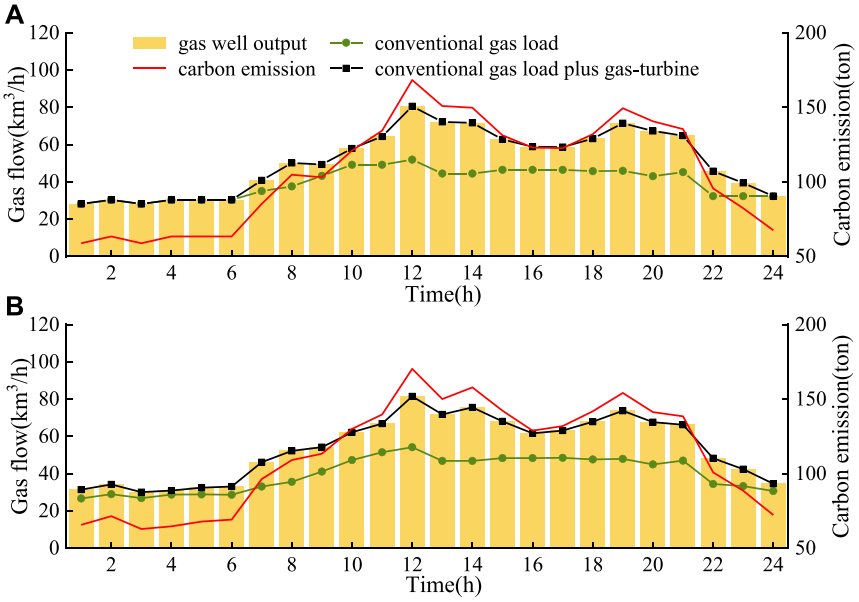

FIGURE 8
Gas network scheduling results of **(A)** Case 1 and **(B)** Case 3.

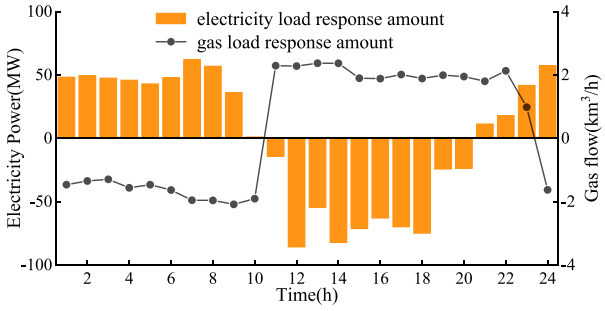

FIGURE 9
Load adjustment results after DSM.

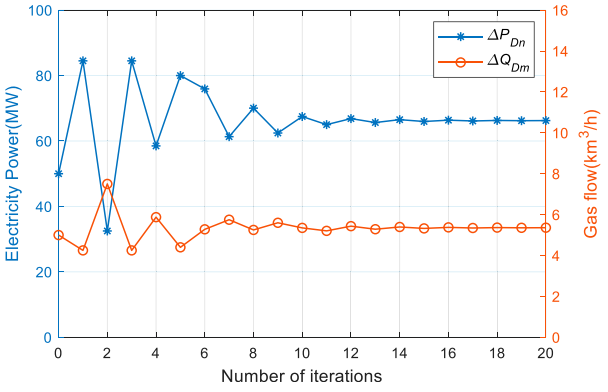

FIGURE 11
Demand response amount at 13:00 in each iteration of Case 3.

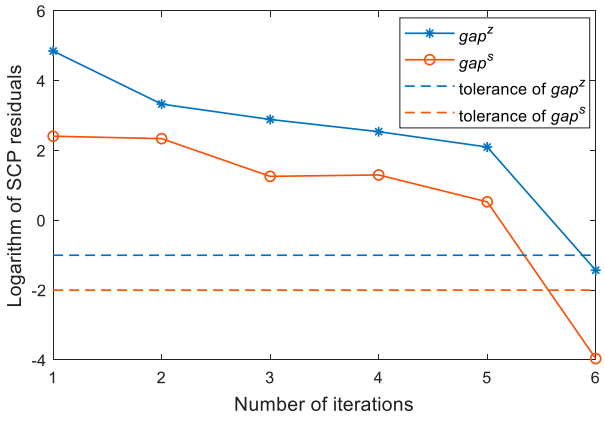

FIGURE 10
Converge curve of sequential cone programming.

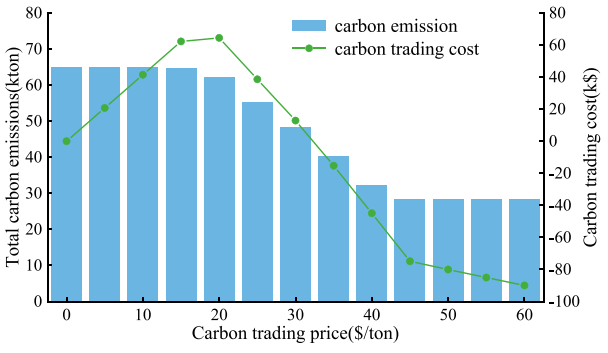

FIGURE 12
Results for different carbon trading price in Case 3.

5 Conclusion

This paper proposes a bi-level scheduling model to investigate the low-carbon economic operation of the electricity and natural gas IES considering DSM and carbon trading. At the upper level, an optimal energy flow model considering carbon trading at the generation side is formulated, where the SCP method is adopted to solve the relaxation gap of the gas flow equation. And the CEF model is applied to track the carbon flows accompanying the energy flows, thus the nodal carbon intensities can be obtained to clarify the emission responsibility from the perspective of end users. At the lower level, a developed demand response model is introduced, in which energy users can adjust their demands to maximize consumer surplus according to the NCIs and LMPs passed from the upper level. Case studies based on the IEEE 39-bus system and the Belgian 20-node natural gas system show that the proposed method can effectively facilitate the low-carbon operation of the IES, both the overall carbon intensities and total emissions have been significantly reduced. It should be noted that this paper adopts the centralized optimization method to model the operation of IES, but in practice the power network and the natural gas network belong to different decision-making utilities, so the decentralized optimization of electricity-natural gas IES considering DSM and carbon trading might be our future work.

Data availability statement

The raw data supporting the conclusion of this article will be made available by the authors, without undue reservation.

Author contributions

QF: methodology, software, validation, investigation, writing—original draft. JW: conceptualization, supervision, writing—review and editing. DL: conceptualization, supervision, data collection, writing—review and editing. All authors contributed to the article and approved the submitted version.

Funding

This work was supported by the National Natural Science Foundation of China–Key Program of Joint Fund in Smart Grid (U2166210).

Conflict of interest

The authors declare that the research was conducted in the absence of any commercial or financial relationships that could be construed as a potential conflict of interest.

Publisher's note

All claims expressed in this article are solely those of the authors and do not necessarily represent those of their affiliated organizations, or those of the publisher, the editors and the reviewers. Any product that may be evaluated in this article, or claim that may be made by its manufacturer, is not guaranteed or endorsed by the publisher.

References

Borraz-Sánchez, C., Bent, R., Backhaus, S., Hijazi, H., and Hentenryck, P. (2016). Convex relaxations for gas expansion planning. *Inf. J. Comput.* 28 (4), 645–656. doi:10.1287/ijoc.2016.0697

Chen, S., Conejo, A., J., Sioshansi, R., and Wei, Z. (2020). Operational equilibria of electric and natural gas systems with limited information interchange. *IEEE Trans. Power Syst.* 35 (1), 662–671. doi:10.1109/TPWRS.2019.2928475

Cheng, Y., Zhang, N., Wang, Y., Yang, J., Kang, C., and Xia, Q. (2019). Modeling carbon emission flow in multiple energy systems. *IEEE Trans. Smart Grid* 10 (4), 3562–3574. doi:10.1109/TSG.2018.2830775

Cheng, Y., Zhang, N., Zhang, B., Kang, C., Xi, W., and Feng, M. (2020). Low-carbon operation of multiple energy systems based on energy-carbon integrated prices. *IEEE Trans. Smart Grid* 11 (2), 1307–1318. doi:10.1109/TSG.2019.2935736

Ember, (2021). The European Union and United Kingdom emissions trading system carbon market price day-by-day. Available: https://ember-climate.org/data/carbon-price-viewer/.

Fang, K., Zhang, Q., Long, Y., Yoshida, Y., Sun, L., Zhang, H., et al. (2019). How can China achieve its intended nationally determined contributions by 2030? A multi-criteria allocation of China's carbon emission allowance. *Appl. Energy* 241, 380–389. doi:10.1016/j.apenergy.2019.03.055

Geidl, M., and Andersson, G. (2007). Optimal power flow of multiple energy carriers. *IEEE Trans. Power Syst.* 22 (1), 145–155. doi:10.1109/TPWRS.2006.888988

Gu, H., Li, Y., Yu, J., Wu, C., Song, T., and Xu, J. (2020). Bi-level optimal low-carbon economic dispatch for an industrial park with consideration of multi-energy price incentives. *Appl. Energy* 262, 114276. doi:10.1016/j.apenergy.2019.114276

Huang, W., Zhang, N., Yang, J., Wang, Y., and Kang, C. (2019). Optimal configuration planning of multi-energy systems considering distributed renewable energy. *IEEE Trans. Smart Grid* 10 (2), 1452–1464. doi:10.1109/TSG.2017.2767860

International Energy Agency (Iea), (2022). Global energy review: CO2 emissions in 2021. Available: https://www.iea.org/data-and-statistics/data-product/global-energy-review-co2-emissions-in-2021.

Jiang, T., Deng, H., Bai, L., Zhang, R., Li, X., and Chen, H. (2018). Optimal energy flow and nodal energy pricing in carbon emission-embedded integrated energy systems. *CSEE J. Power Energy Syst.* 4 (2), 179–187. doi:10.17775/CSEEJPES.2018.00030

Jiang, T., Yuan, C., Bai, L., Chowdhury, B., Zhang, R., and Li, X. (2022). Bi-level strategic bidding model of gas-fired units in interdependent electricity and natural gas markets. *IEEE Trans. Sustain. Energy* 13 (1), 328–340. doi:10.1109/TSTE.2021.3110864

Kang, C., Zhou, T., Chen, Q., Wang, J., Sun, Y., Xia, Q., et al. (2015). Carbon emission flow from generation to demand: A network-based model. *IEEE Trans. Smart Grid* 6 (5), 2386–2394. doi:10.1109/TSG.2015.2388695

Li, Y., Zou, Y., Tan, Y., Cao, Y., Liu, X., Shahidehpour, M., et al. (2018). Optimal stochastic operation of integrated low-carbon electric power, natural gas, and heat delivery system. *IEEE Trans. Sustain. Energy* 9 (1), 273–283. doi:10.1109/TSTE.2017.2728098

Liu, X. (2022). Research on bidding strategy of virtual power plant considering carbon-electricity integrated market mechanism. *Int. J. Electr. Power Energy Syst.* 137, 107891. doi:10.1016/j.ijepes.2021.107891

Lu, Z., Bai, L., Wang, J., Wei, J., Xiao, Y., and Chen, Y. (2023). Peer-to-peer joint electricity and carbon trading based on carbon-aware distribution locational marginal pricing. *IEEE Trans. Power Syst.* 38 (1), 835–852. doi:10.1109/TPWRS.2022.3167780

Olsen, D. J., Zhang, N., Kang, C., Ortega-Vazquez, M., and Kirschen, D. S. (2019). Planning low-carbon campus energy hubs. *IEEE Trans. Power Syst.* 34 (3), 1895–1907. doi:10.1109/TPWRS.2018.2879792

Paudyal, S., Cañizares, C., A., and Bhattacharya, K. (2015). Optimal operation of industrial energy hubs in smart grids. *IEEE Trans. Smart Grid* 6 (2), 684–694. doi:10.1109/TSG.2014.2373271

Pourakbari-Kasmaei, M., Lehtonen, M., Contreras, J., and Mantovani, J. (2020). Carbon footprint management: A pathway toward smart emission abatement. *IEEE Trans. Ind. Inf.* 16 (2), 935–948. doi:10.1109/TII.2019.2922394

Sun, Q., Wang, X., Liu, Z., Mirsaeidi, S., He, J., and Pei, W. (2022). Multi-agent energy management optimization for integrated energy systems under the energy and carbon co-trading market. *Appl. Energy* 324, 119646. doi:10.1016/j.apenergy.2022.119646

Wang, Y., Qiu, J., Tao, Y., and Zhao, J. (2020). Carbon-oriented operational planning in coupled electricity and emission trading markets. *IEEE Trans. Power Syst.* 35 (4), 3145–3157. doi:10.1109/TPWRS.2020.2966663

Wang, Y., Zhang, N., Kang, C., Kirschen, D., S., Yang, J., and Xia, Q. (2019). Standardized matrix modeling of multiple energy systems. *IEEE Trans. Smart Grid* 10 (1), 257–270. doi:10.1109/TSG.2017.2737662

Yan, M., Shahidehpour, M., Paaso, A., Zhang, L., Alabdulwahab, A., and Abusorrah, A. (2021). Distribution network-constrained optimization of peer-to-peer transactive energy trading among multi-microgrids. *IEEE Trans. Smart Grid* 12 (2), 1033–1047. doi:10.1109/TSG.2020.3032889

Zhang, Y., Hu, Y., Ma, J., and Bie, Z. (2018). A mixed-integer linear programming approach to security-constrained co-optimization expansion planning of natural gas and electricity transmission systems. *IEEE Trans. Power Syst.* 33 (6), 6368–6378. doi:10.1109/TPWRS.2018.2832192

Zlotnik, A., Roald, L., Nackhaus, S., Chertkov, M., and Andersson, G. (2017). Coordinated scheduling for interdependent electric power and natural gas infrastructures. *IEEE Trans. Power Syst.* 32 (1), 600–610. doi:10.1109/TPWRS.2016.2545522

frontiers | Frontiers in Energy Research

TYPE Original Research
PUBLISHED 12 September 2023
DOI 10.3389/fenrg.2023.1240611

OPEN ACCESS

EDITED BY
Mingfei Ban,
Northeast Forestry University, China

REVIEWED BY
Zhenhuan Ding,
Anhui University, China
Zicheng Liu,
Huazhong University of Science and Technology, China
Jian Wei,
Northeast Forestry University, China

*CORRESPONDENCE
Dongjun Cui,
cdj1122@126.com

RECEIVED 15 June 2023
ACCEPTED 01 September 2023
PUBLISHED 12 September 2023

CITATION
Cui D, He J, Cheng X and Liu Z (2023), Distributed energy storage participating in power trading mechanism for power system flexibility.
Front. Energy Res. 11:1240611.
doi: 10.3389/fenrg.2023.1240611

Distributed energy storage participating in power trading mechanism for power system flexibility

Dongjun Cui[1,2]*, Jinghan He[1], Xiaochun Cheng[2] and Zhao Liu[1]

[1]School of Electrical Engineering, Beijing Jiaotong University, Beijing, China, [2]Capital Power Exchange Center Co., Ltd., Beijing, China

In the paper of the participation of multiple types of market members, such as photovoltaics, wind power, and distributed energy storage, in market-based trading, the development of new power systems hinges on strengthening the adaptability of power systems to accommodate various types of market participants and improving their flexibility. The establishment of a modern power system also faced major challenges. Such as how to achieving collaborative operation between the main grid, regional distribution networks, and distributed power generation and consumption devices, and how to improving the flexibility of grid operation, and how to increasing device utilization, and reducing operating costs. In view of above-mentioned issues, this study proposed employing the traceability and anti-tampering features of blockchain technology tackle the issue of establishing mutual trust among different types of market participants and, considering the high volatility of new energy output, studies the configuration of a flexible power system in response to output deviations resulting from day-ahead forecasting-intraday operation (DAF-IDO). A market-based trading mechanism involving multiple types of market participants has been established to smooth out the deviation in output from different types of participants, improving the economic benefits of system operation. This study has made innovative contributions as follows: First, this study employed blockchain technology to enable the participation of various types of market participants in trading activities together. Second, this study proposed a method for determining DAF-IDO energy storage action deviations to allow regional distribution networks based on distribution network operators to quantitatively calculate their energy storage supply and demand, providing crucial methodological support for their participation in market trading in the future. Third, the study developed a trading mechanism based on combinatorial auctions for multiple types of market participants, and incorporated an valley compensation mechanism into the pricing mechanism to encourage active and autonomous participation of users, while also considering the economic benefits of all parties involved. Ultimately, numerical simulations were conducted to verify the feasibility and rationality of the trading mechanism, taking into account the DAF-IDO energy storage action deviations while multiple regional networks are participating.

KEYWORDS

multiple types of market participants, blockchain, alliance chain, power system flexibility, energy storage action deviation, market trading mechanism

1 Introduction

In view of the gradual increase in the installed capacity of global renewable energy, the volatility and uncertainty of wind and photovoltaic output has posed significant challenges to the power systems, which can be tackled through the development of market-based trading mechanisms that enhance power system flexibility. At the same time, energy storage devices can be used to efficiently store and discharge energy, providing the necessary flexibility and stability for power systems, thereby facilitating the construction of the energy internet (Zhang et al., 2018). Based on their scale and distribution characteristics, energy storage devices can be broadly categorized into two types: centralized and distributed. Distributed energy storage, in contrast to centralized energy storage, is predominantly installed on the user end to smooth out the variability of renewable energy output. The energy revolution inevitable renders the collaborative operation of renewable energy and distributed energy storage. In addition, with the increasing proportion of renewable energy connected to the grid, there will be a growing demand for distributed energy storage and associated services on the user end (Liu et al., 2017). However, the current underdeveloped commercial models (Li Jianlin et al., 2022), high investment costs (Li Jianlin et al., 2022), and low utilization rates of devices (Li Shanshan et al., 2022) have hindered the development of distributed energy storage, leading to a decrease in user enthusiasm for its configuration (Zhou et al., 2018). Therefore, the exploration of new strategies for user-end distributed energy storage to participate in market activities has emerged as an important research direction in the field of distributed energy trading.

As one of the important application scenarios for distributed energy storage, regional distribution networks are equipped with renewable energy devices, such as wind turbines and photovoltaics. The uncertainty in their output can lead to deviations in day-ahead forecasting-intraday operation (DAF-IDO). On this basis, scholars have conducted research on operation scheduling and market mechanisms. Reference (Huang et al., 2023) proposed a scheduling method for the mutual complementation of multiple energy sources, such as wind, photovoltaics, and storage, on multiple time scales to smooth out the joint output volatility of wind and photovoltaic power. Taking source-load uncertainty into consideration, the authors of reference (Nan et al., 2023) made flexible adjustments to the scheduling plan during the intraday phase based on the day-ahead comprehensive energy system scheduling plan. In terms of operation scheduling, existing literature has primarily concentrated on the collaborative operation of energy storages with wind and photovoltaic power sources that smooths out deviations by adjusting the specific amount of energy storage charging and discharging during the intraday phase to fulfill energy requirements. The authors of reference (Chen Xi et al., 2023) took into account both day-ahead and intraday scenarios during the scenario generation phase and, on this basis, proposed a master-slave gaming model that involves microgrid clusters and shared energy storage operators for trading. However, there has been a relatively limited amount of research conducted on the utilization of market mechanisms to address DAF-IDO deviations despite its importance. In addition, research in this area is often based on the specific amount of energy storage action required to satisfy electricity demand and smooth out DAF-IDO deviations during day-ahead and intraday phases. In short, existing literature on DAF-IDO uncertainty primarily focuses on the amount of energy storage charging and discharging action determined, while disregarding the correlation between the specific day-ahead and intraday amount of action and their market applicability.

In recent years, the booming sharing economy model has facilitated the participation of energy storage in market trading by overcoming the limitations of conventional economic models (Li Shanshan et al., 2022). The model of shared energy storage involves the investment and operation of public energy storage devices by third parties (Li Jianlin et al., 2022) or through joint efforts of all users (Tushar et al., 2016), thereby providing energy storage services to multiple users (Dai et al., 2021). Reference (YAN and CHEN, 2022) provided a detailed introduction to the concept and application scenarios of shared energy storage, and summarized and analyzed the relevant business models and pricing mechanisms associated with this model. The authors of reference (Chen Cen et al., 2023) designed a distributed two-layer P2P cooperation and sharing model, integrating energy storage resources in neighboring communities for capacity sharing. Whereas references (Li et al., 2021; Dai et al., 2022; Hu et al., 2022) introduced blockchain technology into distributed electricity trading, which enabled online trading, optimized matching, and subsequent control of distributed energy storage. The aforementioned studies on shared energy storage can, to some extent, improve the utilization rate of energy storage devices, and mitigate the problem of limited development of energy storage due to the high costs involved. On this basis, Chinese and international scholars have proposed an electricity trading mechanism based on blockchain technology.

Blockchain technology offers several advantages, including decentralization, tamper-proofing, and distributed ledger. Given adequate computational power, it can integrate centralized and distributed trading modes. Reference (Cui et al., 2022) introduced a method for utilizing blockchain technology to facilitate the integration and interconnection of trading and scheduling businesses under the regulatory system. Meanwhile, reference (Yan and Chen, 2022) established a two-layer operator-community-user energy storage capacity sharing model based on centralized energy storage power stations. It also designed an energy storage service pricing mechanism based on the Nash negotiation model to allocate social welfare among all participants. And reference (Ma et al., 2022) proposed a method for users to access energy storage services by renting centralized energy storage managed by energy storage operators, and introduced a bidding mechanism into the energy storage model to improve users' autonomy and trading efficiency. Previous research on energy storage business models have suggested that energy storage service providers must either invest in building centralized energy storage power stations or acquire the rights to use distributed energy storage devices on the user end to consolidate them into a centralized energy storage with a large capacity, which can then be used to provide energy storage leasing services. However, both modes of operations require high upfront investment costs. Most services are based on centralized energy storage power stations, with little participation in distributed energy storage. The process by which distributed energy storage resources on the user end can participate in cloud energy storage services is relatively straightforward, albeit lacking in autonomy.

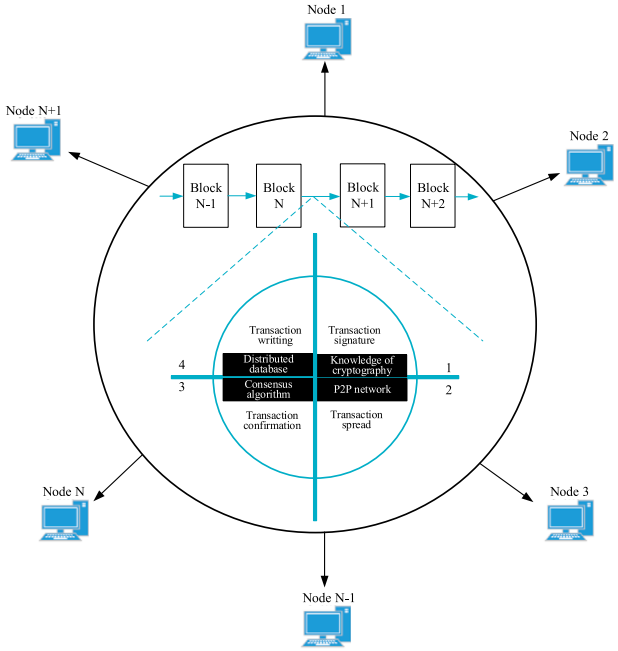

FIGURE 1
The chart of blockchain transaction flow.

Based on the analysis above, this study proposed a distributed energy storage trading mechanism that takes into consideration DAF-IDO energy storage action deviations under multiple distribution network operations to further improve the utilization of distributed energy storage devices and foster the autonomy of multiple types of market participants, such as energy storage users, in market trading. First, taking into account DAF-IDO deviations comprehensively (Wang et al., 2022), a method for determining energy storage trading volume is proposed, which provides crucial methodological support for the participation of distributed energy storage in market trading. Second, a distributed energy storage trading mechanism based on the combinatorial auction mechanism is designed with the support of blockchain technology. This mechanism enables distributed energy storage users to achieve optimal operation costs within a single distribution network and encourages resource sharing among multiple distribution networks, thereby improving the utilization of distributed energy storage resources. In terms of blockchain integration with various market participants, the blockchain serves as a carrier of information and the auction organization. When combined with effective trust mechanisms, this mechanism negates the necessity of centralized energy storage resources as a precondition for service development, thereby reducing the upfront investment required for system operation. It also enables decentralized control of energy storage resources, eliminating the need for centralized control and improving user participation and market competitiveness. Subsequently, the pricing mechanism for market trading is improved, and a compensation mechanism for valley time periods is proposed to augment users' inclination to participate in trading under low tariffs. Finally, the proposed blockchain-based distributed energy storage trading mechanism is evaluated for its feasibility and rationality under multiple distribution network operations through numerical simulations, and the key innovations achieved are as follows.

(1) A method for determining DAF-IDO energy storage action deviations is proposed, which diversifies the forms of energy storage participation in the market trading and improves the participation of energy storage in the market;
(2) A distributed energy storage trading mechanism based on blockchain information transmission and taking into consideration DAF-IDO energy storage action deviations is designed under multiple distribution networks. This mechanism improves users' trading autonomy and enthusiasm while achieving the distributed energy storage resource sharing among different distribution networks, which provides a new market strategy and conceptual framework for the application of blockchain technology in the power industry;
(3) An valley compensation mechanism is incorporated into the pricing mechanism by providing compensation to the blockchain nodes participating in trading, which increases users' inclination to participate in market trading under low tariffs.

2 Blockchain-based distributed energy storage trading taking into consideration DAF-IDO energy storage action deviations

2.1 Design of blockchain trading process

Due to its decentralization nature, information traceability, autonomy, openness, and tamper-proofing features, blockchain technology can be applied to electricity market trading. This proves advantageous in solving problems, such as multi-party trust, data security, and business certification in the context of business interactions involving a large number of external participants in the power market. Blockchain technology has been used in power market data management, resulting in the establishment of an open, collaborative, and secure technical support system for power markets that supports the participation of multiple types of market participants in the future.

The trading process in blockchain can be primarily summarized into four stages, that is, trading signature, trading dissemination, trading confirmation, and trading writing. To begin with, blockchain is transmitted to nearby nodes in the P2P network through signed transactions. Subsequently, upon receipt, adjacent nodes begin to confirm the validity of the trading. Each node creates a trading verification pool based on its own verified trading in chronological order. At this point, the trading in this pool has not been acknowledged by all nodes present in the entire network. Then, upon receiving confirmation from all nodes, the trade is written into the blockchain. After successful mining, the miner transmits the packaged block through the network, and when the entire network has verified the new block, the said black is appended to the main

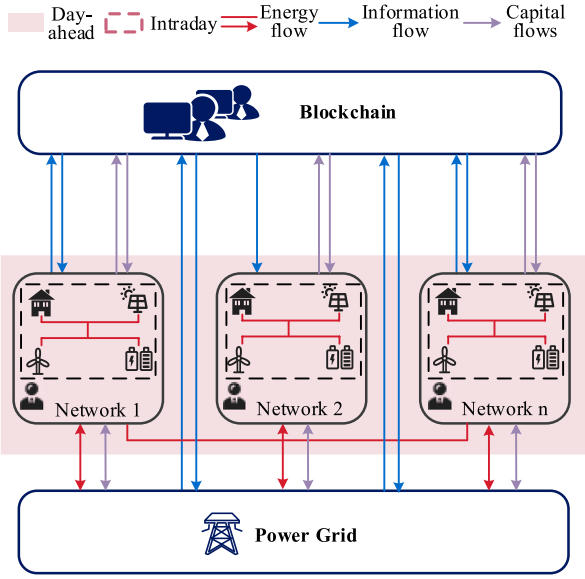

FIGURE 2
Distributed energy storage transaction framework considering DAF-IDO energy storage action deviation in multi-distribution network.

blockchain, thereby confirming the trading process. Figure 1 illustrates the complete process.

Distributed participants can be set as blockchain nodes, and centralized dispatch data can be stored and transmitted on the blockchain, the application of blockchain technology can be used in distributed participants and centralized dispatch participants.

According to the different node permissions, the application modes of blockchain can be categorized into the public chain, alliance chain, and private chain. Alliance chain has less resource occupation and lower cost. Based on the characteristics of different types of blockchain, this study has opted to focus on the alliance chain for further investigation.

2.2 Distributed energy storage trading framework taking into consideration DAF-IDO energy storage action deviations in multiple distribution networks

Existing energy storage business models are predominantly based on centralized energy storage power stations established by energy storage service providers for energy storage capacity leasing services. The participation of distributed energy storage in energy storage services mainly entails the integration of distributed energy storage devices onto the blockchain for unified information transmission and delegation of control over energy storage capacity leasing services. However, there is a lack of investigation into the integration of distributed energy storage with blockchain to participate in energy storage services. Furthermore, under the existing mechanism, the control of energy storage is predominantly held in the hands of energy storage service providers, which constrains users' flexibility to participate in energy storage services. In addition, energy storage service providers typically offer energy storage services within a single time scale, without taking into consideration DAF-IDO deviations. In light of this, this study proposed a distributed energy storage trading framework taking into account DAF-IDO energy storage action deviations in multiple distribution networks, as shown in Figure 2.

Figure 2 demonstrates that the distributed energy storage trading framework taking into consideration DAF-IDO energy storage action deviations in multiple distribution networks proposed in this study comprises blockchain, various distribution network operators, and the main grid operator, of which the blockchain facilitates the interconnection of different distribution networks and various market participants. Through blockchain information transmission, information exchange and fund flow can be achieved between users and between energy storage devices and users. Distribution network operators, as distribution network managers, engage in optimized scheduling and bidding within their respective distribution networks. The distribution network includes wind power, photovoltaic power, and multiple distributed energy storage devices. In this study, various types of market participants in the distribution network conducted transactions and transmitted information through blockchain, and optimized scheduling is achieved through the trust mechanism of the blockchain.

The distributed energy storage trading framework proposed in this study comprised two phases: the trading volume determination phase and the trading phase. In the first phase, each distribution network operator equipped with distributed energy storage devices develops charging and discharging strategies for such devices based on the predicted values of wind power, photovoltaic power, and load, aiming to minimize the daily energy cost of the distribution network during the day-ahead phase. In the second phase, charging and discharging strategies for distributed energy storage devices are formulated based on the actual intraday operating conditions. Then, according to the DAF-IDO energy storage action deviation determination method proposed in this study, the supply and demand quantities of each distribution network are determined for distributed energy storage trading between distribution networks.

Finally, the information interactions among market participants in different distribution networks via the alliance chain, as shown in Figure 2, is used to control the electricity of distributed energy storage devices, so that energy storage resources in surplus distribution networks can be transferred to insufficient ones during different time periods, thereby enabling the sharing of energy storage resources among different distribution networks. This paper is a theoretical study on the premise that the power grid reserve capacity is sufficient and the power grid and the distribution network follow the unified dispatching rules.

2.3 Distributed energy storage trading mechanism based on combinatorial auctions

In the intraday trading phase, trading actions are participated by a range of distribution network operators, as well as centralized and distributed market participants. We consider the TOU tariff mechanism where the corresponding electricity price is different for different time periods of a day. The transaction price between the

distribution network and the power grid will also refer to the TOU price. Due to the differences in energy consumption among different distribution networks and the corresponding demand for energy storage resources, distribution network operators can combinatorially auction energy storage resources to meet energy consumption demand of different distribution networks across different time periods. To ensure the smooth operation of distributed energy storage trading in distribution networks, this study proposed a blockchain-based trading mechanism to achieve centralized scheduling and collaborative trading among distributed market participants, which enables energy storage operators to participate in trading without incurring the significant costs associated with the construction of centralized energy storage stations or the organization of distributed energy storage devices. Instead, they can conduct trading and information transmission through the blockchain, which eliminates the need for complicated centralized control of various energy storage devices, which is conducive to the power system flexibility. The trading process can be divided into six stages as follows.

(1) Integration of distributed energy storage into the alliance chain: The alliance chain facilitates information sharing among market participants, who collaborate in smart contract execution. The chain contains information regarding distributed energy storage service prices, compensation mechanisms, and basic device information. After reaching a trading intention, each distributed energy storage device collaborates with other distributed market participants to balance the electricity within this distribution network.
(2) Trading information determination: Before trading, each distribution network is required to optimize scheduling within this network, determine the charging and discharging strategies for energy storage based on the output of distributed power sources, and determine the quantity of energy storage supply and demand for each intraday time period based on the DAF-IDO energy storage action deviation determination method proposed in this study.
(3) Trading information reporting: Following the determination of the quantity of energy storage supply and demand during each intraday time period, each distribution network submits a bid price for the corresponding electricity quantity to the blockchain to participate in the bidding with the main grid and other distribution networks.
(4) Trading matching: The trading information of each distribution network is matched with the objective of maximizing social welfare. During the matching stage, in the event of a failed round of matching, the trading parties will adjust their trading strategies and continue to match the price until the trading is successfully concluded between the purchaser and the seller. In the event that the supply and demand quantity of the trading parties does not meet the expected trading volume during the auction stage, they will participate in compulsory electricity transfer trading within the main grid.
(5) Trading completion: Each distribution network issues power control instructions to energy storage devices based on the matching information generated during the matching stage, and sells or purchases corresponding energy storage, ultimately leading to the completion of electricity settlement.
(6) Trading settlement: The successfully matched distribution networks settle according to the matching results. Each distributed energy storage operator charges a service fee in accordance with the terms of contract and pays compensation for the corresponding valley time period.

3 Distributed energy optimization operation model for distribution networks

The mechanism proposed in this study is designed to minimize the energy costs of the distribution network when formulating energy storage charging and discharging strategies. Based on the energy optimization sharing model, the charging and discharging strategies for the energy storage day-ahead plan are formulated during the day-ahead phase, and the expected energy storage charging and discharging strategies are formulated during the intraday phase.

3.1 Objective function

The renewable energy output in each distribution network includes centralized wind power and photovoltaic power, with some distribution networks equipped with distributed energy storage devices. In the operation and scheduling of the distribution network, the distribution network operator establishes an objective function aimed at minimizing the energy costs, expressed as follows:

$$\min C_t = \min \sum_{t=1}^{T} \left(P_{t,b}^{grid} \lambda_{t,b}^{grid} \Delta t - P_{t,s}^{grid} \lambda_{t,s}^{grid} \Delta t \right) \tag{1}$$

where $P_{t,b}^{grid}$ and $P_{t,s}^{grid}$ represent the purchasing and selling power of the distribution network at time t, respectively; $\lambda_{t,b}^{grid}$ and $\lambda_{t,s}^{grid}$ represent the purchasing and selling prices of electricity for the distribution network at time t, respectively.

3.2 Electric power balance constraints

$$P_t^{PV} + P_t^{WT} + P_t^{ES_d} + P_{t,b}^{grid} = P_t^{load} + P_t^{ES_c} + P_{t,s}^{grid} \tag{2}$$

where P_t^{PV} and P_t^{WT} represent the output of the photovoltaic and wind turbines in the distribution network at time t, respectively; $P_t^{ES_c}$ and $P_t^{ES_d}$ represent the discharging and charging power of the distributed energy storage device in the distribution network at time t, respectively; P_t^{load} represents the load at time t.

3.3 Device model and constraints

3.3.1 Distributed wind and photovoltaic unit model and constraints

The output model and constraints of the distributed photovoltaic unit are as follows:

$$P_{t,\max}^{PV} = \xi_t P^{PV} \tag{3}$$

$$0 \le P_t^{PV} \le P_{t,\max}^{PV} \tag{4}$$

where $P_{t,\max}^{PV}$ represents the maximum output power of the photovoltaic unit in the distribution network at time t; ξ_t represents the power ratio of the photovoltaic unit at time t, which is influenced by factors such as the intensity of solar radiation, the angle of incidence of light, and the efficiency of the solar panel; P^{PV} represents the installed capacity of the photovoltaic unit in the park.

The processing model and constraints of the distributed wind turbine generator unit are as follows:

$$P_{t,\max}^{WT} = \zeta_t P^{WT} \tag{5}$$

$$0 \le P_t^{WT} \le P_{t,\max}^{WT} \tag{6}$$

where $P_{t,\max}^{WT}$ represents the maximum output power of the wind turbine generator unit in the distribution network at time t; ζ_t represents the power ratio of the wind turbine generator unit at time t, which is influenced by factors such as ambient air density, rotor sweep area, wind speed, and turbine efficiency; P^{WT} represents the installed capacity of the wind turbine generator unit in the distribution network.

3.3.2 Constraints of distributed storage devices

The charging and discharging constraints of distributed storage devices are as follows:

$$\begin{cases} 0 \le P_t^{ES_c} \le aP_{\max}^{ES} \\ 0 \le P_t^{ES_d} \le (1-a)P_{\max}^{ES} \end{cases} \tag{7}$$

where $P_{\max}^{ES}$ represents the power capacity of the energy storage device; a represents the charging/discharging state, which is represented by a binary variable, where a value of 0 indicates charging, while a value of 1 indicates discharging.

To ensure the continuous operation of energy storage devices in subsequent operating days, the net charge capacity for energy storage should be maintained for each operating day. The daily net charge capacity is subject to a constraint, which is defined as follows:

$$\eta_c \sum_{t=1}^{T} P_t^{ES_c} \Delta t - \frac{1}{\eta_d} \sum_{t=1}^{T} P_t^{ES_d} \Delta t = 0 \tag{8}$$

where η_c represents the charging efficiency coefficient of the energy storage device; η_d represents the discharging efficiency coefficient of the energy storage device.

The state of charging constraint of the energy storage device is as follows:

$$SOC_{\min} \le SOC(t) \le SOC_{\max} \tag{9}$$

The charging and discharging constraints of the energy storage device for each operating day are expressed as follows:

$$\begin{aligned} &SOC_{\min} E_{\max}^{ES} \le SOC_{\min} E_{\max}^{ES} + \\ &\eta_c \sum_{t=1}^{T} P_t^{ES_c} \Delta t - \frac{1}{\eta_d} \sum_{t=1}^{T} P_t^{ES_d} \Delta t \le SOC_{\max} E_{\max}^{ES} \end{aligned} \tag{10}$$

where $E_{\max}^{ES}$ represents the storage capacity of the energy storage device.

3.3.3 Power constraints of the purchased and sold electricity

Electricity can only be purchased or sold at the same time for the distribution network. The constraints are expressed as follows:

$$0 \le P_{t,b}^{grid} \le bP_{b,\max}^{grid} \tag{11}$$

$$0 \le P_{t,s}^{grid} \le (1-b)P_{s,\max}^{grid} \tag{12}$$

where $P_{b,\max}^{grid}$ and $P_{s,\max}^{grid}$ represent the upper limits for the power of the purchased and sold electricity, respectively; b is a binary variable that denotes the sale of electricity with a value of 1 and the purchase of electricity with a value of 0.

4 Distributed energy storage trading among intra-day distribution networks based on DAF-IDO energy storage action deviations

4.1 Method for determining DAF-IDO energy storage action deviations

During the day-ahead operational phase, the distribution network operator optimizes the scheduling with the goal of minimizing the energy consumption costs and obtains the charging and discharging strategies for the energy storage plan. The uncertainty of wind and photovoltaic power output can result in deviations between the expected and actual operational performance during the intraday phase. Accordingly, the energy storage charging and discharging strategies obtained through optimized scheduling based on the actual output and load curves during the intraday phase may also deviate from those obtained from the day-ahead phase. The aforementioned factors can lead to scenarios where the energy storage device has insufficient discharge capacity or an excess of electricity stored in the devices during the intra-day phase. At this point, if each distribution network operator continues to charge and discharge according to the day-ahead plan, it may result in additional electricity purchases or idle devices, thereby adversely affecting the economic benefits of the distribution network. Therefore, this study calculated the deviation in the energy storage charging and discharging strategies between the day-ahead plan and the expected intraday plan, and proposed a method for determining the DAF-IDO energy storage action deviation that can reduce the losses caused by the deviation between the predicted conditions in the day-ahead phase and the actual operational performance during the intraday phase in subsequent trading of stored energy.

This method involves determining the energy storage device's action amount and expected trading volume during the intraday phase according to the expected energy storage charging and discharging strategies during the intraday phase and based on the energy storage charging and discharging strategies of each distribution network operator in the day-ahead energy storage plan. This provides a new way for distributed energy storage to participate in the market trading, thereby adding to its market power.

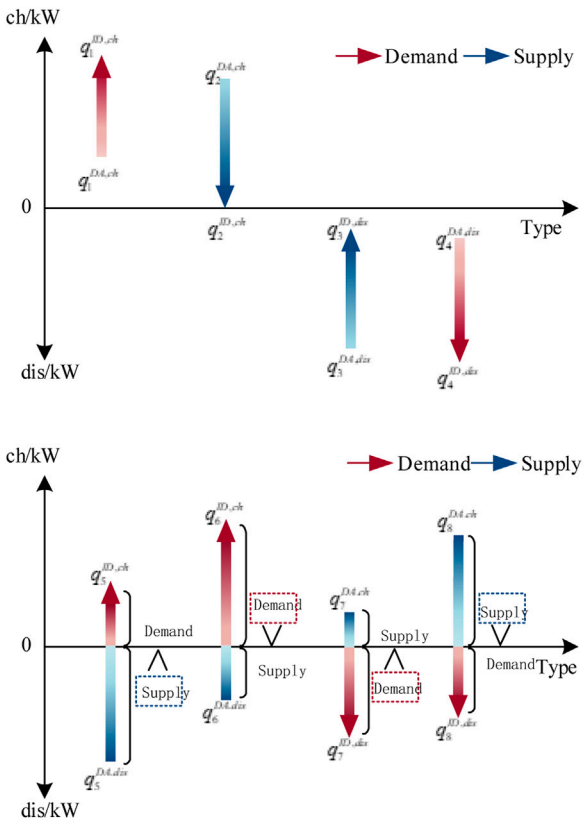

FIGURE 3
DAF-IDO method diagram for determining deviation of energy storage action.

$$Park_t = \left|q_t^{DA}\right| - \left|q_t^{ID}\right| \tag{13}$$

where $Park_t$ represents the quantity of supply and demand of the distribution network at time t, where the distribution network acts as the purchaser when $Park_t < 0$, and acts as the supplier when $Park_t > 0$; q_t^{ID} represents the intra-day action amount of the energy storage device at time t. Where $q_t^{ID} > 0$ indicates charging and $q_t^{ID} < 0$ indicates discharging; q_t^{DA} represents the day-ahead action amount of the energy storage device at time t, where $q_t^{DA} > 0$ indicates charging and $q_t^{DA} < 0$ indicates discharging.

In this case, the specific supply/demand amount of the distribution network is expressed as follows:

$$Q_t = \left|q_t^{ID} - q_t^{DA}\right| \tag{14}$$

Figure 3 illustrates the method for determining the DAF-IDO energy storage action deviation. To more intuitively display the charging and discharging states of energy storage, the depicted charge capacity and discharge capacity are both represented as positive values, where $q^{DA,ch}$ and $q^{DA,dis}$ represent the charging and discharge capacity of energy storage respectively in the day-ahead phase; $q^{ID,ch}$ and $q^{ID,dis}$ represent the charging and discharge capacity of energy storage respectively in the intraday phase. According to the charging and discharging strategies for the energy storage device during the day-ahead and intraday phases, the supply and demand of the distribution network can be categorized into eight cases:

(1) $q_1^{DA.ch} < q_1^{ID,ch}$: The energy storage device of the distribution network has insufficient planned charge capacity in the day-ahead phase, which cannot meet the demand during intraday optimized operation of the network. Consequently, to compensate for the deficit, electricity needs to be purchased from other distribution networks. Therefore, the distribution network is the purchaser, and the demand amount is.

(2) $q_2^{DA.ch} > q_2^{ID,ch}$: The day-ahead planned charge capacity of the energy storage device in the distribution network during the day-ahead phase exceeds the electricity demand of said network, and there remains an excess of electricity stored in the energy storage device. Hence, the surplus electricity can be sold to other distribution networks. Therefore, the distribution network is the supplier, and the supply amount is.

(3) $q_3^{DA.dis} > q_3^{ID,dis}$: The planned discharge capacity of the energy storage device in the distribution network during the day-ahead phase exceeds the electricity demand of said network. Hence, the surplus discharge capacity of the distribution network can be sold to other distribution networks. Therefore, the distribution network is the supplier, and the supply amount is.

(4) $q_4^{DA.dis} < q_4^{ID,dis}$: The energy storage device of the distribution network has insufficient planned charge capacity in the day-ahead phase, which cannot meet the network's electricity demand during intraday phase. Consequently, to compensate for the deficit, electricity needs to be purchased from other distribution networks in accordance with the planned discharge capacity in the day-ahead plan. Therefore, the distribution network is the purchaser, and the demand amount is $q_4^{ID.dis} - q_4^{ID.dis}$.

(5) $q_5^{DA.dis} > q_5^{ID,ch}$: In contrast to the expected action during the intraday phase, the planned action of the energy storage device in the day-ahead phase is notably high. Consequently, the expected charge capacity during the intraday phase is preserved, while the remaining planned discharge capacity is allocated for energy storage electricity trading between distribution networks. Therefore, the distribution network is the supplier, and the supply amount is.

(6) $q_6^{DA.dis} < q_6^{ID,ch}$: The reduction in electricity demand of the distribution network eliminated the need for energy storage discharge. The energy storage device needs to be charged to meet subsequent operational needs. To minimize losses, the original discharge capacity is preserved, while the remaining electricity demand is purchased from other distribution networks. Therefore, the distribution network is the purchaser, and the demand amount is $q_6^{ID.ch} - q_6^{DA.dis}$.

(7) $q_7^{DA.ch} < q_7^{ID,dis}$: The distribution network requires an energy storage device to discharge to meet the electricity demand during the intraday phase. Consequently, the planned charge capacity in the day-ahead phase is first used by the distribution network itself. In the case of inadequate supply, additional electricity should be purchased from other distribution networks. Therefore, the distribution network is the purchaser, and the demand amount is.

(8) $q_8^{DA.ch} > q_8^{ID,dis}$: The energy storage device of the distribution network has excessive planned charge capacity in the day-ahead

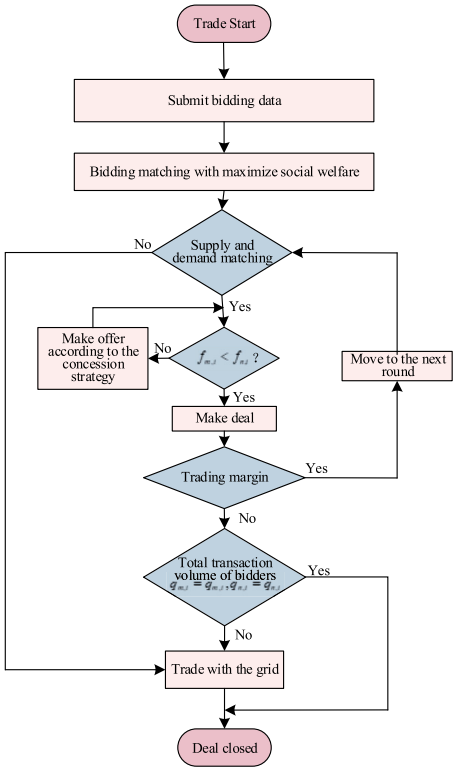

FIGURE 4
The chart of trade flow.

phase. Upon meeting the expected discharge capacity of the distribution network during the intraday phase, the remaining electricity is used for energy storage and traded between distribution networks. Therefore, the distribution network is the supplier, and the supply amount is.

4.2 Combinatorial auction model among distribution networks

Distributed energy storage trading among distribution networks is a competitive non-cooperative behavior, so combinatorial auction is adopted in this study to improve the autonomy of each distribution network participating in the market. The auction process consists three stages, that is, initial bidding, matching, and settlement, as shown in Figure 3. In the initial bidding stage, each distribution network operator, acting as a bidder, uploads the initial bidding price for the bid electricity quantity and conducts supply-demand matching based on the blockchain smart contract and the bidding trading strategy. If the initial bidding price does not meet the conditions for the trading, both the purchaser and seller will re-bid until the trading is concluded. Distribution networks that have successfully traded their expected volume will withdraw from the auction process, whereas those that have not will be added to the queue of unsuccessful networks and participate in the subsequent bidding round. In the event that distribution networks have bids that were not successfully matched or have not fully satisfied their expected volume during the trading process, they will participate in the final compulsory electricity transfer trading with the main grid.

4.2.1 Bidding

During the intraday phase, bidding information from each distribution network operator comprises the energy storage amount and corresponding price for each time period. The supply quantity and initial bidding price of each distribution network are as follows:

$$Q_m = [q_{m,1}, q_{m,2}, ..., q_{m,t}, ..., q_{m,T}] \tag{15}$$

$$F_m = [f_{m,1}, f_{m,2}, ..., f_{m,t}, ..., f_{m,T}] \tag{16}$$

where $q_{m,t}$ and $f_{m,t}$ are respectively the bidding electricity quantity and bidding price of the supplier m for the time period t.

Similarly, the demand quantity and initial bidding price of the distribution network are as follows:

$$Q_n = [q_{n,1}, q_{n,2}, ..., q_{n,t}, ..., q_{n,T}] \tag{17}$$

$$F_n = [f_{n,1}, f_{n,2}, ..., f_{n,t}, ..., f_{n,T}] \tag{18}$$

where $q_{n,t}$ and $f_{n,t}$ are respectively the bidding electricity quantity and bidding price of the purchaser for the time period t.

The bidding data are uploaded by each distribution network operator onto the blockchain, which subsequently records and transmits the data.

4.2.2 Winner determination problem model in auctions

The objective of the auctioneer in a two-way combinatorial auction is to maximize social welfare by determining the winners. Social welfare W_S is the combined surplus of both the seller and the purchaser, that is, the difference between the bidding prices of the purchaser and the seller.

$$\max W_S = \max\left(\sum_{n}^{N}\sum_{t}^{T} q'_{n,t} f_{n,t} - \sum_{m=1}^{M}\sum_{t=1}^{T} q'_{m,t} f_{m,t}\right) \tag{19}$$

where $q'_{m,t}$ and $q'_{n,t}$ represent the trading volume of the supplier and the purchaser, respectively, during the time period t.

4.2.3 Pricing and settlement model

4.2.3.1 First round of auction

In the auction process, distribution network operators with different supply and demand situations in each time period participate in the bidding. Given the fact that both the distributed participants in each distribution network and the centralized distribution network control center act as nodes in the blockchain, they can be coordinated through intelligent cooperation to achieve the objective of maximizing economic efficiency. The bidding strategy on the initial auction price is as follows:

The supplier's bidding price for the distribution network:

$$f_{m,t} = \lambda_{s,t}^{grid} - \delta \frac{q_{m,t}}{q_t^{ES}} \left(\lambda_{t,s}^{grid} - \lambda_{t,b}^{grid}\right) \tag{20}$$

The purchaser's bidding price for the distribution network:

$$f_{n,t} = \lambda_{t,b}^{grid} + \delta \frac{q_{n,t}}{q_t^{load}} \left(\lambda_{t,s}^{grid} - \lambda_{t,b}^{grid}\right) \tag{21}$$

where $f_{m,t}$ and $f_{n,t}$ are the bidding prices of the supplier's and purchaser's distribution network operators, respectively, during time period t; $q_{m,t}$ and $q_{n,t}$ are the bidding electricity quantity of supplier's and purchaser's distribution network operators, respectively, during the first round of trading; q_t^{ES} is the total energy storage capacity of the supplier's distribution network in the first round of trading; q_t^{load} is the total load of the distribution network on the demand end in the first round of trading, δ is the adjustment coefficient, which is set to 0.5 (Wu et al., 2023).

During the initial bidding stage, the distribution network operators on the supply end for each time period are arranged in ascending order based on their bidding price, while the distribution network operators on the demand end are arranged in descending order. The trading proves to be successful if $f_{m,t} < f_{n,t}$. At this point, social welfare is evenly distributed between the purchaser and the seller, so the trading price can be expressed as:

$$f_t^{deal} = \frac{1}{2}\left(f_{m,t} + f_{n,t}\right) \tag{22}$$

The business volume in the first round of trading is:

$$C_{m,1}^{deal} = \sum_{t=1}^{T} f_t^{deal} q_{m,t,1}^{deal} \tag{23}$$

$$C_{n,1}^{deal} = \sum_{t=1}^{T} f_t^{deal} q_{n,t,1}^{deal} \tag{24}$$

where $C_{m,1}^{deal}$ and $C_{n,1}^{deal}$ are respectively the profits and costs of the distribution network operators as the supplier and purchaser in the first round of trading; $q_{m,t,1}^{deal}$ and $q_{n,t,1}^{deal}$ are respectively the trading volume of the supplier and the purchaser for the time period t in the first round of trading, which are equal in value.

It should be noted that in cases where there are multiple purchasers and sellers within a given time frame, the auctioneer always matches them according to the maximum social welfare. If there is no winner in the first round of trading, the next round of the auction queue will follow. If there are multiple distribution networks with the same bidding price for a given time period, they will be matched according to the upload time of the bidding data, with the distribution network that uploaded their data earlier being given priority.

4.2.3.2 Concessional auction

The winning bidders in the first round of trading are removed from the queue while those failed adjust their bidding prices:

$$f_{m,r,t} = f_{m,t} - \Delta f_m \tag{25}$$

$$f_{n,r,t} = f_{n,t} + \Delta f_n \tag{26}$$

where $f_{m,r,t}$ and $f_{n,r,t}$ are the bidding prices of the supplier and the purchaser, respectively, for the time period t in the round r; Δf_m and Δf_n are the concession rates of the seller and the purchaser, respectively, with both sides making concessions at a certain rate until $f_{m,r,t} < f_{n,r,t}$.

Similarly, the trading price in the concessional trading stage is as follows:

$$f_{t,r}^{deal} = \frac{1}{2}\left(f_{m,r,t} + f_{n,r,t}\right) \tag{27}$$

The total trading amount in the concession trading stage is as follows:

$$C_m^{deal} = \sum_{t=1}^{T}\sum_{r=2}^{r} f_{m,t,r}^{deal} q_{m,t,r}^{deal} \tag{28}$$

$$C_n^{deal} = \sum_{t=1}^{T}\sum_{r=2}^{r} f_{n,t,r}^{deal} q_{n,t,r}^{deal} \tag{29}$$

where $C_{m,r}^{deal}$ and $C_{n,r}^{deal}$ are the profits and costs of the distribution network operator as the supplier and the purchaser in the concession stage, respectively; $q_{m,t,r}^{deal}$ is the trading amount corresponding to the supply amount in the concession stage; $q_{n,t,r}^{deal}$ is the trading amount corresponding to the supply amount in the concession stage.

4.2.3.3 Compulsory electricity trading with the main grid

If there is excess capacity in the distribution network after each round of trading, compulsory electricity trading with the main grid will occur. The surplus capacity of the distribution network operators for both the supplier and purchaser during each time period is expressed as follows:

$$q_{m,re,t} = q_{m,t} - q_{m,t,1}^{deal} - \sum_{r=2}^{r} q_{m,t,r}^{deal} \tag{30}$$

$$q_{n,re,t} = q_{n,t} - q_{n,t,1}^{deal} - \sum_{r=2}^{r} q_{n,t,r}^{deal} \tag{31}$$

Therefore, the total revenue generated from the trading between the distribution network and the main grid can be expressed as follows:

$$C_{grid} = \sum_{t=1}^{T} q_{m,re,t}\lambda_{t,s}^{grid} - \sum_{t=1}^{T} q_{n,re,t}\lambda_{t,b}^{grid} \tag{32}$$

4.2.3.4 Valley compensation mechanism

The pricing mechanism proposed in this study established that the bidding prices offered by each distribution network operator always fall within the range between the wind/photovoltaic feed-in tariff and the time-of-use tariff of the grid. For the purchaser, it is cheaper to purchase electricity from other distribution networks rather than the main grid at the time-of-use tariff. For the seller, selling surplus electricity from its distribution network or exporting it to the main grid can generate additional revenue. However, the economic efficiency may be reduced if grid operators continue to trade according to their bidding prices, given that the selling price of the main grid is lower than their bidding prices during valley periods. This may also lower the distribution network operators' enthusiasm to participate in trading during valley periods. To incentivize operators in the park to participate in trading during valley time periods, this study proposed an valley compensation mechanism, in which each distribution network compensates the purchaser and seller who have concluded trading at a certain rate based on the trading volume during valley time periods.

$$C_{cp} = \alpha q_{cp} \tag{33}$$

where α is the compensation rate and q_{cp} is the trading volume during valley periods.

4.2.3.5 Benefit settlement model

The total revenue of the distribution network encompasses the revenue generated by the distribution network operator. The scope

of this study is limited to the analysis of the overall economic benefits of the distribution network. After all trading has been concluded, the total revenue of the distribution network can be obtained as follows:

$$C_p = C_{m,1}^{deal} - C_{n,1}^{deal} + C_m^{deal} - C_n^{deal} + C_{grid} + C_{cp} \tag{34}$$

The total revenue of each participant in the blockchain is determined as follows:

$$C_{ces} = 0.8\left(\beta\left(q_{t,1}^{deal} + \sum_{r=2}^{r} q_{t,r}^{deal}\right) - C_{cp}\right) \tag{35}$$

where β is the service fee of the blockchain. To incentivize market participants to use the blockchain, 20% of the total revenue in the blockchain, determined by the smart contract, is allocated for payment to the distribution network operator as the scheduling fee (Xue, 2015). The transaction flow is shown in Figure 4.

5 Analysis of example

5.1 Setting of example

To verify the effectiveness of the proposed trading mechanism, this study established four distribution networks for the purpose of conducting simulation analysis, each equipped with wind turbines, photovoltaic systems, and distributed energy storage devices. The wind and photovoltaic power output forecasts and original load curves for each distribution network in the day-ahead phase, as well as the actual power output and load curves in the intraday phase are provided. The operating parameters of the distributed energy storage devices (Zhao et al., 2022) and tariffs are shown in Supplementary Appendix SA.

This study employs the Yalmip toolbox within the MATLAB R2021b environment to simulate and resolve the given example.

5.2 Analysis of method for determining DAFIDO energy storage action deviations

In the day-ahead operation phase, each distribution network operator optimizes the scheduling with the goal of minimizing energy consumption costs with their respective distribution network, and then obtains charging and discharging strategies for the energy storage plan during the day-ahead phase. In the intraday phase, due to the uncertainty of wind and photovoltaic power output and the deviations in load forecasting, the actual power output and load in the distribution network may differ from the day-ahead forecast. Based on this, the expected energy storage charging and discharging strategies after distribution network optimization during the intraday phase can be obtained. The energy storage charging and discharging strategies for the day-ahead and intraday phases are shown in Figure 5.

As can be seen from the chart depicting energy storage charging and discharging, there are notable deviations in the charging and discharging strategies of distribution network 1 at hours 7, 9, 10, 12, 13, 14, and 19; distribution network 2 at hours 2, 8, 9, and other time periods; distribution network 3 at hours 1, 9, 10, 11, and other time periods; distribution network 4 at hours 2, 5, 8, and other time periods. The energy storage charging and discharging strategies of each distribution network device exhibit notable deviations during the day-ahead and intraday phases, which satisfy the conditions for intraday incremental calculation. In addition, there are significant differences in the energy storage charging and discharging scenarios across the four distribution networks, making it possible to conduct a more in-depth analysis of the supply and demand of energy storage devices in each distribution network.

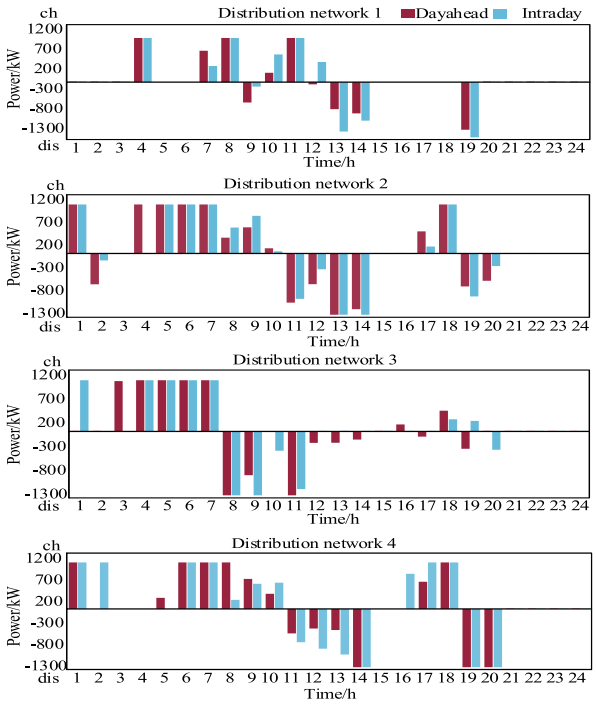

FIGURE 5
The chart of comparison of energy storage, charging and discharging in dayahead and intradays.

The deviation between the actual situation in the intraday phase and the day-ahead phase may result in adverse effects on the distribution network interests if the activities are based on the day-ahead plan. This study proposed to adjust the energy allocation among distribution networks taking into account the expected intraday value on the basis of the day-ahead plan. The energy storage supply and demand quantity proposed in this study is the difference between the day-ahead planned and intraday expected action. The specific supply and demand scenarios for each distribution network are shown in Figure 5.

It can be seen from Figure 6 that there is a significant demand in distribution network 3 at hour 1. At hour 2, distribution network 2, acting as the supplier, has surplus electricity, while distribution network 4, acting as the purchaser, has electricity demand. At hour 11, distribution network 2 and park 3 are both acting as suppliers of electricity, albeit in a relatively small amount, and distribution network 4 is the purchaser, which requires a relatively small amount of electricity. At hour 12, distribution networks 1 and 4 are purchasers, while distribution networks 2 and 3 are suppliers. Therefore, the quantity of supply and demand for each

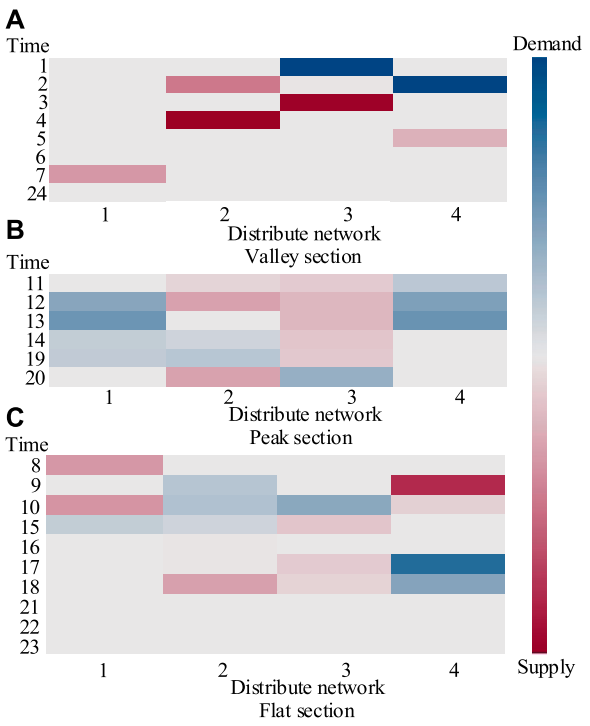

FIGURE 6
Supply and demand diagram of each distribution network. **(A)** Valley section. **(B)** Peak section. **(C)** Flat section.

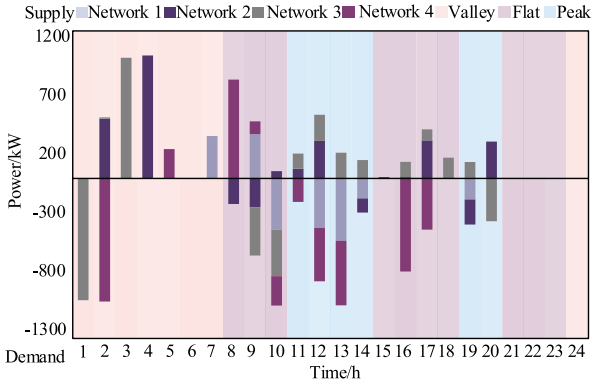

FIGURE 7
Supply and demand bidding diagram of each distribution network.

distribution network during a given time period are interdependent, which can be manifested in various scenarios, such as "one supply, multiple demands," "one demand, multiple supplies," and "multiple demands, multiple supplies". This means that there could exist multiple purchasers and sellers in the same time period during the subsequent trading process.

In addition, the matching of supply and demand in each distribution network occurs more frequently during peak and valley periods, with supply and demand matching at hour 2 in the valley time period. In the subsequent trading process, the majority of trades will occur during peak and valley time periods. The analysis of the specific trading scenario will be conducted later.

5.3 Analysis of distributed energy storage trading mechanism

5.3.1 Analysis of bidding situation

After obtaining the supply and demand quantity, each distribution network operator offers an initial bidding price based on it. The bidding information of the purchaser's and seller's distribution network operators includes the supplied/demanded electricity quantity and the corresponding prices for different time periods.

The schematic diagram of the bidding scenario for the supply and demand quantity of each distribution network is shown in Figure 7. Considering the power deviation day-ahead and intraday, as well as the supply and demand of different distribution networks during the same period, Figure 7 is plotted. It can intuitively show the supply and demand relationship of each distribution network in different time periods, and whether the capacity support of power grid is required. The figure indicates that at hours 1, 3, 4, 5, 7, 15, and 18, there is only one distribution network that has supply or demand, and the supply and demand quantity between distribution networks cannot be matched during these time periods. After submitting the bidding information, the optimized matching results cannot be calculated by the smart contract of the blockchain. Therefore, the supply or demand quantity reported by each distribution network will be directly traded and cleared with the power grid, so no additional analysis will be conducted in this regard. Furthermore, the bidding electricity quantity of each distribution network is more frequently matched during peak and valley periods, with most trading occurring during these two time periods.

The schematic diagram of the bidding price scenario is shown in Figure 8. It can be seen from this figure that the balance of supply and demand within the distribution network takes precedence over the balance of supply and demand between the distribution networks, and the balance of supply and demand between the distribution networks takes precedence over the balance of supply and demand between the distribution networks and the power grid. The supplier's initial bidding price is always lower than the main grid's selling price, and the purchaser's initial bidding price is always lower than the local grid's selling price. Therefore, the trading mechanism proposed in this study is mutually beneficial for the purchaser and the seller, and can ensure the smooth advancement of the trading.

5.3.2 Auction transactions

After obtaining the bidding information of each distribution network, the winning bidder for the trading of each time period is determined by solving the winner determination problem through smart contracts. In the example set in this study, there are 19 time periods that exhibit both supply and demand quantities within the 24 intraday time periods, and 12 time periods that participated in the trading of distributed energy storage trading between distribution networks. The trading scenarios are shown in Figure 9.

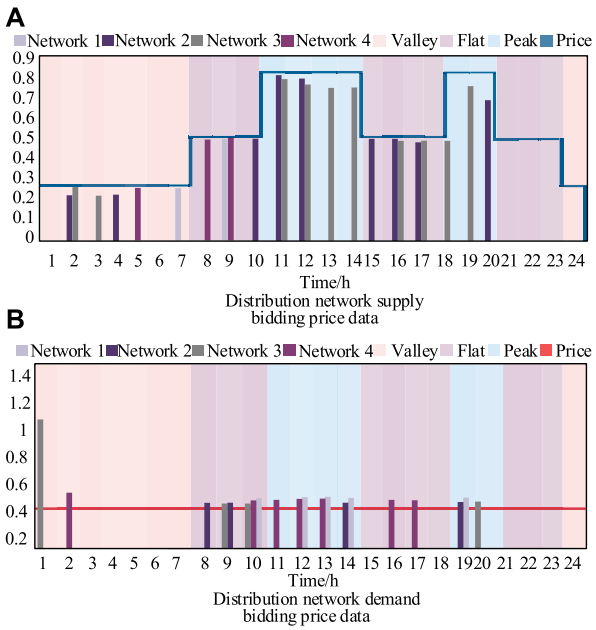

FIGURE 8
Schematic diagram of bidding price data of each distribution network operator. **(A)** Distribution network supply bidding price data. **(B)** Distribution network demand bidding price data.

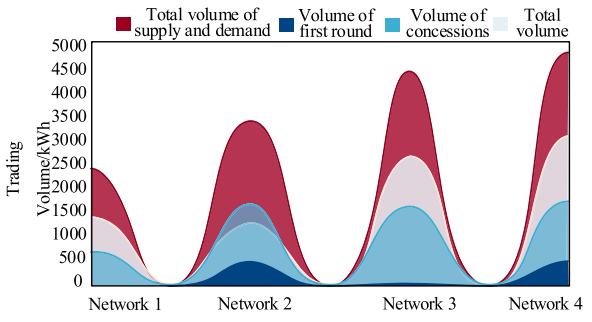

FIGURE 9
The chart of transaction in the auction stage.

It can be seen from Figure 9 that energy flows between distribution networks upon the introduction of the blockchain-based distributed energy storage trading mechanism proposed in this study. The total volume of the three rounds of trading accounts for 28%, 64%, 37%, and 46% of the total supply and demand of each distribution network, which effectively reduces the frequency and quantity of directly purchased and sold electricity between distribution networks, resulting in local consumption of wind and photovoltaic power and effectively reduces their impact on the main grid. At the same time, there is a reduction in the trading volume between the main grid and each distribution network, indirectly indicating that the trading volume between distribution networks increases under the proposed trading mechanism. In other words, the competitiveness of distributed energy storage resources participating in the electricity market trading improves. It improves the dispatching flexibility between the distribution network and the power grid, and among the market participants in the distribution network.

5.4 Analysis of pricing mechanism

The blockchain-based distributed energy storage trading mechanism proposed in this study established that the bidding price of the distribution network operator is always lower than the time-of-use (TOU) tariff of the main grid and the selling price of other distribution networks. However, due to the low tariff during the valley time period, the direct use of the original bidding price for trading will not be conducive to stimulating the sales of electricity from power sources within the distribution network during the valley time period, which will affect the overall electricity balance and scheduling results of the distribution network. To incentivize each distribution network to participate in market-oriented trading during the valley time period, this study introduced an valley compensation mechanism that compensates both trading parties based on the trading volume during the valley time period according to the blockchain smart contract. To verify the rationality of this mechanism, this study has established three scenarios for comparative analysis.

Scenario 1: Each distribution network participates in the distributed energy storage trading mechanism (incorporating the valley compensation mechanism); Scenario 2: Each distribution network participates in the distributed energy storage trading mechanism (without incorporating the valley period compensation mechanism); Scenario 3: Each distribution network does not participate in distributed energy storage trading during the valley time period and directly trades with the main grid.

Based on the data presented in Table 1, it can be observed that at time period 2, distribution networks 2 and 3, acting as sellers, have submitted bidding prices that are lower than the selling price of the main grid, which is RMB 270 per MWh. On the other hand, distribution network 4, acting as the purchaser, has submitted a bidding price that is higher than the selling price of the local power source; as a result, the transaction can proceed. In the first round of trading, distribution networks 2 and 4 traded first, and the trading price they concluded was the average of their bidding prices, that is, RMB 334.80 per MWh. In the second round of trading, distribution network 3 traded with distribution grid 4 at the price of RMB 369 per MWh. The prices of the two rounds of trading are higher than the selling price of the main grid but lower than the selling price of the local power source. Electricity purchasers are more likely to obtain their supply from the distribution network, while electricity sellers are more likely to sell their supply to the distribution network. This will lower the enthusiasm of each park to participate in the distributed energy storage cloud service trading during the valley time period.

Upon the incorporation of the compensation mechanism in Scenario 1, a compensation of RMB 100 per MWh is provided to both the purchaser and the seller during the valley time period according to the smart contract algorithm. The profit of each distribution network in time period 2 across the three scenarios is shown in Table 2.

TABLE 1 The bid situation of the second session.

	Network 2	Network 3	Network 4
Tender volume (Supply+, Demand-)/MWh	4,864.8	105.3	−10,000
Initial offer/(¥/MWh)	228	269	468

TABLE 2 Distribution network profit under different scenarios.

Profits (Profit+,Expense-,Unit: 10,000 yuan)	Network 2	Network 3	Network 4
Scene one	217.878	4.928	−259.118
Scene two	169.210	3.875	−308.839
Scene three	194.672	4.211	−270

By comparing Scenarios 2 and 3, it is evident that distribution network 2 participated in trading without incorporating the compensation mechanism, and the profit in time period 2 was RMB 1.6921 million, which is lower than the profit of RMB 1.94672 million obtained through direct trading with the main grid. In time period 2, distribution network 3 offered a small electricity quantity for bidding, which resulted in unobvious profits, but the quantity offered was still lower than that directly traded with the main grid. When distribution grid 4 participated in trading without incorporating the compensation mechanism, it needed to pay RMB 3.08839 million in time period 2, which is higher than the cost of directly purchasing electricity from the main grid, which amounted to RMB 2.7 million. It can be concluded that in the absence of an valley compensation mechanism, the cost of purchasing electricity from the main grid will be lower for each distribution grid during the valley time period, but it may not be the lowest total cost.

By comparing Scenarios 1 and 3, it is evident that after participating in the trading with the incorporation of the valley compensation mechanism, distribution network 2 earned RMB 2.17878 million in time period 2, which is higher than the profit of RMB 1.94672 million obtained by directly trading with the main grid. The same is true for distribution network 3. Whereas distribution network 4 needs to pay RMB 2.59118 million in time period 2 in trading with the valley compensation mechanism incorporated, which is more favorable compared to the direct purchase of electricity from the main grid, which costs RMB 2.7 million. Therefore, the pricing mechanism proposed in this study suggests that the incorporation of an valley compensation mechanism is more financially advantageous for users who participate in the service compared to direct trading with the main grid, thereby effectively increasing users' inclination to participate in the service during the valley time period.

Data in Table 3 indicate that the incorporation of the distributed energy storage trading mechanism resulted in a reduction of electricity purchases from the main grid by several distribution networks during time period 2. Specifically, distribution network 2 reduced its purchase of electricity by 4,866.80 MWh; distribution grid 3 reduced its purchase of electricity by 105.26 MWh, and distribution grid 4 reduced its purchase of electricity by 4,972.06 MWh. This effectively reduces the quantity of electricity traded between the distribution network and the main grid, thereby reducing the impact of the uncertainty of wind and photovoltaic power on the main grid and improving power system flexibility. It should be noted that the system scheduling under consideration prioritizes the maximization of power output stability and economic efficiency of trading, without taking into account the potential impact on system safety in the event of power supply shortages. In addition, the different division of electricity price periods will affect the electricity consumption habits of market participants in the distribution network, so the transaction price characteristics will also change.

TABLE 3 Transaction volume of each distribution network and power network under different scenarios.

Trading volume (MWh)	Network 2	Network 3	Network 4
Scene one	0	0	5,027.94
Scene two	0	0	5,027.94
Scene three	4,866.80	105.26	10,000

5.5 Analysis of social welfare

The blockchain service fee established in this study is RMB 100 per MWh, and the resulting social welfare outcomes under the proposed trading mechanism are presented in Table 4. It can be seen that after incorporating the distributed energy storage cloud service trading mechanism, distribution network 3 has the highest revenue increase, amounting to RMB 2.68757 million, while distribution network 1 has the lowest revenue increase, amounting to RMB 0.77484 million. However, it should be noted that the revenue of each distribution network has increased compared to before incorporating the mechanism.

According to Table 4, the incorporation of a distributed energy storage cloud service trading mechanism, which takes into account the DAF-IDO energy storage action deviation in the proposed multiple distribution networks, has resulted in an improvement in the economic benefits of each distribution network, which has subsequently increased their inclination to participate in the distributed energy storage market trading. At the same time, this mechanism can ensure that all other parties generate considerable

TABLE 4 Before and after participating in the trading mechanism profit comparison.

Profits (Profit+,Expense-)	Pre-participation benefits	Post-participation benefits	Relative benefits
Network 1	−960.547	−883.063	77.484
Network 2	535.856	762.207	226.351
Network 3	−67.057	201.700	268.757
Network 4	−1,484.619	−1,235.419	249.757
Blockchain operations benefits	/	442.854	/

profits. Profits will positively encourage all market members to participate in market transactions. The degree of positive motivation needs to be further studied.

6 Conclusion and prospects

This study proposed a method for determining DAF-IDO energy storage action deviations, and on this basis, introduced a trading mechanism for blockchain-based distributed energy storage of multiple distribution networks and improved the trading pricing mechanism. Through theoretical and simulation analysis, it can be inferred that.

(1) The trading mechanism for distributed energy storage of multiple distribution networks proposed in this study taking into account the DAF-IDO energy storage action deviations under multiple distribution networks ensures that the energy demand of market participants is met. In addition, this mechanism facilitates the circulation of dispersed distributed energy storage among users, thereby effectively improving the utilization rate of distributed energy storage devices, enhancing economic efficiency, and promoting local consumption of energy.
(2) The method for determining DAF-IDO energy storage action deviations proposed in this study can effectively quantify the supply and demand quantity of energy storage devices participating in the market trading, providing a new perspective for energy storage to participate in market trading and improving its market power.
(3) The incorporation of an valley compensation mechanism within the energy storage price mechanism has resulted in an improved economic efficiency of distribution networks, thereby effectively ensuring distribution networks' inclination to participate in trading during valley time periods.

This study introduced a new market strategy and outlook for distributed energy storage devices to participate in market trading, thereby enhancing the overall flexibility of the power system. The method for determining DAF-IDO energy storage action deviations proposed in this study is not limited to distributed energy storage and can be extended to centralized energy storage. In the future, research should delve deeper into the impact of grid power flow constraints on the proposed trading mechanism in this study, and explore the allocation of benefits between distribution network operators and internal users.

Data availability statement

The original contributions presented in the study are included in the article/Supplementary Material, further inquiries can be directed to the corresponding author.

Author contributions

DC contributions: conceive, simulation and write manuscripts, JH, XC, and ZL, contributions: guide thesis ideas. All authors contributed to the article and approved the submitted version.

Acknowledgments

Thanks for the technical support provided by the State Grid Beijing Electric Power Company.

Conflict of interest

Authors DC and XC were employed by Capital Power Exchange Center Co., Ltd.

The remaining authors declare that the research was conducted in the absence of any commercial or financial relationships that could be construed as a potential conflict of interest.

Publisher's note

Supplementary material

The Supplementary Material for this article can be found online at: https://www.frontiersin.org/articles/10.3389/fenrg.2023.1240611/full#supplementary-material

References

Chen, Cen, Wu, Chuantao, Kang, Kai, Lin, Xiangning, Ma, Yuncong, Quan, Sui, et al. (2023b). Optimal strategy of distributed energy storage two-layer cooperative game based on improved owen-value method. *Proc. CSEE*, 1–14. doi:10.13334/j.0258-8013.pcsee.211275

Chen, Xi, Fu, Wenlong, and Zhang, Hairong (2023a). Optimal dispatching strategy of shared energy storage and multi-microgrid considering the uncertainty of new energy generation. *Power Syst. Technol.*, 1–17. doi:10.13335/j.1000-3673.pst.2022.2541

Cui, Dongjun, He, Jinghan, Zhang, Guofang, and Hou, Zihan (2022). Blockchain-based distributed power market trading mechanism. *Comput. Mater. Continua* 72 (2), 2845–2858. doi:10.32604/cmc.2022.026568

Dai, R., Esmaeilbeigi, R., and Charkhgard, H. (2021). The utilization of shared energy storage in energy systems: A comprehensive review. *IEEE Trans. Smart Grid* 12 (4), 3163–3174. doi:10.1109/tsg.2021.3061619

Dai, Sai, Li, Yuxuan, and Sun, Zhixiang (2022). Online sharing optimization matching transaction mode for distributed energy storage. *High. Volt. Eng.* 48 (07), 2515–2522. doi:10.13336/j.1003-6520.hve.20220097

Hu, Yu, Li, Huaqiang, and Li, Shanshan (2022). Peer-to-peer power trading method for proconsumers based on blockchain. *Electr. Power Autom. Equip.* 42 (01), 101–108. doi:10.16081/j.epae.202112005

Huang, Weidong, Yang, Li, and Li, Jingyan (2023). Multi-time scale joint optimal scheduling for wind-photovoltaic-electrochemical energy storage-pumped storage considering renewable energy uncertainty. *Electr. Power Autom. Equip.*, 1–19. doi:10.16081/j.epae.202210002

Kang, Chongqing, Liu, Jingkun, and Zhang, Ning (2017). A new form of energy storage in future power system: cloud energy storage. *Automation Electr. Power Syst.* 41 (21), 2–8. doi:10.7500/AEPS20170601011

Li, Jianlin, Cui, Yilin, and Ma, Suliang (2022a). Operation mode optimization and economic benefit analysis of demand-side shared energy storage. *Power Syst. Technol.* 46 (12), 4954–4969. doi:10.13335/j.1000-3673.pst.2022.1218

Li, Shanshan, Li, Huaqiang, and Jin, Zhibo (2022b). Distributed energy sharing service mechanism for park based on the concept of sharing economy. *Proc. CSEE* 42 (01), 56–71. doi:10.13334/j.0258-8013.pcsee.202046

Li, Xuan, Li, Huaqiang, and Li, Xuxiang (2021). Peer-to-peer trade and control for distributed energy storage based on blockchain technology. *Power Syst. Technol.* 45 (09), 3424–3432. doi:10.13335/j.1000-3673.pst.2020.1726

Liu, Jingkun, Zhang, Ning, and Kang, Chongqing (2017). Research framework and basic models for cloud energy storage in power system. *Proc. CSEE* 37 (12), 3361–3371+3663. doi:10.13334/j.0258-8013.pcsee.170208

Liu, J., Zhang, N., Kang, C., Kirschen, D. S., and Xia, Q. (2018). Decision-making models for the participants in cloud energy storage. *IEEE Trans. Smart Grid* 9 (6), 5512–5521. doi:10.1109/tsg.2017.2689239

Ma, Yuncong, Wu, Chuantao, Lin, Xiangning, Chen, Cen, Li, Zhengtian, Fanrong, Wei, et al. (2022). Research on peer-to-peer transaction strategy of cloud energy storage based on semi-distributed structured topology. *Proc. CSEE* 42 (21), 7731–7746. doi:10.13334/j.0258-8013.pcsee.211263

Meng, Song, Lin, Gujing, and Meng, Jing (2023). Key technologies and applications of shared energy storage. *J. Shanghai Jiaot. Univ.*, 1–28. doi:10.16183/j.cnki.jsjtu.2022.360

Nan, Bin, Jiang, Chundi, and Dong, Shufeng (2023). Day-ahead and intra-day coordinated optimal scheduling of integrated energy system considering uncertainties in source and load. *Power Syst. Technol.*, 1–15. doi:10.13335/j.1000-3673.pst.2022.2080

Saini, V. K., Seervi, A., Kumar, R., Mahmud, M. A., and Al-Sumaiti, A. S. (2022). Cloud energy storage based embedded battery technology architecture for residential users cost minimization. *IEEE Access* 10, 43685–43702. doi:10.1109/access.2022.3168599

Tushar, W., Chai, B., Yuen, C., Huang, S., Smith, D. B., Poor, H. V., et al. (2016). Energy storage sharing in smart grid: A modified auction-based approach. *IEEE Trans. Smart Grid* 7 (3), 1462–1475. doi:10.1109/tsg.2015.2512267

Wang, Miaomiao, Li, Huaqiang, and He, Yongxiang (2022). Cloud energy storage service mechanism considering multi-agent power transaction. *Electr. Power Constr.* 43 (11), 73–84. doi:10.12204/j.issn.1000-7229.2022.11.008

Wu, S., Li, H., Liu, Y., Lu, Y., and Wang, Z. (2023). A two-stage rolling optimization strategy for park-level integrated energy system considering multi-energy flexibility. *Int. J. Electr. Power & Energy Syst.* 145, 108600. doi:10.1016/j.ijepes.2022.108600

Xiang, You, Li, Huaqiang, and Lu, Yang (2022). Pricing strategy for multi-microgrid centralized trading considering distribution network power flow. *Power Syst. Technol.* 46 (04), 1297–1309. doi:10.13335/j.1000-3673.pst.2021.0492

Xue, Hui (2015). *The reserch on the pricing of cloud computing resources based on combinatorial double auction*. Beijing, China: Beijing University of Posts and Telecommunications.

Yan, Dongxiang, and Chen, Yue (2022). Review on business model and pricing mechanism for shared energy storage. *Automation Electr. Power Syst.* 46 (23), 178–191. doi:10.7500/AEPS20220219003

Zhang, Mingxia, Yan, Tao, Lai, Xiaokang, Chen, Jizhong, Niu, Meng, and Xu, Shaohua (2018). Technology vision and route of energy storage under new power grid function configuration. *Power Syst. Technol.* 42 (05), 1370–1377. doi:10.13335/j.1000-3673.pst.2017.2475

Zhang, Wei, and Hui, Miao (2021). Bidding strategies of wind power and energy storage participating in energy and frequency regulation market based on cloud energy storage leasing services. *Power Syst. Technol.* 45 (10), 3840–3852. doi:10.13335/j.1000-3673.pst.2020.1955

Zhao, Pengjie, Wu, Junyong, and Zhang, Wenhao (2022). Cooperative peer to peer scheduling of multi-microgrids considering distribution network power flow and source-load uncertainty. *Power Syst. Technol.* 46 (12), 4885–4896. doi:10.13335/j.1000-3673.pst.2022.0789

Zhou, Xiaoxin, Chen, Shuyong, Lu, Zongxiang, Huang, Yanhao, Ma, Shicong, and Zhao, Qiang (2018). Technology features of the new generation power system in China. *Proc. CSEE* 38 (7), 1893–1904+2205. doi:10.13334/j.0258-8013.pcsee.180067

frontiers | Frontiers in Energy Research

TYPE Original Research
PUBLISHED 14 September 2023
DOI 10.3389/fenrg.2023.1251496

OPEN ACCESS

EDITED BY
Mingfei Ban,
Northeast Forestry University, China

REVIEWED BY
Feng Li,
Nanjing Normal University, China
Rui Wang,
Northeastern University, China
Dongliang Xiao,
South China University of Technology, China

*CORRESPONDENCE
Zhou Li,
lizhou1985@163.com

RECEIVED 01 July 2023
ACCEPTED 28 August 2023
PUBLISHED 14 September 2023

CITATION
Wang Y, Li Z and Zhang Y (2023), A decision-making method for the operation flexibility enhancement of hybrid cascaded MTDC.
Front. Energy Res. 11:1251496.
doi: 10.3389/fenrg.2023.1251496

A decision-making method for the operation flexibility enhancement of hybrid cascaded MTDC

Yuhan Wang, Zhou Li* and Yuanshi Zhang

School of Electrical Engineering, Southeast University, Nanjing, China

To enable the integration of large-scale renewable energy, hybrid HVDC technology, which combines the technical advantages of LCC-HVDC and VSC-HVDC, is being gradually deployed in the power grid nowadays. The operation of the Wu-dong-de Hybrid DC Project and the Jian-su Hybrid cascaded MTDC Project has proved its advantages. However, for the simultaneous application of different converter station technologies in the system, the control strategies become complex. Issuing appropriate control instructions to ensure system stability according to operational requirements is an issue that cannot be ignored in decision-making. Even under abnormal conditions, when the topology changes due to various failure scenarios, reasonable decision-making and precise control instruction definitions are required. To achieve flexible planning of the MTDC system, this paper presents a decision-making method for control strategies of a hybrid cascaded MTDC system, which analyzes the control strategy combinations selected for normal and abnormal conditions of the MTDC system. In addition, a control instruction calculating method and decision-making process for precise control in normal and abnormal control conditions is proposed. Simulation results based on a five-terminal hybrid cascaded MTDC in PSCAD/EMTDC have verified the effectiveness of the proposed method.

KEYWORDS

LCC-HVDC, VSC-HVDC, hybrid cascaded HVDC, MTDC, decision-making, normal control, abnormal control

1 Introduction

High-voltage direct current technology, including LCC-HVDC and VSC-HVDC, plays an important role in power transmission and allocation, as well as variable renewable energy (VRE) regulation (Liu et al., 2015; Alves et al., 2020). LCC-HVDC power transmission technology has the advantages of large transmission capacity, a high voltage level, low manufacturing cost, and high reliability (Kwon et al., 2018; Chen et al., 2022), making it widely used in large-capacity and long-distance power transmission systems. VSC-HVDC power transmission technology (Flourentzou et al., 2009; Wang R. et al., 2020; Zhao and Tao, 2021; Xu et al., 2023) has advantages of flexible control and easy power flow reversal, making it more advantageous in the fields of large-scale renewable energy integration (Wang et al., 2022), passive grid power supply, and multi-terminal HVDC transmission (Rao et al., 2019; Li et al., 2021a; Li et al., 2021b; Li et al., 2022).

Hybrid HVDC transmission technology (Rao et al., 2022) combines the technical advantages of LCC-HVDC and VSC-HVDC, which not only overcomes the challenges of long-distance transmission with high-power but also solves VRE integration, power quality, and grid asynchronous interconnection in a power system, and is gradually applied in engineering.

Currently, the Wu-dong-de Hybrid DC Project and the Jian-su Hybrid cascaded MTDC Project in China are in operation and have proven their worth (Haleem et al., 2019; Reza Ahrabi et al., 2022).

However, due to the simultaneous use of VSC and LCC commutation technologies (Aziz et al., 2019; Wang T. et al., 2020), the physical mechanism of MTDC is more complex. In this system, there are control requirements related to multiple voltage levels, as well as the determination of power commands at different converter stations. Under normal operating conditions, a variety of available control modes can be selected for different converters, and the control strategy combinations without restriction are complex and confusing for decision-making. In addition, issuing appropriate control instructions to ensure system stability according to operational demands is a problem that cannot be ignored in decision-making. Under abnormal operating conditions, permanent faults occur on the AC or DC side of the system, leading to changes in the topology (Ren et al., 2023). To reduce the impact of faults, decision-making methods are also needed to provide the corresponding combinations of control strategies and solve the allocation problem of transmission power of faulty poles.

Previous research has mainly focused on studying a single strategy in specific scenarios, while little research has been performed at the system level to select control strategy combinations for hybrid cascaded MTDC systems with different converter stations, which cannot provide appropriate control strategies and precise instructions for a system based on regulatory requirements (Li et al., 2020). To achieve flexible planning of the MTDC system, it is necessary to analyze the coupling relationship between different converter stations in the hybrid cascaded MTDC system, sort out various control strategies adopted by multiple converter stations, and identify feasible control strategy combinations under normal and abnormal conditions.

In view of the aforementioned considerations, this paper proposes a control strategy decision-making method for the hybrid cascaded MTDC system with the following contributions:

1) For normal control, a two-stage analysis method is proposed for the selection of control strategy combinations for the selection of the hybrid cascaded MTDC system. In the first stage, VSCs are considered VSCBs, and the control strategies of series LCCs are determined. In the second stage, the station-level control strategies for VSCs are determined.
2) For abnormal control, abnormal conditions that cause the quitting operation of converter stations are classified. In addition, control strategy combinations of the selection method including three control strategy combinations that can deal with the quitting operation of converter stations are proposed.
3) A control instruction calculating method and decision-making process for normal and abnormal controls are proposed. According to the calculation method, under normal conditions, the control instructions are accurately calculated and assigned to the controllers of the MTDC system. Under abnormal conditions, reasonable instructions for converters in bipolar MTDC are calculated to achieve the transfer of active power in faulty poles.

The rest of the paper is organized as follows: in Section 2, the topology and control strategies of the hybrid cascaded MTDC system are analyzed, and the decision-making method for control strategies and the control instruction calculating method for the hybrid cascaded MTDC system under normal and abnormal conditions are proposed. In Section 3, simulations in different scenarios of different control strategies are analyzed to verify the effectiveness of the proposed strategy. Finally, the conclusions are drawn in Section 4.

2 Decision-making method for the control strategy of a hybrid cascaded MTDC system

2.1 Features and control demand of a hybrid cascaded MTDC

As shown in Figure 1, the topology of the hybrid cascaded MTDC system is based on the real hybrid HVDC project. The project is responsible for transmitting abundant hydropower power from the Baihetan Hydropower Station, which is the second largest hydropower station in the world, to the southern part of Jiangsu Province. The DC system adopts a bipolar topology, with the rectifier side composed of LCCs (±800 kV) and the inverters composed of parallel-connected VSCs (±400 kV) connected in series with LCCs (±400 kV). Three VSCs connected in parallel can be equated to a VSCB (Bank of VSCs) as they are at the same voltage level, as shown in Figure 2, and their capacitance is equal to their sum. LCC and VSC inverters are connected to different AC buses and with weak interactions.

To facilitate the analysis of control strategies for hybrid cascaded MTDC systems, LCCs and VSCBs can be categorized into two types, namely, the power control station and voltage control station, depending on the overall control effect of LCC/VSCB, which will be discussed in Section 2.2.

Based on the analysis of the topology of the hybrid cascaded MTDC system, features and control demands of the system can be summarized into the following rules (Li et al., 2020):

Rule 1: Since the receivers LCC and VSCB are connected in series, and there are two voltage levels in the transmission line, to achieve stable control in a hybrid cascade system, it is necessary to have two converter stations serving as voltage control stations. Since the system converter station operates in the series mode, the system must have a converter station that serves as a power control station.

Rule 2: The status of the hybrid cascaded MTDC system can be calculated using Eq. 1 as follows:

$$\begin{cases} U_1 = \dfrac{3\sqrt{2}}{\pi} U_{LR} \cos\alpha - \dfrac{3}{\pi} X_{Rc} I_{dc}, \\ U_2 = \dfrac{3\sqrt{2}}{\pi} U_{Li} \cos\gamma - \dfrac{3}{\pi} X_{ic} I_{dc}, \\ U_1 = U_2 + U_3 + U_L, \\ P_1 = U_1 \times I_{dc}, \\ P_2 = U_2 \times I_{dc}, \\ P_3 = U_3 \times I_{dc}, \end{cases} \tag{1}$$

where U_{LR}, U_{Li}, X_{RC}, and X_{iC} is the AC voltage and equivalent reactance of rectifier and inverter LCC. P_i represents the transmission power of LCC1, LCC2, and VSCB, respectively. In addition, α represents the trigger delay angle of LCC1, and γ represents the extinction angle of LCC2. U_L represents the voltage drop of the DC line.

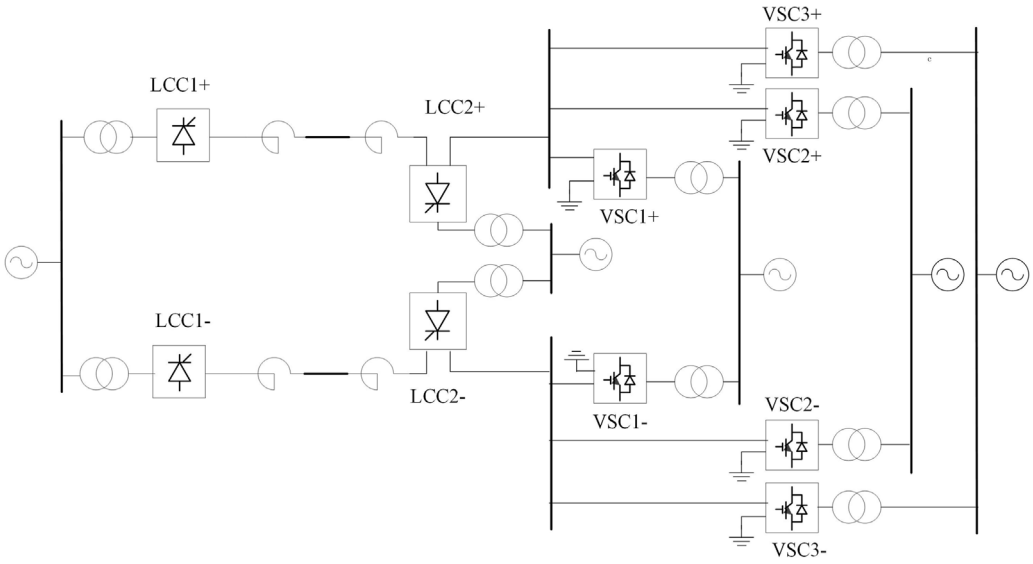

FIGURE 1
Hybrid cascaded MTDC system.

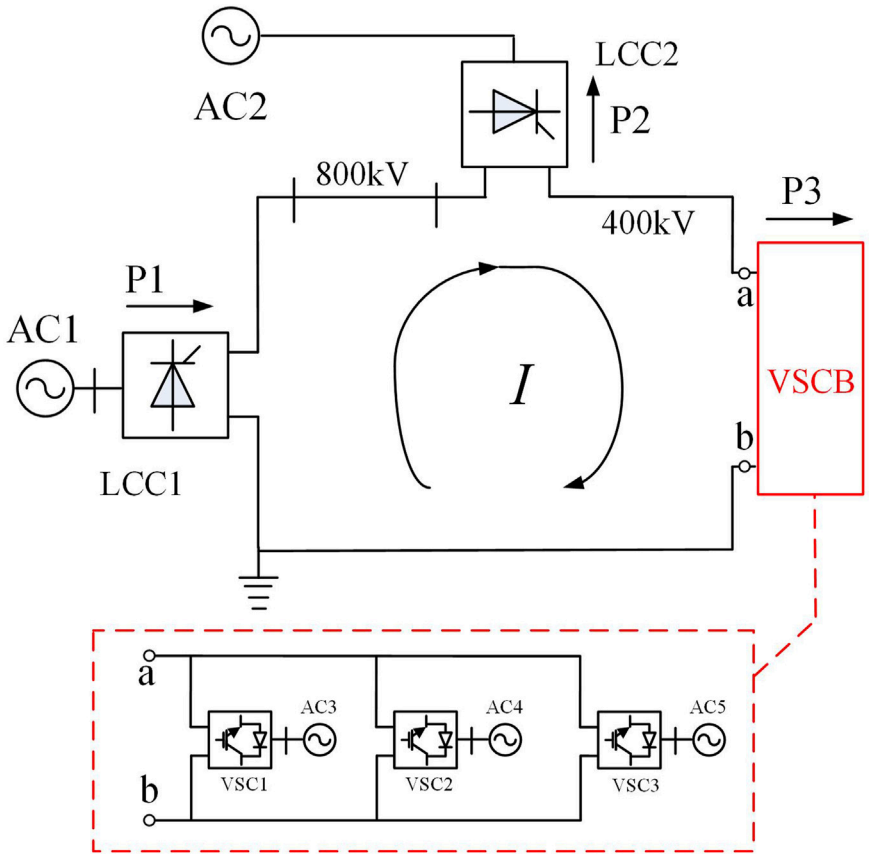

FIGURE 2
Unipolar equivalent circuit of a hybrid cascaded MTDC system.

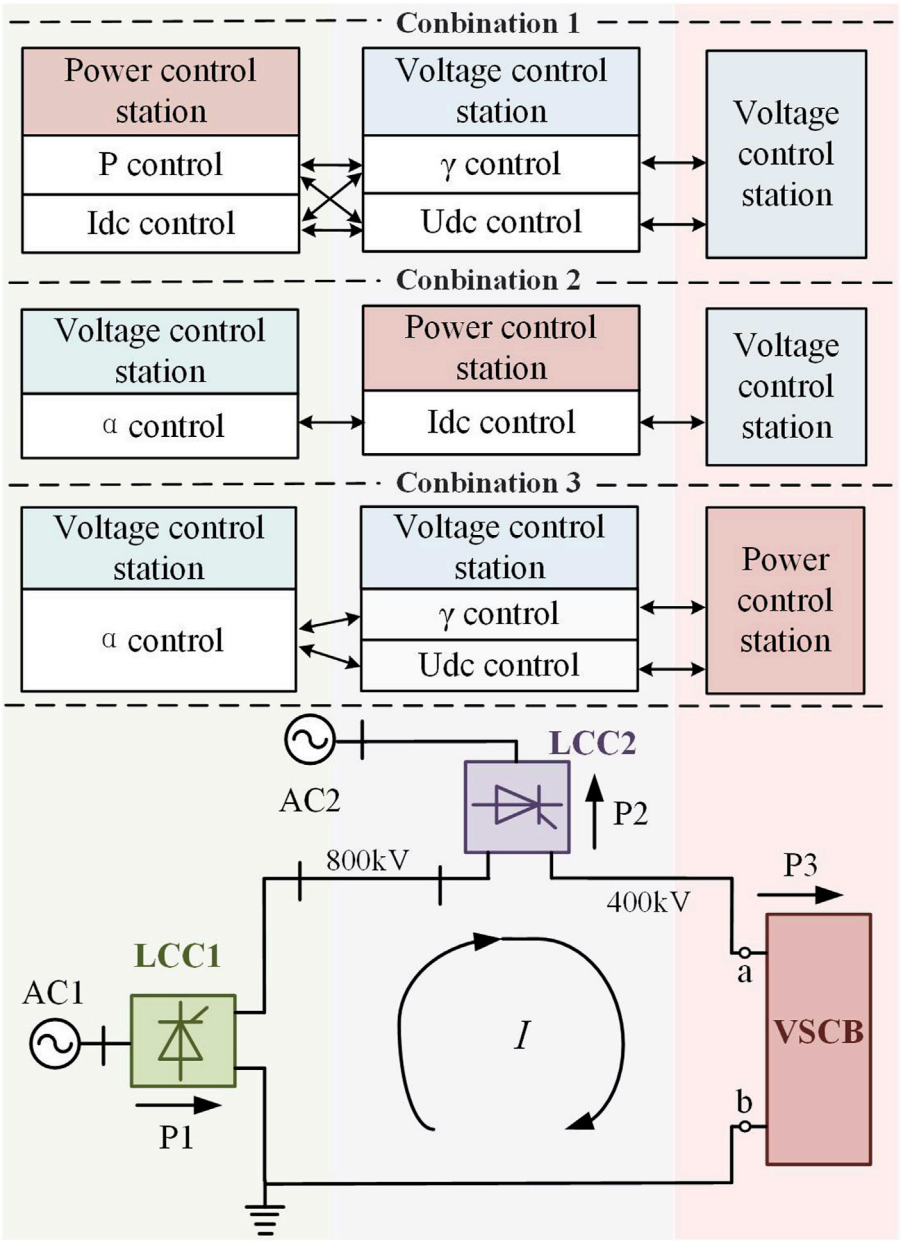

FIGURE 3
Selection of control strategy combinations in the first stage.

Rule 3: The topologies of the hybrid cascaded MTDC system are symmetrical. Therefore, the control strategies in each pole can be symmetrical accordingly.

2.2 Decision-making method for normal control

2.2.1 Control strategy combination selecting method for normal control

To improve the flexibility of the system, different control strategies can be used to maintain the operation of converter stations under different objectives. However, since the hybrid cascaded MTDC system includes both LCCs and VSCs, many available control strategy combinations can be selected for different converters, of which the combination of control strategies without a constraint is complex and confusing for decision-making. Thus, to solve the decision-making problem, reasonable combinations of control strategies based on the system topology and demands are analyzed in this section.

The analysis process is divided into two stages. In the first stage, shown in Figure 3, VSCs are considered VSCBs, and the control strategies of series LCCs are determined. In the second stage, shown in Figure 4, station-level control strategies for VSCs

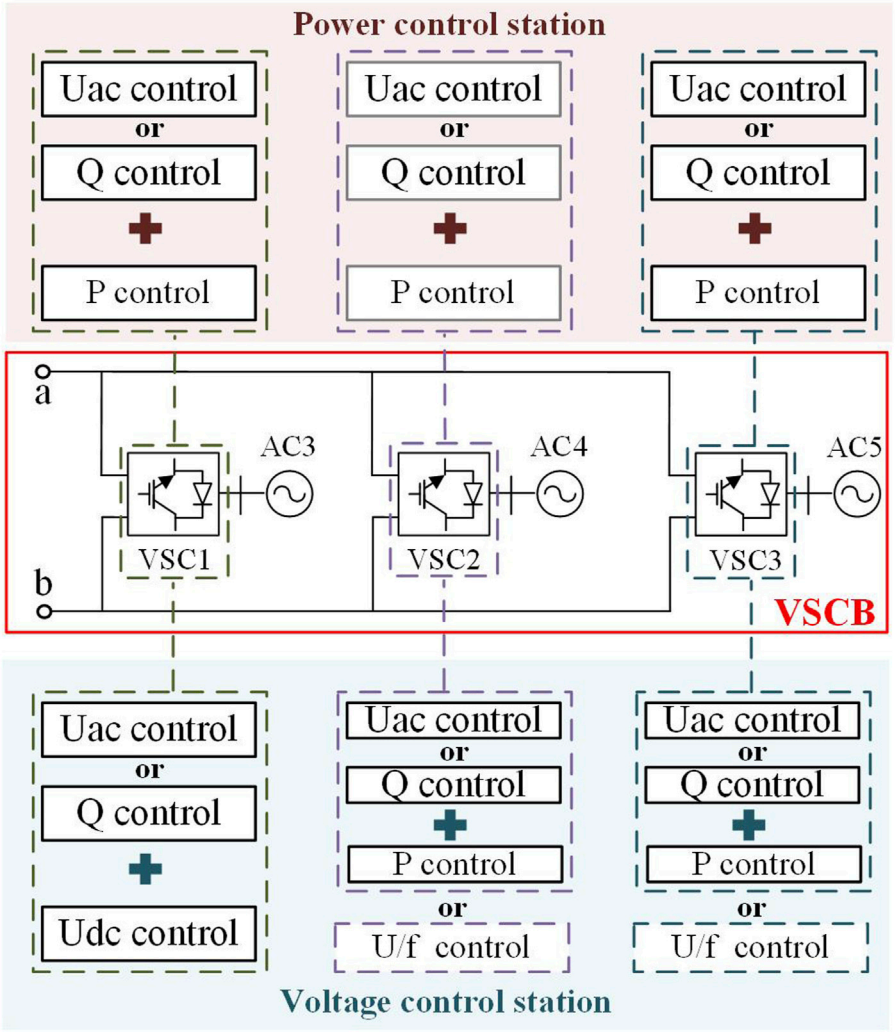

FIGURE 4
Selection of control strategy combinations in the second stage.

are determined, which solves the problem of difficulties in decision-making.

1) Stage 1: The control strategies of LCCs are analyzed under the assumption that VSCs are considered VSCBs. The functions of each converter station (power control station/voltage control station) are determined. Since the selection of control strategies is strongly related to power regulation instructions under normal circumstances, recommended operation control strategies can be provided based on power dispatch instructions from different ends, combined with Figure 3.

When there is a scheduling requirement for LCC1, to be selected as the power control station, LCC2 and VSCB are simultaneously selected as the voltage control station. Based on combination 1 in Figure 3, there are two recommended control modes for LCC1: the constant power control mode or constant DC current control mode. In the constant power control mode, LCC1 directly controls the active power transmission on the AC side. In the constant DC current control mode, power control can be achieved through calculations based on the voltage control station.

When there is a system power dispatch command at LCC2, LCC2 can be used as a power control station or voltage control station for its current coupling relationship with other converter stations. Based on combination 1, when LCC2 is selected as a power control station, it operates in a constant DC current control mode. Based on combinations 1 and 3, when LCC2 is used as a voltage control station, LCC1 or VSCB can also be selected as a power control station to control line current and perform calculations, using current coupling relationships to achieve indirect power control.

When receiving system power scheduling commands in VSCs, VSCB can serve as a voltage control station or power control station.

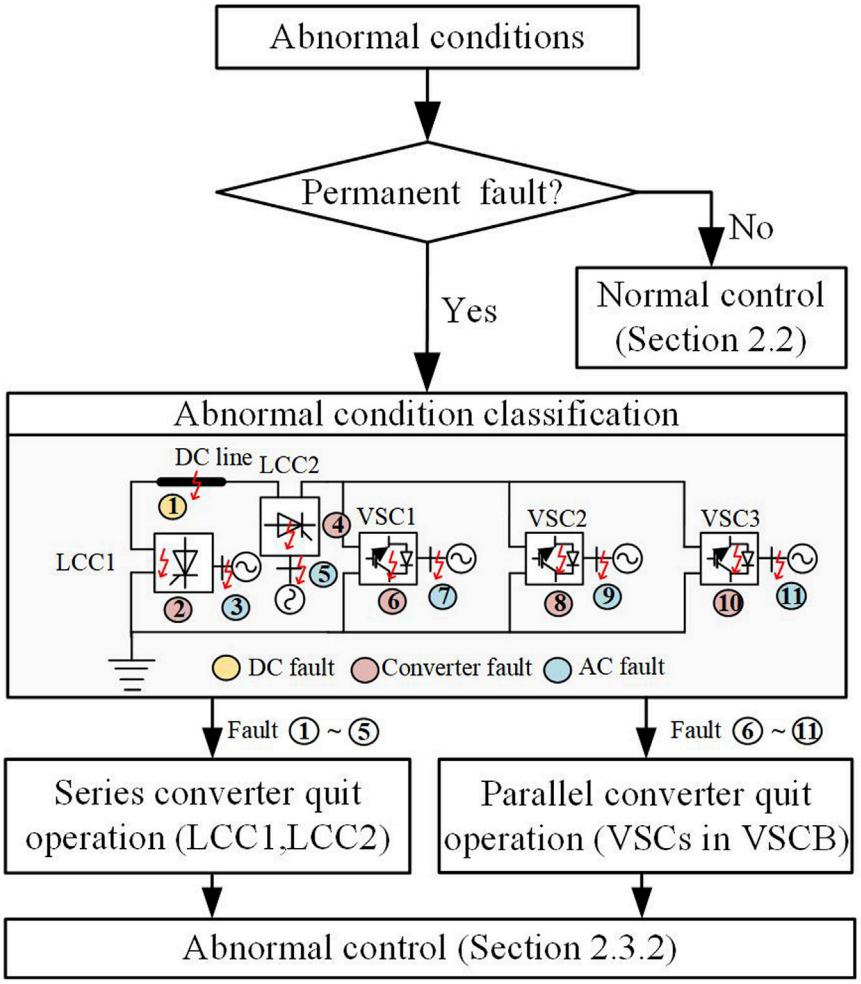

FIGURE 5
Classification of abnormal conditions.

2) Stage 2: The control strategies at the station level are determined for three VSCs. If the VSCB serves as a voltage control station and not all VSCs have power control commands, VSCs without power control commands can be selected to operate in a constant DC voltage control mode, while other VSCs have no restrictions (see Figure 4). If the power control requirement exists in all VSCs, VSCB is selected as the power control station, which means that all VSCs adopt the constant power control mode. In addition, each VSC station can select appropriate reactive power control strategies based on the demand on the AC side of the converter station nearby.

2.2.2 Control instruction calculating method and decision-making process for normal control

After the aforementioned analysis and considering the upper and lower limit issues, equality constraints, and compatibility issues between different converter station control strategies during the operation and control process of hybrid cascaded MTDC systems, the control strategy to achieve the target steady-state operating point of the system can be derived from the following process:

Step 1: Obtain scheduling requirements and select corresponding control strategies. For example, if active power control is required at a converter station in a hybrid cascaded MTDC system, control strategies that can be applied in each converter station can be seen in Figure 3 and Figure 4.

Step 2: Calculation of the operating point. Based on the conditions mentioned in step 1 and the two voltage levels of the system, the system mathematical model within a five-terminal hybrid cascade MTDC system can be expressed as in Eq. 1. Without considering the active power feedback of VSC, the transmission power of VSC in VSCB which adopts a constant power control mode can be expressed as Eq. 2:

$$P^{i}_{VSC\_P} = \frac{P_3}{3}, \tag{2}$$

where P_3 is calculated in Eq. 1.

Step 3: Control reference instruction assignment (U_1, U_2, U_3, P_1, P_2, P_3, α, γ, and I_{dc}). The control reference needed is assigned to the controllers according to control strategy combinations selected in step 1.

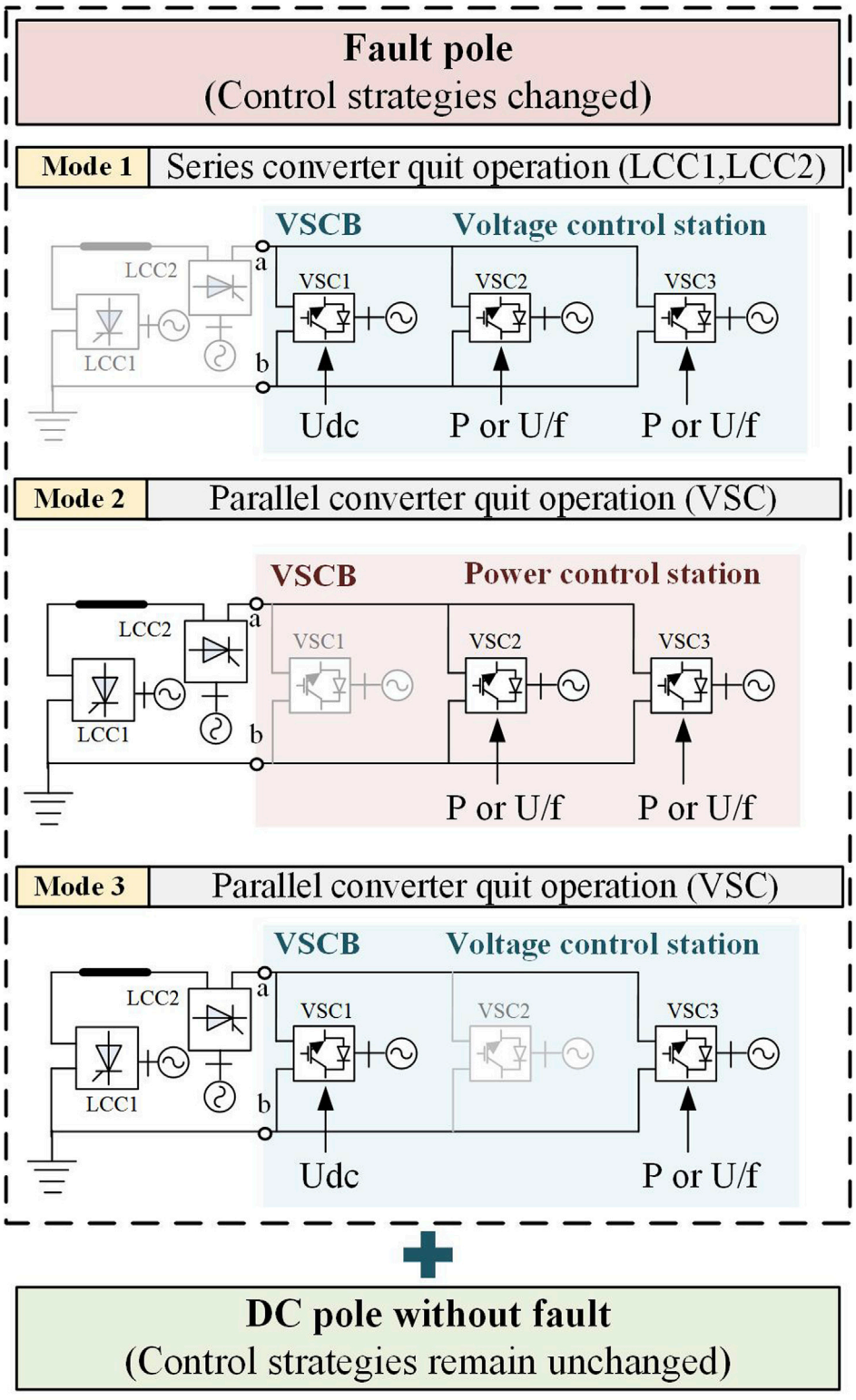

FIGURE 6
Feasible topology and control strategy combinations after a fault.

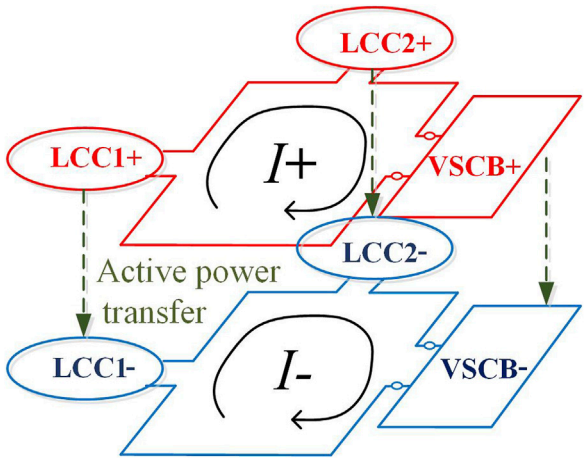

FIGURE 7
Active power transfer under abnormal conditions.

2.3 Decision-making method for abnormal control

2.3.1 Classification of abnormal conditions in a hybrid cascaded MTDC system

As shown in Figure 5, abnormal conditions in a hybrid cascaded MTDC system can be divided according to the duration of the fault. If faults in the MTDC system can be quickly cleared, such faults are classified as transient abnormal conditions, after which the decision-making method for normal control can be re-run for the MTDC system (see Section 2.2). Otherwise, such faults belong to permanent abnormal conditions, and these types of faults will inevitably cause the converter in the system to quit operation.

Permanent abnormal conditions in a hybrid cascaded MTDC system include short circuits and broken line faults in DC and AC lines. When the system is in a permanent abnormal condition, it is necessary to classify the abnormal conditions. The persistence of the fault will cause the neighboring inverter to quit operation. According to the topology analysis in Figure 1, if there is an AC fault near the converter station, both poles of the converter station will quit operation simultaneously due to the connection to the same AC bus. If the fault is in the converter itself or in the DC line, it is generally a unipolar fault. In the following section, decision-making will be analyzed under abnormal conditions based on the quitting of the converter station and the original control strategy combinations of the system.

2.3.2 Control strategy combination selecting method for abnormal control

Due to the bipolar topology of the MTDC system, an independent analysis of the unipolar/bipolar fault is required when the system is in a permanent abnormal condition. It is worth noting that this article mainly analyzes common faults (including N-1) in the MTDC system.

In the case of unipolar faults, the topology of the system fault pole needs to be adjusted after the fault as the converter station quits. Moreover, there are completely different control strategies between the DC pole without fault and the faulty pole of the system. As shown in Figure 6, there are three strategy combinations for the fault pole which can deal with the topology adjustment after the fault. In addition, the DC pole without fault can adjust the power reference value to partially transfer the faulty pole power to itself.

1) According to mode 1 shown in Figure 6, the topology and control strategy of fault response are to solve the operational difficulty when LCC1 or LCC2 quits operation due to faults. In this fault response mode, VSCB must operate as a voltage control station to maintain the DC voltage. According to the principle of voltage control stations, taking VSC1 as an example in Figure 6, one VSC needs to be selected to operate in a constant DC voltage mode internally in VSCB, while the other two converter stations are not restricted in their operating modes.
2) According to mode 2, the parallel converter quits operation in abnormal conditions, when VSCB operates as a power control station. Mode 2 of fault response is to address the fault of VSC quit operation from VSCB, which operates as a power control station. In this mode, after the fault occurs, it is not necessary to adjust the control strategy of each converter station.
3) According to mode 3, VSCB operates as a voltage control station. Mode 3 of fault response is to address the fault of VSC quit operation from VSCB, which operates as a voltage control station. When a fault occurs, if the quit VSC is in constant power or the U/f control mode, the control strategy adopted by inverters remains unchanged. If the quit VSC operates in the constant DC voltage control mode, the system needs to select another VSC for changing the control strategy to the constant DC voltage control mode.

When analyzing bipolar faults in the system, due to the identical topology and control strategy before the positive and negative pole faults, the control strategy after the fault is identical as well and can replicate the control mode for unipolar faults.

After completing the post-fault analysis of the operational control strategy, the calculation of instructions for each converter station with differences between unipolar and bipolar faults will be discussed in detail in Section 2.3.3.

2.3.3 Control instruction calculating method and decision-making process for abnormal control

Based on the previous analysis, we can conclude that the three modes of control strategy combinations to cope with topology adjustment in Figure 6 mainly involve the analysis of VSC. Therefore, the control instructions for each converter station within VSCB must be calculated first, and then, the reference value of the MTDC system can be calculated according to Eq. 1. In this section, a control instruction calculation method and decision-making process based on the power transfer capability of bipolar MTDC (see Figure 7) are proposed to achieve power transfer between converter stations under fault conditions. The calculation method for the control instructions of the VSCB instruction used for abnormal control is as follows:

1) Calculation of control instructions of mode 1. If the fault is a bipolar fault, VSC that can provide active power support will provide power to the other VSCs, as shown in Eq. 3, and there is

TABLE 1 Calculation results of the decision-making method in scenario 1.

Parameter	Mode 1	Mode 2	Mode 3
Idc/kA	2.55	3.78	5.00
γ/°	24.45	20.97	16.91
U3/kV	400.00	400.00	400.00
Pvsc2/MW	339.58	504.60	666.67
Pvsc3/MW	339.58	504.60	666.67

one VSC for each pole operating in a constant DC voltage control mode, instructions of which can be calculated by Eq. 4:

$$P_{\text{ref\_P}} = \frac{1}{2}P_{\text{ref\_U}}, \tag{3}$$

$$U_{dc\_ref1} = U_{dc\_ref0}, \tag{4}$$

where $P_{\text{ref\_P}}$ is the reference value of VSC, which adopts the constant power control mode, $P_{\text{ref\_U}}$ is the reference value of VSC, which can provide power support, which adopts the constant DC voltage control mode and can be obtained from active power of VSC before the fault. U_{dc_ref0} and U_{dc_ref1} represent the control reference value of DC voltage before and after the fault, respectively.

If the fault is a unipolar fault, there is no need for a DC pole without fault to modify the control reference.

2) Calculation of control instructions of mode 2. All the remaining VSCs in each pole operate in the constant power control mode, and the power reference values are shown in Eq. 5:

$$P_{\text{ref\_VSCn}} = \min\left\{P_{\text{converter\_max}}, \frac{6}{6-n}P_{\text{ref0}}\right\}, \tag{5}$$

where $P_{\text{ref\_P0}}$ and $P_{\text{ref\_P1}}$ are the reference value of VSCs, which adopts the constant power control mode before and after the fault, and $P_{\text{converter\_max}}$ is the maximum transmission active power of VSC. n = 1 is under unipolar fault conditions, and when facing a bipolar fault, n = 2.

3) Calculation of control instructions of mode 3. If the VSC that has failed is in the constant power or U/f control mode, the active power reference values of remaining VSCs, which operate in the constant power control mode, are shown in Eq. 6:

$$P_{\text{ref\_P1}} = \min\left\{P_{\text{ref\_P0}} + \frac{\sum_{i=1}^{n}P_{exit}}{6-n}, P_{converter\_\max}\right\}, \tag{6}$$

where $P_{\text{ref\_P0}}$ and $P_{\text{ref\_P1}}$ are the reference value of VSCs, which adopts the constant power control mode before and after the fault, and P_{exit} is the transmission power of the quit VSC before fault. Under unipolar fault conditions, n = 1, and when facing the bipolar fault, n = 2.

If the VSC that has failed is in the constant DC voltage control mode, one VSC in each pole should be selected to operate in the constant DC voltage control mode, and the control instructions are calculated according to Eq. 7:

$$U_{dc\_ref1} = U_3, \tag{7}$$

where U_3 is calculated according to Eq. 1 after the fault. Thus, in abnormal conditions, the decision-making process consists of the following steps:

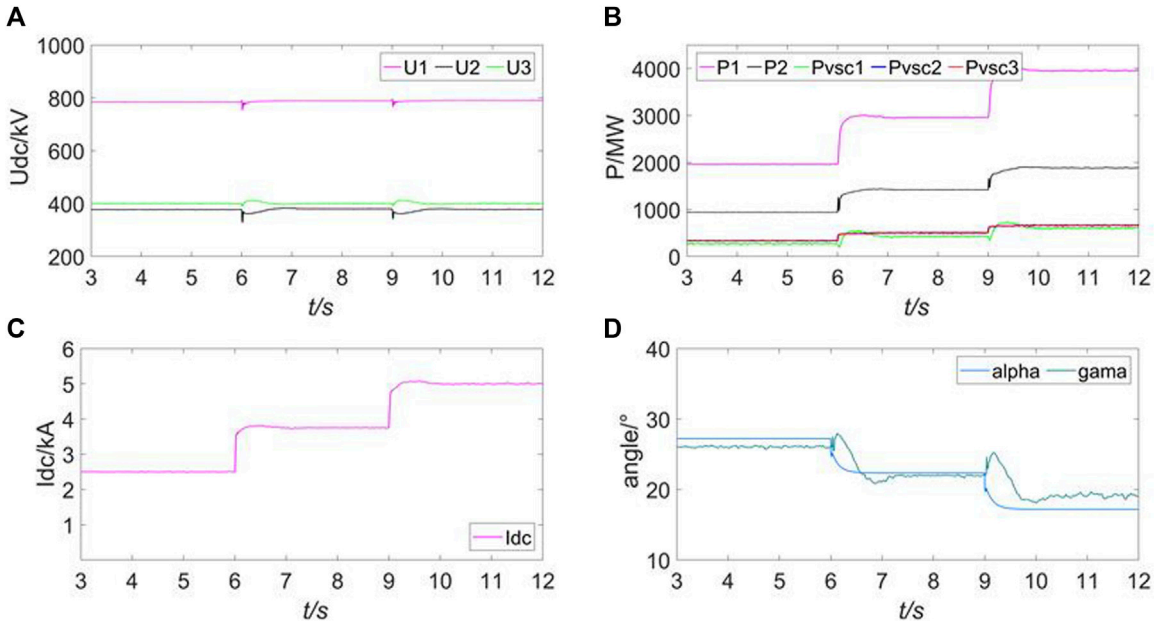

FIGURE 8
Simulation results of different operation modes in scenario 1. **(A)** DC voltage of each converter. **(B)** active power of each converter. **(C)** DC current of the DC grid. **(D)** Trigger delay angle of LCC1 and the extinction angle of LCC2.

TABLE 2 Calculation results of the decision-making method in scenario 2.

Parameter	Mode 1	Mode 2	Mode 3
α/°	26.42	26.42	26.42
Idc/kA	2.55	2.55	2.55
U3/kV	400.00	400.00	400.00
Pvsc1/MW	339.58	0.00	−500.00
Pvsc2/MW	339.58	509.37	759.37
Pvsc3/MW	339.58	509.37	759.37

Step 1: Obtain the status of the quit converter and the status of the system during normal operation before the fault. According to the method in Section 2.3.2, determine the system structure and operation control strategy after the fault.

Step 2: Operation point calculation under abnormal conditions. The calculation of VSCB for adjusting control instructions under different control strategy combinations can be calculated by Eqs 3–7, and then, the system operational point can be calculated by Eq. 1.

Step 3: Control instruction assignment. Assign the calculated instruction values to the corresponding converter station controllers.

3 Simulations and analyses

3.1 Simulation system and scenarios

To verify the effectiveness of the control strategy selection method for the hybrid cascaded MTDC system, a five-terminal simulation system based on the bipolar hybrid HVDC project is set in PSCAD/EMTDC, as shown in Figure 1.

In this simulation system, LCC1 operates as a rectifier, LCC2 operates as an inverter to transmit power to the AC side, and under normal circumstances, VSCs operate as inverters. The rated value of power in the rectifier side is 4000 MW, the voltage is 800 kV, the rated value of power in the inverter side LCC2 is 2000 MW, the rated voltage is 400 kV, the rated value of power in the inverter side VSC is 1000 MW, the rated voltage is 400 kV, and the system rated current is 5 kA.

In this paper, active power allocation scenarios for the five-terminal DC system during winter and summer peak periods are set to verify the effectiveness of the normal control strategy. In addition, scenarios with bipolar and unipolar faults are set to verify the effectiveness of the decision-making method for abnormal control.

3.2 Scenario 1: Power allocation during the hydropower peak period in summer

Scenario 1 is set up to verify the effectiveness of the control strategy combination selection method in allocating power during the summer hydropower peak using the following steps:

Step 1: There is a need for power control for the sending-end LCC1 during the summer hydropower peak. Based on the strategies in Figure 3, the rectifier side can be selected to operate in the constant DC current control mode, the inverter side can be selected to operate in the constant arc extinction angle control mode, any VSC is selected as the voltage control station, and the other VSCs operate in the constant power control mode to distribute the

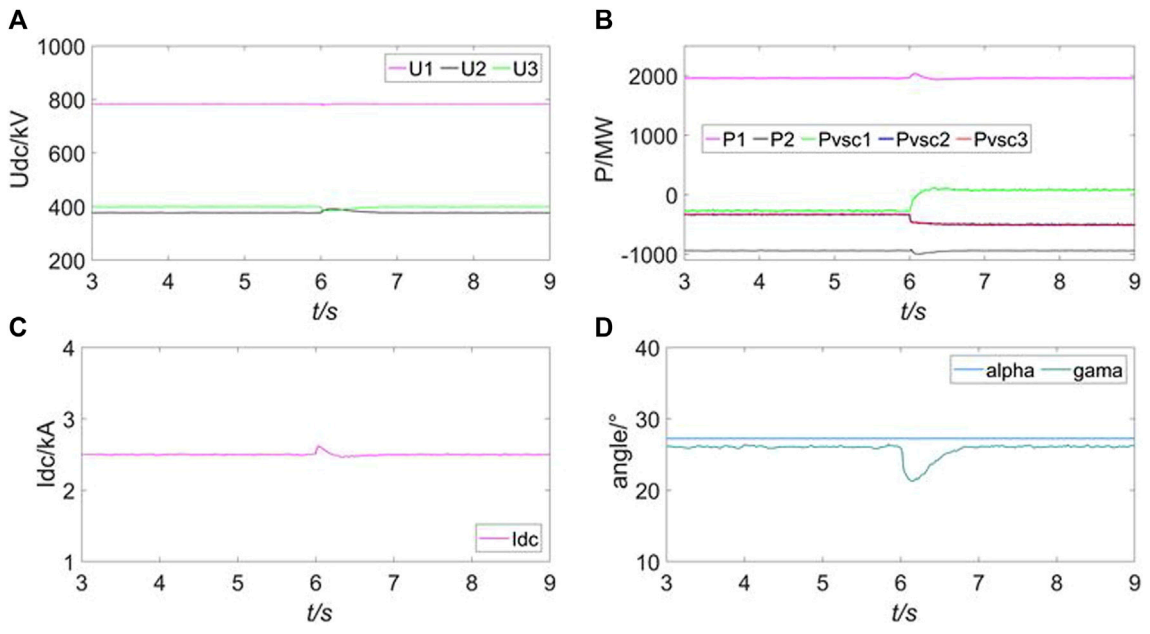

FIGURE 9
Simulation results of different operation modes in scenario 2. **(A)** DC voltage of each converter. **(B)** Active power of each converter. **(C)** DC current of the DC grid. **(D)** Trigger delay angle of LCC1 and the extinction angle of LCC2.

TABLE 3 Calculation results of the decision-making method in scenario 3.

Parameter	Original (+)	After fault (+)	Original (–)	After fault (–)
P1/MW	4000.00	3600.00	4000.00	4400.00
γ/°	16.91	26.53	16.91	16.91
U3/kV	400.00	320.00	400.00	446.68
Pvsc2/MW	666.67	533.33	666.67	800.00
Pvsc3/MW	666.67	533.33	666.67	800.00

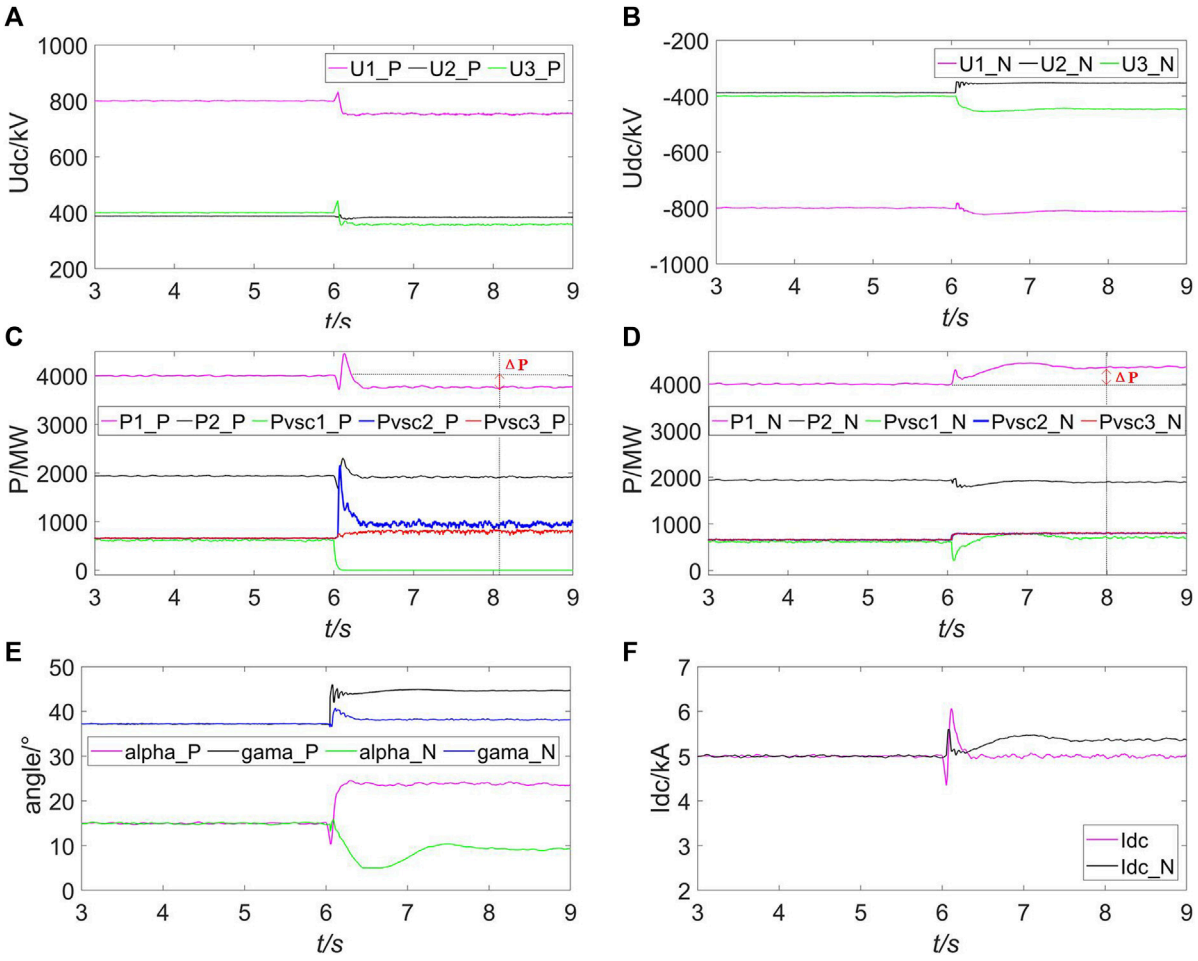

FIGURE 10
Simulation results of different operation modes in scenario 3. **(A)** DC voltage of a positive pole. **(B)** DC voltage of a negative pole. **(C)** Active power of a positive pole. **(D)** Active power of a negative pole. **(E)** Trigger delay angle of LCC1 and the extinction angle of LCC2. **(F)** DC current of the DC grid.

transmission power of the sending LCC. This control mode can prevent large changes of current in the hybrid cascade system while maintaining the highest voltage on the inverter side under normal conditions, which is economical.

Step 2: After selecting a control strategy combination, the control variables can be calculated according to Eqs. 1, 2. The active power of the sending-end LCC gradually increases from 50% to 75% and finally to the rated power. According to the standard operating voltage calculation, the voltage on the rectification side of the system is 800 kV, and the voltage of the inverter is 400 kV. Based on the constraints of the aforementioned variables, the calculated control instructions are shown in Table 1.

Step 3: Based on the control strategy combination selected in step 1, the corresponding control variables can be assigned according to the calculation results in step 2 to obtain the actual operating point of the system, as shown in Figure 8.

TABLE 4 Calculation results of the decision-making method in scenario 4.

Parameter	Original	After fault
α/°	26.42	\
Idc/kA	2.55	\
U3/kV	400.00	400.00
Pvsc1/MW	\	−500
Pvsc2/MW	759.37	250
Pvsc3/MW	759.37	250

The simulation results in Figure 8 show that the control instructions are accurately assigned to the system and that the hybrid cascaded MTDC system operates normally in summer.

3.3 Scenario 2: Power allocation during the wind power peak period in winter

Scenario 2 is set to verify the effectiveness of the control strategy selection method for VSC power reverse transmission during winter.

Step 1: During the wind power peak in winter, the Baihetan Hydropower Station connected to the LCC1 converter station is in the dry season with a transmission capacity of 2000 MW. At the same time, in winter, there is a surplus of wind power in the AC power grid connected to the receiving converter station VSC1, and the active power is sent back to the DC power grid. Based on the control strategy selection method, VSC2/VSC3 have power control demand and operate in the constant power control mode, and VSC1 operates in the constant DC voltage control mode to collectively absorb the transmission power from LCC1. Therefore, VSCB is generally equivalent to a voltage control station. Then, LCC1 operates in the constant α control mode as a voltage control station, while LCC2 can operate in the constant DC current control mode as a power control station.

Step 2: After selecting a control strategy combination, the controlled variables can be calculated according to Eqs. 1, 2. At this time, the transmission power of LCC1 is 2000 MW, and VSC1 is −500 MW. After calculating the standard operating voltage, the voltage of LCC1 is 800 kV, and the voltage of VSCB is 400 kV. Based on the constraints in the system, the calculated control instructions are shown in Table 2:

Step 3: Based on the control strategy combination selected in step 1, control reference instructions are assigned to the corresponding converter station controllers based on the calculation results.

The simulation results in Figure 9 show that VSCB can achieve stable and accurate power support capability under the condition of VSC1 power feedback.

3.4 Scenario 3: Unipolar fault of VSC1 during the hydropower peak period in summer

Scenario 3 is set to verify the effectiveness of the decision-making method for abnormal control of high hydropower generation in summer and VSC1 quitting operation due to faults.

Step 1: Similar to scenario 1, LCC1 is in a state of full power transmission during the period of high hydropower generation in summer. Under normal circumstances, the transmission capacity of LCC1 is 4000 MW and that of LCC2 and VSCB are 2000 MW. At this time, both VSCB and LCC2 serve as voltage control stations. At t = 6s, a fault occurred in the positive pole of VSC1, and it was unable to automatically return to normal control after the transient process. According to mode 3 in Section 2.3.2, if the VSC that has quit adopts the constant DC voltage control mode, another VSC in the VSCB needs to be selected to control the DC voltage (VSC2 is selected in this example), while the control modes of the other converter stations remain unchanged.

Step 2: After selecting a control strategy combination, according to Eq. 6, the control variables for the VSCB are calculated. VSCs adopting constant power control increase the reference value based on control instructions and absorb excess active power. In addition, according to Eq. 1, the voltage reference values of the positive and negative VSCBs are adjusted simultaneously so that the transmission power of LCC2 remains unchanged; the calculated control instructions are shown in Table 3:

Step 3: Based on the control strategy combination selected in step 1, assign the corresponding control variables according to the calculation results in step 2 to obtain the actual operating point of the system. As shown in Figure 10, under the permanent fault, according to the scheduling strategy under the fault, the system adjusts the voltage and power reference values to transfer the faulty pole power part to the VSCs in the normal pole, achieving steady operation of the system.

The simulation results in Figure 10 indicate that when VSC1 quits operation due to a fault, the calculation method for abnormal control can achieve reasonable transfer of power flow under faults, reduce the risk of exceeding limits in various parts of the MTDC, and improve the transmission capacity of the system under permanent faults.

3.5 Scenario 4: Bipolar fault of LCC2 during the wind power peak period in winter

Scenario 4 is set to verify the effectiveness of the decision-making method for abnormal control in the scenario of high wind power generation in winter.

Step 1: Similar to scenario 2, there is excess wind energy in the AC power grid in winter, which is connected to the receiving converter station VSC1, and power is fed back to the DC power grid. If a fault occurs at t = 6s, the transmit power from LCC1 cannot be transmitted to VSCB because LCC2 in the series part of the hybrid cascade system has quit operation. According to mode 1 in Section 2.3.2, LCC1 and LCC2 should quit operation, VSC1 can be used to support the operation of VSCB, and the operation mode of VSCs remains unchanged.

Step 2: After selecting a control strategy combination, control variables for VSCB are calculated according to Eqs 3, 4. VSCs using constant power control reduce the reference value based on control instructions; the calculated control instructions are shown in Table 4:

Step 3: Based on the control strategy combination selected in step 1, assign the corresponding control variables according to the

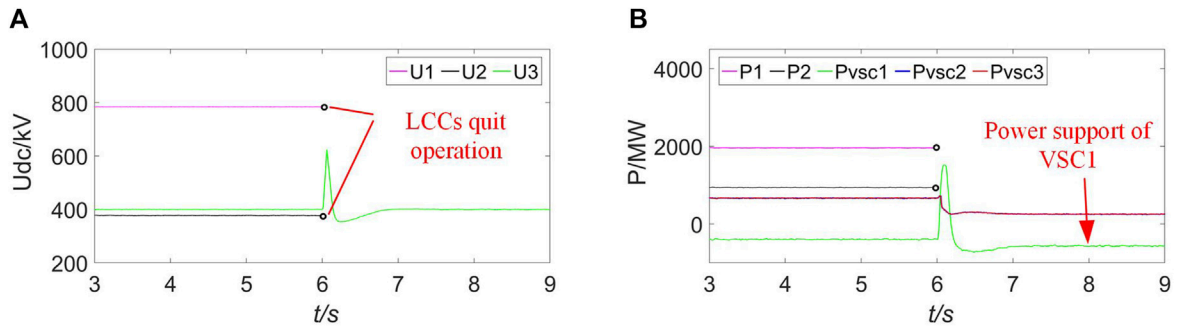

FIGURE 11
Simulation results of different operation modes in scenario 4. **(A)** DC voltage of each converter. **(B)** Active power of each converter.

calculation results in step 2 to obtain the actual operating point of the system. As shown in Figure 11, the operating status of the system positive pole is displayed under the fault.

The simulation results in Figure 11 indicate that when LCC2 quits operation due to a fault, calculation and decision-making methods for abnormal control can achieve the stable operation of VSCB independently after the faults in the sending end of VSCB.

4 Conclusion

This paper proposes a decision-making method that is used for flexible operation of a hybrid cascaded MTDC system. Simulation results based on PSCAD/EMTDC verify the effectiveness of the proposed method with the following contributions:

1) For normal control, a two-stage analysis method for the selection of control strategy combinations selecting the hybrid cascaded MTDC system is proposed. In the first stage, VSCs are considered VSCBs, and the control strategies of series LCCs are determined. In the second stage, station-level control strategies for VSCs are determined, which solves the problem of difficulties in decision-making.
2) The control instruction calculating method and decision-making process for normal control are proposed. According to the calculation method, under normal conditions, the control instructions are accurately calculated, and based on the decision-making process, the system can achieve precise and stable operation control of the MTDC system.
3) For abnormal control, abnormal conditions that lead to the quitting operation of converter stations are classified. A method for selecting control strategy combinations is also proposed, including three control strategy combinations, which can deal with the quitting operation of converter stations, resolving operational issues under system failure.
4) The control instruction calculating method and decision-making process for abnormal control are proposed. Under abnormal conditions, reasonable instructions for converters in bipolar MTDC systems are calculated, and the transfer of active power in the fault pole is achieved, improving the safety operation margin of the system.

Data availability statement

The raw data supporting the conclusion of this article will be made available by the authors, without undue reservation.

Author contributions

YW and ZL were responsible for conceptualization, methodology, validation, formal analysis, and writing—original draft and resources. YZ was responsible for investigation, validation, and writing—review and editing. All authors contributed to the article and approved the submitted version.

Funding

This work was supported by the National Natural Science Foundation of China under Grant 52207083.

Conflict of interest

The authors declare that the research was conducted in the absence of any commercial or financial relationships that could be construed as a potential conflict of interest.

Publisher's note

References

Alves, E. F., Bergna, G., Brandao, D. I., and Tedeschi, E. (2020). Sufficient conditions for robust frequency stability of AC power systems. *IEEE Trans. Power Syst.* 36 (3), 2684–2692. doi:10.1109/tpwrs.2020.3039832

Aziz, S., Peng, J., Wang, H., and Jiang, H. (2019). ADMM-based distributed optimization of hybrid MTDC-AC grid for determining smooth operation point. *IEEE Access* 7, 74238–74247. doi:10.1109/access.2019.2919700

Chen, N., Zha, K., Qu, H., Li, F., Xue, Y., and Zhang, X.-P. (2022). Economy analysis of flexible LCC-HVDC systems with controllable capacitors. *CSEE J. Power Energy Syst.* 8, 1708–1719. doi:10.17775/CSEEJPES.2022.01620

Flourentzou, N., Agelidis, V. G., and Demetriades, G. D. (2009). VSC-based HVDC power transmission systems: an overview. *IEEE Trans. Power Electron.* 24 (3), 592–602. [online]. doi:10.1109/tpel.2008.2008441

Haleem, N. M., Rajapakse, A. D., Gole, A. M., and Fernando, I. T. (2019). Investigation of fault ride-through capability of hybrid VSC-LCC multi-terminal HVDC transmission systems. *IEEE Trans. Power Deliv.* 34 (1), 241–250. doi:10.1109/tpwrd.2018.2868467

Kwon, D.-H., Kim, Y.-J., and Moon, S.-I. (2018). Modeling and analysis of an LCC HVDC system using DC voltage control to improve transient response and short-term power transfer capability. *IEEE Trans. Power Deliv.* 33 (4), 1922–1933. doi:10.1109/tpwrd.2018.2805905

Li, Y., Zhao, J., Liu, H., Kong, Q., Zhao, Y., Cheng, L., et al. (2022). Adaptive droop control of the VSC-MTDC distribution network considering Power–Voltage deviation. *Front. Energy Res.* 9. [online]. doi:10.3389/fenrg.2021.814489

Li, Z., He, Y., Li, Y., Gu, W., Tang, Y., and Zhang, X.-P. (2019). Hybrid control strategy for AC voltage stabilization in bipolar VSC-MTDC. *IEEE Trans. Power Syst.* 34 (1), 129–139. doi:10.1109/tpwrs.2018.2866131

Li, Z., Wei, Z., Zhan, R., Li, Y., Tang, Y., and Zhang, X.-P. (2021a). Frequency support control method for interconnected power systems using VSC-MTDC. *IEEE Trans. Power Syst.* 36 (3), 2304–2313. doi:10.1109/tpwrs.2020.3026035

Li, Z., Wei, Z., Zhan, R., Li, Y., and Zhang, X.-P. (2020). System operational dispatching and scheduling strategy for hybrid cascaded multi-terminal HVDC. *Int. J. Electr. Power and Energy Syst.* 122, 106195. doi:10.1016/j.ijepes.2020.106195

Li, Z., Zhang, T., Wang, Y., Tang, Y., and Zhang, X.-P. (2021b). Fault self-recovering control strategy of bipolar VSC-MTDC for large-scale renewable energy integration. *IEEE Trans. Power Syst.* 37 (4), 3036–3047. doi:10.1109/tpwrs.2021.3127192

Liu, L., Li, H., Xue, Y., and Liu, W. (2015). Reactive power compensation and optimization strategy for grid-interactive cascaded photovoltaic systems. *IEEE Trans. Power Electron.* 30 (1), 188–202. doi:10.1109/tpel.2014.2333004

Rao, H., Zhou, Y., Xu, S., Cai, X., Cao, W., Xu, Y., et al. (2019). Key technologies of ultra-high voltage hybrid LCC-VSC MTDC systems. *CSEE J. Power Energy Syst.* 5, 365–373. doi:10.17775/CSEEJPES.2019.01140

Rao, H., Zou, C., Xu, S., Cai, X., Li, Y., Zhao, X., et al. (2022). The on-site verification of key technologies for kunbei-liuzhou-longmen hybrid multi-terminal ultra HVDC project. *CSEE J. Power Energy Syst.* 8 (5), 1281–1289. doi:10.17775/CSEEJPES.2022.04780

Ren, Y., Sun, H., Wang, S., Zhao, B., Xu, S., Liu, M., et al. (2023). Study on the characteristic of the grounding fault on the cascaded midpoint side of the hybrid cascaded HVDC system. *Front. Energy Res.* 11. [online]. doi:10.3389/fenrg.2023.1187620

Reza Ahrabi, R., Li, Y. W., and Nejabatkhah, F. (2022). Unified control of the parallel LCC-VSCs interlinking converters in a hybrid AC/DC network. *IEEE Trans. Smart Grid* 13 (2), 975–985. doi:10.1109/tsg.2021.3137300

Wang, R., Ma, D., Sun, Q., Sun, Q., Mu, Y., and Wang, P. (2022). Accurate current sharing and voltage regulation in hybrid wind/solar systems: an adaptive dynamic programming approach. *IEEE Trans. Consumer Electron.* 68 (3), 261–272. doi:10.1109/tce.2022.3181105

Wang, R., Qiuye, S., Zhang, P., Gui, Y., Qin, D., and Peng, W. (2020a). Reduced-order transfer function model of the droop-controlled inverter via Jordan continued-fraction expansion. *IEEE Trans. Energy Convers.* 35 (3), 1585–1595. doi:10.1109/tec.2020.2980033

Wang, T., Li, C., Mi, D., Wang, Z., and Xiang, Y. (2020b). Coordinated modulation strategy considering multi-HVDC emergency for enhancing transient stability of hybrid AC/DC power systems. *CSEE J. Power Energy Syst.* 6, 806–815. doi:10.17775/CSEEJPES.2019.02000

Xu, Q., Lou, J., Ning, D., and Li, P. (2023). Transient stability enhancement control through VSC-HVDC system and fast frequency response resources. *Front. Energy Res.* 10. [online]. doi:10.3389/fenrg.2022.1022905

Zhao, J., and Tao, Y. (2021). Control characteristic analysis and coordinated strategy design for hybrid HVDC with multi-infeed MMC inverters. *Front. Energy Res.* 9. [online]. doi:10.3389/fenrg.2021.737294

frontiers | Frontiers in Energy Research

TYPE Original Research
PUBLISHED 25 September 2023
DOI 10.3389/fenrg.2023.1242047

OPEN ACCESS

EDITED BY
Mingfei Ban,
Northeast Forestry University, China

REVIEWED BY
Yushuai Li,
University of Oslo, Norway
Mingyu Yan,
Huazhong University of Science and Technology, China
Zhenjie Li,
Northeast Forestry University, China
Yingjun Wu,
Hohai University, China

*CORRESPONDENCE
Weiyu Wang,
wywang@csust.edu.cn

RECEIVED 18 June 2023
ACCEPTED 07 September 2023
PUBLISHED 25 September 2023

CITATION
Shi X, Guo H, Wang W, Yin B and Cao Y (2023), Modeling and assessing load redistribution attacks considering cyber vulnerabilities in power systems. *Front. Energy Res.* 11:1242047. doi: 10.3389/fenrg.2023.1242047

Modeling and assessing load redistribution attacks considering cyber vulnerabilities in power systems

Xingyu Shi, Huan Guo, Weiyu Wang*, Banghuang Yin and Yijia Cao

School of Electrical and Information Engineering, Changsha University of Science and Technology, Changsha, China

Introduction: Load Redistribution (LR) attacks, as a common form of false data injection attack, have emerged as a significant cybersecurity threat to power system operations by manipulating load buses' measurements at substations. Existing LR attack methods typically assume that any substation can be equally attacked, contributing to the analysis of LR attacks in power systems. However, the diversity of cyber vulnerabilities in substation communication links implies varying costs associated with falsifying load buses' measurements. Thus, quantitatively evaluating these costs and analyzing the impact of LR attacks on power systems within cost constraints holds practical significance.

Methods: In this paper, we employ a Bayesian attack graph model to characterize the intrusion process through cyber vulnerabilities. The costs of falsifying load buses' measurements at substations are quantitatively evaluated using the mean time-to-compromise model. Subsequently, from the attacker's perspective, we propose a bi-level optimization model for LR attacks, considering the mean time to compromise in conjunction with limited attack resources and power flow constraints.

Results: Simulations conducted on the IEEE 14-bus system illustrate the influence of cyber vulnerabilities on LR attacks within power systems. Furthermore, we verify that the attack scenario of the existing LR attack model aligns with a case of the proposed bi-level LR attack model when there is sufficient attack time to compromise all communication links.

Discussion: The findings of this research demonstrate that the impact of cyber vulnerabilities on LR attacks can be quantified by assessing the attack costs. Effective management of LR attacks can be achieved under cost constraints through optimization methods. These insights contribute to enhancing network security strategies for power systems, mitigating potential threats posed by LR attacks in power system operations.

KEYWORDS

cyber-physical systems, false data injection attacks, load redistribution attack, Bayesian attack graph model, mean time to compromise, bi-level model, common vulnerability scoring system

1 Introduction

The cyber-physical power system has become the main feature of modern power systems and attracts countries to compete to develop such a power system (Pliatsios et al., 2020; Liu et al., 2022). The cyber system brings flexibility to the operation of power grids. However, the complex cyber-enabled technologies and communication networks will profoundly impact the physical process of power systems, bringing more cyber security problems to the power system (Xiang et al., 2016; Zhang and Yang, 2022).

In recent years, the militarization of global cyberspace has accelerated, and cyberattacks targeting critical core infrastructure have developed into real threats. Many information technologies were deployed in the power system to defend against cyberattacks. The state estimation has been widely used by energy management systems (EMSs) to filter the measurement noise and detect gross errors. Information encryption technology, network address locking, and modifying defense equipment are used to enhance the security of the power system. However, intruders can still launch various malicious attacks to compromise the power data integrity by exploiting the vulnerabilities and social engineering access to a target network authority. Attackers can mislead the operator to conduct uneconomical power system operations, obtain economic benefits, and even disrupt the stability of the power system (Yuan et al., 2011; Tan et al., 2016; Zhang and Yang, 2022).

Cyberattacks on power systems can be divided into man-in-the-middle (MITM) attacks, replay attacks, and false data injection (FDI) attacks (Deng et al., 2016). Among them, the FDI attack refers to injecting falsified measurements, inducing uneconomic, non-optimal, or even harmful decisions on power dispatch based on security-constrained economic dispatch (SCED). Load redistribution (LR) attacks are typical FDI attacks, which mislead operators by injecting falsified load values (Liang et al., 2016).

In the LR attack model, extensive attention has been paid to constructing a representative attack vector and investigating the system response (Yuan et al., 2011; Liu et al., 2015; Gao et al., 2022). LR attack against state estimation was first proposed by Liu et al. ((2011), which is a coordinated cyberattack against state estimation. In the work of Liu and Li (2014) and Liu and Li (2016), the concept of an attack zone is introduced, and the regional LR attack model is proposed. In the work of Gao et al. (2022), an LR attack model was built based on pre- and post-dispatch, which can lead the system to an uneconomic and insecure operating state. In the work of Liu et al. (2016), a simple approach was used to determine an effective attack vector to change the load data sent to the control center.

The abovementioned works contributed to analyzing the impact of LR attacks in power systems, given that load buses' measurements of substations are equally attackable. However, cyber vulnerabilities in communication links of substations are diverse, and therefore, the feasibility of injecting falsified measurements of different load buses has a significant difference, which will affect the impact of LR attacks on power systems. Hence, assessing LR attacks with cyber vulnerabilities has become non-negligible work.

In the literature, different vulnerability evaluation models have been developed to address cyber security issues of power grids. The Petri net was first proposed by Ten et al. (2008), which can assess the cyber vulnerabilities in power systems and quantify the potential harm cyberattacks may cause. In the work of Bahrami et al. (2020), Petri nets are used to simulate possible intrusion scenarios into substation networks, and a multi-state Markov model is proposed to identify the consequences of cyberattacks on protective devices. However, the abovementioned probabilistic model cannot estimate the attack time that will impact the result of the LR attack. The mean time-to-compromise (MTTC) model is a meaningful way to quantitatively estimate the time intervals of successful attacks on the target cyber components of the SCADA system (Zhang et al., 2015). The MTTC model also was applied to assess the reliability of the wind farm energy management systems (Zhang et al., 2017).

In the paper, the intruding process through cyber vulnerabilities is modeled, and the costs to intrude communication links between substations and the control center are quantitatively evaluated. Then, a bi-level model of LR attack considering cyber vulnerabilities is proposed. The main works of the paper are as follows:

1) This paper introduces a Bayesian attack graph model to simulate the process of intruding communication links between substations and the control center through cyber vulnerabilities. Subsequently, the intruding time is quantitatively assessed through the MTTC model.
2) A bi-level LR attack model is proposed, considering the MTTC, limited attack resources, and power flow constraints, to identify the most damaging LR attack. The upper-level constructs an attack vector to maximize the operation cost of the power system. The lower-level employs the SCED to model the operator response after the LR attack.
3) The IEEE 14-bus system is adopted to test the proposed LR attack model. The MTTC of intruding communication links through cyber vulnerabilities between the substations and the control center is quantitatively evaluated. Then, the impact of the LR attack on operation cost is analyzed with different available attack resources and time.
4) Results show that cyber vulnerabilities will significantly impact the LR attack on power systems. Furthermore, it can be found that the most damaging scenario in the traditional LR attack may not be achieved due to the limited attacking time unable to intrude necessary communication links, and the scenario is just a case in the proposed bi-level LR attack model with the sufficient attack time to intrude all communication links between the substations and the control center.

The remainder of this paper is organized as follows. The evaluation of cyber vulnerabilities is introduced in Section 2. The LR attack model considering cyber vulnerabilities is given in Section 3, Section 4 presents the quantitative analysis, and Section 5 concludes the paper.

2 Cost evaluation of LR attacks on communication links through cyber vulnerabilities

Cyberattacks weaken or destroy the secondary system operation of power systems. Information is interrupted, delayed, or tampered with if the secondary system suffers malicious attacks, such as SCADA, WAMS, and AMI systems (Yang et al., 2022). The control center may give wrong instructions, and the decision-making units misoperate or quit the operation (Che et al., 2019).

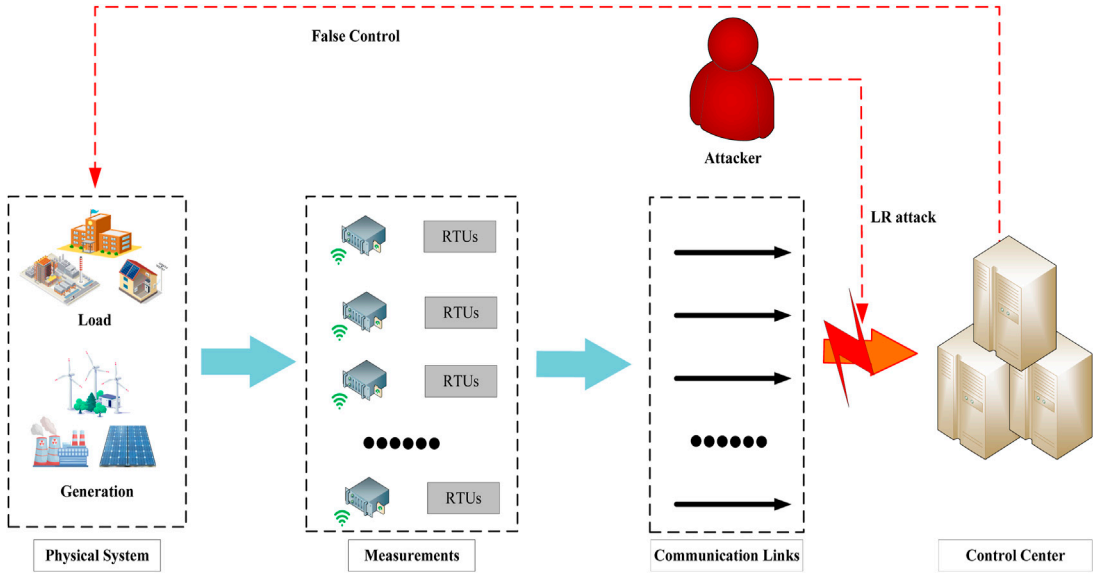

FIGURE 1
LR attacks in cyber-physical systems.

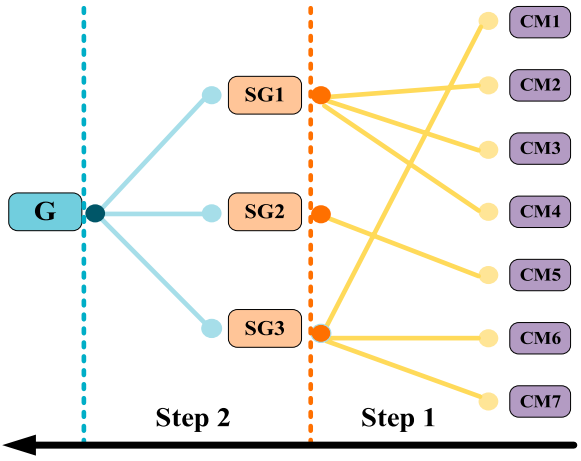

FIGURE 2
Bayesian attack graph model of LR attacks on communication links.

The measured power systems states, such as voltage amplitude, bus load, line state, and transmission line power flow, are transmitted through communication links between the substations and the control center. Power system communication links are easily intercepted and forged (Liang et al., 2016; Li et al., 2022), and an attacker can inject falsified measurements to mislead power system operators (Liu et al., 2016). Therefore, cyberattacks oriented to communication links are more threatening and have practical significance (Liu et al., 2016; Li et al., 2019).

Figure 1 shows LR attacks in cyber-physical systems. Based on measurements through communication links, the power system operator conducts unified scheduling of power generations and consumers according to security-constrained economic dispatch (SCED). Although countermeasures are deployed in power systems, attackers can manipulate measurements by intruding communication links through cyber vulnerabilities of known and zero vulnerabilities in the cyber system of power systems. The manipulated measurements, carefully calculated to avoid being identified as malicious data, mislead SCED to bring the system into an insecure and non-optimal operating condition.

2.1 Modeling intruding process on communication links through cyber vulnerabilities

Inspired by the work of Sommestad et al. (2009), a three-layer structure is employed to model the cyber intrusion of communication links between the targeted substation and the control center, as shown in Figure 2. The right side consists of power system countermeasures. The middle and left parts are the sub-goals and the goal of the LR attack, respectively. Table 1 lists the countermeasures of substations and sub-goals and goal of the LR attack.

To reach the second layer SG_j, for ($j \in \mathcal{J}$), where $\mathcal{J}$ is the set of the LR attack sub-goals, the intruder must first bypass one of the countermeasures CM_i, for $CM_i \in \mathcal{I}$ (SG_j), where $\mathcal{I}$ (SG_j) means the set of countermeasures related with SG_j. When all sub-goals are satisfied, the intruder can inject manipulated data into communication links.

Attackers intrude communication links through cyber vulnerabilities of known and zero vulnerabilities in countermeasures. Without loss of generality, it is assumed that the known and zero-day vulnerabilities are randomly distributed in countermeasures (Zhang et al., 2017). The CVSS scores reflect countermeasures' known and zero-day vulnerabilities from 0 to 10. The details of evaluating CVSS scores can be seen in the work of Zieger et al. (2018).

TABLE 1 Countermeasures, sub-goals, and overall goals.

Node label	Node usage	Node label	Node usage
CM1	Message encryption	CM7	Remote password
CM2	Medium type	SG1	Obtain network connection
CM3	Network address locking	SG2	Interpret message structure
CM4	Physical link protection	SG3	Generate valid data
CM5	Protocol non-public	G	Inject manipulated data
CM6	Signature cryptography		

According to Figure 2, the LR attack probability model can be obtained by the following equations:

$$p_d(CM_i) = \begin{cases} \frac{CVSS_i}{10} \times U(0,1), CM_i \text{ with Known vulnerability} \\ 0.008 \times U(0,1), CM_i \text{ with zero} - \text{day vulnerability} \end{cases}, \quad (1)$$

$$p_d\left(CM_i \wedge SG_j\right) = p_d(CM_i) \times p_d\left(SG_j \mid CM_i\right), \forall i \in \mathcal{I}\left(SG_j\right), \quad (2)$$

$$p_d\left(SG_j\right) = \sum p_d\left(CM_i \wedge SG_j\right), \forall i \in \mathcal{I}\left(SG_j\right), \forall j \in \mathcal{J}, \quad (3)$$

$$p_d(G) = \prod_{j=1}^{\mathcal{J}} p_d\left(SG_j\right), \forall j \in \mathcal{J}. \quad (4)$$

Equation (1) represents the probability of exploiting the known and zero-day vulnerabilities, where $CVSS_i$ indicates the bass score corresponding to known vulnerabilities in CM_i and U (0,1) is the uniform distribution corresponding with three preconditions of service, connection, and privilege to complete vulnerability exploitation. Equation (2) represents the probability of achieving SG_j through CM_i, for $i \in \diamondsuit$ (SG_j), where $p_d(SG_j|CM_i)$ is the conditional probability following a uniform distribution U (0.8, 1) of substation d. Equation (3) is the overall probability of reaching the sub-goal SG_j, for $j \in \mathcal{I}$. Equation (4) represents the probability of reaching the goal G of injecting manipulated data. In order to achieve G, SG_1, SG_2, and SG_3 should be reached.

2.2 Quantitatively evaluating the LR attack cost of intruding communication links

2.2.1 Compromise time model of vulnerabilities

The compromise time $T_{d,\ i}(v_i)$ is a metric to estimate the mean time to compromise vulnerabilities in the CM_i of the communication link of the substation at bus d, where v_i is the number of known or zero-day vulnerabilities in CM_i. $T_{d,\ i}(v_i)$ can be modeled as a stochastic process consisting of the following three sub-processes depending on the nature of the vulnerability and the attacker's skill level.

Process 1 means at least a known vulnerability on CM_i, which can be exploited to launch an attack. Process 2 means that no vulnerability can be exploited to launch an attack, though there is at least a known vulnerability in CM_i. Process 3 means that no known vulnerability can be exploited. Furthermore, new vulnerabilities must be searched for or developed. The {t_1, t_2, and t_3} and {P_1, P_2, and P_3} are the three sub-processes' mean times and probabilities, respectively.

We can see that processes 1 and 2 are mutually exclusive. Process 3 runs continuously and in parallel with processes 1 and 2. For the calculation feasibility of $T_{d,i}$, we assume that process 3 only occurs when processes 1 and 2 are inactive (Lau et al., 2021).

The calculation of $T_{d,\ i}(v_i)$ is as follows:

$$T_{d,i}(v_i) = \int_0^1 t^*(v_i, s, \sigma)^* Beta_{\varepsilon,\theta}(s) ds, \quad (5)$$

subject to

$$t^* = t_1 P_1 + t_2 P_2 + t_3 P_3, \quad (6)$$

$$\begin{cases} P_1 = 1 - e^{-v_i^* \frac{m(s)}{\sigma}} \\ P_2 = (1 - P_1)(1 - u), \\ P_3 = 1 - P_1 - P_2 \end{cases} \quad (7)$$

$$\begin{cases} t_1 = 1 \\ t_2 = 5.8E(s, v_i) \\ \begin{cases} t_3 = \left(\frac{1}{f(s)} - 0.5\right)30.42 + 5.8, \text{CM}_i \text{ with known vulnerability} \\ t_3 = \left(\frac{1}{f(s)} - 0.5\right)65 + 32, \text{CM}_i \text{ with zero} - \text{day vulnerability} \end{cases} \end{cases}, \quad (8)$$

$$\begin{cases} m(s) = 83^*3.5^{4s/2.7} - 82 \\ f(s) = 0.145^*2.6^{2s+0.07} - 0.1 \\ u = (1 - f(s))^{v_i} \\ \bar{f} = f(s)^* v_i \end{cases}, \quad (9)$$

$$\begin{cases} E(s, v_i) = E_1(s, v_i) + E_2(s, v_i) \\ E_1(s, v_i) = \xi\left(\lfloor \bar{f} \rfloor, v_i\right)^*\left(\lceil \bar{f} \rceil - \bar{f}\right) \\ E_2(s, v_i) = \xi\left(\lceil \bar{f} \rceil, v_i\right)^*\left(1 - \lceil \bar{f} \rceil + \bar{f}\right) \\ \xi(b, v_i) = \frac{b}{v_i} + \frac{b(v_i - b)!}{v_i!}\bar{\xi} \\ \bar{\xi} = \sum_{t=2}^{v_i - b + 1}\left[\frac{t(v_i - t + 1)!}{(v_i - b - t + 1)!(v_i - t + 1)}\right] \end{cases}, \quad (10)$$

where $Beta_{\xi,\ \theta}(s)$ is a Beta distribution curve fitting the attacker's skill at different levels s, m is the number of exploitable vulnerabilities; $s \in [0,1]$ is the skill level factor; E is the number of estimated attack attempts; u and ξ are auxiliary variables; and $\lceil \bar{f} \rceil$ and $\lfloor \bar{f} \rfloor$ represent the ceiling and floor of $\bar{f}$, respectively.

2.2.2 MTTC assessment considering network vulnerability

The MTTC is used to estimate the average frequency of cyberattacks on the components of power systems. It measures

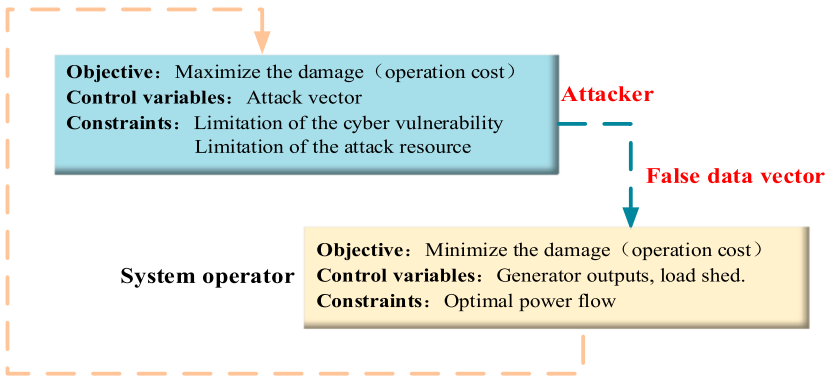

FIGURE 3
Immediate LR attack model considering cyber vulnerability.

the efforts (represented by time) an attacker spends for a successful attack in a statistical form. The MTTC of the LR attack aiming at the communication line can be divided into two parts: the MTTC of SG_j and G, which are modeled as follows:

$$MTTC_d\left(SG_j\right) = \frac{\sum_{i\in\mathcal{I}\left(SG_j\right)} T_{d,i}\left(CM_i\right)\cdot p_d\left(CM_i \wedge SG_j\right)}{p_d\left(SG_j\right)}, \quad (11)$$

where $T_{d,i}(CM_i)$ is the mean time to compromise of CM_i and $p_d(SG_j \wedge CM_i)$ is the probability of the intruder reaching SG_j by invading CM_i, which can be calculated by (2). $p_d(SG_j)$ is the overall probability of SG_j, calculated by (3).

According to the "AND" relationship between SG_j, the MTTC of G is denoted as follows:

$$MTTC_d\left(G\right) = \sum_{j=1}^{\mathcal{J}} MTTC_d\left(SG_j\right). \quad (12)$$

The MTTC model quantitatively evaluates the cost of intruding into communication links of substations through cyber vulnerabilities. In practice, the intruder inevitably has limited attack time to intrude into communication links to inject false data. Hence, from the attacker's perspective, it is necessary to model the LR attack model considering the impact of cyber vulnerability.

3 Bi-level model of LR attack considering cyber vulnerability

From the intruder's perspective, LR attacks are classified into immediate and delayed attacking goals. The immediate LR attack aims to maximize the system's operating cost. A two-layer model representing the behavior of the attacker and operator in Figure 3 is proposed to identify the attack scenario with maximum operating cost, considering multiple restrictions of cyber vulnerability, attack resources, and power flow constraints (Liu et al., 2016). The upper layer represents the attacker, who constructs an attack vector that maximizes the operation cost of the power system. The result of the attack vector is delivery to the lower layer. The lower layer represents the operator, who dispatches the generator output and load shedding to mitigate the impact of the attack decision.

This paper makes the following assumptions about the characteristics of attackers and operators, which are reasonable (Liang et al., 2015):

1) Power system employees may leak power network configuration due to financial interests and revenge behavior.
2) Load measurements are attackable. In power systems, loads are constantly changing. The load measurement should not deviate far from their actual values to prevent attacks from being detected.
3) The measurement of the generator output is not a feasible attacking variable because the integrity of the generator output can be easily verified by communication between the system control center and the power plant.
4) The bus injection measurement of zero-injection buses cannot be attacked. Zero-injection buses have neither generation nor load connection, so LR attacks cannot be carried out through such buses.

3.1 The upper-level problem

The upper-level problem is constructed from the attacker's perspective, aiming to maximize the generation and load shedding costs by the injected bus power.

$$\max_{\Delta \boldsymbol{D}} \sum_{g=1}^{N_g} c_g P_g^* + \sum_{d=1}^{N_d} cs_d S_d^*, \quad (13)$$

$$\text{s.t.}\delta_{t,d} = 1 \Leftrightarrow T - t_d \geq 0 \forall d, \quad (14)$$

$$\sum_{d=1}^{N_d} \Delta D_d = 0, \quad (15)$$

$$-\tau D_d \delta_{t,d} \leq \Delta D_d \leq \tau D_d \delta_{t,d} \forall d, \quad (16)$$

$$\Delta D_d = 0 \Leftrightarrow \delta_{D,d} = 0 \forall d, \quad (17)$$

$$\sum_{d=1}^{N_d} \delta_{D,d} \leq R. \quad (18)$$

Constraint (14) indicates whether intruders can successfully invade the communication link, where T is the limited attacking time of the intruder and t_d is the value of $MTTC_d$ calculated based on cyber vulnerabilities in the communication link between the substation of load bus d and the control center. Constraints

(15)–(16) ensure that falsified load measurements can be injected successfully. It is necessary to ensure that the sum of bus loads remains unchanged before and after the attack and that the load change is within a specific range. The integer variable $\delta_{t,d}$ binds constraint condition (16). Constraint (17) models the logical relationships of the attack vector. In addition, limited by attack resources, the communication links that an attacker can invade simultaneously should not exceed the limit, represented by (18).

3.2 Lower-level problem

$$\{\boldsymbol{P}^*, \boldsymbol{S}^*\} = \arg\left\{ \mathrm{Min}_{\boldsymbol{P},\boldsymbol{S}} \sum_{g=1}^{N_g} c_g P_g + \sum_{d=1}^{N_d} cs_d S_d \right\}, \tag{19}$$

$$s.t. \sum_{g=1}^{N_g} P_g = \sum_{d=1}^{N_d} (D_d - S_d), \tag{20}$$

$$\boldsymbol{PL} = \boldsymbol{SF} \cdot \boldsymbol{KP} \cdot \boldsymbol{P} - \boldsymbol{SF} \cdot \boldsymbol{KD} \cdot (\boldsymbol{D} + \Delta \boldsymbol{D} - \boldsymbol{S}), \tag{21}$$

$$-PL_l{}^{\min} \le PL_l \le PL_l{}^{\max} \ \forall l, \tag{22}$$

$$P_g{}^{\min} \le P_g \le P_g{}^{\max} \ \forall g, \tag{23}$$

$$0 \le S_d \le D_d + \Delta D_d \ \forall d. \tag{24}$$

Lower-level model constraints (19)–(24) can represent the SCED model, which responds according to the decision variables ΔD determined by the upper-level model. Constraint (20) is the power balance constraint of the system. Constraint (21) is the line power flow constraint. Constraints (22)–(24) are the bounds of rated line capacity, generator output, and load shedding, respectively.

In the upper-level problem, Eqs (14) and (17) can be transformed into a mixed integer linearized form. For Eq. (14), we linearize it using the big M method (Yuan et al., 2011; Che et al., 2019), which is (25). Eq. (17) can be linearized in the same way.

$$\begin{cases} (T - t_d)/M \le \delta_{t,d} \le 1 + (T - t_d)/M \\ 0 \le |(T - t_d)| + (T - t_d) \le M \cdot \delta_{t,d} \\ 0 \le |(T - t_d)| - (T - t_d) \le M \cdot (1 - \delta_{t,d}) \\ \delta_{t,d} \in \{0, 1\} \end{cases} \forall d. \tag{25}$$

Replacing the lower-level optimization problem with the Karush–Kuhn–Tucker (KKT) optimal condition can transform the bi-level model into an equivalent single-level mixed integer programming model. The resulting single-level MILP problem can be solved by commercial solvers, such as CPLEX and Gurobi.

4 Quantitative analysis

In order to reflect the impact of the LR attack on the operation cost of the power system, the system parameters of the IEEE 14-bus system are modified. $PL_{1-2}{}^{\max}$ is set to 160 MW, and $PL^{\max}$ of other lines is set to 60 MW. Other configuration data settings are obtained from MATPOWER 6.0 (Zimmerman and Murillo-Sánchez, 2016). The cost of the unmet demand load is set as cs_d = 100 $/MWh. Generator parameters are shown in Table 2. The fabricated magnitude ratio of load measurement is limited at τ = 50%.

The IEEE 14-bus system is used to investigate the impact of LR attacks. The data of substations corresponding with buses are transmitted to the control center through communication links between the substations and the control center. Therefore, the system has 14 communication links, which can be utilized to inject false data through different cyber vulnerabilities.

TABLE 2 Generator parameters.

Number	1	2	3	4	5
Gen. bus	1	2	3	6	8
$P^{\min}$ (MW)	0	0	0	0	0
$P^{\max}$ (MW)	300	50	30	50	20
c (/MWh)	20	30	40	50	35

Figure 4 shows the power system and LR attack model. On the left side of the figure is the topology of the IEEE 14-bus system, and on the right is the attacker's LR attack process on the corresponding substation. The proposed LR attack includes five main steps. The first step is to obtain the measurements of buses. Then, the cost evaluation of intruding into communication links through cyber vulnerabilities is implemented. The evaluation flow of communication links of buses 4, 5, 7, and 8 is taken an example. Later, considering the costs of intruding communication links, the proposed LR attack model solves the attack vector, limited by attack time and resources. Finally, by injecting the solved attack vector, the misled non-optimal operation instruction of generator output and load shedding is implemented by power systems through physical control.

4.1 Cyber vulnerability evaluation of communication links

Five known vulnerabilities, namely, file transfer protocol (ftp), denial of service (dos), the anomaly of buffer overflow (bof), cross-site scripting (xss), and execution code overflow (eco), may exist in countermeasures of communication links (CVE Database, 2023). Due to the uncertainties of zero-day vulnerabilities, for demonstration, it is assumed that no more than five zero-day vulnerabilities may exist in countermeasures of communication links.

4.1.1 Estimates of $T_{d,\ i}(v_i)$ with different types and numbers of vulnerabilities

According to Eq. (5), the skill level, s, of the attacker will influence the compromise time, and s is represented by a Beta distribution with (?, ?) = (1.5, 2.0). The total number of vulnerabilities, ?, was fixed to 9,447, which can be updated based on the available vulnerability database of power system networks (Zieger et al., 2018). Table 3 shows the $T_{d,\ i}(v_i)$ with 1–5 known and zero-day vulnerabilities.

It can be seen from Table 3 that the time of exploiting zero-day vulnerabilities is significantly longer than the time for known vulnerabilities. With the increase in vulnerabilities, $T_{d,\ i}(v_i)$ gradually decreases. This is in line with the reality that as the number of vulnerabilities increases, it gives the intruder more opportunities to choose the attack path, which can reduce the time needed to carry out a cyberattack successfully.

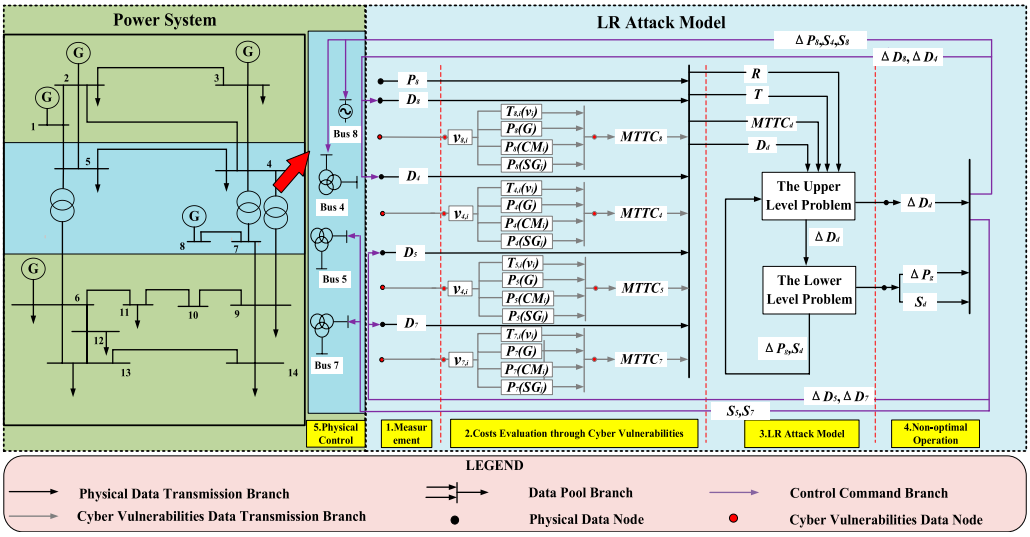

FIGURE 4
Proposed LR attack model for power systems.

TABLE 3 $T_{d,\ i}(v_i)$ with known and zero-day vulnerabilities.

v_i	1	2	3	4	5
Known vulnerability (days)	120.93	100.93	86.87	76.48	68.5
Zero-day vulnerability (days)	271.42	224.93	191.93	165.27	144.94

TABLE 4 CVSS scores of vulnerabilities.

Vulnerability	Zero-day	ftp	dos	bof	xss	eco
CVSS score	0.8	6.4	5.0	6.8	4.5	7.5

TABLE 5 MTTC to invade each communication link.

Bus	1	2	3	4	5	6	7
MTTC (days)	279.9	243.7	198.5	320.5	380.5	356.8	289.4
Bus	8	9	10	11	12	13	14
MTTC (days)	205.6	231.3	328.2	489.5	409.8	231.6	188.9

4.1.2 Estimation of the MTTC on each communication link

For estimating the MTTC, the CVSS scores should be assigned in advance, which can be evaluated based on the access vector, access complexity, and authentications with different grades (Zhang et al., 2015). The CVSS scores for cyber vulnerabilities in countermeasures of communication links are listed in Table 4.

Intruders can find the vulnerability distribution in countermeasures through source code or automation analysis tools. For demonstration, in this paper, the number of these vulnerabilities in countermeasures of communication links is set to a random number of 1–5. According to the MTTC assessment method in Section 2.2.2, the estimated MTTC of each communication link can be obtained, as shown in Table 5.

As seen in Table 5, although the intruder has the same overall goal among these communication links, the MTTC of each communication link is different because the distribution of cyber vulnerabilities in countermeasures of communication links is dissimilar. The intrusion time of bus 14 is the shortest, 188.9 days, which means the intruder can easily tamper with the load measurement in its communication link. The intrusion time of bus 11 is the longest, 489.5 days, indicating that the LR attack executed through fabricating the load measurement of bus 11 needs the maximum attacking time.

4.2 Impact analysis of the LR attack model considering cyber vulnerabilities

The LR attack impact can be obtained by solving the proposed bi-level model of LR attack in Section 3. The most hazardous scenario in the LR attack considering cyber vulnerabilities is subject to the available attack time and resources. The intruder's available attack time decides the number of intruded communication links. Meanwhile, the available attack resources decide the number of simultaneously falsified measurements of load buses.

4.2.1 LR attack with the different available attack times

Table 6 shows the most damaging LR attack scenarios with the limitation of the different available attack times, T, and the static attack resource, R = 4. Although the intruder has the attack resource to falsify four load-bus measurements simultaneously, the attack time T = 200 limits the intruder from attacking indispensable communication links. According to Table 5, with T = 200, the intruder only has time to attack two

TABLE 6 LR attacks with different attack time limitations.

Attacking time T	0 (SCED)	200	300	400	500
Attacked bus	--	3 and 14	2, 3, 9, and 14	2, 3, 4, and 9	2, 3, 4, and 9
No. of attacked buses	0	2	4	4	4
Load shedding (MW)	0	0	9.35	19.12	19.12
Operation cost ($/h)	6205.6	6252.7	6828.3	7609.6	7609.6

TABLE 7 Fabricated quantities of LR attacks with T = 300 days.

Number of bus	Measurement	Fabricated quantity (MW)
2	P_2^{inj}	10.85 (50%)
3	P_3^{inj}	−33.05 (35.1%)
9	P_9^{inj}	14.75 (50%)
14	P_{14}^{inj}	7.45 (50%)

TABLE 8 Fabricated quantities of LR attacks with T = 500 days.

Number of bus	Measurement	Fabricated quantity (MW)
2	P_2^{inj}	10.85 (50%)
3	P_3^{inj}	−47.1 (50%)
4	P_4^{inj}	21.5 (45%)
9	P_9^{inj}	14.75 (50%)

communication links, i.e., communication links of substations corresponding with buses 3 and 14. By falsifying load measurements of buses 3 and 14, an increase of 4.1 $/h in the operation cost and no load shedding occurs. The more attack time the intruder has, the more communication links can be attacked. When the attack time $T \geq 300$ days, the intruder can attack enough communication links to falsify four load-bus measurements. However, due to the cyber vulnerability distribution, the attack scenario causing the maximum operation cost and load shedding of 7609.6 $/h and 19.12 $/h, respectively, happens when the attack time $T \geq 400$ days, for the reason that the communication link that corresponds with bus 4 needs 320.5 days to invade.

Table 7 shows the fabricated quantities of measurements in intruded communication links of substations corresponding with load buses. It can be seen that the sum of fabricated load injections is zero. Table 7 shows that when T = 300 days, the fabricated quantities of load measurements of substations at buses 2, 9, and 14 reach the ratio limitation of the fabricated magnitude. The falsified load injection of bus 3 is the maximum, which tries to transfer the load at buses 2, 9, and 14 to bus 3. Table 8 shows that when T = 500 days, the fabricated quantities of buses 2, 3, and 9 reach the maximum ratio limitation. The falsified load injection of bus 3 is the maximum, which tries to transfer the load on buses 2, 4, and 9 to bus 3.

4.2.2 LR attack with different attack resource limitations

Table 9 shows the most damaging LR attack scenarios with the limitation of different available attack resources, R, and the static attack time, T = 300. As seen from Table 5, when the attack time T = 300, the intruder has time to attack five substations' communication links corresponding with load buses 2, 3, 9, 13, and 14. The available attack resources limit the number of simultaneously falsified load measurements. The more available attack resources the intruder has, the more the measurements of buses with load can be falsified simultaneously. When the attack resource, R = 1, the LR attacks cannot be implemented because the LR attack model's constraints cannot be satisfied. With the increase of attack resources from 2 to 5, the operation cost increased from 6351.4 $/h to 7244.9 $/h, and the load shedding increased from 0 MW to 14.56 MW. Although the intruder has more attack resources with R = 6, the intruder does not have sufficient time to attack enough communication links due to the attack time limitation. Therefore, the operation cost and load shedding of R = 6 are the same as the results of R = 5.

4.3 Comparison of LR attack models

Table 10 compares the scheduling results and operating costs of the SCED without attack and different LR attack models. As shown in Table 10, it can be found that under the SCED without attack, the total operation cost is 6205.6 $/h, and no load shedding occurs. The attack scenario in the traditional LR attack causes an operation cost of 7609.6 $/h and a load shedding of 19.12 MW. However, when cyber vulnerabilities in communication links are considered, the attack scenario in the traditional LR attack may not be achieved due to the limitation of attacking time to occupy essential communication links to launch an attack. Therefore, with a limited attack time of 300 days, a more practical attack scenario can be found by the LR attack model considering cyber vulnerabilities, where the operation cost is 6828.3 $/h and a load shedding of 9.35 MW occurs. With a limited attack time of 500 days, the impacts of the LR attack considering cyber vulnerabilities and the traditional LR attack are the same. The reason for the same attack impact is that, based on Table 5, the attack time of 500 days means that the attacker has enough time to intrude into communication links of all buses with load to inject falsified data, which is unified with the assumption in the traditional LR attack that all buses with load can be intruded. Hence, the attack scenario found by the traditional LR attack model is just a case in the proposed bi-level LR attack model with sufficient attack time.

TABLE 9 LR attacks with different attack resource limitations.

Attacking resources R	1	2	3	4	5	6
Attacked bus	--	2 and 9	2, 3, and 9	2, 3, 9, and 14	2, 3, 9, 13, and 14	2, 3, 9, 13, and 14
No. of attacked buses	0	2	3	4	5	5
Load shedding (MW)	0	0	2.43	9.35	14.56	14.56
Operation cost ($/h)	6205.6	6351.4	6449.5	6828.3	7244.9	7244.9

TABLE 10 Comparison of the scheduling results and operating costs of the SCED without attack and different LR attack models with $R = 4$.

		LR attacks with T = 300 days	LR attacks with T = 500 days	Traditional LR attacks	Original SCED
Generation dispatch on gen. bus (MW)	1	199.65	189.88	189.88	180.17
	2	0	0	0	45.11
	3	30	30	30	13.72
	6	0	0	0	0
	8	20	20	20	20
Total generation (MW)		249.65	239.88	239.88	259
Operation cost ($/h)		6828.3	7609.6	7609.6	6205.6

5 Conclusion

This paper studied the modeling and impacts of LR attacks by considering cyber vulnerabilities in power systems. Unlike the existing works about LR attacks in power systems, the costs of falsifying load measurements through intruding into communication links of substations are quantitatively evaluated by the MTTC and considered in the proposed bi-level LR attack model. The proposed model can find the practical attack scenario because the intruder inevitably faces attack time limitations. Finally, a quantitative analysis was conducted to evaluate cyber vulnerabilities and LR attack impact on power systems. The cyber vulnerabilities will impact the available attack vector. Moreover, the attack scenario of the existing LR attack model is verified as an attack vector found by the proposed bi-level LR attack model with sufficient attack time to intrude into all communication links of substations.

Data availability statement

Publicly available datasets were analyzed in this study. These data can be found at: MATPOWER, a MATLAB power system simulation package [on-line], available at: http://www.pserc.cornell.edu/matpower/.

Author contributions

XS, HG, and YC contributed to the conception and design of the study. HG organized the mathematical model. WW and BY performed the statistical analysis. XS and HG wrote sections of the manuscript. XS and YC contributed to the manuscript revision and proofreading. All authors contributed to the article and approved the submitted version.

Funding

The authors are grateful for the financial support from the National Natural Science Foundation of China (Grant No. 52107070), the Provincial Natural Science Foundation of Hunan (Grant No. 2022JJ40490), the National Key R&D Program of China (Grant No. 2022YFE0129300), and the Research Foundation of the Education Department of Hunan Province (Grant No. 21B0325).

Conflict of interest

The authors declare that the research was conducted in the absence of any commercial or financial relationships that could be construed as a potential conflict of interest.

Publisher's note

References

Bahrami, M., Fotuhi-Firuzabad, M., and Farzin, H. (2020). Reliability evaluation of power grids considering integrity attacks against substation protective IEDs. *IEEE Trans. Industrial Inf.* 16 (2), 1035–1044. doi:10.1109/tii.2019.2926557

Che, L., Liu, X., Li, Z., and Wen, Y. (2019). False data injection attacks induced sequential outages in power systems. *IEEE Trans. Power Syst.* 34, 1513–1523. doi:10.1109/tpwrs.2018.2871345

CVE Database (2023). CVE details. Available at: https://www.cvedetails.com/index.php (Accessed March 23, 2023).

Deng, R., Xiao, G., Lu, R., Liang, H., and Vasilakos, A. V. (2016). False data injection on state estimation in power systems—attacks, impacts, and defense: A survey. *IEEE Trans. Industrial Inf.* 13 (2), 411–423. doi:10.1109/tii.2016.2614396

Gao, S., Lei, J., Wei, X., Liu, Y., and Wang, T. (2022). A novel bilevel false data injection attack model based on pre-and post-dispatch. *IEEE Trans. Smart Grid* 13 (3), 2487–2490. doi:10.1109/tsg.2022.3156445

Lau, P., Wang, L., Liu, Z., Wei, W., and Ten, C. W. (2021). A coalitional cyber-insurance design considering power system reliability and cyber vulnerability. *IEEE Trans. Power Syst.* 36 (6), 5512–5524. doi:10.1109/tpwrs.2021.3078730

Li, T., Chen, L., Jensen, C. S., Pedersen, T. B., Gao, Y., and Hu, J. (2022). "Evolutionary clustering of moving objects," in Proceedings of the 2022 IEEE 38th International Conference on Data Engineering (ICDE), Kuala Lumpur, Malaysia, May 2022 (IEEE), 2399–2411.

Li, Y., Zhang, H., Liang, X., and Huang, B. (2019). Event-triggered-based distributed cooperative energy management for multienergy systems. *IEEE Trans. Industrial Inf.* 15 (4), 2008–2022. doi:10.1109/tii.2018.2862436

Liang, G., Weller, S. R., Zhao, J., Luo, F., and Dong, Z. Y. (2016). The 2015 Ukraine blackout: implications for false data injection attacks. *IEEE Trans. Power Syst.* 32 (4), 3317–3318. doi:10.1109/tpwrs.2016.2631891

Liang, J., Sankar, L., and Kosut, O. (2015). Vulnerability analysis and consequences of false data injection attack on power system state estimation. *IEEE Trans. Power Syst.* 31 (5), 3864–3872. doi:10.1109/tpwrs.2015.2504950

Liu, S., Yu, J., Deng, X., and Wan, S. (2022). FedCPF: an efficient-communication federated learning approach for vehicular edge computing in 6G communication networks. *IEEE Trans. Intelligent Transp. Syst.* 23 (2), 1616–1629. doi:10.1109/tits.2021.3099368

Liu, X., Bao, Z., Lu, D., and Li, Z. (2015). Modeling of local false data injection attacks with reduced network information. *IEEE Trans. Smart Grid* 6 (4), 1686–1696. doi:10.1109/tsg.2015.2394358

Liu, X., and Li, Z. (2016). False data attacks against AC state estimation with incomplete network information. *IEEE Trans. Smart Grid* 8 (5), 2239–2248. doi:10.1109/tsg.2016.2521178

Liu, X., and Li, Z. (2014). Local load redistribution attacks in power systems with incomplete network information. *IEEE Trans. Smart Grid* 5 (4), 1665–1676. doi:10.1109/tsg.2013.2291661

Liu, X., Li, Z., Shuai, Z., and Wen, Y. (2016). Cyber attacks against the economic operation of power systems: A fast solution. *IEEE Trans. Smart Grid* 8 (2), 1023–1025. doi:10.1109/tsg.2016.2623983

Liu, Y., Ning, P., and Reiter, M. K. (2011). False data injection attacks against state estimation in electric power grids. *ACM Trans. Inf. Syst. Secur. (TISSEC)* 14 (1), 1–33. doi:10.1145/1952982.1952995

Pliatsios, D., Sarigiannidis, P., Lagkas, T., and Sarigiannidis, A. G. (2020). A survey on SCADA systems: secure protocols, incidents, threats and tactics. *IEEE Commun. Surv. Tutorials* 22 (3), 1942–1976. doi:10.1109/comst.2020.2987688

Sommestad, T., Ekstedt, M., and Nordstrom, L. (2009). Modeling security of power communication systems using defense graphs and influence diagrams. *IEEE Trans. Power Deliv.* 24 (4), 1801–1808. doi:10.1109/tpwrd.2009.2028796

Tan, S., Song, W. Z., Stewart, M., Yang, J., and Tong, L. (2016). Online data integrity attacks against real-time electrical market in smart grid. *IEEE Trans. Smart Grid* 9 (1), 313–322. doi:10.1109/tsg.2016.2550801

Ten, C. W., Liu, C. C., and Manimaran, G. (2008). Vulnerability assessment of cybersecurity for SCADA systems. *IEEE Trans. Power Syst.* 23 (4), 1836–1846. doi:10.1109/tpwrs.2008.2002298

Xiang, Y., Ding, Z., Zhang, Y., and Wang, L. (2016). Power system reliability evaluation considering load redistribution attacks. *IEEE Trans. Smart Grid* 8 (2), 889–901. doi:10.1109/TSG.2016.2569589

Yang, L., Sun, Q., Zhang, N., and Li, Y. (2022). Indirect multi-energy transactions of energy internet with deep reinforcement learning approach. *IEEE Trans. Power Syst.* 37 (5), 4067–4077. doi:10.1109/tpwrs.2022.3142969

Yuan, Y., Li, Z., and Ren, K. (2011). Modeling load redistribution attacks in power systems. *IEEE Trans. Smart Grid* 2 (2), 382–390. doi:10.1109/tsg.2011.2123925

Zhang, F., and Yang, Q. (2022). False data injection attack detection in dynamic power grid: A recurrent neural network-based method. *Front. Energy Res.* 10, 1005660. doi:10.3389/fenrg.2022.1005660

Zhang, Y., Wang, L., Xiang, Y., and Ten, C. W. (2015). Power system reliability evaluation with SCADA cybersecurity considerations. *IEEE Trans. Smart Grid* 6 (4), 1707–1721. doi:10.1109/tsg.2015.2396994

Zhang, Y., Xiang, Y., and Wang, L. (2017). Power system reliability assessment incorporating cyber attacks against wind farm energy management systems. *IEEE Trans. Smart Grid* 8 (5), 2343–2357. doi:10.1109/tsg.2016.2523515

Zieger, A., Freiling, F., and Kossakowski, K. P. (2018). "The β-time-to-compromise metric for practical cyber security risk estimation," in Proceedings of the 2018 11th International Conference on IT Security Incident Management & IT Forensics (IMF), Hamburg, Germany, May 2018 (IEEE), 115–133.

Zimmerman, R., and Murillo-Sánchez, C. (2016). MATPOWER 6.0 user's manual. Available at: http://www.pserc.cornell.edu/matpower/manual.pdf (Accessed October 8, 2020).

Nomenclature

Indices and sets	
n	Bus index
d	Load bus index
l	Transmission line index
g	Generator index
CM	Countermeasures in LR attack
SG	Sub-goal in LR attack
G	Goal in LR attack
$I(SG_j)$	Set of countermeasures CM_i needed to defeat to achieve SG_j
J	Set of the LR attack sub-goals SG_j
CVSS	Common Vulnerability Scoring System
MTTC	Mean time to compromise
Parameters	
M	Sufficiently large positive constant
ε	Sufficiently small positive constant
τ	Bound of $\Delta D_d/D_d$ for each load d
c_g	Generation cost (/MWh) of generator g
cs_d	Load shedding cost (/MWh) of load bus d
D_d	Actual value of load bus d (in MW)
KD	Bus–load incidence matrix
KP	Bus–generator incidence matrix
N_n	Number of buses
N_d	Number of load buses
N_g	Number of generators
N_l	Number of transmission lines
P_g^{max}, P_g^{min}	Maximum and minimum generation outputs (in MW) of generator g
PL_l^{max}	Capacity (in MW) of the transmission line
R	Attacking resources
T	Limited attacking time of the intruder
SF	Shifting factor matrix
σ	Number of total vulnerabilities
Variables	
$P_d(CM_i)$	Probability that CM_i is reached for the communication link of substation at bus d
$P_d(SG_j)$	Probability that SG_j is reached for the communication link of substation at bus d
$P_d(G)$	Probability that G is reached for the communication link of substation at bus d
$T_{d,i}(v_i)$	Compromise time in CM_i of the communication link of substation at bus d
v_i	Number of known vulnerabilities of the component
s	Skill factor of the intruder
ΔD_d	Attack on the measurement (in MW) of load d
ΔP_g	Output power change of generator g
PL_l	Power flow (in MW) of transmission line l
P_g	Generation output (in MW) of generator g
S_d	Load shedding (in MW) of load d
t_d	Compromise time of load d
$\delta_{D,d}$	Binary variable 1, if load d is attacked
$\delta_{t,d}$	Binary variable 1, if load d could be attacked
t_1, t_2, t_3	The mean time of three sub-processes
P_1, P_2, P_3	The probabilities of three sub-processes

frontiers | Frontiers in Energy Research

TYPE Original Research
PUBLISHED 20 October 2023
DOI 10.3389/fenrg.2023.1281267

OPEN ACCESS

EDITED BY
Mingfei Ban,
Northeast Forestry University, China

REVIEWED BY
Guangsheng Pan,
Southeast University, China
Meng Song,
Southeast University, China

*CORRESPONDENCE
Yongqi Li,
2631764464@qq.com

RECEIVED 22 August 2023
ACCEPTED 13 October 2023
PUBLISHED 20 October 2023

CITATION
Li L, Li Y, Wan M and Tan Q (2023), Evaluating and aggregating the grid-support capability of energy storage clusters by considering the peak regulation requirements.
Front. Energy Res. 11:1281267.
doi: 10.3389/fenrg.2023.1281267

Evaluating and aggregating the grid-support capability of energy storage clusters by considering the peak regulation requirements

Leqing Li, Yongqi Li*, Minhui Wan and Qipeng Tan

China Southern Power Grid Power Generation Co., Ltd., Energy Storage Research Institute, Guangzhou, China

With the rapid progression of Energy Storage Systems (ESSs), the capability of extensively distributed and heterogeneous ESSs to support the power grid remains largely underexplored. To better exploit the potential of these numerous ESSs and enhance their service to the power grid, this paper proposes a model for evaluating and aggregating the grid-support capability of energy storage clusters by considering the peak regulation requirements. To begin with, the proposed model employs subjective and objective combination weighting methods to establish a grid-support capability matrix between ESSs indicators and grid demand scenarios, thereby facilitating the identification of the ESSs with a strong ability to regulate peak power. Next, based on the dual-peak pattern of grid load and diverse characteristics of ESSs, the ESSs in the peak regulation cluster are evaluated by clustering again. In addition, taking into account the operational constraints of the ESSs and the peak regulation requirements, a grid-support capability aggregation model for energy storage clusters based on the revised Chino polytope is proposed. The case study results demonstrate that the proposed model not only balances computational efficiency and aggregation accuracy to a certain extent but also enhances the capability of energy storage clusters to participate in peak regulation of the power grid.

KEYWORDS

peak regulation requirements, combination weighting method, grid-support capability evaluation, grid-support capability aggregation, revised Chino polytope

1 Introduction

As the integration of large-scale renewable energy sources into the power grid escalates (Hua et al., 2019; Li et al., 2023) the lack of peak-shaving performance of the power system is becoming increasingly evident (Li et al., 2019). Novel Energy Storage Systems (ESSs) are proving to be crucial assets with their innate flexibility and adaptability, playing a substantial role in achieving rapid peak shaving (Cui B. et al., 2021a). This is particularly noteworthy as their incorporation within the grid systematically amplifies (Yi et al., 2022). However, due to the numerous and diverse indicators of individual ESSs, their scattered locations, and varying support capabilities for the power grid (Zhang and Hredzak, 2021; Han and Zhang, 2022), it is challenging for individual ESSs to form effective regulatory resources and administer them in isolation (Zhao et al., 2022). Nevertheless, energy storage clusters can provide scientific decision-making basis for power system operation scheduling by managing dispersed ESSs. Therefore, to enable the overall participation of ESSs in system peak shaving, it is necessary

to evaluate the grid-support capability of massive ESSs and establish an aggregation model for the energy storage clusters.

In regard to the evaluation and analysis of energy storage clusters, extensive research has been conducted, focusing remarkably on the indices associated with individual ESSs. Ding et al. (2018) propose a comprehensive performance index system that combines structural and functional aspects, as well as an improved genetic algorithm for cluster evaluation. Ding et al. (2021) introduce the cluster flexibility supply-demand balance index and flexibility balance index and combine them with the modularity index to propose an evaluation method that comprehensively considers cluster topology and flexibility balance for energy storage clusters. A distributed dynamic evaluation clustering algorithm is introduced that utilizes energy storage capacity and local demand as state features, aiming to save computational resources (Zhang et al., 2021). However, most existing research focuses on evaluating different technical indicators of ESSs without considering the varying demands of the power grid or the balance between subjectivity and objectivity, which is not conducive to energy storage to better serve the power grid. To address this gap, this paper employs subjective and objective combination weighting methods to establish a grid-support capability evaluation model for energy storage clusters based on the peak shaving demands in a dual-peak grid pattern. In the first step, a grid-support capability matrix is solved to determine the support capability of each ESS for various grid demand scenarios, facilitating the selection of peak-shaving ESSs. In the second step, a comprehensive evaluation of power, capacity, and ramping indicators is conducted, using the K-means clustering algorithm to perform evaluations on power-type and energy-type ESSs.

The aggregation of energy storage cluster grid-support capability essentially characterizes the feasible domain of cluster flexibility. Energy storage capability can be described as the feasible region of output power in all periods (Sajjad et al., 2016), which is influenced by its operational constraints and grid scheduling constraints (Zhang and Hredzak, 2021). Analyzing the feasible region of an energy storage cluster requires considering the temporal coupling characteristics, such as the time dependency of charging and discharging (Wen et al., 2022a). Directly aggregating the feasible region of an energy storage cluster may lead to the curse of dimensionality (Muller et al., 2019), while approximating solutions may reduce aggregation accuracy (Chen and Li, 2021; Ayesha et al., 2023). Thus, there is a need for an efficient and accurate method to aggregate the energy storage clusters, which will lay the foundation for their efficient participation in grid peak shaving. This paper presents a novel method for aggregating ESSs based on the grid-support capability evaluation of energy storage clusters, thereby improving the rationality and computational efficiency of the aggregation process.

Regarding the aggregation of grid-support capability for ESSs, there are primarily two approaches: top-down and bottom-up (Wang and Wu, 2021; Bhatti et al., 2023). The top-down approach directly constructs the feasible domain of a cluster through data analysis and probabilistic modeling (Yi et al., 2020). Wang and Wu (2021) propose the high-dimensional polytope based bound shrinking method to calculate the feasible region of distributed energy resources considering the network constraints. The kth-order approximate models and two types of multi-timescale approximate models are proposed to analyze the exact aggregate feasible region of ESSs. Wen et al. (2022b) propose a flexibility optimization method and a backtracking elimination method to aggregate the temporally coupled grid-support capability of ESSs considering system security constraints. Nonetheless, an inherent problem associated with these top-down approaches is that when the computational scale enlarges, there is a concomitant and substantial degradation in computational efficiency. On the other hand, the bottom-up approach describes the feasible domain of individual resources (Ma et al., 2023), followed by aggregating multiple independent operating domains into a unified whole.

A plethora of scholarly research posits that calculating the feasible domain of a cluster from a bottom-up perspective involves computing the Minkowski sum of multiple high-dimensional polytopes, for which there is no efficient general solution. Therefore, existing research mainly focuses on approximating the feasible domain using a concise and compact model. Several basic geometric shapes, such as boxes (Chen et al., 2020), ellipsoids (Chen and Li, 2021), and medians (Calero et al., 2021), have been attempted for internal approximation. Among them, the Chino polytope preserves the characteristics of the feasible domain and has high aggregation efficiency (Cui Y. et al., 2021b). However, there is a geometric difference between the Chino polytope and the original feasible domain. To address this issue, this paper proposes a feasible domain weight adjustment strategy that prioritizes the high-demand peak-shaving feasible domain portions to enhance the overall peak-shaving capability of the energy storage cluster.

In summary, the contributions of this paper are as follows:

(1) To address the issue of incomplete evaluation of energy storage clusters, this paper establishes a grid-support capability evaluation model based on peak regulation requirements, utilizing a subjective and objective combination weighting method and the K-means clustering algorithm, which facilitates a more comprehensive evaluation and set the stage for aggregation.
(2) To address the issue of impractical computational scale and low accuracy in aggregating energy storage clusters, this paper proposes a novel grid-support capability aggregation method based on the revised Chino polytope, which not only strikes a balance between computational efficiency and aggregation accuracy but also enhances the capability of energy storage clusters to participate in peak regulation.

The remaining contents of the paper are as follows: Section 2 restates the background of the research question. Section 3 introduces the grid-support capability evaluation of energy storage clusters. Section 4 proposes grid-support capability aggregation based on the revised Chino polytope. Section 5 analyzes the result through the simulation. Section 6 summarizes the whole paper and gives the conclusion.

2 Problem statement

According to the typical power load curves of various provincial power grids published by the National Development and Reform Commission and the National Energy Administration, most provincial typical daily power load curves show a clear dual-peak

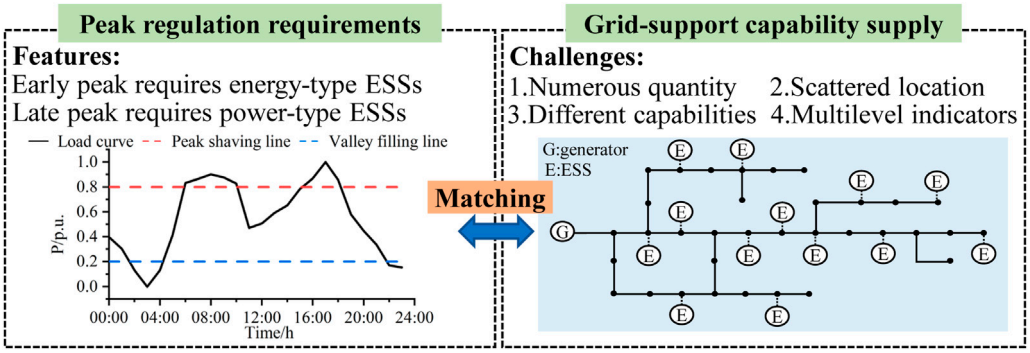

FIGURE 1
The illustration of the problem background.

trend. Specifically, there is an early peak during the daytime, while a late peak occurs during the nighttime. During the daytime peak period, the load is mainly driven by residential, commercial, and industrial electricity consumption, with a longer duration of peak load. During the nighttime peak period, the load is mainly driven by residential and commercial electricity consumption, with a shorter duration of peak load. The power grid regulation requirements differ under these two modes.

The integration of a high proportion of renewable energy has become an inevitable trend in power grid development (Leng and Zhang, 2023). Meanwhile, the intermittency and volatility of renewable energy sources will become crucial factors affecting the peak-to-valley difference in the power system (Yang et al., 2023). In addition, the output adjustment range and speed of traditional energy sources such as conventional thermal power and cogeneration are limited and cannot meet the peak load regulation requirements of future power systems. Therefore, the insufficient peak load regulation capacity of the power system has become increasingly prominent under the existing energy structure. In contrast, ESSs possess strong flexibility and rapid adjustment characteristics, enabling them to effectively address the peak-shaving challenges arising from both renewable and conventional energy sources. According to the peak shaving market rules, as a third-party independent entity, ESSs are required to strictly follow the day-ahead generation schedule for their output (Nan et al., 2022). When the load curve exceeds the peak-shaving line, the ESS discharges electricity, and when the load curve falls below the valley-filling line, the ESS charges. Based on the dual-peak mode, ESSs manifest two typical discharge periods during the early and late peaks. During the daytime early peak, the load curve is relatively stable, requiring energy-type ESSs to participate in peak regulation. During the nighttime late peak, the load curve has a steep slope, requiring power-type ESSs to participate in peak regulation. Given the extensive and diverse operational indicators of individual ESSs, their disparate geographic distribution, and their differing capabilities to bolster the power grid, it is a formidable challenge to consolidate individual ESSs into effective regulatory resources. Nevertheless, clusters of ESSs can provide a scientific basis for decision-making in power system operational scheduling by proficiently managing these ESSs. Consequently, with the objective of ensuring the comprehensive participation of ESSs in system peak shaving, it becomes imperative to undertake a detailed evaluation of the grid-support potential of numerous ESSs and to develop a robust model that encapsulates the capability inherent within these ESS clusters. Figure 1 shows the illustration of the problem background.

To comprehensively consider the peak regulation requirements of the power grid and the operational characteristics of ESSs, this paper proposes a grid-support capability evaluation and aggregation model for energy storage clusters, based on the dual-peak mode of the power grid. This model not only optimizes computational resource utilization but also accommodates varying regulation requirements at different times, to a certain extent, improving the capability of energy storage clusters to participate in peak shaving. The illustration of the proposed evaluating and aggregating model is shown in Figure 2.

In the first stage, a grid-support capability evaluation model for energy storage clusters is established. To begin with, a multilevel indicator system for ESSs is built, and based on this, a grid-support capability matrix is created using the combination weighting method to evaluate the compatibility between the ESSs and the grid demand scenarios. Next, we identify ESSs with strong peak-shaving support capabilities to form the selected cluster. In addition, using the power, capacity, and ramp rate as characteristic indicators, the K-means clustering algorithm is employed to conduct the second step evaluation for power-type and energy-type ESSs.

In the second stage, based on the grid-support capability evaluation model, a grid-support capability approximate model for individual ESS is established utilizing the revised Chino polytope. This model accurately characterizes the feasible region of energy storage participating in grid peak regulation at different times by solving the weight correction factor during peak regulation periods. Leveraging this approximate model, the grid-support capability of all ESSs is aggregated using the Minkowski sum, thereby obtaining the feasible region of the entire energy storage cluster. To visually compare the approximate effect of the existing model on the original feasible domain, this paper projects the high-dimensional results onto a two-dimensional plane. Moreover, the effectiveness of the proposed model is validated through peak-shaving verification involving the participation of an energy storage cluster.

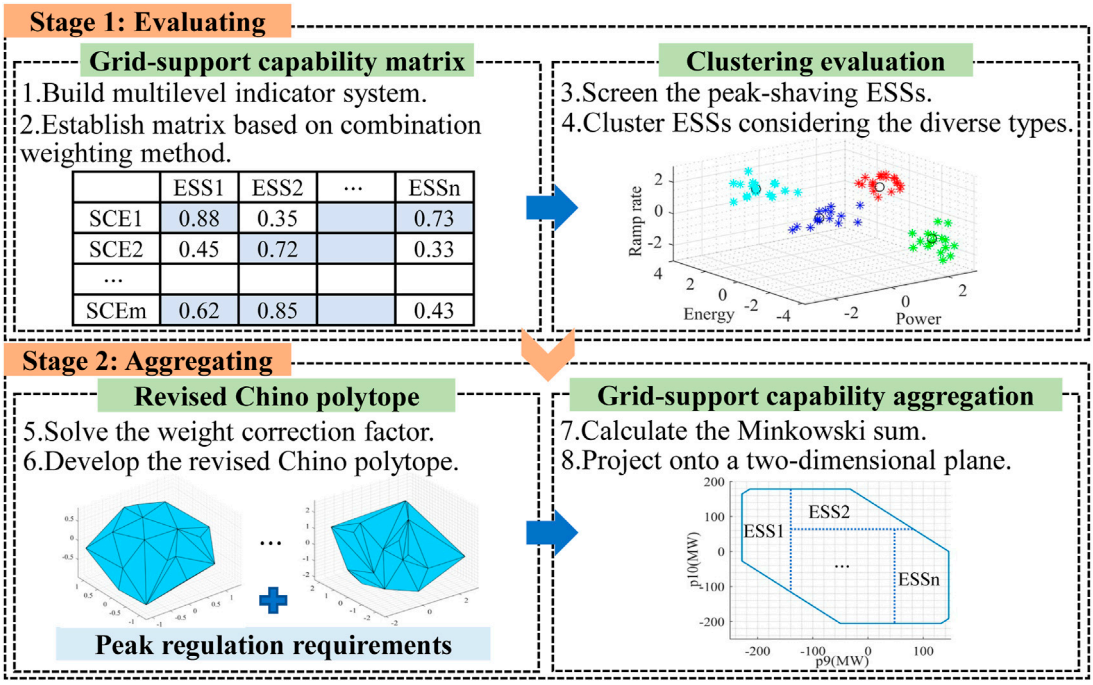

FIGURE 2
The illustration of the proposed evaluating and aggregating model.

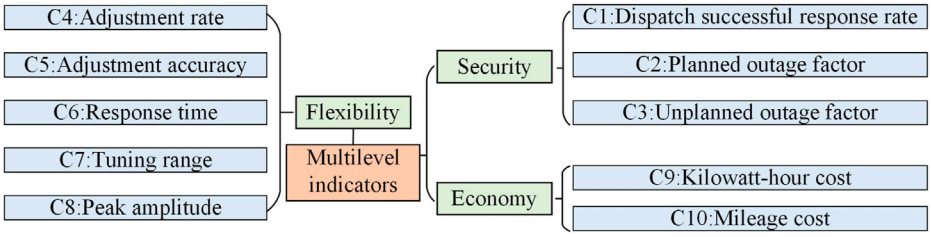

FIGURE 3
Multilevel indicator system for ESSs.

3 Grid-support capability evaluation of energy storage clusters

3.1 Grid-support capability matrix based on combination weighting method

To evaluate the grid-support capability of various individual ESSs under different demand scenarios, we adopt a combination of analytic hierarchy process (AHP) and entropy weighting method to refine the technical indicators of ESSs. This results in the establishment of a hybrid subjective-objective matrix for evaluating the support capability between ESSs and grid demands. Compared to the conventional single-weighting method, the combination weighting method weakens the weights of larger indicators and strengthens the weights of smaller indicators, thus avoiding the problem of some indicators becoming ineffective due to large differences in weights.

Considering the perspectives of security, flexibility, and economy, a multilevel indicator system for the ESSs is constructed. The specific primary and secondary indicators are shown in Figure 3.

Subsequently, following the establishment of a multilevel indicator system, we construct a grid-support capability matrix based on the combined subjective and objective weighting method which is realized through the following distinctive steps:

Step 1: The indicators of the energy storage systems are normalized and standardized. The judgment matrices for various primary indicators under different grid demand scenarios are constructed, focusing mainly on peak shaving, frequency regulation, and

emergency power support as the typical application scenarios in this study.

Step 2: The maximum eigenvalue of the corresponding matrix is deduced from the judgment matrices with a consistency test performed thereafter. If the test fails, return to step 1 to reconstruct the judgment matrices. If the test passes, proceed to the next step.

Step 3: Calculate the weights of the primary indicators for various demand scenarios. Mirroring this process, obtain the weights of the secondary indicators.

Step 4: Based on the historical data of the multilevel indicators corresponding to different grid demands of each ESS, the entropy weight method is employed to acquire the weights of the technical indicators for different demand scenarios.

Step 5: Integration of the Analytic Hierarchy Process (AHP) and entropy weight method facilitates the establishment of a model for harmonizing subjective and objective weighted attribute values, consequently deriving the combined weights of the indicators. The proposed model for harmonizing subjective and objective weighted attribute values is solved using mathematical programming, ensuring the consistency between the two types of attribute values and avoiding the problem of one weight dominating over the other. The model is represented as follows:

$$\begin{cases} \min H = \sum_{j=1}^{m}\sum_{i=1}^{n}\left(\alpha_1 w_i^1 x_{ij} - \alpha_2 w_i^2 x_{ij}\right)^2 \\ \text{s.t}\ \alpha_1\alpha_2 \geqslant 0, \alpha_1 + \alpha_2 = 1 \end{cases} \tag{1}$$

where x_{ij} represents the standardized value of indicator j for ESS i. m is the number of energy storage power stations and n is the number of indicators. w_i^1 and w_i^2 are the subjective weights determined by the AHP and the objective weights determined by the entropy weight method, respectively. α_1 and α_2 are the allocation coefficients for the subjective and objective weights, respectively. H represents the deviation of the combined subjective and objective attribute values.

Step 6: The grid demand scenarios and the indicators of the ESSs are restored, and the processed indicators are multiplied by the weights of the indicators under different grid demand scenarios, resulting in the grid-support capability matrix between the ESSs and the power grid demand scenarios. Consequently, the support capability matrix is shown as follows:

$$AS = \begin{bmatrix} a_{11} & a_{21} & \cdots & a_{m1} \\ a_{12} & a_{22} & \cdots & a_{m2} \\ \cdots & \cdots & \cdots & \cdots \\ a_{1k} & a_{2k} & \cdots & a_{mk} \end{bmatrix} \tag{2}$$

where AS represents the grid-support capability matrix, and a_{mk} represents the grid-support capability of ESS m under the power grid demand scenario k.

By establishing the aforementioned grid-support capability matrix, we can evaluate the grid-support capability of various large-scale energy storage systems under different power grid scenarios. Then, select energy storage systems with grid-support capability exceeding 0.5 for peak shaving requirements and categorize them as peak shaving energy storage.

3.2 Clustering evaluation considering different types of ESSs

The first step evaluation has successfully identified energy storage systems that possess strong peak shaving support. Following this, the second step is primarily focused on further evaluating the selected peak-shaving energy storage through clustering algorithms based on the dual-peak pattern, thus establishing the groundwork for subsequent aggregation.

Specifically, due to the obvious dual-peak pattern of the power grid load, the peak shaving period can be divided into two distinct periods: the morning peak period, which requires sustained discharge at a relatively low power level, and the evening peak period, which demands high-power short-duration discharge. In this approach, the ratio of power-to-energy for each ESS is computed and subsequently sorted based on a numerical value. Standardization is then applied, further ranking these ratios. Simultaneously, the deviations between the load curve and the peak-shaving line during both the early and late peak periods are calculated and sorted using the same methodology. It is crucial to note that when a certain rank exhibits a higher number of deviations corresponding to the early peak, the ESSs within this rank are categorized as energy-type. Conversely, if a rank presents a predominant number of deviations associated with the late peak, the ESSs within this rank are classified as power-type. Therefore, the peak shaving energy storage systems are further classified into power-type and energy-type based on their energy-to-power ratio, which sets the foundation for peak shaving during the dual-peak pattern of the power grid. Subsequently, to facilitate the scheduling of the energy storage clusters, clustering analysis is performed separately on the power-type and energy-type peak-shaving energy storage clusters. The clustering analysis considers the maximum ramping rate, maximum charging and discharging power, and capacity of the energy storage as feature states and utilizes the K-means clustering algorithm for the second stage evaluation.

The specific steps of this method are as follows:

1) Standardize the feature states of each energy storage system, including the maximum ramping rate, maximum charging and discharging power, and capacity.
2) Randomly select K energy storage systems as initial cluster centers, denoted as y_k.
3) Calculate the Euclidean distance between each energy storage system and the K cluster centers, and assign them to the cluster with the shortest distance.
4) Calculate the average feature states of each cluster's energy storage systems and update them as the new cluster centers.
5) Check if the clustering results have converged, if not, go back to step 3).

The illustration of the proposed clustering evaluation method is shown in Figure 4. The proposed evaluation model can provide a comprehensive evaluation of energy storage systems in the cluster,

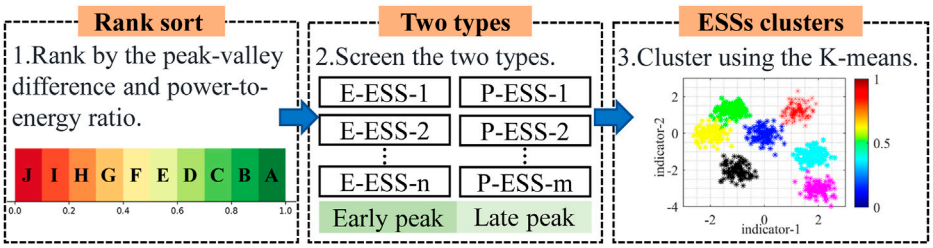

FIGURE 4
The illustration of the proposed clustering evaluation method.

facilitating their effective deployment and utilization in supporting the power grid demand. Furthermore, this aims to enhance the efficiency of subsequent energy storage cluster aggregation.

4 Grid-support capability aggregation based on revised chino polytope

The impact of time-domain coupled energy constraints on energy storage, coupled with a burgeoning increase of the feasible boundary plane description with the rise of dimension and addition of parameter operation sets, presents a considerable challenge. Computationally, the aggregation of the grid-support capability in energy storage clusters involves computing the Minkowski sum of multiple high-dimensional polytopes, and direct solving leads to the curse of dimensionality. Therefore, to enhance the rationality and efficiency of the solution, this study utilizes the Chino polytope approximation method to characterize the feasible region of individual energy storage systems based on the previous grid-support capability evaluation results. The Chino polytope differs from the convex polytope of the original feasible domain in a geometric shape. To address this issue, this paper proposes a feasible domain weighting adjustment strategy based on the Chino polytope model that considers the difference in load demand at different periods and prioritizes retaining the flexibility part with higher peak shaving demands to improve the peak shaving capability of the energy storage clusters. In summary, the aggregating model considering the peak regulation requirements is the revision and improvement of the Chino polytope model.

4.1 Chino polytope model

The overall overview of the core ideas and key steps of the Chino polytope model are as follows. Firstly, considering the power, energy, and ramping constraints, the original flexibility of energy storage systems is obtained. Secondly, by constructing the matrix of the running constraints, the in-Chino polytope approximation model is established. Finally, the model is solved by transforming it into an optimization problem with original and approximate flexibility of normal vector direction.

For different types of ESSs, when considering a finite and discrete scheduling decision period with N scheduling points, where each segment has a time interval of t_s, the output of the energy storage stations within the scheduling interval is represented by $p(t)$, thus describing the feasible domain based on convex polytopes with the following constraints.

a)Power constraints

If the power is assumed to be p_k constant in a certain scheduling period, the power constraints can be expressed as follows:

$$\begin{aligned} &p_{k,\min} \leqslant p_k \leqslant p_{k,\max} \\ &k = 0, \cdots, N-1 \end{aligned} \tag{3}$$

b) Energy constraints

The energy state of ESS may change with the change of its power, and the relationship between the discrete energy state s_k and the power variable p_k is as follows:

$$\begin{aligned} &s_{k+1,\min} \leqslant s_k + cp_k \leqslant s_{k+1,\max} \\ &k = 0, \cdots, N-1 \end{aligned} \tag{4}$$

c) Ramp rate constraints

The ramp rate constraint represents the rate of change of power, expressed in discrete form as follows:

$$\begin{aligned} &r_{k,\min} \leqslant p_k - p_{k-1} \leqslant r_{k,\max} \\ &k = 1, \cdots, N-1 \end{aligned} \tag{5}$$

Taking into account the aforementioned constraints, the operationally feasible region of a single ESS $\mathcal{P}$ is described as a convex polytope characterized by a set of inequality constraints.

$$\mathcal{P} = \left\{ \boldsymbol{p} \in \mathbb{R}^N \,\middle|\, \boldsymbol{A}\boldsymbol{p} \leq \boldsymbol{b} \right\} \tag{6}$$

where $\boldsymbol{p}$ represents the power of energy storage in the decision-making period of N periods. $\boldsymbol{A}$ and $\boldsymbol{b}$ are the coefficients after expressing all inequality constraints of the feasible domain in matrix form. Therefore, the operational grid-support capability of ESS can be abbreviated as $\mathcal{P}(A, b)$.

To establish a Chino polytope model, the grid-support capability of a single ESS is utilized by the following expression:

$$\mathcal{Z} := \{ \boldsymbol{p} \in \mathbb{R}^N \mid \boldsymbol{p} = \boldsymbol{c} + \boldsymbol{G}\boldsymbol{\beta} \} \tag{7}$$

where $\boldsymbol{p} \in \mathbb{R}^N$ denotes the output flexibility of a single ESS within a decision cycle considering N periods, and $\boldsymbol{c} \in \mathbb{R}^N$ represents the

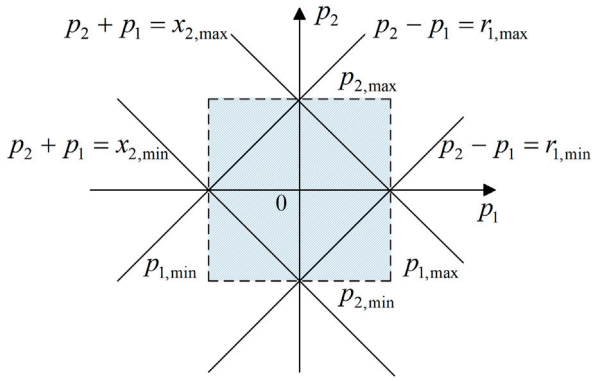

FIGURE 5
Construction vector matrix diagram.

center of a chino polytope. $\boldsymbol{G}$: $= [g_1, \cdots, g_{N_g}] \in \mathbb{R}^{N \times N_g}$ stands for construction matrix, and g_i represents the i-th construction vector. $\boldsymbol{\beta} = [\beta_1, \cdots, \beta_{N_g}]^T$ represents the scaling factors corresponding to each construction vector, which determines the extension distance of each construction vector. N_g indicates the number of construction vectors.

The shape characterization parameters of the Chino polytope include construction matrix $\boldsymbol{G}$, polytope center $\boldsymbol{c}$, and shrinkage coefficient $\boldsymbol{\beta}$. In this paper, $\boldsymbol{G}$ is regarded as a known quantity, and $\boldsymbol{c}$ and $\boldsymbol{\beta}$ are both decision variables of the optimization problem. Firstly, a construction matrix is constructed which can effectively represent all power, energy, and ramp rate constraints.

$$\begin{cases} \mathbf{g}_{\text{power}}(k) = \left[0, \cdots, 0, \underset{k+1}{1}, 0, \cdots, 0\right] \in R^N \\ \mathbf{g}_{\text{energy}}(k) = \left[0, \cdots, 0, \underset{k+1}{-1/\sqrt{2}}, \underset{k+2}{1/\sqrt{2}}, 0, \cdots, 0\right] \in R^N \\ \mathbf{g}_{\text{ramp}}(k) = \left[0, \cdots, 0, \underset{k+1}{1/\sqrt{2}}, \underset{k+2}{1/\sqrt{2}}, 0, \cdots, 0\right] \in R^N \end{cases} \tag{8}$$

where $\mathbf{g}_{\text{power}}(k)$, $\mathbf{g}_{\text{energy}}(k)$ and $\mathbf{g}_{\text{ramp}}(k)$ represent construction vectors corresponding to power, energy, and ramp rate constraints at $k = 0, 1, \cdots, \mathrm{N}-1$ period, and the construction matrix can generate hyperplanes parallel to the corresponding constraints. Taking t_1 and t_2 as two adjacent moments, the construction vector matrix diagram is shown in Figure 5.

Considering the power, ramp rate, and capacity constraints of the ESSs, the original matrix parameters of a single ESS are obtained.

$$\boldsymbol{A}_1 = \begin{bmatrix} 1 & 0 & \cdots & 0 \\ 0 & 1 & \cdots & 0 \\ \vdots & \vdots & \ddots & \vdots \\ 0 & 0 & \cdots & 1 \end{bmatrix}_{N \times N} \tag{9}$$

$$\boldsymbol{A}_3 = \begin{bmatrix} 1 & 0 & \cdots & 0 \\ 1 & 1 & \cdots & 0 \\ \vdots & \vdots & \ddots & \vdots \\ 1 & 1 & \cdots & 1 \end{bmatrix}_{N \times N} \tag{10}$$

$$\boldsymbol{A}_2 = \begin{bmatrix} -1 & 1 & 0 & \cdots & 0 \\ 0 & -1 & 1 & \cdots & 0 \\ \vdots & \vdots & \ddots & \ddots & \vdots \\ 0 & 0 & \cdots & -1 & 1 \end{bmatrix}_{(N-1) \times N} \tag{11}$$

$$\boldsymbol{A} = \left[A_1 - A_1 A_2^{\top} - A_2^{\top} A_3^{\top} - A_3^{\top}\right]^{\top} \tag{12}$$

$$\boldsymbol{b} = \left[p_{\max} - p_{\min} r_{\max} r_{\min} e_{\max} - e_{\min}\right]^{\top} \tag{13}$$

where $p_{\max}$ and $p_{\min}$ represent the upper and lower limits of the ESS power respectively. $r_{\max}$ and $r_{\min}$ represent the upper and lower limits of the ESS ramp rate respectively. $e_{\max}$ and $e_{\min}$ represent the upper and lower limits of ESS capacity respectively.

To facilitate a more concise and coherent depiction of the similarity between the Chino polytope and the original polytope, this study randomly selects a sufficient number of polytope normal vectors. The similarity is then characterized by calculating the ratio of their diameters on the normal vectors. Therefore, the similarity between the Chino polytope and the original polytope is as follows:

$$\Lambda_s = d_s^{\mathcal{Z}} / d_s^{\mathcal{P}} \tag{14}$$

where $d_s^{\mathcal{Z}}$ and $d_s^{\mathcal{P}}$ represent the diameters of the Chino polytope $\mathcal{Z}$ and the original polytope $\mathcal{P}$ along the normal vector direction α^s respectively. S represents the number of normal vectors. The closer the $\Lambda_s \in [0, 1]$ value is to 1, the higher the similarity between $d_s^{\mathcal{Z}}$ and $d_s^{\mathcal{P}}$.

If a certain normal vector α^s is known, the optimization problem of finding the tangent point of a convex polytope and calculating its diameter can be expressed as follows:

$$\begin{aligned} & d_s^{\mathcal{P}} = \left|\max\left(\boldsymbol{\alpha}_s \boldsymbol{p} - \varepsilon\right) - \min\left(\boldsymbol{\alpha}_s \boldsymbol{p} - \varepsilon\right)\right| / \left\|\boldsymbol{\alpha}_s\right\|_2 \\ & \text{s.t. } \boldsymbol{A}\boldsymbol{p} \leqslant \boldsymbol{b} \end{aligned} \tag{15}$$

where ε represents a sufficiently large constant.

Furthermore, the diameter of the Chino polytope in the direction represented by the normal vector α^s is as follows:

$$d_s^{\mathcal{Z}} = 2\left|\boldsymbol{\alpha}_s \boldsymbol{G}\right|\boldsymbol{\beta} \tag{16}$$

4.2 Aggregating model considering the peak regulation requirements

Under different peak shaving demands in different periods of the power grid, the output of the energy storage cluster varies. To enhance the peak shaving capability of the energy storage cluster in power grid integration, it is advisable to improve the approximation accuracy of the flexible feasible domain during peak shaving periods. In response to this issue, this paper primarily adopts two measures to adjust the grid-support capability of the energy storage cluster. The first measure involves establishing a correction factor for peak load periods based on the difference among the peak shaving line, valley filling line, and load curves. The second measure involves considering the influence of uncertain factors such as temperature on energy storage and characterizing its dynamic probability distribution during peak load periods.

To begin with, based on the typical daily dual-peak load curve of the power grid, the peak shaving line, valley filling line, and the absolute difference between the load curve are normalized. This process determines the peak shaving weight for each time interval, thereby obtaining the weight correction factor. The specific calculation formula is shown as follows:

$$\begin{cases} \Delta P_t = \left| P_{load,t} - P_{line,t} \right| \\ \mu_t = \dfrac{\Delta P_t - \Delta P_{\min}}{\Delta P_{\max} - \Delta P_{\min}} \\ \boldsymbol{w}_i = [\mu_1, \mu_2, \cdots, \mu_N] \end{cases} \tag{17}$$

where $P_{load,t}$ represents the load curve at time t. $P_{line,t}$ represents the peak shaving and valley filling line at time t. P_{min} and P_{max} represent the minimum and the maximum value of the load curve respectively. $\boldsymbol{w}_i$ is the weight correction vector for the i-th ESS, and N is the number of scheduling periods.

The approximate degree of the grid-support capability in the normal vector direction can be modified according to the weight correction factor.

$$\boldsymbol{\Lambda}_S{}' = \boldsymbol{\Lambda}_S(\boldsymbol{w}(\boldsymbol{\alpha}_s)^2) = \boldsymbol{\Lambda}_S\left(\sum_{i=1}^{N} w_i x_i^2\right) \tag{18}$$

where $\boldsymbol{\alpha}_s = (x_1, x_2, \cdots, x_N)$.

Moreover, the output of energy storage is subject to uncertainties caused by factors such as temperature and state of health (SOH). To characterize this characteristic, the dynamic probability distribution of energy storage output during peak load periods is obtained based on historical energy storage output data using non-parametric kernel density estimation theory. Based on this, a certain confidence level is selected to dynamically represent the uncertainty of energy storage output during peak load periods. By considering its probabilistic characteristics in the process of aggregation, general chance constraints can be formulated as follows:

$$\mathbb{P}\{\boldsymbol{a}^\top \boldsymbol{e} + \boldsymbol{b}^\top \boldsymbol{x} \le c\} \ge 1 - \alpha \tag{19}$$

where $\boldsymbol{x}$ represents the decision variable, i.e., the energy storage output. $\boldsymbol{e}$ represents the prediction error vector. $\boldsymbol{a}$, $\boldsymbol{b}$, and c are constants and $1 - \alpha$ represents the confidence level.

The joint probability function of the prediction error $\boldsymbol{e}$ for a Gaussian Mixture Model (GMM) can be approximated by a linear combination of several Gaussian functions (Goel et al., 2023). Then, the quantiles of the random variable $\boldsymbol{a}^\top \boldsymbol{e}$ at a confidence level $1 - \alpha$ can be calculated using the following equation, thereby transforming chance constraints into deterministic constraints.

$$c - \boldsymbol{b}^\top \boldsymbol{x} \ge \mathrm{Quant}(1 - \alpha \mid \boldsymbol{a}^\top \boldsymbol{e}) \tag{20}$$

where $\mathrm{Quant}(1 - \alpha \mid \boldsymbol{a}^\top \boldsymbol{e})$ represents the quantile of the random variable $\boldsymbol{a}^\top \boldsymbol{e}$ at the $1 - \alpha$ confidence level.

After considering output uncertainty, the original feasible domain model for the energy storage cluster is as follows:

$$\begin{cases} \boldsymbol{p} = \left\{ \boldsymbol{p} \in \mathbb{R}^N \middle| \boldsymbol{A}'\boldsymbol{p} \le \boldsymbol{b}' \right\} \\ \boldsymbol{A}' = \left[\boldsymbol{A}_1 \ \ -\boldsymbol{A}_1 \ \ \boldsymbol{A}_2{}^\top \ \ -\boldsymbol{A}_2{}^\top \ \ \boldsymbol{b}^\top \right]^\top \\ \boldsymbol{b}' = \left[\boldsymbol{p}_{\max} \ \ -\boldsymbol{p}_{\min} \ \ \boldsymbol{r}_{\max} \ \ \boldsymbol{r}_{\min} \ \ \boldsymbol{q} \right]^\top \\ \boldsymbol{q} = c - \mathrm{Quant}(1 - \alpha \mid \boldsymbol{a}^\top \tilde{\boldsymbol{e}}), \alpha = 0, 0.1, \cdots, 1.0. \end{cases} \tag{21}$$

After solving $d_s^{\mathcal{P}}$ for the flexible feasible solutions in S directions, the feasible domain of the Chino polytope can be determined through the following optimization problem.

TABLE 1 Calculation results of weighting for ESSs multilevel indicator.

Indicator	Sub-weight	Obj-weight	Com-weight
C1	0.114	0.147	0.132
C2	0.087	0.186	0.140
C3	0.132	0.267	0.204
C4	0.090	0.059	0.019
C5	0.084	0.083	0.023
C6	0.133	0.064	0.035
C7	0.073	0.055	0.010
C8	0.087	0.034	0.010
C9	0.105	0.042	0.017
C10	0.096	0.062	0.010

$$\begin{aligned} &\max_{\boldsymbol{c},\boldsymbol{\beta}_{\max}} \frac{1}{S}\sum_{s=1}^{S} \boldsymbol{\Lambda}_S{}' \\ &s.t. \boldsymbol{A}'\boldsymbol{c} + \left|\boldsymbol{A}'\boldsymbol{G}\right|\boldsymbol{\beta} \le \boldsymbol{b}' \\ &\boldsymbol{p} = \boldsymbol{c} + \boldsymbol{G}\boldsymbol{\beta} \end{aligned} \tag{22}$$

The expression for aggregating the construction matrix $\boldsymbol{G}$, polytope center $\boldsymbol{c}$, and construction scaling coefficient matrix $\boldsymbol{\beta}$ to obtain the aggregated grid-support capability of the energy storage cluster based on the revised Chino polytope is as follows:

$$\begin{cases} \boldsymbol{G}^{\mathcal{M}} = \mathrm{U}([\boldsymbol{G}^1, \cdots, \boldsymbol{G}^m]) \\ \boldsymbol{c}^{\mathcal{M}} = \sum_{j \in \mathcal{M}} \boldsymbol{c}^j \\ \boldsymbol{\beta}_{\mathcal{M}} = \sum_{j \in \mathcal{M}} \boldsymbol{\beta}^j \\ \boldsymbol{p}_{\mathcal{M}} = \boldsymbol{c}^{\mathcal{M}} + \boldsymbol{G}^{\mathcal{M}}\boldsymbol{\beta}^{\mathcal{M}} \end{cases} \tag{23}$$

where $\mathrm{U}(\,)$ is a unique operator that returns all the distinct columns in $[\boldsymbol{G}^1, \cdots, \boldsymbol{G}^m]$. $\boldsymbol{p}_{\mathcal{M}}$ is the grid-support capability of the energy storage clusters.

5 Case study

The case study is carried out on IEEE 39-bus system. The MATLAB R2021b software with the YALMIP toolbox and GUROBI solver is used to solve the optimization problems.

5.1 Grid-support capability evaluation and analysis

Initially, based on the multilevel technical indicator data of various ESSs in the three application scenarios of peak shaving, frequency regulation, and emergency power support, the secondary indicators are standardized and positively transformed. Subsequently, the combination weighting method is employed to determine the weights of each indicator. Based on the calculated results of subjective and objective weights, the allocation coefficients for subjective weight and objective weight can be obtained by solving

TABLE 2 The parameters and calculation results of ESSs.

ESS	1	2	3	4
Power/MW	17.2	50	14	37.4
Energy/(MW·h)	100	210	27	222
Ramp rate/MW·h $^{(-1)}$	8.6	25	7	18.7
Initial SoC	[0.2,0.8]	[0.2,0.8]	[0.2,0.8]	[0.2,0.8]
Similarity index	0.7529	0.7474	0.7751	0.7535

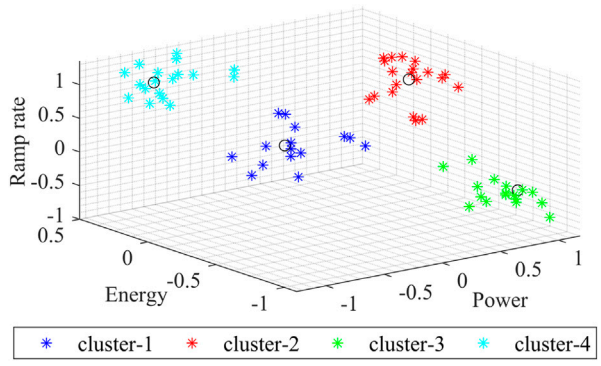

FIGURE 6
The clustering evaluation results.

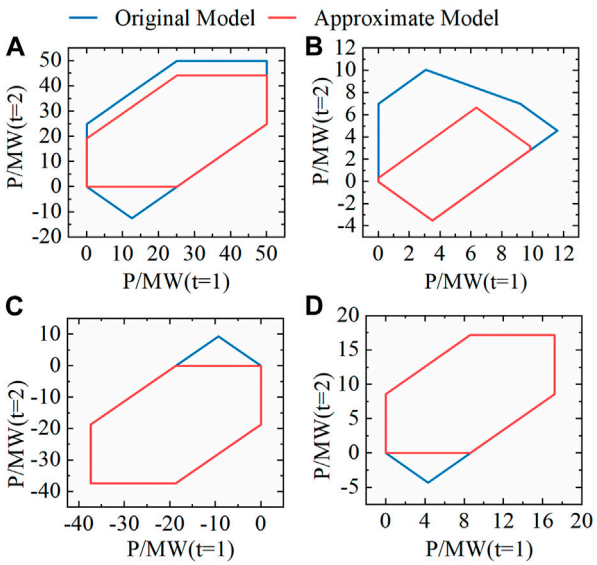

FIGURE 7
The comparison of original and approximate projected feasible region for different ESSs: **(A)** ESS-1; **(B)** ESS-2; **(C)** ESS-3; **(D)** ESS-4.

Eq. 1, and the results are $\alpha_1 = 0.5342$ and $\alpha_2 = 0.4658$ respectively. Ultimately, the combined weight can be calculated by appropriately weighting these coefficients. The results of the weight calculation based on peak shaving are shown in Table 1.

According to the calculation results in Table 2, it can be observed that among the various indicators of the ESSs applied for peak shaving scenarios, the weight of the non-planned outage coefficient indicator is 0.204, which has the highest proportion. The next significant indicators include dispatch success response rate and planned outage coefficient, which play a crucial role in the participation of ESSs in power grid peak shaving. Moreover, based on the weight calculation results, compared to the single weighting method, the combination weighting method combining subjective and objective weights weakens the influence of indicators with higher weights and strengthens the influence of indicators with smaller weights, which avoids potential issues of some indicators becoming ineffective due to large differences between them.

Randomly generated massive ESSs with indicators following a normal distribution, and calculate their support level in peak shaving scenarios. Proceeding with the supportiveness results, a value of 0.5 is chosen as the threshold to select ESSs demonstrating strong peak-shaving capabilities. As a result, a total of 70 ESSs that fulfill the requirements for peak shaving are selected.

To facilitate the subsequent grid-support capability aggregation of energy storage clusters, the maximum ramp rate, maximum charging and discharging power, and capacity are taken as characteristic states. After standardizing the indicators, the K-means clustering algorithm is adopted to conduct a second stage evaluation and analysis on the selected peak shaving energy storage clusters. The clustering evaluation results are shown in Figure 6.

5.2 Grid-support capability aggregation and analysis

The manuscript under consideration adopts a bottom-up approach to aggregate grid-support capabilities, whereby the feasibility domain pertaining to individual ESS is preliminarily delineated in accordance with a case study analysis. Considering a decision cycle T = 24 h and a time interval t = 1 h, with S = 100 normal vectors, the flexibility of 15 ESSs in cluster 1 is modeled using the approximate Chino polytope method. To demonstrate the derived outcomes in a succinct manner, four ESSs have been selectively extracted from this cluster and their results are tabulated in Table 2.

The incorporation of adjustable margins at any given time is paramount in ensuring the stability and efficiency of the ESS. As a result, in the study presented, the State of Charge (SoC) of the ESS is fixed between 0.2 and 0.8, providing a certain level of adjustability. It can be seen from the results that for the four different parameters of energy storage systems, the similarity index of the feasible region obtained by the Chino polytope and its original flexibility feasible region is more than 70%, indicating that the proposed method in this paper successfully reduces the conservatism typically inherent in feasible region, thus resulting in a larger scope for grid-support capability.

The existing evaluation methods generally involve the problem of not being able to directly draw high-dimensional spatial graphics. To visually compare the approximate effect of existing models on the original feasible domain, this paper projects the high-dimensional results onto a two-dimensional plane, which displays the feasible domains of two adjacent time points. Taking the power projection of t = 1 and t = 2 as an example, with θ varying from 0 to 2π, and by

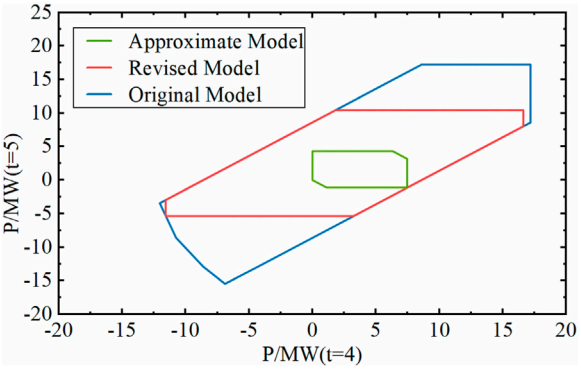

FIGURE 8
The comparison of projected feasible region for three types of models.

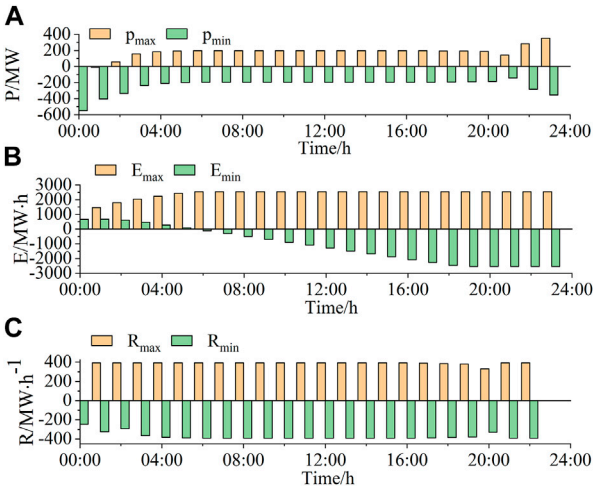

FIGURE 9
The upper and lower operation bounds of the aggregated ESSs: **(A)** power bounds, **(B)** energy bounds, **(C)** ramp bounds.

computing the following series of optimization problems, the projection contour can be obtained point by point.

$$\begin{aligned} &\max \quad p_1 \sin\theta + p_2 \cos\theta \\ &\quad \boldsymbol{p} = \boldsymbol{c} + \boldsymbol{G\beta} \\ &s.t. \quad \boldsymbol{Ap} \le \boldsymbol{b} \\ &\quad \theta \in (0, 2\pi) \end{aligned} \tag{24}$$

The projection of the original feasible domain of single energy storage and the feasible domain of the polytope Chino is shown in Figure 7.

Furthermore, considering the peak shaving demand of the power grid in different time periods, the similarity is further adjusted. According to the typical daily dual-peak load curve of the region, the absolute value of the difference between the peak cutting line and the valley filling line and the load curve is normalized. In addition, due regard is attributed to the probability distribution of energy storage output during peak load periods, facilitating the determination of each moment's peak load weight. The correction result for t = 4 and t = 5 is shown in Figure 8.

Based on the daily load curve, it is known that the peak shaving demand of the power grid is high during the t = 4 and t = 5 periods. Therefore, in the approximation model of a single energy storage polytope, the weight for this period is set to a higher value. The result shows that the revised polytope approximation accuracy for this period is much higher than the unmodified approximate polytope. This result demonstrates the feasibility of the revised model.

In this paper, the selected 15 ESSs are regarded as a peak shaving cluster. The time scale is T = 24 h, and the time interval is t = 1 h. Considering the constraints on ramp rate, power, and energy for ESSs, the grid-support capability aggregation of the energy storage cluster is performed using the Minkowski sum method. The power, energy, and ramping limits of the cluster are shown in Figure 9. It is verified in the case study that compared with the direct Minkowski sum of the original feasible region, the method based on the revised Chino polytope proposed in this paper has the potential to significantly conserve computational resources.

The power limits of the energy storage cluster indicate that this method can obtain the maximum output power range of the cluster. Under the constraints of these limits, the energy storage cluster forms a feasible domain. As a result, the operational range of the 15 energy storage clusters within one scheduling cycle is obtained, which facilitates their participation as a whole in peak shaving in the power system and reduces the computational burden on the dispatch center.

5.3 Analysis of energy storage clusters in peak regulation

To demonstrate that the proposed grid-support capability aggregation method based on the revised Chino polytope can improve the ability of energy storage clusters to participate in grid peak regulation, this paper takes the IEEE 39-bus system as an example.

The power grid consists of 39 busbars, including 10 generator busbars and 19 load busbars. In addition to these, one wind turbine and 15 ESSs are incorporated, with the collective ESSs treated as a singular unit for purposes of grid peak regulation. In the peak regulation model, we assume that the configured energy storage capacity is sufficient. In addition, since the load prediction is more accurate, it is assumed that the forecast value of day and day load is the same curve. The peak regulation model posits the minimum peaking cost of each unit as the objective function. It employs the power upper and lower limits, together with the power balance of each unit, as the constraint conditions. Consequently, a peak regulation strategy for the energy storage cluster is devised on a time scale of 1 hour. The comparison graph of the peak shaving correction amount between the revised and original model at different time intervals is shown in Figure 10.

Among them, T = 22 represents the energy storage cluster participating in the peak regulation strategy at time t = 2, and T = 21 represents the energy storage cluster participating in peak regulation at time t = 3. It can be seen from the results that, compared with the original model, the revised model based on the Chino polytope proposed in this paper makes the adjustment amount of the energy storage cluster at the later moment smaller in the process of participating in the peak regulation of the power grid, that is, the ability of the energy storage cluster to participate in the peak regulation of the power grid is improved.

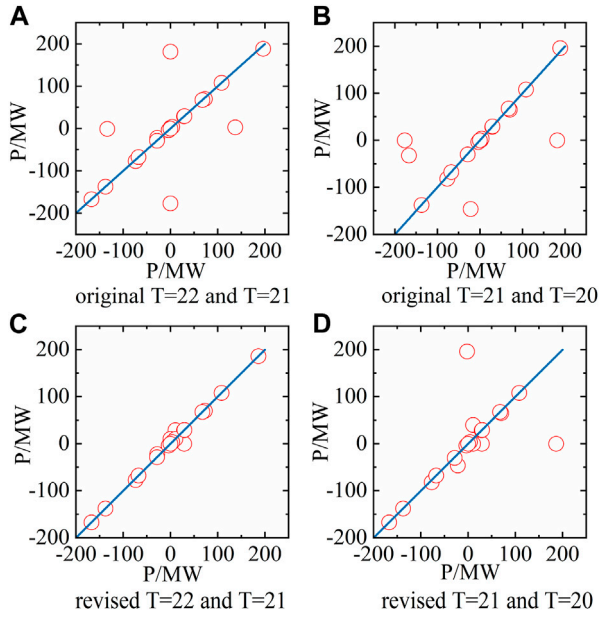

FIGURE 10
The comparison graph of peak shaving correction amount between the revised and original model at different time intervals. **(A)** original at T = 22 and T = 21, **(B)** original at T = 22 and T = 21, **(C)** revised at T = 22 and T = 21, **(D)** revised at T = 21 and T = 20.

6 Conclusion

This paper presents a model for evaluating and aggregating the grid support capability of energy storage clusters by considering the peak regulation requirements. The model's effectiveness is demonstrated based on the IEEE 39-bus system, and several conclusions have been drawn. Primarily, the combined subjective and objective weighting method proposed in this paper circumvents issues arising from significant weight discrepancies across different indices, a problem often encountered with traditional single-weighting methods. Furthermore, grid-support capability aggregation based on evaluation increases the efficiency and rationality of massive ESSs aggregation analysis. Notably, the aggregation model based on the revised Chino polytope not only saves computing resources but also improves the ability of energy storage clusters to participate in power grid peak regulation. The method considers both aggregation precision and computing efficiency to some extent. Future work will look into constraints such as power flow within the power grid for the energy storage clusters to depict the grid-support capability of energy storage clusters more accurately.

Data availability statement

The original contributions presented in the study are included in the article/Supplementary Material, further inquiries can be directed to the corresponding author.

Author contributions

LL: Conceptualization, Data curation, Investigation, Project administration, Writing–original draft. YL: Writing–original draft, Formal Analysis, Funding acquisition, Resources, Validation. MW: Writing–original draft, Investigation, Project administration, Supervision. QT: Formal Analysis, Methodology, Resources, Writing–review and editing.

Funding

The author(s) declare financial support was received for the research, authorship, and/or publication of this article. This work is supported by the China Southern Power Grid Power Generation Co., Ltd., Energy Storage Research Institute (020000KK52220002). The funder was not involved in the study design, collection, analysis, interpretation of data, the writing of this article, or the decision to submit it for publication.

Conflict of interest

Authors LL, YL, MW, and QT were employed by China Southern Power Grid Power Generation Co., Ltd., Energy Storage Research Institute.

Publisher's note

References

Ayesha, Numan, M., Baig, M. F., and Yousif, M. (2023). Reliability evaluation of energy storage systems combined with other grid flexibility options: a review. *J. Energy Storage* 63, 107022. doi:10.1016/j.est.2023.107022

Bhatti, B. A., Hanif, S., Alam, J., Mitra, B., Kini, R., and Wu, D. (2023). Using energy storage systems to extend the life of hydropower plants. *Appl. Energy* 337, 120894. doi:10.1016/j.apenergy.2023.120894

Calero, F., Canizares, C. A., and Bhattacharya, K. (2021). Aggregated BESS dynamic models for active distribution network studies. *IEEE Trans. Smart Grid* 12, 2077–2088. doi:10.1109/tsg.2020.3048648

Chen, X., Dall'Anese, E., Zhao, C., and Li, N. (2020). Aggregate power flexibility in unbalanced distribution systems. *IEEE Trans. Smart Grid* 11, 258–269. doi:10.1109/tsg.2019.2920991

Chen, X., and Li, N. (2021). Leveraging two-stage adaptive robust optimization for power flexibility aggregation. *IEEE Trans. Smart Grid* 12, 3954–3965. doi:10.1109/tsg.2021.3068341

Cui, B., Zamzam, A., and Bernstein, A. (2021a). Network-cognizant time-coupled aggregate flexibility of distribution systems under uncertainties. *IEEE Control Syst. Lett.* 5, 1723–1728. doi:10.1109/lcsys.2020.3045080

Cui, Y., Zhou, H., Zhong, W., Hui, X., and Zhao, Y. (2021b). Two-stage day-ahead and intra-day rolling optimization scheduling considering joint peak regulation of generalized energy storage and thermal power. *Power Syst. Technol.* 45, 10–20. doi:10.13335/j.1000-3673.pst.2020.0206

Ding, M., Gao, P., Bi, R., Hu, D., Yu, H., and Zhang, Y. (2021). Cluster partition method for high-permeability renewable energy considering flexibility. *Proc. CSU-EPSA* 33, 115–122+150.

Ding, M., Liu, X., Bi, R., Hu, D., Ye, B., Zhang, J., et al. (2018). Pyrazolo[1,5-a] pyrimidine TRPC6 antagonists for the treatment of gastric cancer. *Automation Electr. Power Syst.* 42, 47–55. doi:10.1016/j.canlet.2018.05.041

Goel, K., Michael, N., and Tabib, W. (2023). Probabilistic point cloud modeling via self-organizing Gaussian mixture models. *Ieee Robotics Automation Lett.* 8, 2526–2533. doi:10.1109/lra.2023.3256923

Han, X. T., and Zhang, Y. J. (2022). Decomposition-coordination-based voltage control for high photovoltaic-penetrated distribution networks under cloud-edge collaborative architecture. *Int. Trans. Electr. Energy Syst.* 2022, 1–20. doi:10.1155/2022/7280220

Hua, H., Qin, Y., Hao, C., and Cao, J. (2019). Optimal energy management strategies for energy Internet via deep reinforcement learning approach. *Appl. Energy* 239, 598–609. doi:10.1016/j.apenergy.2019.01.145

Leng, Y. J., and Zhang, H. (2023). Comprehensive evaluation of renewable energy development level based on game theory and TOPSIS. *Comput. Industrial Eng.* 175, 108873. doi:10.1016/j.cie.2022.108873

Li, H., Zhang, N., Kang, C., Xie, G., Li, Q., Yang, X. Q., et al. (2019). Inducing secondary metabolite production by Co-culture of the endophytic fungus phoma sp. and the symbiotic fungus armillaria sp. *Proc. Chin. Soc. Electr. Eng.* 39, 1009–1013. doi:10.1021/acs.jnatprod.8b00685

Li, Y., Han, M., Shahidehpour, M., Li, J. Z., and Long, C. (2023). Data-driven distributionally robust scheduling of community integrated energy systems with uncertain renewable generations considering integrated demand response. *Appl. Energy* 335, 120749. doi:10.1016/j.apenergy.2023.120749

Ma, G. L., Li, J. N., and Zhang, X. P. (2023). Energy storage capacity optimization for improving the autonomy of grid-connected microgrid. *Ieee Trans. Smart Grid* 14, 2921–2933. doi:10.1109/tsg.2022.3233910

Muller, F. L., Szabo, J., Sundstrom, O., and Lygeros, J. (2019). Aggregation and disaggregation of energetic flexibility from distributed energy resources. *IEEE Trans. Smart Grid* 10, 1205–1214. doi:10.1109/tsg.2017.2761439

Nan, B., Jiang, C., Dong, S., and Xu, C. (2022). Day-ahead and intra-day coordinated optimal scheduling of integrated energy system considering uncertainties in source and load. *Power Syst. Technol.*, 1–15.

Sajjad, I. A., Chicco, G., and Napoli, R. (2016). Definitions of demand flexibility for aggregate residential loads. *IEEE Trans. Smart Grid* 7, 2633–2643. doi:10.1109/tsg.2016.2522961

Wang, S., and Wu, W. (2021). Aggregate flexibility of virtual power plants with temporal coupling constraints. *IEEE Trans. Smart Grid* 12, 5043–5051. doi:10.1109/tsg.2021.3106646

Wen, Y., Hu, Z., and Liu, L. (2022a). Aggregate temporally coupled power flexibility of DERs considering distribution system security constraints. *IEEE Trans. Power Syst.*, 1–13. doi:10.1109/tpwrs.2022.3196708

Wen, Y., Hu, Z., You, S., and Duan, X. (2022b). Aggregate feasible region of DERs: exact formulation and approximate models. *IEEE Trans. Smart Grid* 13, 4405–4423. doi:10.1109/tsg.2022.3179998

Yang, Z., Yibo, W., Chuang, L., Guowei, C., Weichun, G., Yueyang, X., et al. (2023). Research on the deep peak-shaving cost allocation mechanism considering the responsibility of the load side. *Front. Energy Res.* 11. doi:10.3389/fenrg.2023.1182620

Yi, W., Liangzhong, Y., Siyang, L., Yunxin, L., Jian, L., and Xinying, W. (2022). A peak shaving method of aggregating the distributed photovoltaics and energy storages based on the improved K-means++ algorithm. *Power Syst. Technol.* 46, 3923–3931.

Yi, Z., Xu, Y., Gu, W., and Wu, W. (2020). A multi-time-scale economic scheduling strategy for virtual power plant based on deferrable loads aggregation and disaggregation. *IEEE Trans. Sustain. Energy* 11, 1332–1346. doi:10.1109/tste.2019.2924936

Zhang, R., and Hredzak, B. (2021). Distributed dynamic clustering algorithm for formation of heterogeneous virtual power plants based on power requirements. *IEEE Trans. Smart Grid* 12, 192–204. doi:10.1109/tsg.2020.3020163

Zhang, R., Hredzak, B., and Fletcher, J. (2021). Dynamic aggregation of energy storage systems into virtual power plants using distributed real-time clustering algorithm. *IEEE Trans. Industrial Electron.* 68, 11002–11013. doi:10.1109/tie.2020.3038074

Zhao, X., Li, L., Tao, Y., Lai, S., Zhou, X., and Qiu, J. (2022). Aggregated operation of heterogeneous small-capacity distributed energy resources in peer-to-peer energy trading. *Int. J. Electr. Power & Energy Syst.* 141, 108162. doi:10.1016/j.ijepes.2022.108162

frontiers | Frontiers in Energy Research

TYPE Original Research
PUBLISHED 05 December 2023
DOI 10.3389/fenrg.2023.1290805

OPEN ACCESS

EDITED BY
Mingfei Ban,
Northeast Forestry University, China

REVIEWED BY
Xiaofei Wang,
National Renewable Energy Laboratory (DOE), United States
Jiyu Wang,
National Renewable Energy Laboratory (DOE), United States

*CORRESPONDENCE
Aihong Tang,
tah@whut.edu.cn

RECEIVED 08 September 2023
ACCEPTED 14 November 2023
PUBLISHED 05 December 2023

CITATION
Zhang K, Wang T, Zhou H, Li H, Tang A, Yang H and Peng J (2023), Research on load transfer planning model for equipment maintenance in the substation.
Front. Energy Res. 11:1290805.
doi: 10.3389/fenrg.2023.1290805

Research on load transfer planning model for equipment maintenance in the substation

Kanjun Zhang[1], Ting Wang[1], Hubing Zhou[1], Hengxuan Li[1], Aihong Tang[2]*, Huiyuan Yang[2] and Jiao Peng[2]

[1]State Grid Hubei Electric Power Research Institute, Wuhan, China, [2]School of Automation, Wuhan University of Technology, Wuhan, China

The maintenance, inspection, and refurbishment of substation equipment are crucial for ensuring the stability of the power grid's operation and the reliability of power supply to users. However, currently, there is a lack of methods for rapidly and effectively planning load transfer solutions during substation equipment maintenance periods. To address this, this study is founded on the principles of transmission network planning theory, and an analysis of the similarities and disparities between the planning methods for load transfer solutions during substation equipment maintenance and traditional approaches to transmission network planning is conducted. Furthermore, this paper integrates practical constraints related to maintenance engineering and power grid load flow balance constraints. With the primary optimization objectives of minimizing investment and operational costs during system maintenance while maximizing power grid reliability, a load transfer planning model for equipment maintenance in the substation has been developed. Simultaneously, in conjunction with linear programming theory, the nonlinear constraint terms of the model have been equivalently simplified to enhance the computational performance of the model. Simulation analysis is conducted on case studies constructed based on the IEE-RBTS6 and IEEE-RTS79 systems to validate the effectiveness of the proposed model in solving the optimal maintenance planning problem.

KEYWORDS

maintenance of substation, 220 kV, transmission planning, reliability, linear

1 Introduction

The substation plays a crucial role in the power system of China. Serving as the hub of the transmission and distribution network, its reliability is essential. It not only affects the supply of electrical power to the lower-level distribution loads but also has a significant impact on the stability of the transmission system grid (Bagen et al., 2019; Sarantakos et al., 2019). Hence, it is crucial to perform necessary operational maintenance, inspections, and improvements on the substation structure. This is essential for maintaining the stability of the power grid and ensuring reliable electricity supply to customers. The maintenance of the substations is divided into two types: one is multi-bay maintenance, and the other is complete shutdown maintenance. The former refers to the maintenance where specific equipment within the substation is powered down. For instance, during the maintenance of a single busbar, the isolating switches and circuit breakers on both sides of that busbar will be taken out of operation, resulting in a partial shutdown of the power supply to certain sections. The latter refers to a complete shutdown of all equipment in the substation for a

comprehensive equipment fault investigation. For example, during a complete shutdown maintenance of the dual busbars within the station, all the isolating switches on both sides of the two busbars are disconnected, leading to a complete interruption of power supply to all sections of the substation.

Regardless of the maintenance mode, the power system primarily faces two operational challenges: (1) During the period of equipment maintenance at the substation, the external transmission lines will be affected and shut down. As a result, the existing structural stability of the electrical network in the vicinity of the substation will be weakened, leading to a reduction in the reliability of power supply within the regional electrical network. (2) During the period of substation maintenance, there is a possibility that the transformers may be affected and require shutdown, potentially resulting in partial or complete loss of the electrical load they carry. This can have an impact on the normal power supply to the users.

Currently, to address the maintenance issue mentioned above, power companies typically employ a method of connecting the outgoing lines with on-site transformers while simultaneously connecting the remaining outgoing lines outside the substation. This approach ensures uninterrupted power supply to the loads during the substation maintenance period and enhances the overall reliability of the power grid operation. However, there is still a lack of effective evaluation measures for selecting the optimal maintenance plan.

During the design of maintenance plans, the staff first needs to develop various alternative maintenance plans. Subsequently, they evaluate and select the most reliable plan based on the reliability levels of each option. Reference (DING and FENG, 2004) employs the Monte Carlo risk assessment method to evaluate various maintenance plans for different 220 kV power grids. Based on the assessment results, it determines the risk levels of different plans, thus identifying the optimal maintenance measures. Reference (WANG et al., 2015), based on power grid operational risk and its management theory, establishes a risk framework. It comprehensively employs various system analysis methods to analyze different schemes and select the optimal planning and control measures to reduce system risk. In reference (Qi et al., 2018), the risk assessment process takes into account conditional risk value factors. It quantitatively compares different power grid planning schemes and selects the optimal one among them. However, when the substation structure is complex, and there are numerous alternative plans, using risk assessment methods can incur significant computational time costs.

Therefore, in response to the aforementioned issues, this paper draws upon the theoretical foundations of power grid planning (Majidi-Qadikolai and Baldick, 2016; Garcí a-Bertrand and Mí nguez, 2017; ZHANG et al., 2017; LIU et al., 2019) and incorporates engineering practicalities. Considering the cost-effectiveness and safety implications, we propose the development of a comprehensive planning model for the maintenance of 220 kV substations on the basis of economic and reliability considerations. This model aims to assist personnel in efficiently formulating appropriate maintenance strategies for the 220 kV substation. This paper firstly elaborates on the definition of substation maintenance planning and highlighting the similarities and differences between substation maintenance planning and general power transmission network planning, which providing the theoretical foundation for the development of the maintenance planning model; Subsequently, this paper integrates practical constraints from maintenance engineering and power grid load flow balance constraints. It formulates a maintenance planning model with the objective of optimizing the combined investment and operational costs as well as reliability costs during the maintenance period; Finally, this paper designs case studies based on the IEEE-RBTS6 and the IEEE-RTS79 system to validate the effectiveness of the model.

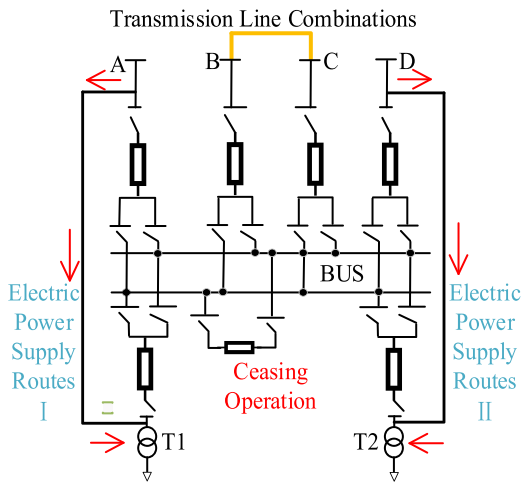

FIGURE 1
Topology of 220 kV side in a substation.

2 The maintenance planning theory for the substation

2.1 The definition of maintenance planning

The substation maintenance planning model is primarily utilized for making decisions on how to carry out temporary structural modifications of the power grid during substation maintenance to minimize system operational risks and economic costs to the greatest extent possible. Specifically, it involves two aspects of decision-making: How to establish internal power supply transfer paths within the substation to ensure continuous operation of the main transformers that are forced to be shut down during maintenance; How to combine the transmission lines that are forced to shut down due to maintenance in order to enhance the stability of the power grid, which are referred as external line combination.

For instance, as illustrated in Figure 1, the topology of 220 kV side in a substation. Using the typical 220 kV substation's 220 kV side structure as an example to illustrate the specific form of maintenance planning.

The substation's 220 kV side structure, as illustrated in the figure, is a typical double-bus configuration. It is interconnected with the 220 kV transmission system through four incoming lines labeled A, B, C, and D. Additionally, it is linked to the low-voltage

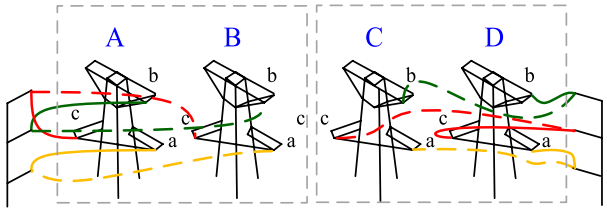

FIGURE 2
Diagram for line connection outside of the substation.

system via two main transformers, denoted as T1 and T2. When the 220 kV side of the substation undergoes a complete shutdown maintenance, the main busbar equipment within the grey area in the diagram goes out of operation. This indirectly leads to the disconnection of the main transformers T1 and T2 from the 220 kV system. During this period, it is possible to establish an internal power supply transfer path to enable the internal load of the substation to be supplied. By establishing power pathways on both sides of A and T1, as well as on both sides of D and T2, as shown in the diagram, it ensures the continuous supply of partial loads. The amount of power that the supply pathways can transmit is determined by the rated capacity of the lines and the distribution of the system's power flows.

Besides, during the maintenance of the 220 kV side of the substation, the lines A, B, C, and D shown in Figure 1 are out of service. And various methods of interconnection can be employed to combine the transmission lines to stabilize the system network configuration. For instance, as illustrated in Figure 2, the diagram for line connection outside of the substation.

2.2 Comparison of maintenance planning and power transmission network planning

The common aspects between substation maintenance planning and transmission network planning include:

(1) In the investment planning phase, both require assessing the optimal connectivity and disconnection status of lines under constraint conditions. In the investment phase of transmission network planning, decision-makers often need to decide on the construction feasibility of existing transmission corridor lines (MA et al., 2015; LIU et al., 2018; Qian et al., 2018).However, in the investment phase of maintenance planning, decision-makers need to determine, based on the system's topology after the substation's components are out of operation, how to establish internal power pathways within the substation, as well as how to combine the remaining lines that are forced to shut down outside the substation. Since all feasible combinations of pre-established alternative power pathway options and the interconnection of external lines are known, the maintenance planning involves deciding the construction of different power pathways and whether to build specific line combinations, making it quite similar in form to transmission network planning.
(2) In the operational phase, both require calculating the system operating costs under constraint conditions. Whether it is transmission network planning or maintenance planning, both need to determine the optimal combination of unit operation and load shedding strategy to minimize the sum of unit operating costs and load shedding penalty loss costs.
(3) Both share similar network constraint conditions. Whether it is optimizing substation maintenance plans or transmission network planning, both need to satisfy comparable constraints related to power balance and variable boundary conditions (Mavalizadeh et al., 2014; Chen and Wang, 2016; Zhang and Conejo, 2018).

However, there are still certain differences between maintenance planning and transmission network planning, specifically including:

(1) In substation maintenance planning, decision-makers are more concerned with the safe and stable operation of the system during the maintenance period. At the same time, due to the significant power transmission tasks often borne by the 220 kV side of the substation, even with the establishment of internal power supply transfer paths, it can be challenging to ensure the transfer of the entire load.
(2) In addition to determining the external line connection form, substation maintenance planning also involves deciding on the optimal method for constructing internal power supply routes within the substation. Furthermore, substation maintenance plans have maintenance constraints (MC) that differ from those in transmission planning.
(3) In transmission network planning, investment cost primarily refers to the cost of line construction, and the planning typically considers longer timeframes, usually in terms of years. In maintenance planning, investment cost primarily refers to the operation and maintenance of transfer equipment and the temporary combination of lines. The maintenanceperiod is not excessively long, typically measured in weeks or months.

In summary, both maintenance planning and transmission network planning share many similarities in terms of optimization objectives and constraint conditions, yet they also exhibit distinct differences. Therefore, this paper is based on transmission network planning theory and takes into account the characteristics of maintenance planning to construct an optimization model for substation maintenance planning.

3 Load transfer planning model for equipment maintenance in the substation

3.1 Optimization objective

Assuming that the maintenance is carried out at substation located at node i, The power value carried by the transformer t before maintenance is denoted as p_t. After establishing internal power supply transfer paths, the equivalent power capacity p_{di} connected to node i can be represented as shown in Eq. 1:

$$p_{di} = \sum_{t\in T} m_t p_t + \sum_{t\in T} n_t p_t \tag{1}$$

Where m_t indicates whether the t main transformer is restored with power through the internal power supply transfer path, T represents the set of main transformers. n_t represents whether the specific main transformer is disconnected under the current maintenance mode. In the complete shutdown maintenance mode, this value is always 0. m_t and n_t are both Boolean variables, for a specific transformer t, they satisfy the following relationship:

$$\begin{cases} m_t + n_t = 1 \\ m_t \star\ n_t = 0 \end{cases} \tag{2}$$

As mentioned above, the optimization objectives of the substation maintenance planning model can be divided into three categories. The first is unit operating costs, the second is investment costs, and the third is load shedding penalty costs that reflect the system's reliability.

Since load shedding occurs during the operational phase and is determined in real-time, it is possible to combine the unit combination operating costs with the necessary load shedding penalty costs into a comprehensive operational cost. The investment cost of substation maintenance planning can be categorized into two types: one is the cost of reconstructing the transmission network and constructing in the substation, and the other is the cost associated with load shedding penalties imposed due to the necessary forced outages. The former includes the cost of shutting down external lines and the cost of constructing internal power supply transfer paths within the substation; The latter includes additional penalty costs due to load shedding caused by insufficient capacity and quantity of load transfer lines.

We define an integrated cost "C", encompassing investment-related load shedding penalties and margin-based rewards, to evaluate the transfer capability of different plans for the load carried by the substation during the investment phase. Its expression is presented in Eq. 3.

$$C = \begin{cases} c_i \mathrm{T_M}\left(n_T - \sum_{i\in \mathrm{L^-}} x_i\right)\mathrm{p}_t + \sum_{i\in \mathrm{L^-}} c_{li} x_i \left(\mathrm{p_t} - \overline{p_{li}}\right), V = 220 \\ c_i \mathrm{T_M} \min\left\{\left[\sum_{i\in \mathrm{N_G}} p_{gi} + \left(\mathrm{n_T} - \sum_{i\in \mathrm{L^-}} x_i\right)\mathrm{p_t} - \sum_{\substack{j\in \mathrm{N} \\ j\neq i}} p_{di}\right], 0\right\} \\ + \sum_{i\in \mathrm{L^-}} c_{li} x_i \left(\mathrm{p_t} - \overline{p_{li}}\right), V = 500 \end{cases} \tag{3}$$

Where represents the rated capacity value of the line (MW),N represents the set of system nodes, represents the set of system generator nodes, represents the maintenance time (h),V represents the voltage level of the substation(kV).

The above equation consists of two cost components. The first component is the cost incurred due to load shedding during maintenance when the temporary transfer transformer capacity is insufficient. The reduced load is equal to the maximum capacity of the temporary transfer line minus the user load demand. The second component is the cost used to measure the capacity margin cost for different lines acting as transfer lines. This is defined as an incentive cost added to the investment cost in this paper.

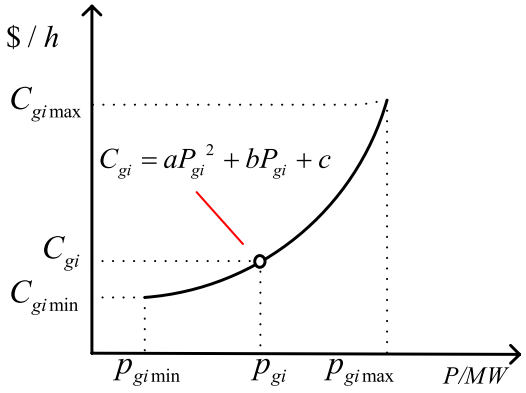

FIGURE 3
The cost function for operating a generator unit.

Therefore, the objective function of load transfer planning model for equipment maintenance in the substation can be expressed as:

$$\begin{aligned} \min_{\substack{p_{gi}, p_{li}, \theta_i, \\ x_i, r_i, p_{ci}}} & \sum_{\mathrm{i}\in \mathrm{N_x}} c_{xi} x_i + \sum_{\mathrm{i}\in \mathrm{N_r}} c_{ri} y_{li} + C \\ & + \sum_{\mathrm{i}\in \mathrm{N_G}} f_p\left(p_{gi}\right)\mathrm{T_M} + \sum_{\mathrm{i}\in \mathrm{N}} c_i p_{ci} \mathrm{T_c} \end{aligned} \tag{4}$$

Where represents the active power output of the generator (MW), represents the load shedding at node due to substation maintenance (MW), represents whether the i-th power supply transfer path is constructed or not, represents whether the i-th incoming line combination is constructed or not, represents the load shedding penalty cost coefficient ($/MWh), represents the comprehensive cost of constructing and maintaining power supply transfer paths($), represents the comprehensive cost of investment and construction of the temporary line combination ($), represents the investment load shedding penalty cost coefficient ($), represents the load shedding time (h), represents the active power flow passing through the branch (MW), represents the phase angle at node(rad), represents the cost function of the generator, represents the set offeasible power supply transfer paths, N_r represents the set of temporary line combinations, N_G represents the set of generators, N represents the set of nodes.

The above optimization objective is divided into three parts. The first three terms represent the investment costs of maintenance planning, including the construction cost of power transfer routes, the cost of line connections, and the investment-related system load shedding penalty and capacity reward costs; The fourth term represents the operating cost of the system's generator unit; The fifth term represents the cost of load shedding during maintenance, reflecting the system's reliability.

The operating cost of the generator units follows a quadratic function relationship with the generator output, as illustrated in Figure 3, the cost function for operating a generator unit.

3.2 Maintenance constraints

During the maintenance period, a total of n_t transformers in the substation are disconnected from the 220 kV transmission system, and there are a total of a incoming lines that are out of service. Starting from 1, each line will be denoted as $L_i\,(i \in [1, a])$.

Let $X = [x_1, \cdots, x_a]^T$ represent the connectivity status of L_i to the transformers during the maintenance. $x_i\,(i \in [1, a])$ is a 0–1 integer variable,0 indicates that line L_i is not connected to the main transformer through the power supply pathway, while 1 indicates that line L_i is connected to the main transformer. And the following constraint need to be satisfied:

$$\sum_{i=1}^{a} x_i \le n_t \tag{5}$$

The above equation indicates that the total number of constructed load transfer paths should be less than or equal to the total number of transformers.

Besides, the incoming lines of the substations can be stabilized through temporary combinations, resulting in a total of $a\,(a-1)/2$ possible combinations. However, the above-mentioned incoming lines cannot be combined arbitrarily and must satisfy the following constraint conditions. We define a matrix of dimensions $a \times a$ called the line connectivity matrix R. Each element r_{ij} within the matrix is a binary integer variable 0–1, used to indicate whether the line L_i and L_j should be connected during the maintenance. The connectivity matrix needs to satisfy the following constraints:

$$r_{ij} = r_{ji}, \forall i、\ j \in [1, a] \tag{6}$$

$$0 \le \sum_{i=1}^{a} r_{ij} \le 1, \forall j \in [1, a] \tag{7}$$

$$0 \le \sum_{j=1}^{a} r_{ij} \le 1, \forall i \in [1, a] \tag{8}$$

$$0 \le \sum_{i=1}^{a} \sum_{j=1}^{a} r_{ij} \le (a - n_t)/2 \tag{9}$$

$$r_{ij} = 0, i、\ j \in N_{\mathrm{dl}} \tag{10}$$

Eq. 6 implies that the matrix is symmetric; Equations (7) and (8) implies that the sum of each row or each column in the connectivity matrix is not greater than 1, indicating that each line can be connected to at most one other line at the same time; Eq. 9 represents the constraint on the number of line connection combinations; In Equation 10, N_{dl} represents the set of double-circuit lines with the same starting and ending buses. This constraint implies that double-circuit lines with the same starting and ending nodes cannot be connected.

In addition, the lines serving as load transfer paths during maintenance cannot be connected to other incoming lines, which following constraint:

$$\sum_{i=1}^{a} \left(x_i \sum_{j=1}^{a} r_{ij} \right) = 0, i、\ j \in [1, a] \tag{11}$$

3.3 Network constraints

The substations are directly connected to the transmission system, thus the maintenance planning model proposed in this paper also needs to comply with the operating constraints of the transmission system. Based on references (Samarakoon et al., 2001; LIU et al., 2021), the Network Constraints (NC) constraints for load transfer planning model are as follows.

3.3.1 Branch power flow constraints

$$p_{li} - b_i\left(\theta_{fi} - \theta_{ti}\right) = 0, \forall i \in L_0 \tag{12}$$

$$p_{li} - x_i b_i\left(\theta_{fi} - \theta_{ti}\right) = 0, \forall i \in L^- \tag{13}$$

$$p_{li} - y_{li} b_i\left(\theta_{fi} - \theta_{ti}\right) = 0, \forall i \in L^+ \tag{14}$$

The three equations represent the branch power flow balance equations for the transmission lines not directly connected to the substation, the incoming lines to the substation, and the new lines created through temporary combination respectively. Where b_i represents the admittance of branch i, θ_{fi} represents the phase angle at the starting node of branch i, θ_{ti} represents the phase angle at the ending node of branch i, L_0 represents transmission lines in the power grid that are not directly connected to the substation, L^- represents incoming lines that are planned to be shut down due to maintenance, L^+ represents the set of lines that can betemporary combined, y_{li} represents the state of each line in set L^+, and it is a binary integer variable, and value 0 indicates that the line will not be constructed, while value 1 indicates that the line will be constructed.

The relationship between y_{li} and the connectivity matrix R is as follows:

$$y_{lj} = \begin{cases} r_{1,i+1}, \forall i \in [1, a-1] \\ r_{row,row+i-[(a-1)a-(a-row+1)(a-row)]/2} \\ r_{a-1,a}, i = (a-1)a/2\,(\forall i \in [1,\ (a-1)a/2]) \end{cases} \tag{15}$$

The row is as follows:

$$row = min\{a - t - 1 \mid (t+1)t/2 \le (a-1)a/2 - i\} \tag{16}$$

3.3.2 Node power balance constraints

$$\sum_{m \in Nig} p_{gim} - p_{di} + \sum_{j} p_{lj} - \sum_{t} p_{lt} + p_{ci} = 0, \forall i \in N_G, \forall j \in N_{fi}, \forall t \in N_{ti} \tag{17}$$

$$-p_{di} + \sum\nolimits_{j} p_{lj} - \sum\nolimits_{t} p_{lt} + p_{ci} = 0, \forall i \in N_{nonG}, \forall j \in N_{fi}, \forall t \in N_{ti} \tag{18}$$

N_{ig} represents the set of generators connected to node i, p_{di} represents the load demand at node i, p_{lj} and p_{lt} represent the incoming and outgoing power at a node i respectively, N_G represents the set of generator nodes, N_{nonG} represents the set of non-generator nodes, Due to some generator nodes being composed of multiple units, we use p_{gim} to represent the output of the m-th generator connected to node i, and we use p_{gi} to uniformly describe the total output of generator at node i.

3.3.3 Boundary constraint

$$\underline{p_{li}} \le p_{li} \le \overline{p_{li}}, \forall i \in L_0 \cup L^+ \cup L^- \tag{19}$$

$$\theta_i \in [-2\pi, 2\pi], i \in N \tag{20}$$

$$\underline{p_{gi}} \le p_{gi} \le \overline{p_{gi}}, i \in N_G \tag{21}$$

$$0 \le p_{ci} \le p_{di}, i \in N \tag{22}$$

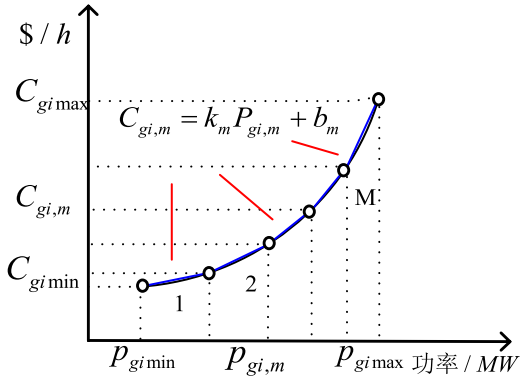

FIGURE 4
Linearized function for generator unit operating cost.

Eq. 19 represents the boundary constraint for branch power flows, Eq. 20 represents the boundary constraint for node phase angles, Eq. 21 represents the boundary constraint for generator outputs, and Eq. 22 represents the boundary constraint for node load shedding. Where $\overline{p_{li}}$ represents the rated capacity of the branch, $\overline{p_{gi}}$ and $\underline{p_{gi}}$ represent the upper and lower limits of generator outputs respectively.

3.4 Model linearization

The equations (4)–(22) collectively constitute the optimization model for the load transfer planning model for equipment maintenance in the substation. To improve the efficiency of solving the model, the nonlinear objective and constraints in the above model need to be linearized.

3.4.1 Generator unit operating cost function linearization

The cost function of the generator is quadratic, we linearize this quadratic function using piecewise linearization methods. The generator output range is divided into multiple intervals, within each interval it is approximated that the generator unit operating cost is linearly related to the generator output, as shown in Figure 4, the linearized function for generator unit operating cost.

Using multiple sets of piecewise linear function $k_p(\cdot)$ to substitute the generator output cost in Eq. 4, the linearized form of the objective function is obtained as follows:

$$\min_{\substack{p_{gi},p_{li},\theta_i,\\ x_i,r_i,p_{ci}}} \sum_{i\in N_x} c_{xi}x_i + \sum_{i\in N_r} c_{ri}y_{li} + C + \sum_{i\in N_G} k_p\left(p_{gi}\right)T_M + \sum_{i\in N} c_i p_{ci} T_c \tag{23}$$

Where $k_p(\cdot)$ is:

$$k\left(p_{gi}\right) = \sum_{m=1}^{M} x_{gm}\left(k_m p_{gi} + b_m\right) \tag{24}$$

Where x_{gm} is the generator output in m – th segment of the cost linearization function, M represents the total number of linearized segments of the generator cost function.

3.4.2 Load transfer constraints linearization

Eq. 11 is a nonlinear constraint. For the product xy of the 0–1 variables x and y, it can be converted to the following linearized form:

$$\begin{cases} z = xy \\ z \le x \\ z \le y \\ z \ge x + y - 1 \end{cases} \tag{25}$$

Based on the above formula, the linearized form of (11) can be obtained as follows:

$$r_{ij} \le 1 - x_i, \forall i、\ j \in [1, a] \tag{26}$$

3.4.3 The branch power flow equation is linearized

Equations (13) and (14) contain the product of 0–1 integer variable and continuous variable, which belongs to nonlinear term. According to (Zhuo et al., 2020; Han et al., 2019), using the large M method, it can be transformed into the following linearized form:

$$-M_{\text{xi}}(1 - x_i) \le p_{li} - b_i\left(\theta_{fi} - \theta_{ti}\right) \le M_{\text{xi}}(1 - x_i), \forall i \in L^- \tag{27}$$

$$-M_{\text{li}}(1 - y_{li}) \le p_{li} - b_i\left(\theta_{fi} - \theta_{ti}\right) \le M_{\text{li}}(1 - y_{li}), \forall i \in L^+ \tag{28}$$

Where, M_{xi} and M_{li} are M values of the large M method.

The original nonlinear model is transformed into a mixed-integer linear programming (MILP) model. For this MILP model, the branch-and-bound algorithm can be employed to solve the problem. The detailed process of the branch-and-bound algorithm can be found in the literature (Gao et al., 2021).

4 Case study

To validate the proposed load transfer planning model, this study employs two cases based on the IEEE-RBTS6 node system and the IEEE-RTS79 system to examine the applicability of the model.

4.1 IEEE-RBTS6 system

The original topology and parameters of the RBTS6 node system are presented in reference (Yang et al., 2022). This paper proposes a modification to the existing system. Assuming Bus 3 to represent the 220 kV side of a certain substation, adopting a double busbar configuration, and being connected to the low voltage level network through two main transformers, the modified RBTS-6 node system (System A) is illustrated in Figure 5, the topology of the system A.

In Figure 5, the right half illustrates the original topology of the RBTS-6 node system, while the left half, enclosed by the dashed box, represents the primary bus configuration of Bus3. Incoming lines L1, L6, L4, and L5 carry power through transformers within the substation to supply the low-voltage system. L1 and L6 are double-circuit transmission lines on the same tower. When the entire substation undergoes a complete shutdown for maintenance,

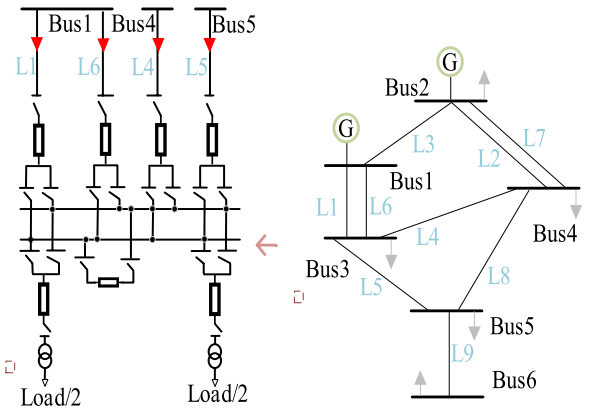

FIGURE 5
Topology of the system A.

all four incoming lines are disconnected from the load at BUS3. The loads of the two transformers are equal.

In this case, the construction cost coefficient for each load transfer line is $300,000 per line. The temporary line connection cost is $2,000 per meter (including the cost of tower construction). The load penalty cost coefficient is $5,000 per MWh, The power loss due to the absence of constructed power transfer lines is set as $0.596 per kWh. The maintenance period is set as 30 days. Based on the parameters mentioned above, The following 5 maintenance strategies are analyzed:

1) Method 1: No maintenance measure is adopted.
2) Method 2: Constructing a power supply route within the substation without external line combination.
3) Method 3: Constructing a power supply route within the substation and performing external line combination.
4) Method 4: Constructing two power supply routes within the substation without performing external line combination.
5) Method 5: Constructing two power supply routes within the substation and performing external line combination.

The optimized results for the best planning scenarios are presented in the following Table 1:

The optimal topology diagrams corresponding to the above-mentioned strategies are depicted in the Figure 6, the optimal topology diagram:

When constructing multiple power paths, the total cost is much lower compared to constructing a single path or not constructing any, with a difference of nearly tenfold. This is mainly due to the significant cost of load loss during the maintenance period. Furthermore, when comparing Method 2 with Method 3, and Method 4 with Method 5, it can be observed that using external line connections actually leads to higher costs. This is because, regardless of whether external line connections are constructed or not, the system's generation cost remains the same, while line connections add extra investment costs.

Comparing the power flow in the system before maintenance and during maintenance using methods 4 and 5, as shown in Figure 7, the comparison of power flow results between Method 4 and Method 5 in system A.

By connecting the lines as shown in figure (c), it can be observed that the connected lines share the power burden of L8, resulting in a reduction of about one-third in its power load. Therefore, though the method of connecting lines doesn't directly impact the system's operational cost and adds extra investment cost, it enhances the system's security in two ways: it resolves the long-term outage issue of the L4 and L5 lines; it alleviates the flow burden on L8, which enhances the transmission margin of the system.

In conclusion, during the maintenance of the substation, both the construction of load transfer lines and the temporary combination of incoming lines not only affect the initial investment and construction costs but also play a significant role in enhancing the system's reliability and security.

4.2 IEEE-RTS79 system

The original topology and network parameters of the IEEE-RTS79 system are presented in reference (Kim et al., 2022). Based on the IEEE-RTS79 system, we assume that the node Bus21 is substation with a double-bus configuration, the power is transmitted to the system through two main transformers. The modified IEEE-RTS79 system (System B) is illustrated in Figure 8, the topology of the system B.

TABLE 1 Optimization results for maintenance plans in System A substation under four different shutdown methods.

Maintenance method	Cost/×10,000$				
	Total cost	Investment cost		Integrated operation cost	
		Investment construction	Comprehensive cost	Generation operation	Load shedding penalty
Method 1	3761.49	0	3647.52	113.97	0
Method 2	2011.92	10	1823.76	178.17	0
Method 3	2071.92	70	1823.76	178.17	0
Method 4	306.74	20	−5.7	286.74	0
Method 5	328.74	41.99	−5.7	286.74	0

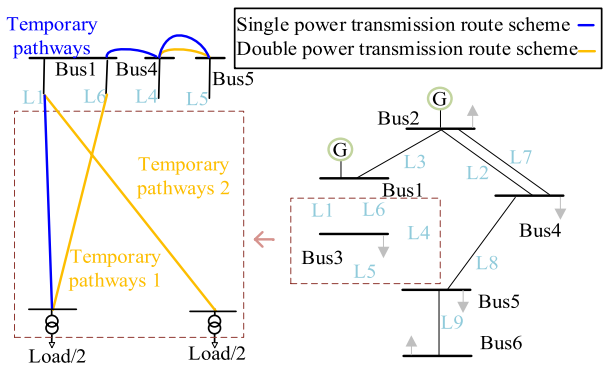

FIGURE 6
Optimal topology diagram.

In Figure 8, electrical power is transmitted through two transformers to 5 incoming lines marked L1-L5. When the substation undergoes a complete shutdown for maintenance, the external incoming lines are affected and shut down. The generating units at BUS21 in the system B lose its connection path to the system. As a result, the system experiences a shortfall in power supply, and it weakens the network architecture of the original system. Therefore, the maintenance plan for System B is analyzed using the load transfer planning model described in this paper. The parameters are the same as described in Section 3.1, the following 5 maintenance strategies are analyzed:

1) Method 1: Not adopting any maintenance measures
2) Method 2: Constructing a power supply route within the station without external line combination

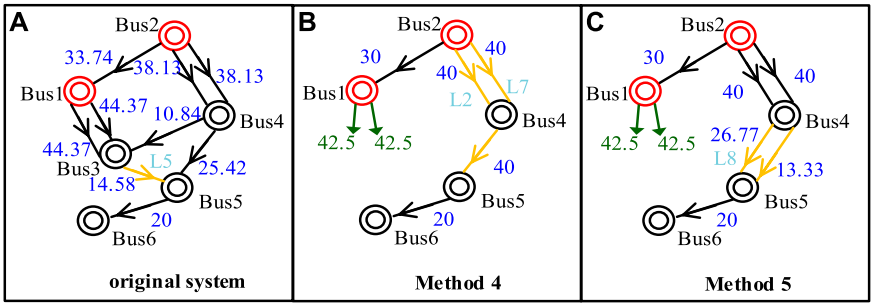

FIGURE 7
Comparison of power flow results between Method 4 and Method 5 in system A.

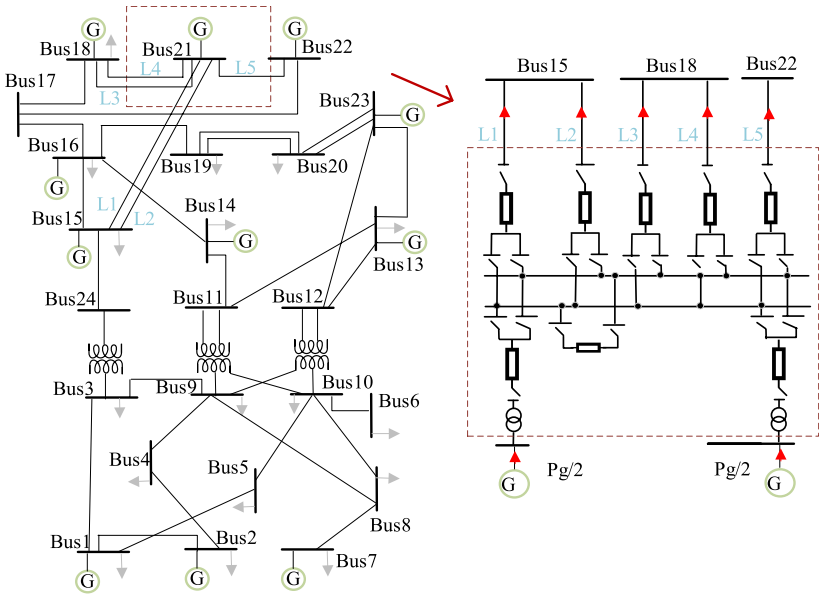

FIGURE 8
Topology of the system B.

TABLE 2 Optimization results for maintenance plans in System B substation under four different shutdown methods.

Maintenance method	Cost/10,000$				
	Total cost	Investment cost		Integrated OperationCost	
		Investment construction	Comprehensive cost	Generation operation	Load shedding penalty
Method 1	5737.3	0	0	5737.3	0
Method 2	5112.1	30	−30	5082.1	0
Method 3	5176.1	84	−30	5082.1	0
Method 4	4535.3	60	−60	4435.3	0
Method 5	4561.3	86	−60	4435.3	0

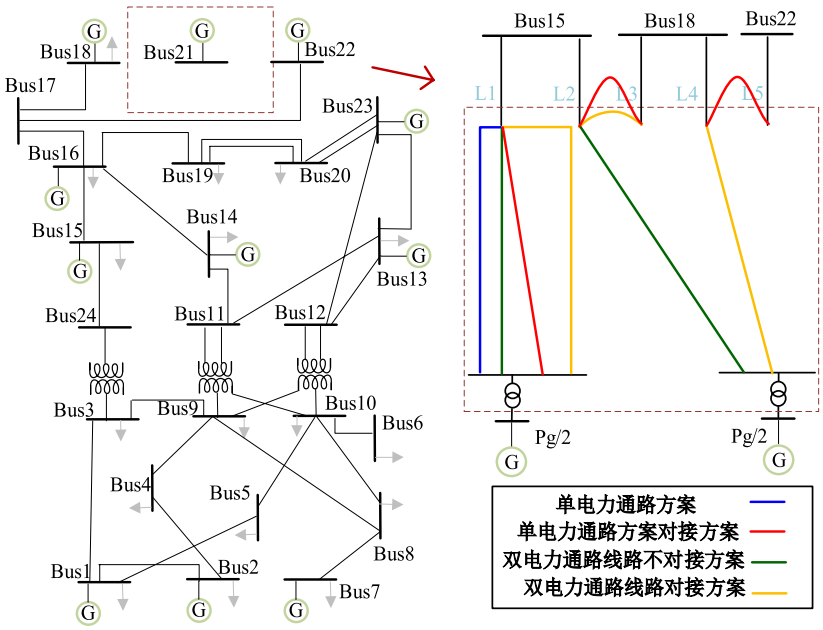

FIGURE 9
Optimal topology diagram.

3) Method 3: Constructing a power supply route within the station and performing external line combination
4) Method 4: Constructing two power supply routes within the station without performing external line combination
5) Method 5: Constructing two power supply routes within the station and performing external line combination

The optimized results for the best planning scenarios are presented in the Table 2:

The optimal topology structures for the above scenarios are shown in the following Figure 9, the optimal topology diagram:

From Table 2, it can be seen that when multiple load transfer routes are constructed within the substation, the total cost is much lower compared to not constructing load transfer routes or constructing only one load transfer route. The main reason for this is that the operating costs of the connected generating units are lower within the station when there are multiple load transfer routes: in other words, the economic viability of a single generator producing a high power output is not as favorable as that of multiple generators producing lower power outputs.

In addition, by comparing Method 2 with Method 3 and Method 4 with Method 5 reveals that using external line connections actually results in higher costs for the system. This is because, regardless of whether external line connections are used or not, the system's generation costs remain unchanged, while line connections introduce additional investment costs. The main reason for this phenomenon is the high generation capacity reserve in the

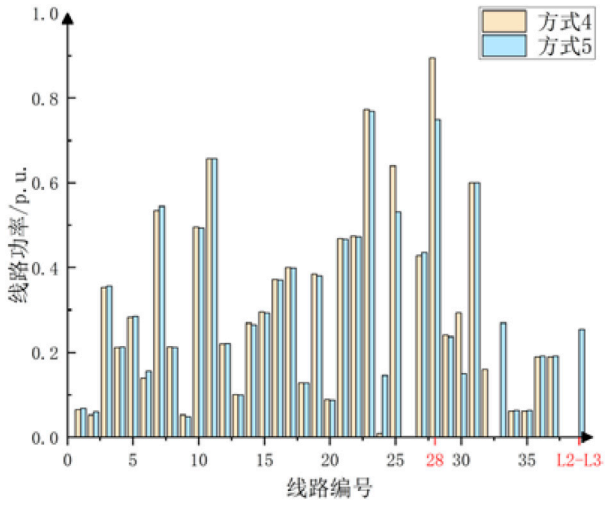

FIGURE 10
Comparison of power flow results between Method 4 and Method 5 in system B.

RTS79 system. Even when considering the load demand at peak levels and the outage of generator at Bus21, the system still has surplus generation capacity, which is sufficient to ensure a balanced power supply. Simultaneously, the rated capacities of the transmission lines are very high, and there will not be issues of transmission congestion. Therefore, the external line connection will not affect generator outputs or improve overload of lines.

To validate the impact of incoming lines connection on the improvement of system load flow distribution, an analysis was conducted on the load flow distribution of the lines in System B under maintenance methods 4 and 5, respectively. The results are illustrated in the following Figure 10, the comparison of power flow results between Method 4 and Method 5 in system B.

It can be observed that in the case of Method 4, the load in Line 28 approaches 0.9 p.u., which is close to its rated capacity. Based on the topology diagram shown in Figure 8, Line 28 is a transmission line located between BUS16 and BUS17. Under maintenance method 4, with the line between BUS15 and BUS21 out of service, leading to a significant increase in power transmission through Line 28. However, by connecting the lines L2 and L3, a new path is created between BUS15 and BUS18, which effectively reducing the load on Line 28. Therefore, under maintenance mode 5, Line 28 has a higher transmission margin, which improved the reliability of the system.

5 Conclusion

This study has established a load transfer planning model during the equipment maintenance in the substation. Drawing upon transmission network planning theory, an analysis has been conducted to highlight the similarities and differences between maintenance planning and transmission network planning. The study presents the optimization objectives, maintenance constraints, power balance constraints, and network operation safety constraints for the load transfer planning model. Furthermore, these constraints have been linearized to facilitate ease of solution. The analysis of case studies using IEEE-RBTS6 and IEEE-RTS79 demonstrates that:

(1) In the case of the IEEE-RTS6 system, compared to methods without constructing load transfer pathways and methods with the construction of a single load transfer pathway, the introduction of two load transfer pathways results in a reduction of 21% and 12% in the operational costs of generating units respectively. Furthermore, by implementing an internal load transfer pathway within the substation, it effectively mitigates economic losses caused by the load losses, leading to a noticeable enhancement in economic feasibility. Upon connecting external incoming lines, there is a slight increase in the cost of load transfer, but it simultaneously reduces the transmission power on the line with the highest load by 33%, thus improving the system's safety and reliability.

(2) In case of the IEEE-RTS79 system, the construction of the load transfer pathway effectively prevents the increase in operating costs for the generators in the system caused by the shutdown of the power source directly connected the substation undergoing maintenance. Compared to methods without constructing load transfer pathways and methods with the construction of a single load transfer pathway, the introduction of two load transfer pathways results in a reduction of 91% and 84% in the operational costs of generating units respectively, which demonstrating a noticeable improvement in economic feasibility. Upon connecting external incoming lines, there is a slight increase in the cost of load transfer, but it simultaneously reduces the transmission power on the line with the highest load by 15%.

In conclusion, the model proposed in this paper can be applied to optimize load transfer planning during substation equipment maintenance. The case study results demonstrate that by constructing internal load transfer pathways within the substation and connecting incoming lines out of the substation, it is possible to effectively reduce the system's economi

Data availability statement

The raw data supporting the conclusion of this article will be made available by the authors, without undue reservation.

Author contributions

KZ: Conceptualization, Project administration, Writing–original draft. TW: Data curation, Formal Analysis, Writing–original draft. HZ: Funding acquisition, Investigation, Writing–original draft. HL: Methodology, Writing–original draft. AT: Project administration, Supervision, Writing–original draft. HY: Validation, Writing–original draft. JP: Visualization, Writing–original draft.

Funding

The author(s) declare financial support was received for the research, authorship, and/or publication of this article. This work is supported by the Key R&D Program of Hubei Province (2023BAB002); and the Science and technology project of State Grid Hubei Electric Power Co., Ltd. (52153223000A).

Conflict of interest

The authors declare that the research was conducted in the absence of any commercial or financial relationships that could be construed as a potential conflict of interest.

The authors declare that this study received funding from the Science and technology project of State Grid Hubei Electric Power Co., Ltd. (52153223000A). The funder had the following involvement in the study: the decision to submit it for publication.

Publisher's note

References

Bagen, B., Huang, D., and Fattal, K. (2019). Enhanced probabilistic approach for substation reliability assessment. IET Generation. *Transm. Distribution* 13 (12), 2488–2495. doi:10.1049/Q17iet-gtd.2019.0133

Chen, B., and Wang, L. (2016). Robust transmission planning under uncertain generation investment and retirement. *IEEE Trans. Power Syst.* 31 (6), 5144–5152. doi:10.1109/TPWRS.2016.2538960

Ding, M., and Feng, Y. Research on the modeling and algorithm to global generator and transmission maintenance scheduling. *Proc. CSEE*, 2004, (05): 22–27. doi:10.13334/j.0258-8013.pcsee.2004.05.004

Gao, S., Song, T. E., Liu, S., Zhou, C., Xu, C., Guo, H., et al. (2021). Joint optimization of planning and operation in multi-region integrated Energy systems considering flexible demand response. *IEEE Access* 9, 75840–75863. doi:10.1109/ACCESS.2021.3081798

Garcí a-Bertrand, R., and Mí nguez, R. Dynamic robust transmission expansion planning. *IEEE Trans. Power Syst.*, 2017,32(4): 2618–2628. doi:10.1109/tpwrs.2016.2629266

Han, X., Qiang, S. I., Yu, C., Chen, Z., Wang, C., Luo, W., et al. (2019). Distribution network self-healing optimization method based on mixed-integer linear programming. *Smart Grid* 47 (06), 107–112+126. doi:10.3969/j.issn.1673-7598.2019.06.016

Kim, Y.-K., Lee, G.-S., Yoon, J.-S., and Moon, S.-I. (2022). Evaluation for maximum allowable capacity of renewable Energy source considering AC system strength measures. *IEEE Trans. Sustain. Energy* 13 (2), 1123–1134. doi:10.1109/TSTE.2022.3152349

Liu, D., Cheng, H., Jia, L., Zeng, P., Zhang, J., and Lu, J. Review and prospects of robust transmission expansion planning. *Power Syst. Technol.*, 2019, 43(1): 135–143. doi:10.13335/j.1000-3673.pst.2018.1351

Liu, D., Lu, L., Cheng, H., Li, A., Gang, L., and Zhang, X. (2021). Transmission network planning method based on the generalized master-slave splitting theory and coordination with distribution networks. *Proc. CSEE* 41 (17), 5856–5866. doi:10.13334/j.0258-8013.pcsee.201322

Liu, Z., Yu, H., Wang, S., Shi, R., Wang, Z., and Luo, Y. (2018). Comprehensive transmission network planning, considering both operational efficiency and wind curtailment losses. *Power Syst. Technol.* 42 (03), 827–834. doi:10.13335/j.1000-3673.pst.2017.1354

Majidi-Qadikolai, M., and Baldick, R. (2016). Stochastic transmission capacity expansion planning with special scenario selection for integrating N-1 contingency analysis. *IEEE Trans. Power Syst.* 31 (6), 4901–4912. doi:10.1109/tpwrs.2016.2523998

Mavalizadeh, H., Ahmadi, A., and Heidari, A. (2014). Probabilistic multi-objective generation and transmission expansion planning problem using normal boundary intersection. *IET Gener. Transm. &Distribution* 9 (6), 560–570. doi:10.1049/iet-gtd.2014.0278

Ma, Y., Wang, W., and Wen, Q. (2015). Transmission network planning based on the chaotic search strategy and bat algorithm. *Power Syst. Prot. Control* 43 (15), 17–21. JournalArticle/5b3beda1c095d70f0099191a.

Qi, Z., Junjie, Q., Dahai, Y., et al. (2018). "Risk assessment for transmission network planning scheme based on conditional value-at-risk," in 2018 8th International Conference on Power and Energy Systems (ICPES), Colombo, Sri Lanka, 21-22 December 2018, 49–53.

Qian, X., Fang, B., Zhou, L., Cheng, H., and Jia, L. Research on the embedding and transformation methods of loss-of-load probability constraints in transmission network planning models. *Power Syst. Technol.*, 2018, 42(06): 1760–1768. doi:10.13335/j.1000-3673.pst.2017.2659

Samarakoon, H. M. D. R. H., Shrestha, R. M., and Fujiwara, O. (2001). A mixed integer linear programming model for transmission expansion planning with generation location selection. *Int. J. Electr. Power & Energy Syst.* 23 (4), 285–293. doi:10.1016/s0142-0615(00)00042-9

Sarantakos, I., Greenwood, D. M., Yi, J., et al. A method to include component condition and substation reliability into distribution system reconfiguration. *Int. J. Electr. Power & Energy Syst.*, 2019, 109: 122–138. doi:10.1016/j.ijepes.2019.01.040

Wang, J., Chen, H., Zhang, Y., and Huang, H. Basic studies on risk management of power grid operation. *South. Power Syst. Technol.*, 2015, 9(02): 1–8. doi:10.13648/j.cnki.issn1674-0629.2015.02.001

Yang, H., Zhang, K., and Tang, A. (2022). Risk assessment of main electrical connection in substation with regional grid safety constraints. *IEEE Access* 10, 27750–27758. doi:10.1109/ACCESS.2022.3157750

Zhang, X., and Conejo, A. J. (2018). Robust transmission expansion planning representing long-and short-term uncertainty. *IEEE Trans. Power Syst.* 33 (2), 1329–1338. doi:10.1109/tpwrs.2017.2717944

Zhang, H., Cheng, H., Zeng, L., Zhang, J., Lu, J., and Cong, L. (2017). Overview of transmission network expansion planning based on stochastic optimization. *Power Syst. Technol.* 41 (10), 3121–3129. doi:10.13335/j.1000-3673.pst.2017.1176

Zhuo, Z., Du, E., Zhang, N., Kang, C., Xia, Q., and Wang, Z. (2020). Incorporating massive scenarios in transmission expansion planning with high renewable Energy penetration. *IEEE Trans. Power Syst.* 35 (2), 1061–1074. doi:10.1109/TPWRS.2019.2938618

Nomenclature

p_t	the power value carried by the transformer t before maintenance
p_{di}	the equivalent power capacity connected to node i
m_t	whether the main transformer is restored with power through the internal power supply transfer path
T	the set of main transformers
n_t	hether the specific main transformer is disconnected under the current maintenance mode
C	the integrated cost
$\overline{p_{li}}$	the rated capacity value of the line (MW)
N	the set of system nodes
N_G	the set of system generator nodes
T_M	the maintenance time (h)
V	the voltage level of the substation(kV)
p_{gi}	the active power output of the generator (MW)
p_{ci}	the load shedding at node due to substation maintenance (MW)
x_i	whether the i-th power supply transfer path is constructed or not
y_{li}	whether the i-th incoming line combination is constructed or not
c_i	the load shedding penalty cost coefficient ($/MWh)
c_{xi}	the comprehensive cost of constructing and maintaining power supply transfer paths($)
c_{ri}	the comprehensive cost of investment and construction of the i temporary line combination ($)
c_{trans}	the investment load shedding penalty cost coefficient ($)
T_c	the load shedding time (h)
p_{li}	the active power flow passing through the branch i (MW)
θ_i	the phase angle at node (rad)
$f_p(\cdot)$	the cost function of the generator
N_x	the set of feasible power supply transfer paths
N_r	the set of temporary line combinations
n_t	the number of transformers disconnected from the transmission system in the substation during maintenance
a	the number of incoming lines outages during maintenance
L_i	the number of each outage line
X	the connectivity status of L_i to the transformers during the maintenance
x_i	a 0–1 integer variable
r_{ij}	a binary integer variable 0–1
N_{dl}	the set of double-circuit lines with the same starting and ending buses
b_i	the admittance of branch i
θ_{fi}	the phase angle at the starting node of branch i
θ_{ti}	the phase angle at the ending node of branch i
L_0	transmission lines in the power grid that are not directly connected to the substation
L^-	incoming lines that are planned to be shut down due to maintenance
L^+	the set of lines that can be temporary combined
y_{li}	represents the state of each line in set L^+
N_{ig}	the set of generators connected to node i
p_{di}	the load demand at node i
p_{lj}	the incoming power at a node i respectively
p_{lt}	he outgoing power at a node i respectively
N_{nonG}	the set of non-generator nodes
p_{gim}	the output of the m-th generator connected to node i
p_{gi}	the total output of generator at node i
$\overline{p_{gi}}$	represent the upper limits of generator outputs respectively
$\underline{p_{gi}}$	represent the lower limits of generator outputs respectively
x_{gm}	the generator output in m–th segment of the cost linearization function
$k_p(\cdot)$	multiple sets of piecewise linear function
M	the total number of linearized segments of the generator cost function
M_{xi}	M values of the large M method
M_{li}	M values of the large M method

Frontiers in
Energy Research

Advances and innovation in sustainable, reliable and affordable energy

Explores sustainable and environmental developments in energy. It focuses on technological advances supporting Sustainable Development Goal 7: access to affordable, reliable, sustainable and modern energy for all.

Discover the latest Research Topics

See more →

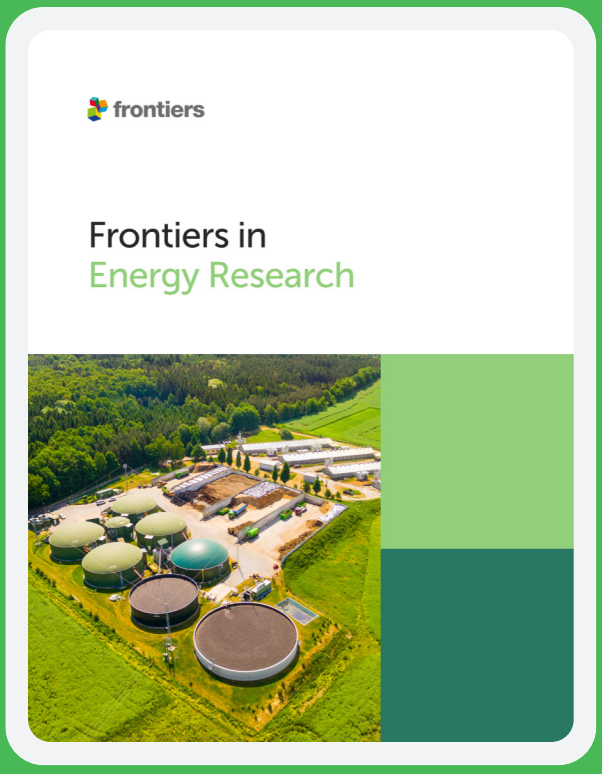

Frontiers

Avenue du Tribunal-Fédéral 34
1005 Lausanne, Switzerland
frontiersin.org

Contact us

+41 (0)21 510 17 00
frontiersin.org/about/contact